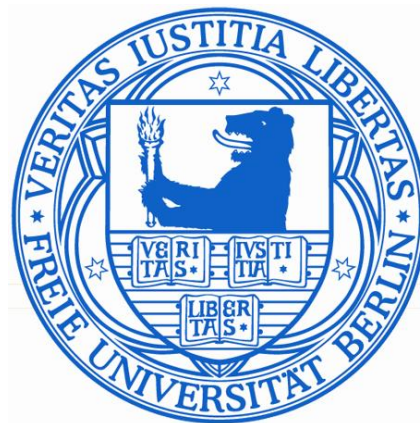


Ultrafast Relaxation Dynamics after Optical Excitation of Hybrid Inorganic/Organic Systems

Ultraschnelle Relaxationsprozesse
nach optischer Anregung von
anorganisch/organischen Hybridsystemen



Im Fachbereich Physik
der Freien Universität Berlin
eingereichte

Dissertation

zur Erlangung des Grades eines
Doktors der Naturwissenschaften
vorgelegt von

Lea Bogner

Berlin, November 2015

This work was performed between June 2011 and March 2013 in the group Prof. Dr. Petra Tegeder in the Department of Physics, Freie Universität Berlin and from April 2013 until November 2015 in the group of Dr. Julia Stähler in the Department of Physical Chemistry (Director: Prof. Dr. Martin Wolf) at the Fritz Haber Institute of the Max Planck Society.

Berlin, November 2015

Erstgutachterin: Prof. Dr. Petra Tegeder

Zweitgutachter: Prof. Dr. Martin Wolf

Datum der Disputation: 04.12.2015

Abstract

This work focuses on fundamental processes which influence the efficiencies of organic solar cells and LEDs, for instance the formation and decay dynamics of excitons, their diffusion, the charge transfer at interfaces between organic materials and inorganic electrodes and the correlated energy level alignment at these interfaces. These processes are investigated on the basis of four model systems, which represent different parts of a solar cell or an LED, by means of time-resolved photoelectron spectroscopy which facilitates the measurement of occupied and unoccupied states as well as the acquisition of ultrafast processes.

ZnO is a promising material for transparent electrodes and as an active LED medium, therefore the processes in optically excited ZnO are of great interest. The investigations show that the electronic structure of the O-terminated ZnO surface is strongly influenced by the adsorption of hydrogen and that the exciton formation slows down at higher electron densities at the surface as the electron phonon coupling is screened.

The SP6/ZnO interface can serve on the one hand as a model system for charge transfer processes, however SP6 in thick films represents a potential LED medium. In addition to the already known relaxation processes which have been observed before by time-resolved optical spectroscopy, photoelectron spectroscopy reveals another ultrafast component. The interaction of long-lived triplet states results in this system in the emission of electrons. Furthermore, photoelectron spectroscopy allows to draw conclusions on the absolute energies of the excited states.

The energy level alignment at the interface between a metal electrode and π -conjugated molecules is investigated on dicyanovinyl-substituted oligothiophenes on gold. The gold surface influences not only the electronic structure of the monolayer, it also significantly affects the lifetimes of excited states that increase with the distance to the metal surface.

As a model system for a polymer semiconductor P3HT was established. The investigation of two films with different amounts of crystalline fractions shows that the relaxation dynamics proceeds faster in the film that features higher crystallinity and therefore superior transport properties.

These results give an insight into the complex interrelated relaxation processes of optically excited states. The detailed comprehension of these processes promises their targeted utilization to optimize the efficiency of organic solar cells and LEDs.

Deutsche Kurzfassung

Diese Arbeit befasst sich mit fundamentalen Prozessen, welche die Effizienz organischer Solarzellen und LEDs beeinflussen, beispielsweise die Entstehungs- und Zerfallsdynamik von Exzitonen, deren Diffusion, der Ladungstransfer an Grenzflächen zwischen organischen Molekülen und anorganischen Elektroden und der damit korrelierten Anordnung der Energieniveaus an diesen Grenzflächen. Anhand von vier Modellsystemen, welche unterschiedliche Teile einer Solarzelle oder LED darstellen, werden diese Prozesse mittels zeitaufgelöster Photoelektronenspektroskopie, welche die Messung besetzter und unbesetzter Zustände, sowie die Erfassung ultraschneller Prozesse ermöglicht, untersucht.

ZnO ist ein vielversprechendes Material für transparente Elektroden und als aktives LED-Medium, weshalb die Prozesse in optisch angeregtem ZnO von großem Interesse sind. Die Untersuchungen zeigen, dass die elektronische Struktur der O-terminierten ZnO-Oberfläche stark durch Adsorption von Wasserstoff beeinflusst wird und dass die Exzitonentstehung mit größerer Elektronendichte an der Oberfläche langsamer wird, da die effiziente Elektron-Phonon-Kopplung abgeschirmt wird.

Die SP6/Zn-Grenzfläche dient einerseits als Modellsystem für Ladungstransfer, in dicken Filmen jedoch stellt SP6 ein potentiell LED-Medium dar. Zusätzlich zu den bereits bekannten Relaxationsprozessen, die mit zeitaufgelöster optischer Spektroskopie beobachtet wurden, zeigt die Photoelektronenspektroskopie eine weitere ultraschnelle Komponente. Die Wechselwirkung langlebiger Tripletzustände führt in diesem System zur Emission von Elektronen. Außerdem erlaubt die Photoelektronenspektroskopie Rückschlüsse auf die absoluten Energien der angeregten Zustände.

Die Anordnung molekularer Energieniveaus an der Grenzfläche zwischen einer Metallelektrode und π -konjugierten Molekülen wird an dicyanovinyl-substituierten Oligothiophenen auf Gold untersucht. Die Goldoberfläche hat nicht nur Einfluss auf die elektronische Struktur der Monolage, sie beeinflusst auch erheblich die Lebensdauer der angeregten Zustände, welche mit dem Abstand zur Metalloberfläche zunimmt.

Als Modellsystem für einen polymeren Halbleiter wurde P3HT eingesetzt. Die Untersuchung zweier Filme mit unterschiedlich großen kristallinen Anteilen zeigt, dass die Relaxationsdynamik in dem Film schneller abläuft, der die größere Kristallinität und somit die besseren Transporteigenschaften aufweist.

Diese Ergebnisse geben einen Einblick in die komplexen zusammenhängenden Relaxationsprozesse optisch angeregter Zustände. Das detaillierte Verständnis dieser Prozesse verspricht deren gezielte Ausnutzung, um die Effizienz von organischen Solarzellen und LEDs zu optimieren.

Contents

Abstract	I
Deutsche Kurzfassung	III
List of Figures	XIII
List of Abbreviations	XIV
1 Introduction	1
2 Theoretical Background	7
2.1 Metal and Semiconductor Surfaces and Interfaces	8
2.1.1 Electronic States at Metal Surfaces	8
2.1.2 Energy Level Alignment at Metal/Organic Interfaces	11
2.1.3 Band Bending at Semiconductor Surfaces	14
2.2 Elementary Excitations in Semiconductors	17
2.2.1 Elementary Excitations in Inorganic Semiconductors	18
2.2.2 Excitons in Organic Semiconductors	21
3 Investigated Systems	29
3.1 Electronic Properties and Excited State Dynamics at the Mixed- and the O-terminated ZnO Surface	30
3.1.1 Morphology of the O- and the Mixed-terminated ZnO Surface	32
3.1.2 Surface Metallization due to H-adsorption on ZnO Surface . .	33
3.1.3 Surface Exciton Dynamics at ZnO Surfaces	36
3.2 Electronic Structure and Excited State Dynamics in SP6 on ZnO . .	39
3.3 Electronic Structure of Dicyanovinyl-Substituted Oligothiophenes on Au(111)	43
3.3.1 Adsorption and Electronic Properties of DCV5T-Me ₂ /Au(111)	46
3.3.2 Adsorption and Electronic Properties of DCV6T/Au(111) . .	48
3.4 Electronic Structure of the Au(111) Surface	50
3.5 P3HT: Electronic Structure, Excited State Dynamics and the Influ- ence of Crystallinity	53
4 Methods and Experimental Details	59
4.1 Photoelectron Spectroscopy	59
4.1.1 Two-Photon Photoemission	61
4.1.2 Time-Resolved Two-Photon Photoemission	65
4.1.3 2PPE <i>vs.</i> Optical Spectroscopy	69

4.2	Experimental Setup	71
4.2.1	The Femtosecond Laser System	71
4.2.2	Pulse Characterization	74
4.2.3	The Ultrahigh Vacuum Chamber	75
4.2.4	Electron Analysers	79
4.3	Sample Preparation	85
4.3.1	Preparation of the O-terminated ZnO Surface and Quantification of the H-Dosage	85
4.3.2	Preparation of the SP6 Films and Determination of the Film Thickness Using a Quartz Microbalance	87
4.3.3	Preparation of the DCV6T and DCV5T-Me ₂ Films on Au(111)	91
5	Results	95
5.1	H-induced Metallicity and Excited State Dynamics at the O-terminated ZnO Surface	96
5.1.1	Hydrogen Induced Metallicity at the O-terminated ZnO Surface	97
5.1.2	Surface Exciton Formation and Decay Dynamics at the H-doped Polar ZnO Surface	104
5.2	Exciton Formation and Decay Dynamics in SP6 Films on ZnO	113
5.2.1	Ultrafast Dynamics of Excited States in SP6 Films	114
5.2.2	Triplet-Triplet Annihilation Leading to Electron Emission	123
5.3	Electronic Structure and Excited State Dynamics in DCV-substituted Oligothiophenes on Au(111)	135
5.3.1	Coverage-Dependent Electronic Structure of DCV5T-Me ₂ on Au(111)	136
5.3.2	Coverage-Dependent Electronic Structure of DCV6T/Au(111)	143
5.3.3	Excited State Dynamics in DCV5T-Me ₂ on Au(111)	147
5.3.4	Excited State Dynamics in DCV6T on Au(111)	150
5.4	Electronic Properties of P3HT Films and the Influence of Crystallinity	155
5.4.1	Electronic Structure of P3HT Films with Different Degrees of Crystallinity	156
5.4.2	Influence of Crystallinity on the Excited State Dynamics in P3HT Films	161
6	Summary and Conclusions	165
A	Mass Spectra and TPD of DCV6T & DCV5T-Me₂	169
B	Calculation of the Excitation Density	173

C Differential Equation Solution	175
References	197
Acknowledgement	200
Academic Curriculum Vitae	201
List of Publications	203

List of Figures

2.1	Schematic of a bilayer solar cell	7
2.2	Schematic depiction of an image charge and image potential states	9
2.3	Schematic of (a) charge density distribution at a metal surface, (b) relevant energies connected to the work function	11
2.4	Vacuum level alignment for (a) low and (b) high work function metals, (c) interface dipole induced work function change	12
2.5	Fermi level pinning for (a) low and (b) high work function metals	13
2.6	Decrease of HOMO-LUMO gap due to interaction with a metal surface	13
2.7	(a) Upward and (b) downward band bending at metal and n -type semiconductor contacts	14
2.8	(a) Upward surface band bending at the clean ZnO(000 $\bar{1}$) surface, (b) reversed surface band bending upon H-adsorption	15
2.9	Excitation and electron-hole pair formation in (a) an inorganic and (b) an organic semiconductor. (c) Delocalized Mott-Wannier exciton and (d) localized Frenkel exciton	17
2.10	(a) Excitation below and (b) above the Mott density	18
2.11	(a) Surface photovoltage at low excitation density, (b) enhanced surface photovoltage at higher excitation density	20
2.12	Illustration of the exciton binding energy in an organic semiconductor	21
2.13	Probing (a) an occupied, (b) an unoccupied state and (c) an excitonic state with 2PPE	22
2.14	(a) Singlet and (b) triplet exciton. (c) Jablonski diagram	24
2.15	(a) Förster and (b) Dexter transfer	26
3.1	Hexagonal unit cell of ZnO	31
3.2	(a) Mixed-terminated ZnO(10 $\bar{1}$ 0) and (b) O-terminated ZnO(000 $\bar{1}$) surface	32
3.3	Schematic of the energy band structures of the clean and H-covered ZnO(10 $\bar{1}$ 0) surface, adopted from [Oza10]	34
3.4	Evolution of work function and CAL intensity as a function of H-dosage, adopted from [Dei15b]	35
3.5	(a) Excitation density and (b) H-dosage dependent pump-induced signal of H ₂ /ZnO(10 $\bar{1}$ 0), adopted from [Dei14]	37
3.6	Lewis formula and ball and stick model of SP6	39
3.7	Energy level diagrams for SP6/ZnO and SP6/ZnMgO, adopted from [Blu08]	40

3.8	(a) τ_{POP} vs. probe photon energy obtained from excited states transmission, (b) schematic of the involved electronic processes, adopted from [Fog15]	41
3.9	Ball and stick model of (a) DCV5T-Me ₂ and (b) DCV6T	43
3.10	STM images, dI/dV spectra and maps of a DCV5T-Me ₂ island, adopted from [Bog15].	46
3.11	STM images and dI/dV spectra of the second DCV5T-Me ₂ layer	47
3.12	(a) dI/dV spectra and (b) STM image of DCV6T island, adopted from [Yan14a]	48
3.13	(a) Unit cell of the fcc-lattice and (b) the Au(111) surface	50
3.14	(a) STM image of the reconstructed Au(111) surface (image courtesy of E. Varène and Y. Penneç). (b) Sketch of the herringbone reconstruction, adopted from [Nar92]	51
3.15	Calculated bandstructure of gold and Brillouin zone of the fcc-lattice adopted from [Eck84]	52
3.16	Lewis formula of (a) RR-P3HT and (b) RRa-P3HT	53
3.17	(a) Schematic of the microstructure of RR-P3HT, (b) AFM image of a P3HT-mc film, adopted from [Wu10]	54
4.1	Schematic depictions of (a) a PES experiment, (b) electron emission under conservation of the wave vector component parallel to the surface	60
4.2	1C-2PPE pump-probe schemes in case of (a) occupied, (b) unoccupied and (c) final states; (d) corresponding 2C-2PPE schemes	62
4.3	Energy cutoffs in a 2PPE spectrum	63
4.4	Commonly used energy axes in 2PPE spectra	64
4.5	(a) Possible pump-probe schemes during a TR-2PPE experiment, (b) population of an unoccupied state <i>via</i> an electron from the metal or intramolecularly	65
4.6	Exemplary TR-2PPE spectrum of H-doped ZnO, sketch of the pump-probe scheme, XC-traces and spectra of different time delays	67
4.7	Diagram of a 3- and a 4-level system	69
4.8	Probing of the intermediate state population in (a) excited state transmission and (b) 2PPE	70
4.9	Schematic of the laser setup, adopted from [Weg14]	72
4.10	(a) Example laser spectrum and (b) laser intensity profile	74
4.11	Schematic of the UHV chamber	75
4.12	Sketch of the sample holder, adopted from [Hag09]	77
4.13	Schematic of the hemispherical analyser modified from [Bra09]	79
4.14	Schematic of the time-of-flight spectrometer, adopted from [Hag09]	82

4.15	Bias correction	84
4.16	(a) Pressure trace taken during H ₂ dosing, (b) H ₂ cracking by electron emission from the ion gauge filament	85
4.17	QMB trace for the determination of the tooling factor and the SP6 film thickness.	88
4.18	TPDs of SP6/ZnO(10 $\bar{1}$ 0) (a) of a 16 nm thick film and (b) of different film thicknesses	89
4.19	(a) Downfield and (b) upfield H-NMR spectra of SP6 before and after evaporation	90
4.20	2PPE spectra series as a function of DCV6T coverage	91
4.21	Coverage dependent 2PPE spectra of higher DCV6T coverages	92
4.22	2C-2PPE spectra series taken on different coverages DCV5T-Me ₂ on Au(111)	93
5.1	(a) Valence band 2PPE spectra of the ZnO(000 $\bar{1}$) surface, (b) energy level diagram	98
5.2	(a) Direct photoemission spectrum of 100 L H ₂ /ZnO(000 $\bar{1}$), (b) energy level diagram of the pristine and (c) the H-doped surface	99
5.3	(a) Direct photoemission spectra monitoring the CAL build-up with increasing H-dosage, (b) work function decrease and CAL intensity increase as function of H-coverage	100
5.4	(a) Work function and CAL intensity as a function of H ₂ dosage for ZnO(000 $\bar{1}$) and (10 $\bar{1}$ 0), (b) surface unit cells of the two surfaces	102
5.5	Equilibrium and non-equilibrium 2PPE spectra of H-doped polar ZnO	104
5.6	(a) Time-resolved 2PPE spectrum of 100 L H ₂ /ZnO(000-1) (b) XC traces for different energies	105
5.7	(a) Comparison of the measured fast time constants with calculated values from [Zhu10], (b) energy dependent evolution of the relaxation times and SX formation	107
5.8	(a) SX emission signal of 63 L H ₂ /ZnO(000 $\bar{1}$) for different excitation densities. Exciton density (b) below and (c) above the Mott density	108
5.9	Illustration of the electronic processes after photoexcitation, modified from [Dei14]	109
5.10	Comparison of the fast relaxation times of 100 L H ₂ on the (000 $\bar{1}$) and the (10 $\bar{1}$ 0) surfaces	110
5.11	Comparison between the time constants for different total carrier densities and (a) same and (b) different pump photon energies	111
5.12	(a) 2PPE spectra for different time delays, (b) TR-2PPE spectrum of 21 nm SP6/ZnO, (c) XC-traces with triexponential fits	114

5.13	Time constants obtained from triexponential fitting of XC-traces from a TR-2PPE spectrum of 21 nm SP6/ZnO	115
5.14	(a) Excited state transmission <i>vs.</i> (b) 2PPE	116
5.15	Comparison of a 2PPE cross-correlation with a transient transmission trace	118
5.16	Schematic of the time-dependent diffusion model	119
5.17	Schematic of the diffusion model including the exciton diffusion length	119
5.18	(a) Simulated temporal evolution of the S ₁ population, (b) S ₁ start population, (c) comparison of S ₁ population dynamics averaged of the whole SP6 film and at the surface	121
5.19	Normalized 2PPE spectra of 21 nm SP6 on ZnO(10 $\bar{1}$ 0) taken at different delays	122
5.20	(a) Schematic of two laser pulses with different duration, (b) emission intensity as a function of the pulse duration	123
5.21	Overlap of the laser pulses with the triplet population for (a) 200 kHz and (b) 40 kHz, (c) repetition rate dependent spectra of 10 nm SP6/ZnO(10 $\bar{1}$ 0)	124
5.22	(a) 2PPE pump-probe scheme, (b) photon energy dependent spectra series of 20 nm SP6/ZnO(10 $\bar{1}$ 0)	125
5.23	Jablonski diagram illustrating possible excitation energy transfer processes	126
5.24	(a) Triplet-triplet coupling in an autocorrelation experiment, (b) simplified singlet and triplet population decays	127
5.25	Modeled autocorrelation traces for (a) triplet-singlet and (b) triplet-triplet coupling	128
5.26	(a) 2D-spectrum of the autocorrelation measurement, (b) spectra taken at different time delays, (c) background subtracted signal at different time delays	129
5.27	Schematic of the triplet-triplet annihilation process	129
5.28	Fluence dependence of the electron emission signal due to TTA	130
5.29	Temperature dependent spectra of 20 nm SP6 on ZnO	131
5.30	(a) Coverage dependent spectra series of SP6/ZnO(10 $\bar{1}$ 0), (b) background subtraction and peak fitting	132
5.31	Jablonski diagram of the observed processes in SP6/ZnO	133
5.32	(a) 1C-2PPE spectrum of 0.3 ML DCV5T-ME ₂ /Au(111), (b) photon energy dependent peak positions	136
5.33	(a) 2C-2PPE spectrum of 0.3 ML DCV5T-ME ₂ /Au(111), (b) photon energy dependent peak positions	137

5.34	(a) 1C-2PPE spectrum of 0.8 ML DCV5T-ME ₂ /Au(111), (b) peak positions as function of the photon energy	138
5.35	(a) 1C-2PPE spectrum of 0.8 ML DCV5T-ME ₂ /Au(111), (b) peak positions as function of the photon energy	139
5.36	(a) 1C-2PPE spectrum and (b) 2C-2PPE spectrum of 3 ML DCV5T-Me-2/Au(111)	140
5.37	Energy level diagrams of (a) submonolayer, (b) monolayer and (c) multilayer coverages DCV5T-Me ₂ /Au(111)	141
5.38	(a) 2C-2PPE spectra series of 2 ML DCV5T-Me ₂ /Au(111) and (b) peak maxima as a function of the emission angle	143
5.39	(a) 1C-2PPE spectrum of 1.4 ML DCV6T/Au(111), (b) peak positions as function of the photon energy	144
5.40	(a) 2C-2PPE spectrum of 1.4 ML DCV6T/Au(111), (b) peak positions as function of the photon energy	144
5.41	(a) 1C-2PPE and (b) 2C-2PPE spectra of a multilayer DCV6T/Au(111)	145
5.42	Energy level diagram of (a) a monolayer and (b) a multilayer coverage DCV6T on Au(111)	146
5.43	Time-resolved 2PPE spectra of (a) 10 ML and (b) 20 ML DCV5T-Me ₂ /Au(111), (c) spectra taken at t = 0 and (d) corresponding XC-traces	148
5.44	(a) 2PPE spectrum of 20 ML DCV5T-Me ₂ at t= 0 ps, (b) TR-2PPE spectrum and (c) XC-trace	149
5.45	Time-resolved 2PPE spectra of (a) 3 ML and (b) 5 ML DCV6T on Au(111), (c) spectra at t = 0 ps and (d) XC-traces	151
5.46	(a) 2PPE spectrum of a 20 ML thick DCV6T film on Au(111) recorded at t= 0 ps, (b) time-resolved spectrum and (c) XC-trace	152
5.47	Comparison of the XC-traces of 20 ML thick DCV5T-Me ₂ and DCV6T films on Au(111)	153
5.48	Direct photoemission spectra of P3HT-mc and P3HT-as	156
5.49	1C-2PPE spectra of (a) P3HT-mc and (b) P3HT-as films	157
5.50	(a) Photon energy dependent 1C-2PPE spectra series taken on P3HT-mc, (b) peak maxima as a function of the photon energy	158
5.51	2C-2PPE spectra of (a) P3HT-mc and P3HT-as (b) of P3HT-mc at different time-delays	159
5.52	Energy level diagram of (a) P3HT-mc and (b) P3HT-as films	160
5.53	(a) Time-resolved 2PPE spectrum of P3HT-mc, (b) XC-traces with triexponential fits	161

5.54 (a) Time-resolved 2PPE spectrum of P3HT-as, (b) XC-traces with triexponential fits	163
A.1 Mass spectrum of DCV6T	169
A.2 TPD of DCV6T/Au(111) evaporated on the cold surface	170
A.3 TPDs of DCV6T/Au(111) evaporated on the surface at 300 K	170
A.4 Mass spectrum of DCV5T-Me ₂	171
A.5 TPDs of DCV5T-Me ₂ /Au(111)	172
C.1 Simplified model describing singlet and triplet poulation decays	175

List of Abbreviations

1C-2PPE	one-colour 2PPE.
2C-2PPE	two-colour 2PPE.
2PPE	two-photon photoelectron spectroscopy.
8T	octithiophene.
AC	autocorrelation.
A-D-A	acceptor-donor-acceptor.
AFM	atomic force microscopy.
ARPES	angle-resolved photoelectron spectroscopy.
as	as-spun.
ASE	amplified spontaneous emission.
BBO	β -barium borate.
CAL	charge accumulation layer.
CB	conduction band.
CBM	conduction band maximum.
CS	charge separation.
D-A	donor-acceptor.
DCV-	dicyanovinyl-.
DCV5T-Me₂	bimethylated dicyanovinyl-quinquethiophene.
DCV6T	dicyanovinyl-sexithiophene.
DF	delayed fluorescence.
DOS	density of states.
EA	electron affinity.
fcc	face centered cubic.
FHI	Fritz Haber Institute.
FL	fluorescence.
FRET	Förster resonance energy transfer.
fs	femtoseconds.
FU	Freie Universität Berlin.
GaAs	gallium arsenide.
hcp	hexagonal close packed.
HOMO	highest occupied molecular orbital.
ID	interface dipole.
IP	ionization potential.
IPES	inverse photoelectron spectroscopy.
IPS	image potential state.

ISC	intersystem crossing.
ITO	indium tin oxide.
IVR	internal vibrational relaxation.
LEDs	light emitting diodes.
LEED	low-energy electron diffraction.
LO	longitudinal optical.
LUMO	lowest unoccupied molecular orbital.
mc	melt-crystallized.
MCP	micro-channel-plates.
ML	monolayer.
NMR	nuclear magnetic resonance.
OLEDs	organic light emitting diodes.
OPA	optical parametrical amplifier.
OPVC	organic photovoltaic cell.
P3HT	poly(3-hexylthiophene).
PCBM	phenyl-C61-butyric acid methyl ester.
PCE	power conversion efficiency.
PEDT:PSS	poly(ethylenedioxythiophene):poly(styrenesulfonate).
PES	photoelectron spectroscopy.
PH	phosphorescence.
PHD	pinhole doser.
PL	photoluminescence.
ps	picoseconds.
QMB	quartz crystal microbalance.
QMS	quadrupol mass spectrometer.
RGA	rest gas analysis.
RR	regioregular.
RRa	regiorandom.
SFG	sum-frequency generation.
SP6	2,7-bis(biphenyl-4-yl)-2',7'-di- <i>tert</i> -butyl-9,9'-spirobifluorene.
SS	surface state.
STM	scanning tunneling microscopy.
STS	scanning tunneling spectroscopy.
SX	surface exciton.
Ta	tantalum.
TC	thermocouple.
TOF	time-of-flight.
TPD	temperature programmed desorption.

TR-2PPE	time-resolved two-photon photoemission.
TTA	Triplet-triplet annihilation.
UHV	ultrahigh vacuum.
UPS	ultraviolet photoelectron spectroscopy.
VB	valence band.
VBM	valence band maximum.
XC	cross-correlation.
XPS	X-ray photoelectron spectroscopy.
ZnMgO	zinc magnesium oxide.
ZnO	zinc oxide.

1 Introduction

Utilizing solar power to generate electricity is an environmental friendly alternative of power production. The preparation of inorganic solar cells usually requires high energy costs whereas organic solar cells can be produced energy efficiently since the active materials can be synthesized on petroleum basis and only a small amount of material is needed for the molecular/polymer films of nanometer thickness. In addition, organic photovoltaic cells (OPVCs) are of particular interest as they promise light weight and low cost devices and thus a great flexibility for future applications. In contrast to inorganic solar cells the efficiency of OPVCs increases for low light intensities and elevated temperatures, which are often present under real life conditions [Hel15]. However, the maximum efficiencies of organic solar cells are still much lower compared to their inorganic counterparts, e.g. GaAs based thin film solar cells yield maximum efficiencies of 29 % while the maximum efficiency of organic solar cells amounts to 11.0 %, as reported in the latest solar cell efficiency tables [Gre15].

OPVCs typically consist of two different organic materials: A donor material which absorbs light and an acceptor material in which the electrons are conducted towards the electrode. These active materials are either small molecule or polymer based. The photon-to-electron conversion in a solar cell can be described by a five step process: i) Light absorption leading to the formation of an exciton, *i.e.* electron-hole pairs bound by Coulomb interaction. ii) Exciton diffusion towards the donor/acceptor interface followed by iii) the formation of a charge-transfer state, iv) charge separation and v) charge extraction by the electrodes. As light has to get into the device to excite the donor material one of the electrodes needs to be transparent.

In light emitting diodes (LEDs) the process works *vice versa*: Charges are injected into the active materials and form excitons when the charges meet at the interface. In this case the excitons decay *via* electron-hole recombination under the emission of photons. Excitons are, thus, the key quasiparticles in light harvesting and generating devices. The efficiencies of solar cells and LEDs are influenced by several interacting parameters and processes such as the film morphology and the energy level alignment at the interfaces between the electrodes and the organic materials as well as at the organic/organic interfaces. In addition, exciton formation, decay and diffusion as well as charge carrier mobility play a crucial role.

The definition of loss channels depends on the application: While electron-hole recombination under emission of light is desired in LEDs, this process is unwanted in

OPVCs where the excitons need to reach the donor/acceptor interface within their lifetimes in order to be separated. Triplet excitons can also represent either a loss channel in LEDs or a desired species in devices which are based on phosphorescence or fluorescence up-conversion [Hof11]. In order to improve the efficiencies of solar cells and LEDs, a detailed understanding of the elementary electronic processes at the interfaces and within the active materials is required.

This work focuses on the following questions related to fundamental aspects and processes relevant for light-harvesting and generation:

- 1) How do the molecular energy levels align at the interface with the substrate and within the film?
- 2) How and on which time scales do exciton formation and decay occur?
- 3) How do these quasiparticles interact and what is the result of this interaction?
- 4) How are the lifetimes of excitons affected by manipulation of side conditions, e.g. by reducing the distance to the substrate surface or by increasing the temperature?

The materials investigated in this work represent model systems for different active parts of a solar cell or an LED. The electronic processes in optically excited ZnO are of interest for energy transfer in LEDs, but ZnO is also a candidate for transparent electrodes when combining it with an organic semiconductor: The spirobifluorene derivative SP6 is used to investigate, on the one hand, charge transfer processes at the interface with ZnO, but also, on the other hand, as a model system for an LED medium. In order to study the energy level alignment at an interface between a metallic electrode and a donor material, dicyanovinyl(DCV)-substituted oligothiophenes on Au are investigated. In a next step, the complexity is increased by using P3HT, which is a polymer donor material.

The questions presented above are tackled using time-resolved two-photon photoemission (2PPE). 2PPE is a powerful method for the investigation of energy level alignment as it provides access to both occupied and unoccupied states. In addition time-resolved 2PPE allows to measure the excited state dynamics on a femto- to picosecond time scale.

H-induced Metallicity and Excited State Dynamics at the O-terminated ZnO Surface

As mentioned above, ZnO is attractive as active LED medium as well as for the use as transparent electrode material [Blu06]. The influence of hydrogen on the electronic structure and the excited state dynamics in ZnO and its surfaces is of particular interest, as hydrogen is a nearly inevitable impurity under almost all experimental conditions, in production as well as during device operation. From previous studies it is known that a charge accumulation layer (CAL) emerges upon H-adsorption at the

mixed-terminated surface which is reduced for higher H-coverages [Oza11, Dei14]. A 2PPE study on the H-covered non-polar ZnO surface revealed that after photoexcitation the hot electrons relax on an ultrafast timescale *via* scattering with longitudinal optical phonons and subsequently form a surface exciton [Dei14].

In this work, by comparing previous results with those for the fully O-terminated surface, the influence of the Zn-ions on the electronic surface structure and the CAL intensity is investigated. Another question is how the exciton formation dynamics are influenced by enhanced charge carrier density at the ZnO surface. In particular it is shown that H-adsorption on the O-terminated ZnO surface leads to a switch from upward to downward surface band bending and the formation of a CAL which saturates for higher H-coverages. Comparison of these results with those for the non-polar ZnO surface demonstrates that the formation of ZnH-bonds, absent on the polar surface, strongly affects the CAL intensity and the work function. In addition it is shown that both the polar and the non-polar surface can be tuned by H-doping so that they exhibit nearly identical electronic structures at the surface: The hot electron relaxation dynamics at the H-covered polar ZnO surface exhibit a behaviour similar to the one observed for the non-polar surface. Furthermore it is discovered that increasing the total, photo- and H-induced, charge carrier density leads to slower relaxation of the low excess energy electrons due to screening.

With these results I showed that, in the case of ZnO, the electronic surface structure is drastically influenced by adsorption of an electron donor, in particular the work function which is a key ingredient for energy level alignment, and that the intensity of the metallic surface state is highly affected by the formation of ZnH-bonds. In addition, the increased electron density at the surface modifies the scattering of the hot electrons through quasiparticle interactions, thus influencing the surface exciton formation process.

Exciton Formation and Decay Dynamics in SP6 Films on ZnO

The spirobifluorene derivative SP6 exhibits strong blue luminescence making it an ideal medium for LEDs or solid state lasers [Sch04a]. Adsorbed on the non-polar ZnO surface, it forms the type-II level alignment which is required for charge and energy transfer studies [Blu08]. Previous time-resolved excited state transmission experiments on SP6 films on ZnO revealed that after resonant excitation the system relaxes *via* internal vibrational relaxation within several ps [Fog15]. Two excited states were observed which decay on a timescale of 200 ps through several competing pathways, such as electron-hole recombination, formation of a long-lived dark state and diffusion towards the ZnO interface where charge separation occurs. Note that only one of the excited states is affected by the diffusion to the ZnO interfaces

and thus exhibits a faster decay. The dynamics of the long-lived dark state and the absolute energetic positions of the excited states, however, remained unknown and are tackled in this thesis.

First the 2PPE experiments conducted in this work reveal an additional ultrafast decay on a timescale of 300 fs which is most likely related to polarization effects due to the exciton formation process. The subsequent dynamics observed by 2PPE are in good agreement with the results from excited state transmission, although 2PPE is very surface sensitive while optical spectroscopy also probes bulk contributions. Second, the long-lived dark state observed in excited state transmission is related to a triplet state which undergoes triplet-triplet annihilation leading to electron emission. The triplet lifetime is on the order of 25 μ s and decreases for increasing temperatures as the diffusion is enhanced. Furthermore, charge separation at the ZnO interface leads also to a decrease of the triplet lifetime demonstrated by a decrease of the triplet-triplet annihilation induced signal for lower coverages. In addition, the absolute energies of the groundstate and the excited states could be uncovered.

With these results most of the questions formulated above can be answered for the SP6/ZnO model system: Long-lived triplet states were found to decay *via* triplet-triplet annihilation, *i.e.* quasiparticle interaction, and other diffusion-controlled processes, e.g. charge separation at the ZnO interface. In addition, the energy level alignment at the SP6 interface was uncovered and the singlet exciton formation and decay processes could be disentangled merging 2PPE and excited state transmission results.

Electronic Structure and Excited State Dynamics in DCV-substituted Oligothiophenes on Au(111)

Dicyanovinyl(DCV)-substituted oligothiophenes are of high relevance as they yield high power conversion efficiencies as donor materials in small molecule based solar cells. The two molecules investigated in this work, DCV5T-Me₂ and DCV6T, yield significantly different efficiencies despite their similar optoelectronic properties [Fit11, Fit12b]. This behaviour was explained by enhanced intermolecular interactions in the case of DCV5T-Me₂ promoting exciton transport. A recent scanning tunneling microscopy and spectroscopy study (STM/STS) showed that both molecules form well-ordered monolayers on the Au(111) surface [Yan14a]. Moreover it was found that the electron affinity levels in the monolayer shift to lower energies, compared to the molecules in the second layer, due to hybridization with the metal surface. In this work the electronic structure with focus on the occupied states and the electronic structure of the multilayer regime, which were not observed by STS,

are studied. Further questions concern the excited state dynamics and how they are affected by the metal surfaces and the different molecular interactions.

The results gained reveal additional occupied and unoccupied states for several coverage regimes which have not been observed in STS before. The excited state dynamics exhibit a highly coverage dependent behaviour demonstrating efficient charge separation at the metal interface. Comparing the dynamics for both molecules in thick molecular films reveals faster dynamics in the case of DCV5T-Me₂. This can be attributed to the enhanced transport properties resulting from a larger number of intermolecular interactions.

In conclusion, it could be demonstrated that both energy level alignment and excited state lifetime are influenced by the metal substrate and that these influences can be tuned by increasing the distance to the metal surface.

Electronic Properties of P3HT Films and the Influence of Crystallinity

The polythiophene P3HT is a widely investigated polymer due to its high charge carrier mobility. It is known that the degree of crystallinity in P3HT films significantly influences the electronic structure, charge carrier transport and exciton diffusion and dissociation [Pan15, Kan10]. Previous 2PPE studies of P3HT on conductive substrates did not yield well-resolved spectra and, thus, did not succeed in characterizing the electronic structure [Var12c, Soh07].

In this thesis the influence of different degrees of crystallinity on the electronic structure and excited state dynamics is studied. In addition, the question whether the electronic structure of a polymer is at all accessible by 2PPE or if this technique is too surface sensitive will be answered: The 2PPE spectra obtained in this work from two P3HT samples with different degrees of crystallinity allow the determination of the electronic structure demonstrating that 2PPE is applicable as well on polymer films if those are of high chemical and structural purity. Two long-lived states are observed of which one is related to the exciton and the other is most likely due to polaron pairs and/or polarons. The excitonic state is located at lower energies and decays on a slower timescale compared to the polaron pair/polaronic feature. Comparing the dynamics of the two films shows that the dynamics are faster in the film with the higher degree of crystallinity. This behaviour can be explained by the larger fraction of crystalline phases which are known to control and promote the transport properties in P3HT. Nevertheless, both the electronic structure and the excited state dynamics are only weakly affected by the difference in crystallinity.

These results demonstrate that already small changes of the film morphology, which in turn influences the exciton diffusion and charge transport properties, have an impact on the excited state lifetimes.

In summary, several elementary processes relevant for light-harvesting or generation were investigated in four different model systems. First, the transparent conductive oxide ZnO was investigated demonstrating that the electronic surface structure changes significantly upon H-adsorption. It was shown that the exciton formation slows down when the relaxation processes are screened by enhanced charge carrier density at the surface. The processes after photoexcitation of an organic semiconductor were investigated using the model system SP6 on ZnO. The excited state populations were found to decay *via* several competing pathways, as, for example formation of a long-lived triplet state or diffusion towards the ZnO interface where charge separation occurs. Interactions between a metal and an organic semiconductor were studied for two DCV-substituted oligothiophenes, demonstrating that both the energy level alignment and the excited state dynamics are influenced by the metal substrate. In addition enhanced diffusion due to a larger number of intermolecular interactions was found to efficiently increase the decay rates. A higher degree of order in the film morphology of the donor polymer P3HT was found to lead to faster decays, too.

In conclusion, the non-equilibrium dynamics in organic/inorganic hybrid systems can be manifold and are very sensitive to the respective material properties. Key aspects in this context are energy level alignment and diffusion, which strongly influence the potential relaxation pathways of excitons in condensed matter.

2 Theoretical Background

The photophysics of semiconductors plays a crucial role in solar cell and LED technology. The central processes thereby are related to formation, decay and diffusion of bound electron-hole pairs, namely excitons. While in inorganic solar cells both excitons and free carriers can be generated in the same material, organic solar cells need two different active materials, the donor and the acceptor material. Figure 2.1

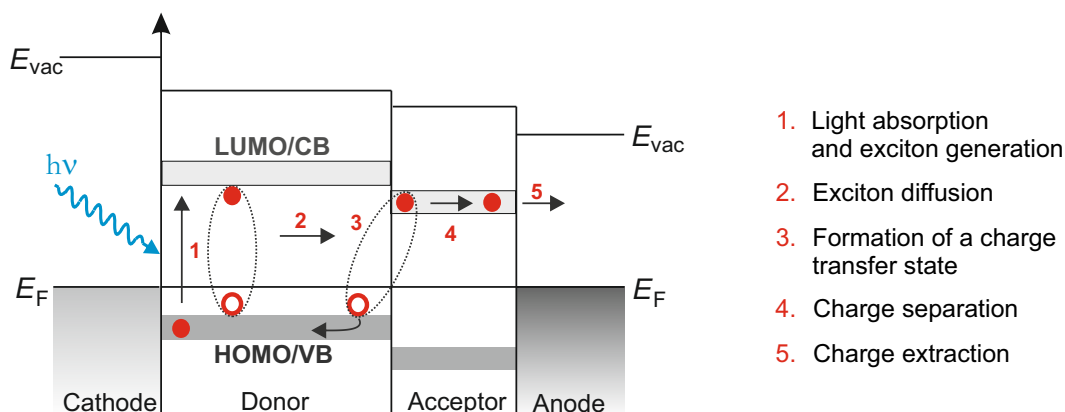


Figure 2.1: Schematic of a bilayer solar cell illustrating the five step mechanism of charge generation.

shows a schematic depiction of a bilayer organic solar cell: In the first step light is absorbed by the donor material and an exciton is formed (1). The exciton diffuses (2) towards the donor-acceptor interface where the charges are separated (3). The electron is conducted (4) by the acceptor material to the anode where the charge is extracted (5), while the hole travels back to the cathode. One of the electrodes has to be transparent to light in order to allow photoexcitation of the donor material. The light generating process in LEDs, electroluminescence, works *vice versa*: Charges are injected into the active material forming excitons which recombine under emission of photons. The efficiency of solar cells and LEDs is influenced by several aspects, such as energy level alignment, exciton diffusion length, charge carrier mobility and undesired loss channels [Koc07]. In order to improve the efficiency of optoelectronic and light harvesting devices a detailed understanding of the elementary electronic processes in the involved materials is of major interest. For example the exciton dissociation rate and thus the open circuit voltage of an organic solar cell highly depends on the so-called photovoltaic gap, which is defined as the energetic difference between the highest occupied molecular orbital (HOMO) of the donor and the lowest unoccupied molecular orbital (LUMO) of the acceptor material [Ams15]. The exciton diffusion length is related to the exciton lifetime and sets a limit to the

employed film thicknesses since excitons have to reach the donor-acceptor interface within their lifetime to be separated. The focus of this thesis lies on the investigation of the electronic structure and the excited state dynamics in different model systems which will be introduced in Section 3.

In the following sections the theoretical concepts this work is based upon are introduced. Fundamentals on metal surfaces and interfaces, such as adsorption induced workfunction change and energy level alignment are presented in Sections 2.1.1 and 2.1.2, whereas Section 2.1.3 discusses the concept of band bending at pristine and adsorbate covered semiconductor surfaces with focus on the *n*-type semiconductor zinc oxide (ZnO). The basic theoretical background concerning excitations in inorganic and organic semiconductors with focus on excitons will be treated in Sections 2.2.1 and 2.2.2.

2.1 Metal and Semiconductor Surfaces and Interfaces

The energy level alignment between electrode and conjugated organic material strongly affects the efficiency of charge carrier extraction and injection and thus the performance of optoelectronic devices. Therefore the electronic processes at the interfaces between the different materials is of particular interest. In the following sections basic surface and interface phenomena, which are essential for the understanding and interpretation of the results gained in this work, are introduced. First surface states emerging at metal surfaces are treated in Section 2.1.1. The concepts of work function and surface dipole, as well as energy level alignment upon adsorption of organic semiconducting molecules on metal surfaces are introduced in Section 2.1.2. The effect of band bending at semiconductor surfaces is discussed in Section 2.1.3.

2.1.1 Electronic States at Metal Surfaces

At the surface, the periodicity of the crystal lattice is broken. Due to this loss of symmetry, the electronic band structure of the bulk changes at the surface and a surface band structure emerges. New electronic states, which are located parallel to the surface and decay exponentially into the vacuum and the bulk, appear within the local band gaps. These so-called surface states were first described by Tamm and Shockley [Tam32, Sho39]. Shockley states are suitable to describe electronic states at metal or small band gap semiconductor surfaces, whereas Tamm states serve as a valid description of transition metal and wide bandgap semiconductor surface states. Surface states are very sensitive towards changes of the surface electronic structure and thus towards adsorption of atoms and molecules [For03]. The energetic position of a surface state can change upon adsorption, e.g. the Shockley surface states of

several metal surfaces have been found to shift towards the Fermi level while their dispersion remains unchanged [For03, For07, Hag10, Var12b].

Another kind of surface state is the image potential state (IPS), originating from the interaction of the metal with an electron, which was transferred from the bulk by e.g. a laser pulse, and is now located in a distance z in front of the metal surface. Since electrons are able to move freely within the metal, they redistribute in response

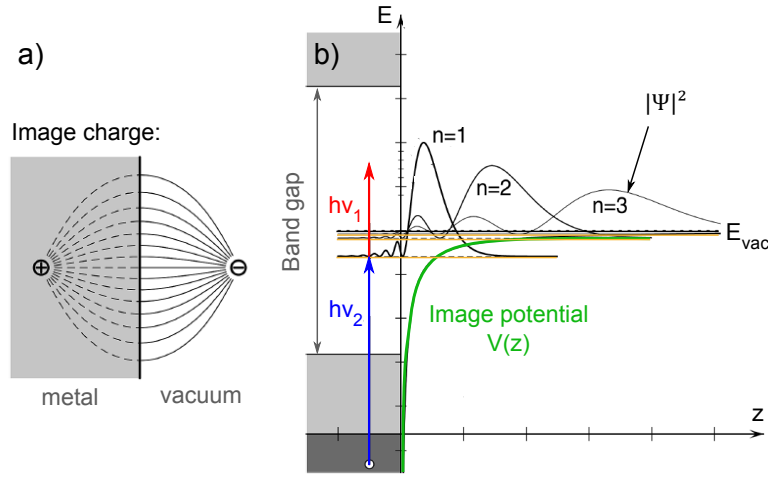


Figure 2.2: a) Creation of an image charge by electron induced polarization of the metal. b) The first three ($n = 1, 2, 3$) image potential states for the case of weak coupling to the substrate, such as Cu(100), adopted from Ref. [Güd06].

to the negative charge in front of the surface. Therefore an electric field, identical to the Coulomb field, develops and a positive mirror charge is created in the distance z to the surface, as illustrated in Figure 2.2 (a). Thus an attractive force is generated [Fau02]:

$$F(z) = \frac{e^2}{4\pi\epsilon(2z)^2} \quad (2.1)$$

Where ϵ corresponds to the dielectric constant of the surface and e to the elementary charge. This description differs from the original Coulomb's law in the way that here the force depends only on the z -coordinate. Thus a one-dimensional problem is obtained and moving the charge parallel to the surface is not force demanding. The image force described in Equation (2.1) is obtained from a hydrogen-like potential, the so-called image potential V_{IP} , depending on the distance z between electron and surface, as illustrated by the green curve in Figure 2.2 (b) [Fau02]

$$V_{IP}(z) = E_{vac} - \frac{e^2}{1\pi\epsilon} \frac{1}{4z} \quad (2.2)$$

where E_{vac} is the vacuum level, to which the energetic position of the IPS is ‘pinned’. A Rydberg-like series of bound states develops due to this image potential. The energy of these states with quantum number $n = 1, 2, 3, \dots$ is given relative to the vacuum level by [Ech78]

$$E_n = E_{\text{vac}} - \frac{0.85}{(n + a)^2} \text{eV} \quad (2.3)$$

Where n is the quantum number and the energy of 0.85 eV equals 1/16 of the Rydberg energy of the hydrogen atom in a three-dimensional Coulomb potential. The quantum defect a describes the lowering of the binding energy due to the fact that the metal surface is not a potential barrier of infinite height. Therefore the electronic wave function still decays into the metal and the probability density is finite at the surface, which is the reason why the maximal probability density is shifted away from the surface [Fau02]. In Figure 2.2 (b) the absolute squares of the wave functions of the first three IPS are depicted. The energy of the IPS converges to the vacuum level with increasing quantum number n and the distance between the surface and the maximal probability density is elongated.

Image potential states are as well affected by adsorption of atoms or molecules. Adsorbate induced work function changes shift the IPS either towards or away from the Fermi level which in turn influences their lifetimes [Wol96]. Moreover adsorption of atomic or molecular layers can give rise to new kinds of states. For example when the image potential is shielded by a dielectric adsorbate film it is pushed away from the adsorbate surface towards the metal interface. And at the adsorbate/vacuum interface a new image potential emerges as a superposition of an image potential originating from a charge in front of the metal surface and the potential of the adsorbate [Güd05]. This new potential gives rise to another Rydberg-like series of states, so-called interface states. These states depend on the distance to the metal interface, i.e. the film thickness and are in contrast to image potential states not pinned to the vacuum level. Experimentally interface states have been observed, e.g. for thick Ar films on Cu(111) and for an imine derivative adsorbed on the Au(111) surface [Roh05, Hag10].

2.1.2 Energy Level Alignment at Metal/Organic Interfaces

Metal surfaces play an important role as electrodes in organic electronic devices. Therefore it is crucial to understand the electronic processes and the electronic structure upon adsorption of organic molecules.

In a metal, the electronic states are occupied up to the Fermi level, also called total chemical potential μ . The potential inside the bulk material $\phi(-\infty)$ is usually set to zero, such that it equals the Fermi level. At the surface the positive charge density created by the atomic nuclei $n(z)$ drops to zero, as illustrated in Figure 2.3 (a). In contrast the probability for electrons to reside in front of the metal surface is non-zero, therefore they spill out. The work function (Φ) can be expressed in terms of the total change in the electrostatic potential $\Delta\phi$, when going from the bulk across the surface, and the chemical potential $\bar{\mu}$ of the electrons in the bulk metal relative to the mean electrostatic potential (Figure 2.3 (b)): $\Phi = \Delta\phi - \bar{\mu}$ [Lan71], (note that $\Delta\phi$ is often referred to as surface dipole). Another definition of the work function is the difference between the vacuum and the Fermi level: $\Phi = E_{\text{vac}} - E_{\text{F}}$.

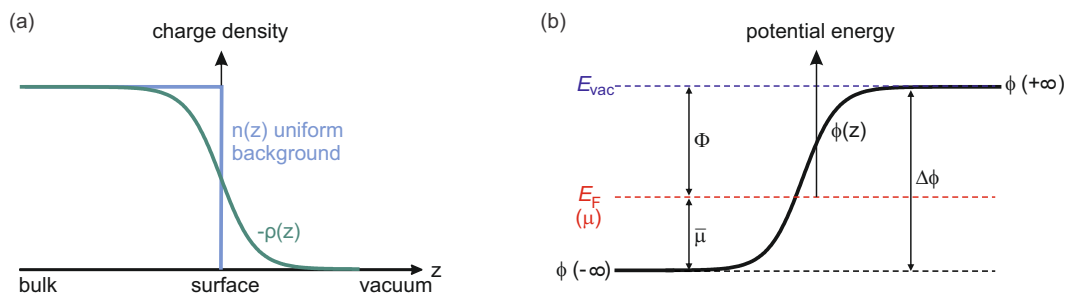


Figure 2.3: Schematic of (a) charge density distribution at a metal surface and (b) relevant energies connected to the work function, modified from Ref. [Lan71].

When a molecule is adsorbed on a metal surface the electron density of the molecule interacts with the electron density at the metal surface *via* Coulomb repulsion so that the tail of the spilling out electron wave function is locally pushed into the metal which leads to a reduction of the surface dipole and thus the work function [Cri01]. This behaviour is called the ‘pushback’ effect. In the case of charge transfer between the adsorbed molecules and the metal surface the net surface dipole depends as well on the dipole of the charge transfer: In the case of a donor molecule, *i.e.* electron transfer from the molecule to the metal, the net surface dipole additionally decreases. For an acceptor molecule electrons are transferred from the metal into the molecule increasing the surface dipole and thus the work function.

When molecules are adsorbed on a metal surface two possible regimes for energy level alignment are possible, as illustrated in Figures 2.4 and 2.5:

(i) Vacuum level alignment, also known as Schottky-Mott limit, in which the work

function stays constant while the electron and hole injection barriers (Δ_e and Δ_h), *i.e.* the energetic positions of HOMO and LUMO relative to the Fermi level, change. (ii) Fermi level pinning in which the work function changes while Δ_e and Δ_h stay constant.

Vacuum level alignment is only possible when the Fermi level of the metal is located between the initial EA/LUMO and IP/HOMO of the molecule [Ams15] as illustrated in Figure 2.4 (a) and (b). In this case the hole and electron injection barriers Δ_h

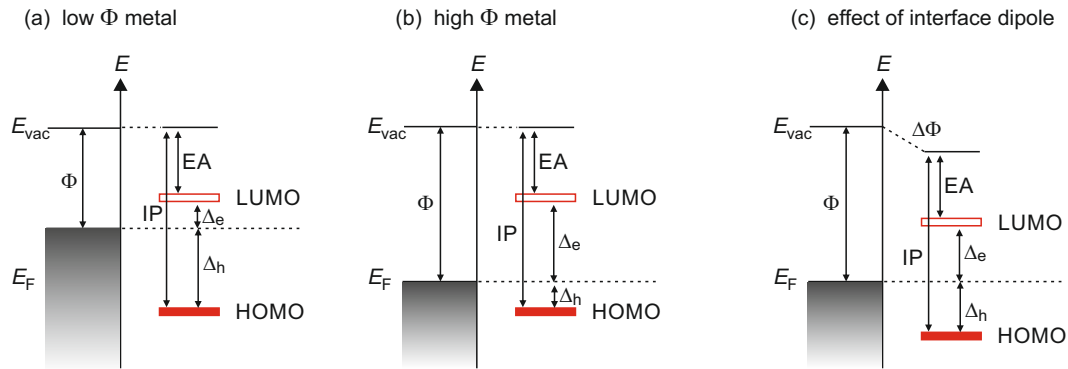


Figure 2.4: Vacuum level alignment for (a) low and (b) high work function metals, (c) interface dipole induced work function change.

and Δ_e are given by

$$\Delta_h = \text{IP} - \Phi \quad (2.4)$$

$$\Delta_e = \Phi - \text{EA} \quad (2.5)$$

But this holds only under the assumption of an interface dipole (ID) of $\text{ID} = 0$ which is usually not the case for interfaces between organic semiconductors and atomically clean metals. The interface dipole in these systems emerges due to the ‘pushback’ effect, charge transfer or bond formation between adsorbate and substrate and leads to a change of the work function as illustrated in Figure 2.4 (c). The concept of vacuum level alignment thus becomes invalid and the hole and electron injection barriers Δ_h and Δ_e write as

$$\Delta_h = \text{IP} - \Phi + \text{ID} \quad (2.6)$$

$$\Delta_e = \Phi - \text{EA} - \text{ID} \quad (2.7)$$

The second possibility, Fermi level pinning, occurs when the metal work function is so low or high that the alignment of the vacuum levels would position the Fermi level of the metal within the unoccupied or occupied molecular level [Koc12]. This leads to the two limiting cases of LUMO-pinning in the case of a low work function

metal and HOMO-pinning for high work function metals, as depicted in Figure 2.5 [Oeh14]. The resulting non-equilibrium situation can be compensated by charge

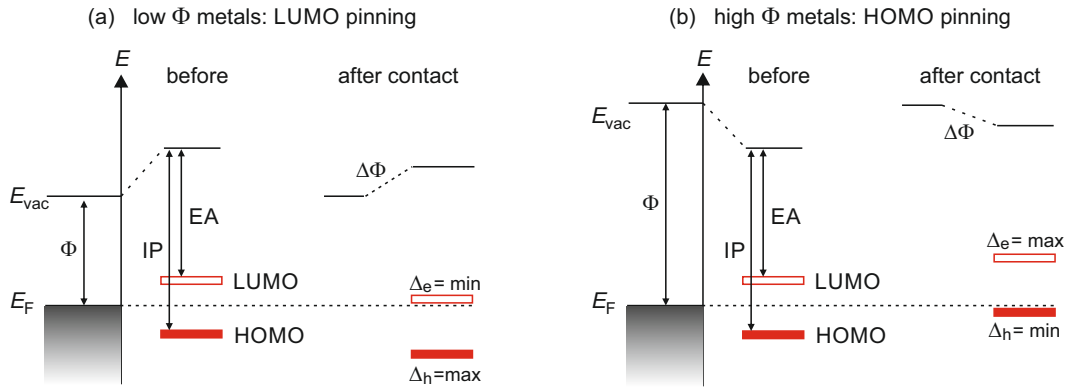


Figure 2.5: Fermi level pinning for (a) low and (b) high work function metals.

transfer, *i.e.* partially filling the LUMO with electrons or the HOMO with holes from the metal [Koc12]. The energetic positions of the molecular levels relative to the Fermi level stay constant for further work function changes, therefore this behaviour is called Fermi level pinning. In principle it should be possible that electron or hole injection barriers become zero, but in photoelectron spectroscopy (PES) and inverse photoelectron spectroscopy (IPES) studies only values of at least a few 100 meV have been measured [Koc12].

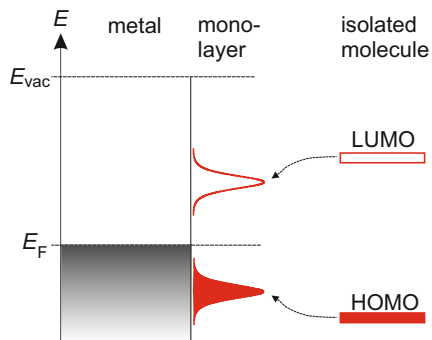


Figure 2.6: Broadening of the frontier orbitals and reduction of the free molecule gap upon adsorption on a metal surface.

A possible effect that can occur when a molecule is brought into contact with a metal surface is the reduction of the HOMO-LUMO gap, as will be demonstrated in Section 5.3.1. When a molecule approaches a metal surface, both the occupied and the unoccupied molecular levels give rise to mirror charges in the metal [Hei13]. In turn the ionization and affinity levels are attracted by their mirror charges, so that the LUMO shifts to lower energies and the HOMO to higher energies, thus reducing the energy gap as illustrated in Figure 2.6. Thereby the molecular levels undergo hybridization with the metal and are broadened with respect to the discrete levels of the free molecule [Nea06].

2.1.3 Band Bending at Semiconductor Surfaces

The concept of surface band bending was first developed by Schottky and Mott in order to explain the adjustment of the semiconductor bands in contact with a metal surface [Sch38, Mot38]. When an n -type semiconductor, in which electrons are the majority carriers, and a metal with a work function larger than the semiconductor ($\Phi_m > \Phi_s$) are brought into contact the electrons flow from the semiconductor to the metal until the Fermi levels are aligned. This gives rise to an electric field at the metal-semiconductor interface. In equilibrium a Helmholtz double layer is formed where the metal is negatively and the semiconductor is positively charged in its surface region, as depicted in Figure 2.7 (a). This electric field between metal and semiconductor cannot be screened effectively in the semiconductor since the concentration of free carriers is too low. Therefore the carrier concentration near the semiconductor surface is reduced compared to the bulk, forming a so-called depletion layer. In general the surface-near region in which the concentration of free majority carriers differs from the bulk is called space charge region [Lüt10]. In the space charge

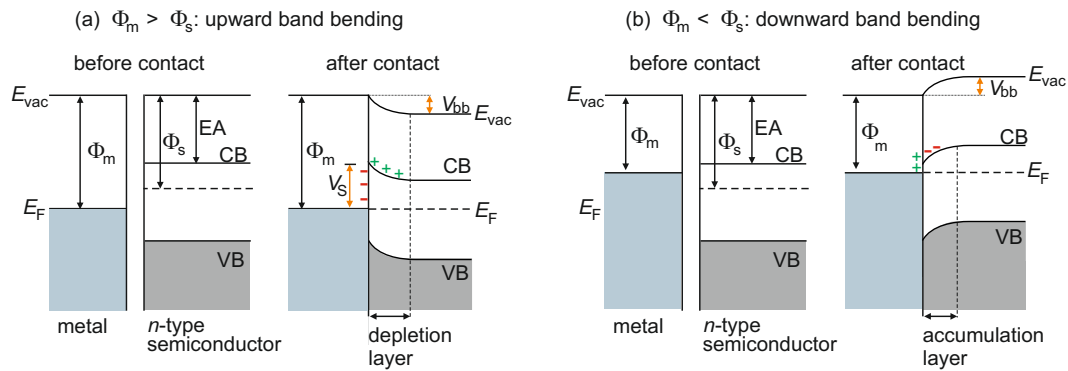


Figure 2.7: Energy level diagrams of metal and n -type semiconductor contacts: (a) When $\Phi_m > \Phi_s$ upward band bending is induced and (b) $\Phi_m < \Phi_s$ results in downward band bending.

region the band edges of the semiconductor shift continuously due to the charge transfer induced electric field between semiconductor and metal. In the case of $\Phi_m > \Phi_s$ (Figure 2.7 (a)) upward band bending occurs since electrons moving towards the negatively charged Helmholtz layer in the metal feel the Coulomb repulsion so that their potential energy rises [Zha12b]. The degree of band bending (V_{bb}) corresponds to the energetic difference between the metal and the semiconductor work functions

$$V_{bb} = |\Phi_m - \Phi_s| \quad (2.8)$$

The barrier which is formed at the metal-semiconductor interface when $\Phi_m > \Phi_s$ is called Schottky barrier (V_S) and corresponds to the difference between the metal work function and the electron affinity of the semiconductor

$$V_S = (\Phi_m - EA) \quad (2.9)$$

When the work function of the metal is smaller than the work function of the semiconductor ($\Phi_m < \Phi_s$), electrons flow from the metal to the semiconductor so that the metal is positively and the semiconductor negatively charged, as illustrated in Figure 2.7 (b). In this case the electron concentration at the semiconductor surface is higher than in the bulk thus forming a so-called accumulation layer in which the band edges are bent downwards.

Band bending can be induced not only by a metal interface but as well by external electric fields, adsorption of atoms/molecules or by surface states [Zha12b]. In this work the effect of hydrogen adsorption on the electronic structure of the O-terminated ZnO(000 $\bar{1}$) surface is investigated, as will be discussed in Section 5.1.1. This ZnO surface is polar due to the negatively charged O-ions at the surface, therefore the pristine surface exhibits upward surface band bending, as depicted in Figure 2.8 (a). Adsorption of donor atoms, in this case hydrogen, leads to electron trans-

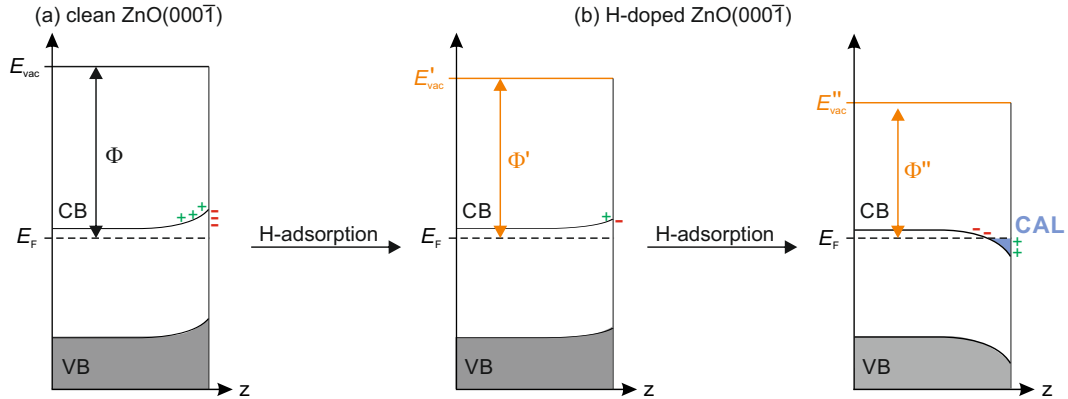


Figure 2.8: (a) Upward surface band bending at the clean ZnO(000 $\bar{1}$) surface, (b) reversed surface band bending upon H-adsorption.

fer from the donor to the semiconductor thus reducing the work function and the upward surface band bending. Figure 2.8 (b) illustrates that further H-adsorption leads to an enhanced work function reduction and downward surface band bending. When the conduction band maximum (CBM) crosses the Fermi level, a charge accumulation layer (CAL) is formed which is populated by electrons donated by the H-atoms. In comparison to other semiconductors such as Si and gallium arsenide

(GaAs) surface band bending in *n*-type ZnO only extends a few tens of Å into the bulk instead of a few hundreds of nm [Lüt10], leading to a strongly confined CAL [Dei15b].

2.2 Elementary Excitations in Semiconductors

In the following sections the fundamental processes resulting from illumination of semiconductors are introduced. First a general introduction about the concept of semiconductor excitons will be given. Section 2.2.1 is dedicated to elementary excitations in inorganic semiconductors relevant for this thesis and Section 2.2.2 treats the properties of excitons in organic semiconductors.

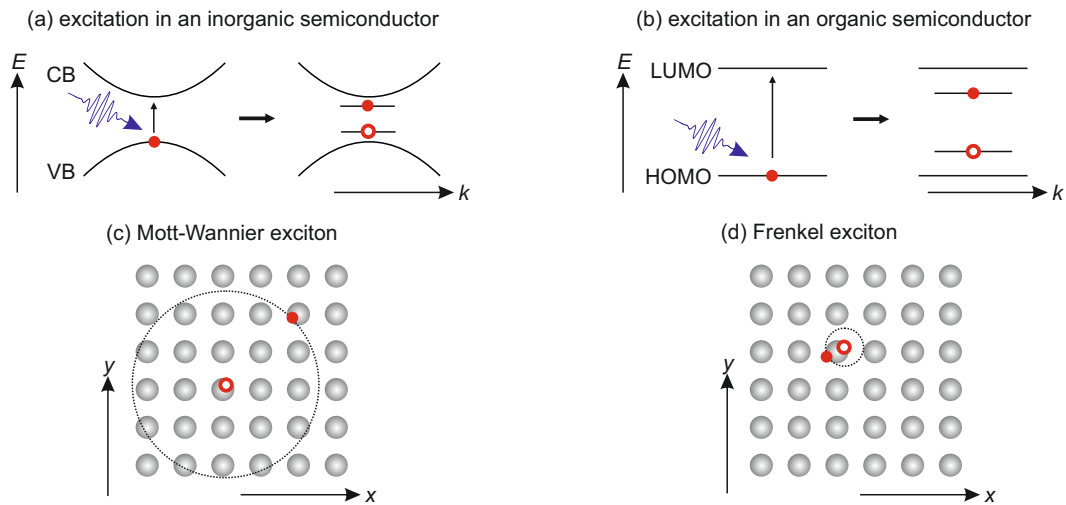


Figure 2.9: Excitation and electron-hole pair formation in (a) an inorganic and (b) an organic semiconductor. (c) Delocalized Mott-Wannier exciton and (d) Frenkel exciton localized on a single molecule.

Photoexciting an electron from the valence band (VB) in case of an inorganic semiconductor (Figure 2.9 (a)), or the HOMO¹ in a molecular semiconductor (Figure 2.9 (b)) to the conduction band (CB) or the LUMO leads to the formation of Coulomb bound electron-hole pairs, so-called excitons. The holes are treated as electron-like particles with a positive charge and a different effective mass. Excitons are neutral quasiparticles which move through a dielectric medium transporting excitation energy, not charge. There are two limiting cases of excitons which differ in their binding radius and accordingly their binding energy: (i) Mott-Wannier excitons (Figure 2.9 (c)), which usually have binding energies in the range of 0.001 - 0.1 eV and radii exceeding the lattice constant. (ii) In contrast Frenkel excitons (Figure 2.9 (d)), are confined to the size of a molecule and possess larger binding energies in the range of 0.1 - 1 eV. Mott-Wannier excitons are usually found in inorganic semiconductors while Frenkel excitons occur in organic semiconductors.

¹In organic polymeric semiconductors both terminologies HOMO/LUMO and VB/CB are used.

2.2.1 Elementary Excitations in Inorganic Semiconductors

Excitons in inorganic semiconductors, Mott-Wannier excitons, can be understood as hydrogen-like particles, which consist of an electron and a hole instead of a proton, thus yielding a Rydberg-like series of energies depending on the exciton Rydberg energy R_{ex} [Mun10]

$$R_{\text{ex}} = \frac{\mu}{m_0 \varepsilon^2} R_{\infty} \quad (2.10)$$

with the reduced mass of the electron-hole pair $\mu = \frac{m_e \cdot m_h}{(m_e + m_h)}$, the free electron mass m_0 , the dielectric constant ε and the Rydberg constant R_{∞} . The exciton energy is significantly smaller than the Rydberg energy of 13.6 eV of a hydrogen atom since the effective electron and hole masses are smaller and the dielectric constant of the semiconductor screens the Coulomb interaction between electron and hole [Koc06]. The Bohr radius of the exciton r_{ex} is given by

$$r_{\text{ex}} = \frac{m_0 \varepsilon}{\mu} a_0 \quad (2.11)$$

where a_0 is the Bohr radius of a hydrogen atom in its ground state.

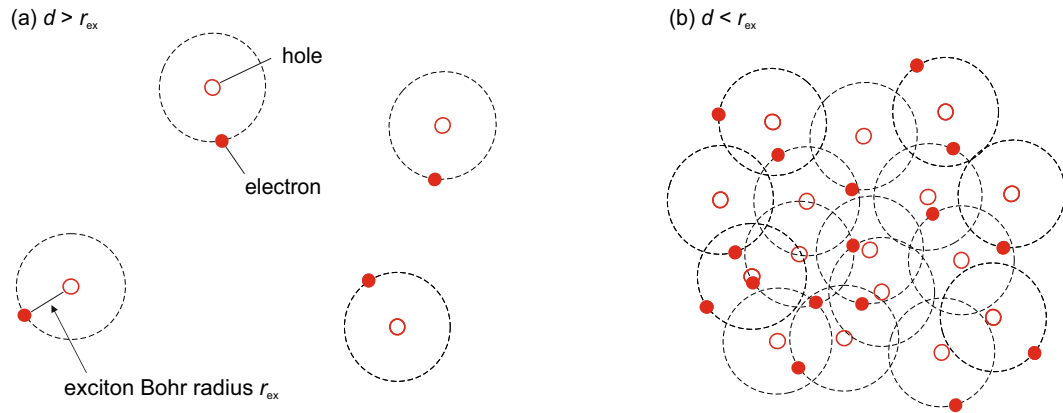


Figure 2.10: (a) Excitation below Mott density: distance between excitons is larger than the exciton radius, (b) excitation above Mott density: distance between excitons is smaller than the exciton radius.

The properties of excitons in inorganic semiconductors highly depend on the excitation density and the temperature. Figure 2.10 (a) shows the exciton gas at low excitation densities where the distance between the excitons is larger than the exciton Bohr radius $d > r_{\text{ex}}$. At high excitation densities, the distance between the excitons becomes smaller than the exciton Bohr radius $d < r_{\text{ex}}$, as illustrated in Figure 2.10 (b). This leads to an enhanced screening of the attractive Coulomb interaction between electron and hole, so that exciton formation becomes less probable [Mot68, Hen07, Ver11]. This critical electron-hole density is called Mott density or Mott

limit and will play a role when it comes to the interpretation of excitation density-dependent measurements of the H-covered ZnO(000 $\bar{1}$) surface in Section 5.1.2. Since the reported values scatter over a broad range between $4 \times 10^{16} \text{ cm}^{-3}$ and $3.7 \times 10^{19} \text{ cm}^{-3}$ [Hen07, Sch11, Ver12, Sun05], I will not refer to it as a strict limit but reference the excitation densities used in this work to the lower or upper Mott density regime.

Versteegh *et al.* calculated a phase diagram of the electron-hole gas in ZnO as a function of the electron-hole density and the temperature [Ver12]. They yielded 5 different regimes of which 2 are relevant for this work: The exciton gas which exists in the low excitation density regime for temperatures above 1 K and the electron hole plasma which forms at temperatures higher than ≈ 20 K for high excitation densities.

The exciton formation and decay dynamics depend on the interaction between the excited electrons and later the excitons with their surrounding. There are various possible interactions such as scattering with electrons and holes, acoustic and optical phonons or scattering with impurities and defects [Sha96]. After weak non-resonant and above band gap excitation of a polar semiconductor like ZnO or GaAs the interaction of excited electrons with phonons dominates the exchange of energy and momentum between the carriers and the lattice. For large excess energies the scattering with polar longitudinal optical (LO) phonons, Fröhlich interaction, prevails. The Fröhlich interaction rate is given by [Sha96]

$$W(E) = W_0 \sqrt{\frac{\hbar\omega_{\text{LO}}}{E}} \left[\frac{n(\hbar\omega_{\text{LO}})}{\sinh\left(\frac{E}{\hbar\omega_{\text{LO}}}\right)} + \frac{(n(\hbar\omega_{\text{LO}}) + 1)}{\sinh\left(\left(\frac{E}{\hbar\omega_{\text{LO}}}\right) - 1\right)} \right] \quad (2.12)$$

With the phonon occupation number $n(\omega_{\text{LO}})$ and

$$W_0 = \frac{e^2 \sqrt{2m_0 \hbar\omega_{\text{LO}}}}{4\pi \hbar^2} \left(\frac{1}{\varepsilon_\infty} - \frac{1}{\varepsilon_S} \right) \quad (2.13)$$

Where $\hbar\omega_{\text{LO}}$ is the LO phonon energy, m_0 the free electron mass, and ε_∞ and ε_S are the optical and static permittivities. For low energy electrons the exciton formation proceeds *via* coupling with acoustic phonons. The interaction with acoustic phonons occurs either *via* deformation potential or piezoelectric scattering mechanisms, of which usually the first prevails [Sha96].

The decay of excitons is often dominated by radiative electron-hole recombination (luminescence), which is desired in light-generating applications but needs to be avoided in solar cells. Another decay channel is the dissociation of excitons into free charge carriers, *i.e.* electrons and holes, giving rise to the formation of another type of quasiparticles, namely polarons. In general a polaron can be described as a

charge surrounded by a polarization field. Since the polarization fields can have different origins and dimensions different kinds of polarons are distinguished. Polarons originate not exclusively from dissociated excitons, they form as well directly from excited charge carriers. One example for a polaronic species is the ‘large polaron’, as well called ‘Fröhlich-polaron’, which consists of an electron (or hole) and the polarization induced by LO phonons [Dev96]. In this case the polarization exceeds the lattice constant, explaining the name ‘large polaron’. Another kind of polaron is the ‘small polaron’, where the polarization is confined to the lattice constant, consisting of a charge which is trapped in a potential well resulting from its self-induced ionic displacement. In principle ‘large’ and ‘small polarons’ can coexist in a material, but concerning ZnO only ‘large polarons’ were found to be stable [Dev96, Sez15, Var12d].

An effect which prevents exciton formation is surface photovoltage. It can occur upon photoexcitation of a semiconductor which exhibits surface band bending, as discussed before in Section 2.1.3. Figure 2.11 shows an example for the case of downward surface band bending as it is the case for H-doped ZnO(10 $\bar{1}$ 0) and (000 $\bar{1}$). The electric field at the surface attracts the excess electrons while the excess holes

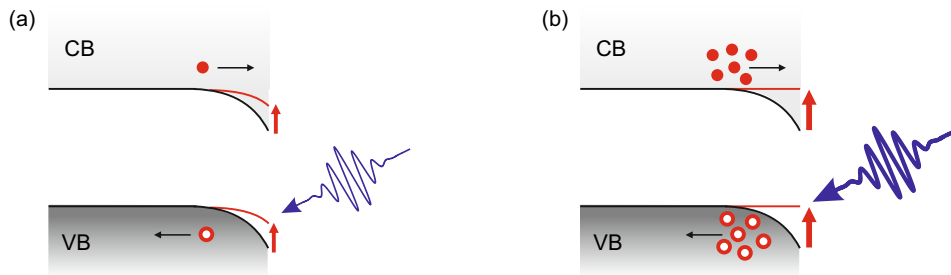


Figure 2.11: (a) Surface photovoltage at low excitation density, (b) enhanced surface photovoltage at higher excitation density.

are drawn into the bulk; this leads to a compensation of the surface dipole and thus to reduced band bending as sketched in Figure 2.11 (a) [Kro11]. The surface photovoltage is then the change in the surface potential due to illumination. In two-photon photoelectron spectroscopy (2PPE) measurements this effect would be visible *via* a transient work function shift induced by illumination, which recovers when illumination is stopped. Another evidence for surface photovoltage effects in 2PPE is its dependence on the excitation density as illustrated in Figure 2.11 (b): For higher excitation densities the reduction of the surface band bending, and thus the surface photovoltage, is enhanced until flat band conditions are reached.

2.2.2 Excitons in Organic Semiconductors

In this section the concept of exciton binding energy in organic semiconductors is introduced and the experimental accessibility of the relevant states is discussed. Moreover different kinds of excitonic species will be presented.

The dielectric model introduced in Section 2.2.1 is only suitable to describe delocalized Mott-Wannier excitons since the dielectric constant is a macroscopic quantity and is thus not applicable to describe Frenkel excitons which are localized on one molecular unit [Mun10]. The binding energy of Frenkel excitons can be defined as the energy needed to separate a bound electron-hole pair located on one molecule into free charges located at two molecules far away from each other. According to Knupfer the exciton binding energy E_b^{exc} is composed of three contributions [Knu03]

$$E_b^{\text{exc}} = E_b^{\text{intra}} + U - W \quad (2.14)$$

where E_b^{intra} is the intramolecular binding energy which is lost by going from a bound to an unbound electron-hole pair located on the same molecular unit, as illustrated in Figure 2.12 (a) and (b). U is the charging, or Coulomb repulsion, energy which has to be paid when the separated charges locate on two different molecules which have been neutral before (Figure 2.12 (c)) and is defined as

$$U = E(N + 1) + E(N - 1) - 2E(N) \quad (2.15)$$

where E is the energy and N is the number of electrons. W is the intermolecular band width and thus the maximum amount of energy the separated charges can gain. But since the band width in molecular solids is rather small and roughly of

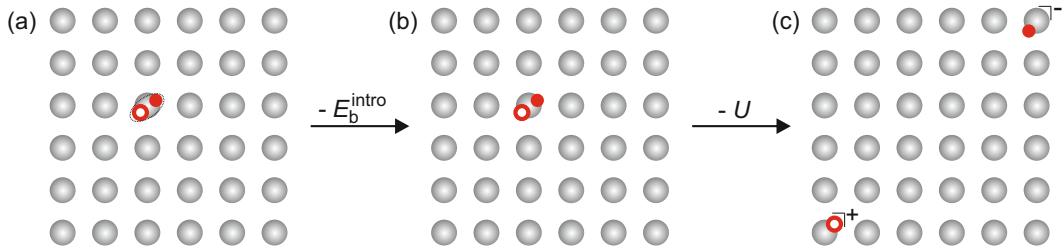


Figure 2.12: (a) Bound electron-hole pair located on one molecular unit, (b) unbound electron and hole and (c) electron and hole are located on two different molecules far away from each other.

the same amount of energy as E_b^{intra} , the exciton binding energy can be approximated to [Knu03]

$$E_b^{\text{exc}} \approx U + 0.1 \text{ eV} \quad (2.16)$$

In the following paragraph the experimental determination of the exciton binding energy by means of 2PPE will be discussed. Moreover the comparability of molecular levels derived from photoemission and scanning tunneling spectroscopy (STS) will be debated briefly, as in Section 5.3 STS will be used complementary to 2PPE. Experimentally the exciton binding energy can be determined by subtracting the optical gap (E_{opt}) from the transport gap (E_{trans})

$$E_{\text{b}} = E_{\text{trans}} - E_{\text{opt}} \quad (2.17)$$

The transport gap corresponds to the HOMO-LUMO gap, as indicated in Figure 2.13, and is called thus since the transport of free charge carriers occurs in these energetic levels. The energetic positions of the HOMO and the LUMO can be measured e.g. by 2PPE, as will be explained in Section 4.1.1, PES and IPES or STS. All of the mentioned methods measure the HOMO as the difference between the N electron state and the cation ($N-1$ electron state), while the LUMO is measured as the difference between the negative ion ($N+1$ electrons) and the ground state (N electrons). Since the charge transporting molecules are as well ions, the measured HOMO/LUMO levels correspond to the electron/hole transport levels.

The optical gap corresponds to the threshold of photon absorption and can be measured for instance by means of absorption spectroscopy or with 2PPE. In order to illustrate the different 2PPE processes, especially the difference between the population of the LUMO and the exciton, Figure 2.13 shows pump-probe schemes for photoemission from (a) the HOMO (b) the LUMO and (c) the exciton. The HOMO

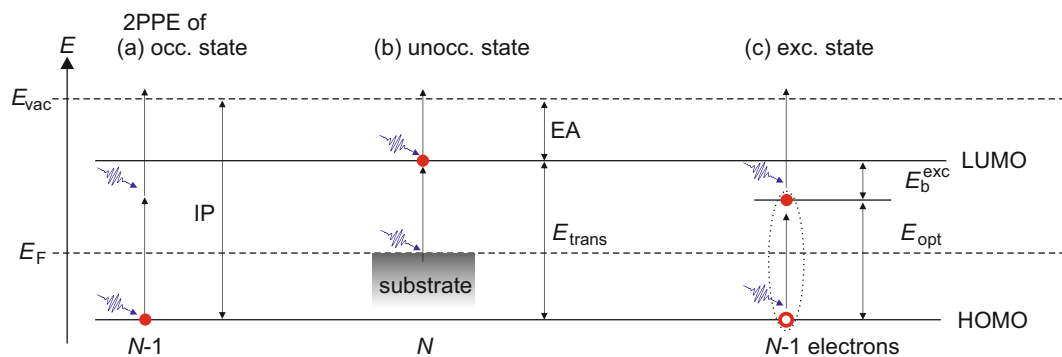


Figure 2.13: Probing (a) an occupied, (b) an unoccupied state and (c) an excitonic state with 2PPE. The energetic position of the HOMO relative to the vacuum level corresponds to the ionization potential (IP) and the position of the LUMO to the electron affinity (EA).

is probed in a concerted 2PPE process as sketched in Figure 2.13 (a) and corresponds to the IP. Figure 2.13 (b) shows the pump-probe scheme employed to measure the LUMO, *i.e.* the EA level: An electron from the substrate is excited by the first

photon into the LUMO of the molecular adsorbate from where it is subsequently probed by the second photon. In contrast intermolecular excitation of an electron from the HOMO to the LUMO leads to the formation of an exciton as depicted in Figure 2.13 (c). The exciton binding energy corresponds then to the energetic difference between the kinetic energy of the electron emitted from the LUMO and the kinetic energy of the electron emitted from the excitonic state. The optical gap is given by the difference between HOMO and excitonic level. Since the exciton binding energy is actually carried by both electron and hole, but only the electron is emitted one could think that the measured kinetic energy actually corresponds only to the energetic position of the Coulomb bound electron. But it has to be taken into account that additional energy is needed to break up the exciton before the electron can be emitted. This amount of energy is paid by the probe photon energy and therefore this method is considered to be a good approximation. Thus 2PPE provides the possibility to measure the energetic positions of all the relevant states: the HOMO/IP by photoemission from an occupied state, LUMO/EA level by charge injection from the substrate, and the excitonic level by intramolecular excitation from the HOMO.

Excitons usually decay *via* several competing mechanisms such as electron-hole recombination, relaxation into other states (e.g. charge-transfer states, polarons or trap states) and they can diffuse towards the substrate interface where charge-separation occurs. Typical for the latter case is a coverage dependent lifetime since with increasing coverage the surface-near electrons, probed by 2PPE, are not affected anymore by the substrate. An increase of exciton lifetime as a function of the distance to the metal surface will be discussed in Section 5.3 and has been observed before for C₆₀ and 6T on Au(111) [Dut05, Var12a].

In the following paragraphs different types of excitons which are relevant for this thesis will be presented and discussed.

Charge Transfer Excitons

There are two different kinds of charge transfer excitons which should not be confused:

(i) When electron and hole are located on two different materials or simply on two neighbouring molecules they form a charge transfer state, also called charge transfer exciton, polaron pair or polaron exciton [Dei10]. They can occur at donor-acceptor interfaces as well as in homomolecular films and are considered to be precursors for exciton dissociation leading to the formation of free charge carriers or polarons (polarons have been introduced in Section 2.2.1 for inorganic semiconductors; the polarons in organic semiconductors are similar to the ‘small polaron’ type).

(ii) The second type of charge transfer excitons occurs at the vacuum interface of an organic semiconductor. In this case the electron is attracted not only by the positive charge of the hole but as well by the image potential which emerges due to the electron being located in front of the surface. This scenario is as well similar to a hydrogen-like problem giving rise to a series of excitonic states which converge toward the continuum of image potential states [Mun10]. These kinds of charge transfer excitons have been studied at the surface of pentacene and tetracene films by means of 2PPE [Zhu09].

Singlet and Triplet Excitons

Excitons can appear in different spin multiplicities, as singlet states with antiparallel spins (2.14 (a)) or as triplets with parallel spins, as illustrated in Figure 2.14 (b). Singlets are usually formed after absorption of a photon with sufficient energy as depicted in the Jablonski diagram in Figure 2.14 (c): Excitation from the ground state S_0 into higher excited vibrational states of the first excited state $S_{1,n}$ is often followed by internal vibrational relaxation (IVR) into the vibrational ground state $S_{1,0}$. The population partially decays *via* electron-hole recombination under emission of photons ($S_n \rightarrow S_0$), so-called fluorescence (FL), while another part of the population undergoes intersystem crossing (ISC) forming triplet states. The singlet-to-triplet ratio is often assumed to be 1:3, but there is experimental and theoretical evidence that the ratio can be completely different, due to carrier trapping and the spin-dependent formation process [Kal02].

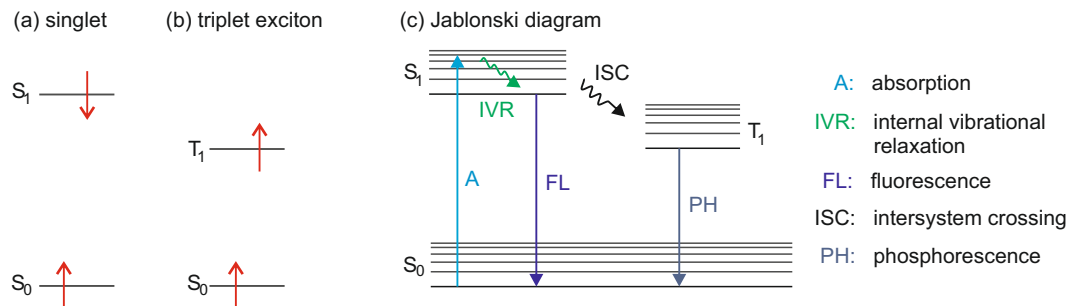


Figure 2.14: (a) Singlet and (b) triplet exciton. (c) Jablonski diagram illustrating relevant processes which can happen after photoexcitation of an organic semiconductor.

Since transitions from a singlet ground state to a triplet excited state ($S_0 \rightarrow T_n$), and *vice versa* ($T_n \rightarrow S_0$), require a spin-flip, thus violating the conservation of spin these transitions are considered to be ‘forbidden’ [Pow15]. Actually this is only true when spin orbit coupling is zero but as soon as spin orbit coupling is present, *i.e.* for angular quantum numbers $l \geq 1$, these transitions are allowed. Strictly speaking when spin orbit coupling is non-zero, spin and orbital angular momentum are no

good quantum numbers anymore and singlet and triplet excitations mix [Pow15]. However, spin orbit coupling is usually weak compared to other relevant effects such as dipole coupling and therefore the probability for direct triplet formation is very small so that triplets are formed *via* ISC from singlet states, as illustrated in Figure 2.14 (c). ISC is a radiationless transition from an excited state to another excited state with a different spin multiplicity. ISC is more efficient when singlet and triplet are energetically close, their vibrational levels overlap and when the spin orbit coupling is large. Due to the rather small probabilities for the radiative transition from an excited triplet state to the singlet ground state, phosphorescence (PH), the decay rates are typically orders of magnitudes slower than the FL decay rates. In compounds containing heavy atoms, however, PH can be very efficient due to the enhanced spin orbit coupling and the mixing with singlet states. Those efficient phosphors provide the possibility to gain unity charge-to-photon conversion and are already widely employed in phosphorescent organic light emitting diodes (OLEDs) [Rei12]. Therefore PH presents in OLEDs using materials with weak spin orbit coupling a significant loss channel, which needs to be avoided, while in the case of strong spin orbit coupling PH can be exploited.

Another process leading to the formation of triplet excitons is singlet fission during which one singlet state splits up into two triplet states:



This process is very attractive for light harvesting devices since it promises quantum yields to exceed 100% by converting 1 photon into 2 charge carriers, but up to now it has been observed only for a few materials [Yos14]. Singlet fission requires a large S_1 - T_1 splitting and weak spin orbit coupling in order to avoid ISC [Yos14]. Singlet fission has been reported as well in 2PPE measurements of pentacene and tetracene by Zhu and co-workers [Cha11, Cha12b, Cha12a].

Singlet and triplet excitons travel *via* different excitation energy transfer mechanisms:

- Singlet transfer occurs *via* Förster resonance energy transfer [För48] (Figure 2.15(a)) which is a dipole coupling mechanism, *i.e.* that the transition dipole moments of the coupling molecules have to be aligned parallel for efficient transfer. Another condition is that the absorption and emission spectra of the coupling molecules overlap, otherwise the amount of energy being transferred is not sufficient. Förster transfer decays with the distance, R , of the coupling molecules with R^{-6} [Yos12].
- In contrast triplet transfer takes place *via* a two electron exchange mechanism,

so-called Dexter transfer [Dex53], (Figure 2.15(b)) since Förster transfer would necessarily involve a spin flip and is therefore improbable. Dexter transfer requires orbital overlap and decreases exponentially with the distance [Lag09].



Figure 2.15: (a) Förster resonance energy transfer and (b) Dexter transfer.

Dexter transfer occurs on a slower timescale than Förster transfer but due to the long triplet lifetimes in the μs to ms range, whereas singlet excitons have lifetimes up to 1 ns, they can travel rather long distances up to several μm while singlet diffusion is limited to a few hundred nm [Yos12]. These long diffusion lengths might allow to use thicker layers in organic solar cells and thus to harvest more light [Yos12].

Besides decaying *via* electron-hole recombination or dissociation excitons can interact with each other in various annihilation processes:

1. Triplet-triplet annihilation:
 - (i) $T_1 + T_1 \rightarrow S_n + S_0 \rightarrow S_0 + S_0 + h\nu$
leading to delayed fluorescence [Mer68, Hof11, SR08]
 - (ii) $T_1 + T_1 \rightarrow T_n + S_0$
formation of a higher excited triplet state [Kel64]
2. Singlet-singlet annihilation:
 - (i) $S_1 + S_1 \rightarrow S_0 + M^+ + e^-$
leading to autoionization [Fri09, Wes90, Zau07, Ono98]
 - (ii) $S_1 + S_1 \rightarrow S_n + S_0 \rightarrow S_0 + S_0 + h\nu$
leading to luminescence [Yag08]
3. Singlet-triplet annihilation:

$$S_1 + T_1 \rightarrow T_n + S_0$$
 formation of a higher excited triplet state [Zau07, MB78]
4. Singlet/triplet annihilation due to interaction with charges (free electrons or holes, polarons, trapped carriers) leading to autoionization [Haa71, Arn79]

Triplet-triplet annihilation (TTA) is of particular interest for this work, as it is most likely the process leading to electron emission in films of a spiro-bifluorene derivative

(SP6) on ZnO as will be discussed in Section 5.2. In the following paragraph basic properties of the TTA process, relevant for the interpretation of the 2PPE data obtained for SP6 films on ZnO, will be discussed. Usually TTA is identified in luminescence measurements by detecting the delayed fluorescence resulting from the singlet due to TTA mechanism (i) [Mer68, Hof11, SR08]. If the higher excited singlet state S_n lies energetically above the vacuum level autoionization might occur in an analogous manner to the singlet-singlet annihilation process (i) reported before in the literature [Fri09, Wes90, Zau07, Ono98]. Moreover TTA is a bimolecular process and thus depends quadratically on the triplet concentration. A quadratic dependence of the delayed fluorescence signal intensity on the incident laser power has been observed experimentally by Singh-Rachford *et al.* [SR08].

In addition delayed fluorescence (DF), and thus TTA, was found to be temperature dependent, since the TTA rate constant is controlled by the triplet diffusion which increases for higher temperatures [Hof11]. Hoffmann *et al.* observed maximum DF at a temperature of 100 K in the case of a ethylhexyl-substituted poly(fluorene) trimer.

In the following chapter the systems investigated in this work will be introduced and previous studies relevant for this work will be presented.

3 Investigated Systems

As mentioned before in Section 2 the active materials in organic photovoltaic cell (OPVC)s and OLEDs consist of organic semiconducting materials. Thereby two classes of materials are distinguished, so-called small molecules and polymers [Koc07]. While polymer films have to be prepared from solution, small molecule based devices can be as well prepared *via* vapour deposition. Therefore small molecular films are usually of higher order and purity compared to polymer films. The efficiencies of solar cells and LEDs depend on several aspects such as the energy level alignment at the interfaces of the active materials and exciton lifetime and diffusion. Depending on the application different processes are considered as loss channels, e.g. strong luminescence is desired in LEDs while it is an unwanted side effect in solar cells where the excitons have to reach the donor/acceptor interface within their lifetime. Therefore the elementary processes in the active materials are of particular interest to enable device optimization. The central aspects of this thesis are the electronic structure and the excited state dynamics of different model systems representing anode-donor interfaces, small molecule and polymer donor films and a transparent electrode material.

In the following sections the systems investigated in this work will be introduced and the questions which will be examined in this work will be formulated. The systems studied in this thesis can be divided into four parts:

- 1) The H-covered polar ZnO(000 $\bar{1}$) surface
- 2) The spirobifluorene derivative SP6 on ZnO(10 $\bar{1}$ 0)
- 3) Two dicyanovinyl-substituted oligothiophenes on Au(111)
- 4) Two P3HT films with different degree of crystallinity

To provide a comprehensive basis for the investigations carried out in this work each material is introduced in a separate section and if available recent studies on the investigated systems are presented: In Section 3.1 the morphology of the mixed- and the O-terminated ZnO surface are presented and the effects of H-adsorption on the morphology, the electronic structure and the excited state dynamics will be discussed on the basis of previous studies. Section 3.2 treats fundamental properties of SP6 as well as recent photoemission and excited state transmission studies on SP6/ZnO. The oligothiophenes are introduced in Section 3.3 with focus on their adsorption geometry and electronic structure on Au(111), as investigated recently by scanning tunneling microscopy (STM) and STS. The morphology and the electronic structure of the Au(111) surface is presented in Section 3.4. Section 3.5 treats besides relevant studies on the electronic structure and excited state dynamics in P3HT films the preparation and characterization of the films.

3.1 Electronic Properties and Excited State Dynamics at the Mixed- and the O-terminated ZnO Surface

In the following section fundamental, structural and electronic properties of zinc oxide will be introduced. The two investigated surfaces, the mixed-terminated ZnO(10 $\bar{1}$ 0) and the O-terminated ZnO(000 $\bar{1}$) surface, are presented in Section 3.1.1. The phenomenon of surface metallization due to H-adsorption will be discussed in Section 3.1.2 while Section 3.1.3 deals with previous studies on surface exciton formation and decay dynamics at the two relevant ZnO surfaces.

ZnO is a promising candidate for the application in various optoelectronic devices, such as LEDs and solar cells, due to its wide bandgap of $E_g = 3.37$ eV (300 K), which makes it transparent to visible light, and its intrinsic n -type conductivity [Bla99]. In addition ZnO has a large exciton binding energy of $E_b^{\text{ex}} = 59.5 \pm 0.5$ meV, compared to e.g. the exciton binding energy of silicon which amounts to 15 meV [Gre13], and thus exhibits strong luminescence even at room temperature [Kli10]. Moreover the topmost LO phonon has a relatively high energy of 72 meV in ZnO due to the light mass of oxygen [Kli10] and plays a central role in the relaxation dynamics of hot electrons in ZnO, as will be discussed in Sections 3.1.3 and 5.1.2. The application of ZnO as transparent electrode material and indium tin oxide (ITO) substitute is particularly attractive since it is a cheap, easily accessible and non-toxic material. ZnO is already used in a huge variety of everyday life products, e.g. as UV blocker in sun creams, as white pigment in paints, as fungicide in the food industry, in dental inlays and ointments due to its antibacterial properties [Mor09, Kli10]. Furthermore it is used in nanorod gas sensors [Wan05a] and in heterogeneous catalysis for e.g. methanol synthesis, where especially the polar surfaces showed enhanced catalytic reactivity [Bow83, Wil03, Kur05]. A still unsolved problem is p -type doping in ZnO, which is needed for p - n -homojunctions in LEDs or transistors. ZnO is very vulnerable to defect states, which strongly influence the electronic structure. Oxygen vacancies and Zn interstitials have been regarded as explanations for intrinsically n -type doping in ZnO. But it has been discovered during the past 15 years that oxygen vacancies are deep donors and thus cannot contribute to n -type conductivity. Moreover it has been shown that Zn interstitials are as well unlikely to cause n -type conductivity and that impurities acting as shallow donors play an important role. Oxygen vacancies and Zn-interstitials however do play a role in p -type doping acting as compensating centers [Jan09].

Hydrogen for example is present in almost every fabrication environment, even under UHV conditions it shows a significant effect on the electronic structure of ZnO [Kin11, Jan09, Dei15b] as will be discussed in detail in Section 3.1.2. Usually

hydrogen behaves amphoteric and incorporates as electron donor in p -type and as electron acceptor in n -type materials, countervailing the predominating conductivity. But in bulk ZnO hydrogen is incorporated only as an electron donor, forming OH-bonds, and thus enhancing n -type conductivity [Jan09]. At the mixed-terminated ZnO $(10\bar{1}0)$ surface however, a complex interplay between OH- and ZnH-bonding has been observed, as will be discussed in Section 3.1.2 [Dei15b].

ZnO crystallizes in the wurtzite structure in which the Zn^{2+} and O^{2-} ions are coordinated tetrahedrally forming a hexagonal diamond lattice. Figure 3.1 shows the hexagonal unit cell of wurtzite ZnO with lattice constants of $a = 3.25 \text{ \AA}$ and $c = 5.21 \text{ \AA}$ [Bla99], the Zn^{2+} ions are coloured grey and the O^{2-} ions are depicted in red. The hexagonal wurtzite structure (space group C_{6v}^4 or $P6_3mc$) is favoured over the cubic zincblende due to the mostly ionic bonding radii of 0.74 \AA for Zn^{2+} and 1.4 \AA for

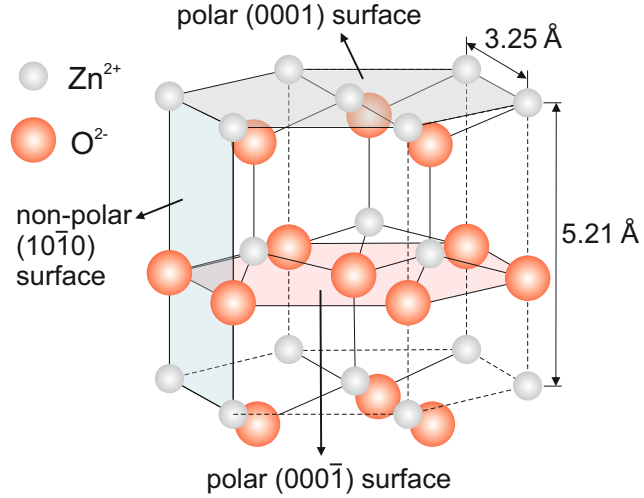


Figure 3.1: Hexagonal unit cell of ZnO, the grey plain illustrates the Zn-terminated (0001) , the red plain the O-terminated $(000\bar{1})$ and the blue plain the mixed-terminated $(10\bar{1}0)$ surface.

O^{2-} . This large electromechanic coupling explains the strong piezoelectricity of ZnO. At high pressures, around 10 GPa, ZnO converts to the rocksalt structure [Özg05]. There are three coloured planes drawn into the unit cell depicted in Figure 3.1: the grey coloured plane corresponds to the polar Zn-terminated (0001) surface, the light red one indicates the polar O-terminated $(000\bar{1})$ surface and the light blue plane depicts the non-polar mixed terminated $(10\bar{1}0)$ surface which is thermodynamically the most stable one. The atomic structure of these surfaces have been widely investigated by various surface science techniques such as STM and low-energy electron diffraction (LEED) [Dul02, Die04, Wöl07]. Previous studies on the morphology and electronic structure of the mixed-terminated ZnO $(10\bar{1}0)$ and the O-terminated ZnO $(000\bar{1})$ surface, which are subject of this work, are presented in the next sections.

3.1.1 Morphology of the O- and the Mixed-terminated ZnO Surface

Since the Zn-terminated ZnO(0001) surface is not subject of this work I will from now on refer to the O-terminated ZnO(000 $\bar{1}$) surface as the polar surface. Figure 3.2 (a) depicts the ZnO(10 $\bar{1}$ 0) surface which consists of equal amounts of Zn- and O-ions arranged in alternating rows. Since the negative charge of each O²⁻ ion is compensated by the positive charge of a Zn²⁺ ion the surface is non-polar. This surface is atomically flat and presents the most stable ZnO surface. The O-terminated

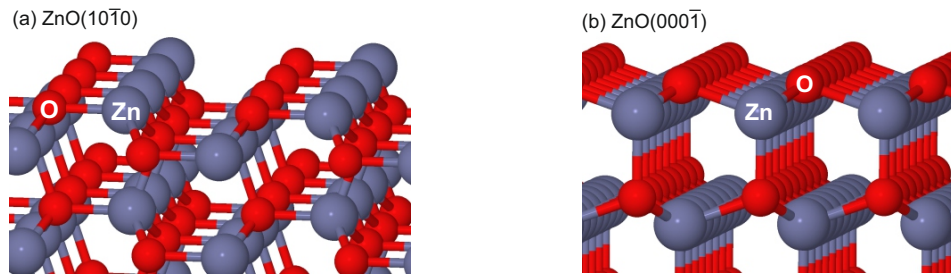


Figure 3.2: (a) Mixed-terminated ZnO(10 $\bar{1}$ 0) and (b) O-terminated ZnO(000 $\bar{1}$) surface, image courtesy by B. Bieniek

ZnO(000 $\bar{1}$) surface, shown in Figure 3.2 (b), is exclusively composed of O-ions and therefore a polar surface, *i.e.* it exhibits a surface dipole which points with its negative end into the vacuum. Despite its polarity the O-terminated surface is surprisingly stable and shows, like the non-polar surface, a 1×1 termination [Dul02]. But it is still under debate whether the observed 1×1 pattern is really due to the clean O-terminated surface or corresponds to a H-overlayer, since the clean surface is expected to show a 1×3 reconstruction [Kun02]. In contrast to the atomically flat non-polar surface the polar surface features a terrace structure consisting of flat hexagonal terraces with no additional holes or islands [Dul02].

The density of oxygen ions on the polar surface is ≈ 1.9 times higher than on the non-polar surface; this will play a role when comparing the amounts of adsorbed hydrogen on the polar with the non-polar surface in Section 5.1.1.

The surface properties are of great interest since they play a central role in lots of applications. The stability and reactivity of surfaces are crucial in e.g. catalytic processes while the electronic structure plays a major role in optoelectronic devices where energy level alignment and conductivity are important issues. Oxygen vacancies at the polar (000 $\bar{1}$) surface are discussed as active centers in methanol synthesis and are therefore particularly interesting [Fin06]. K. Fink calculated the energetic positions of several defect states at the polar ZnO(000 $\bar{1}$) surface [Fin06]. She chose as initial situation the H-covered polar ZnO(000 $\bar{1}$) surface and calculated the geometry and the electronic structure of different defects, such as the O-defect (V_O)

and the OH defect (V_{OH}). In the case of the O-defect a neutral O-atom is removed from the surface leaving two electrons in the vacancy. For the OH defect a neutral OH-group is withdrawn and only one electron is left in the vacancy. The defect levels of these two cases were found to be located 1.8 eV above valence band maximum (VBM), *i.e.* 1.6 eV below CBM [Fin06]. Experimentally luminescence from defect states has been observed at comparable energies around 1.8 eV below the CBM in our group by L. Foglia [Fog15]. This information will be of particular interest for the interpretation of the photoelectron spectra discussed in Section 5.1.1.

3.1.2 Surface Metallization due to H-adsorption on ZnO Surface

In the following section a short overview on recent studies investigating the effect of H-adsorption on the electronic structure of ZnO surfaces will be given. These previous studies are of great interest for this thesis in which the influence of H-doping on the electronic structure of the O-terminated ZnO surface is investigated, as will be discussed in Section 5.1.1.

Wöll and co-workers performed several studies using various surface science techniques and discovered that hydrogen adsorbs on the non-polar $(10\bar{1}0)$ surface at low temperatures in a $2\text{H}(1\times 1)$ overlayer binding to Zn- and O-ions, while at room temperature the overlayer changes towards a $\text{H}(1\times 1)$ fashion in which the hydrogen atoms are bonded only to the surface oxygen [Bec01, Kun03]. This temperature dependent binding behaviour demonstrates that the OH-bonds are stronger than the ZnH-bonds. The formation of OH-bonds leads to the development of a CAL, *i.e.* a metallic surface state, since hydrogen acts as an electron donor in the OH-bond and partially fills the CB, as discussed before in Section 2.1.3 [Bec01, Kun03, Wan05b].

Hydrogen adsorption on the O-terminated polar surface leads to $\text{H}(1\times 1)$ overlayers which are formed directly during the adsorption process and give rise to a metallic surface state, too. (This metallic surface state does not exist at the Zn-terminated surface since hydrogen has a negative partial charge in the ZnH-bond and thus cannot donate electrons to the CB.)

Ozawa and Mase investigated in an angle-resolved photoelectron spectroscopy (ARPES) study the effect of H-adsorption on the electronic structure of the stable ZnO surfaces [Oza11]. On the clean O-terminated surface they observe upward surface band bending which was reverted to downward surface band bending upon H-adsorption accompanied by a large work function decrease of ≈ 1.2 eV. Upon H-adsorption they found adsorbate induced surface metallization in the case of the O-terminated $\text{ZnO}(000\bar{1})$ and the mixed-terminated $\text{ZnO}(10\bar{1}0)$ surfaces, but not for the Zn-terminated $\text{ZnO}(0001)$ surface [Oza11]. They estimated the charge density accumulating on the ZnO surfaces due to H-adsorption to 10^{13} cm^{-2} . In addi-

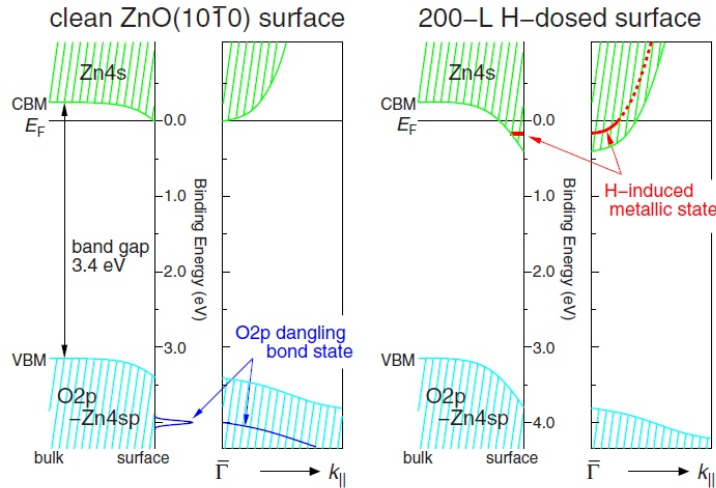


Figure 3.3: Schematic of the energy band structures of the clean (left) and H-covered ZnO(10 $\bar{1}0$) surface (right) with the metallic surface state (red) as published by Ozawa and Mase, adopted from Ref. [Oza10].

tion they investigated the non-polar ZnO(10 $\bar{1}0$) surface as a function of hydrogen, methanol and water adsorption [Oza10]. They found that all three adsorbates induce bending of the CB below the Fermi level and thus the formation of a CAL, which was explained by all three adsorbates acting as electron donors.

Figure 3.3 shows schematics of the band structures of the clean and the H-covered ZnO(10 $\bar{1}0$) surfaces observed by Ozawa *et al.* [Oza10]. The valence electronic structure of the pristine surface (left) is characterized by the O2 p -Zn4 sp (blue shaded area) hybrid band, with the O2 p dangling bond state, located between 3 - 9 eV below the Fermi energy. The conduction band consists of the empty Zn4 s levels (green shaded area). The H-covered ZnO surface exhibits an enhanced downward surface band bending giving rise to a CAL (red line) with a thickness of several 10 Å [Wan05b] and a maximum surface charge density of 10^{13} cm $^{-2}$ due to the electrons donated by the adsorbed hydrogen, partially occupying the CB [Oza11].

While Ozawa *et al.* studied the H $_2$ -dosage regime between 200 and 2000 L Deinert *et al.* investigated the low dosage regime between 6 and 500 L by means of 2PPE [Dei14, Dei15b]. They also observed a pronounced work function decrease correlated with increased downward surface band bending and the formation of a CAL upon hydrogen adsorption. Figure 3.4 shows the work function and the integrated CAL intensity plotted as a function of H $_2$ -dosage. The work function saturates around 3.8 eV with a maximal shift of $\Delta\Phi_{\max} = -0.65$ eV, while the CAL intensity decreases for H $_2$ -dosages higher than 150 L. The reduction of the

3.1 Electronic Properties and Excited State Dynamics at the Mixed- and the O-terminated ZnO Surface

CAL intensity was explained by the formation of ZnH-bonds which compensate the surface dipole induced by the OH-bonds because hydrogen acts as an electron acceptor in the zinc-hydride bond [Dei15b]. According to DFT calculations presented in the same work, ZnH-bond formation sets in at a H-coverage of $\approx 18\%$ leading to a complex and competitive behaviour of OH- and ZnH-bond formation.

They found out that next to an H-terminated O-atom H-adsorption on a Zn-ion is energetically favoured over the formation of another OH-bond. This was explained by the reduction of the work function, and consequently the IP and EA, due to OH-bond formation, thus making charge transfer from the electron donor (H in OH-bond) to the ZnO less favourable while charge transfer from the ZnO to an acceptor (H in ZnH-bond) becomes profitable.

In addition the calculations revealed that the CAL starts to delocalize at a critical H-coverage of $\approx 25\%$ when the potential wells, which are due to a significant reduction of the surface potential induced by the OH-bonds and have a diameter of ≈ 5 nm, start to overlap [Dei15b]. Concerning the extension of the CAL perpendicular to the surface, they found it located right at the surface since the OH-bond induced changes of the surface potential reach less than 20 \AA into the bulk.

On the basis of the results presented in this section questions for the behaviour of the O-terminated surface towards H-adsorption can be derived. The absence of Zn-ions at the polar surface should lead to a larger work function shift upon H-adsorption compared to the non-polar surface. Moreover no decrease of the CAL intensity above a certain H_2 -dosage is expected since no ZnH-bonds, countervailing the effects of OH-bond formation, should be formed. The saturation of the work function is expected to be reached at higher H_2 -dosages since there are nearly twice as many O-ions on the polar than on the non-polar surface.

In the following section previous studies on surface exciton (SX) dynamics at ZnO surfaces will be presented.

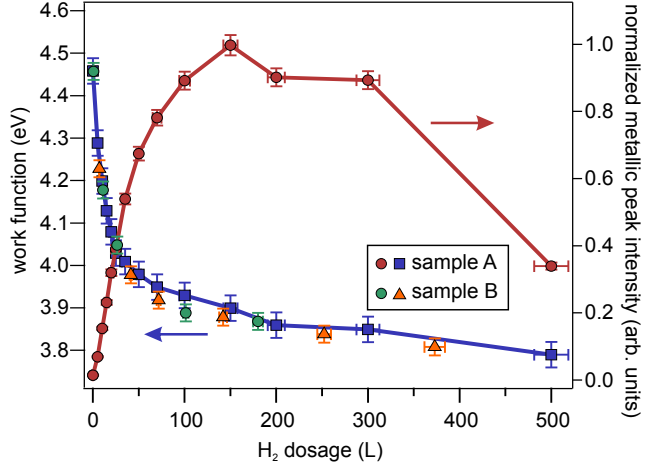


Figure 3.4: Work function and CAL intensity as a function of H-dosage as measured by Deinert *et al.*, adopted from Ref. [Dei15b].

3.1.3 Surface Exciton Dynamics at ZnO Surfaces

In this section general information about surface excitons on ZnO surfaces is given, relevant studies for the understanding of the results obtained in this work are presented and open questions will be motivated. Exciting ZnO above the band gap leads to the formation of excitons which are important quasi-particles for optoelectronic and light harvesting devices. In ZnO the existence of several excitonic species, such as free excitons, donor- and acceptor-bound and SX, have been reported [Özg05, Kue13, Dei14, Tis08]. Surface excitons are of great interest since energy transfer processes between different materials take place at their interfaces and usually involve short distance energy transfer processes such as Förster resonance energy transfer (FRET). They deserve particular attention because also exciton free surface layers in ZnO, potentially inhibiting energy transfer at the surface, have been reported [Lag63]. Surface excitons have been observed on single crystal surfaces [Tis08, Dei14], pseudomorphically grown thin films [Kue13, Fri15] and even in confined nanoscale systems [Bis11, Ric08, Yan07] in which so-called 'exciton dead layers' are expected to prevent exciton localization at the surface [Fon04].

The origin of SX was investigated by Biswas et al. who concluded that the existence of surface excitons was due to modification of the surface by an adsorbate, in their case most likely an OH-related species [Bis11]. Other studies demonstrated that the SX can be influenced by adsorbates, irradiation or particle bombardment [Kue13, Bis11, Yan07, Ric08]. For example Kuehn et al. reported an enhancement of the signal intensity related to the SX by adsorbing organic molecules with carboxylic anchor groups [Kue13]. In contrast the SX related signal was quenched in another study upon treatment with titanium plasma as [Yan07].

The emission signals from the SX were found around 3.365 - 3.368 eV, *i.e.* between the free and the donor-bound excitons, in photoluminescence measurements [Kue13, Bis11, Ric08]. The SX were reported to be spatially located right at the surface [Fri15], within 5 nm from the surface [Yan07] and around 20 Å below the surface [Dei14].

A time-resolved 2PPE study on the SX dynamics on the H-doped ZnO(10 $\bar{1}$ 0) surface has been performed in our group by J.-C. Deinert [Dei14]. He found that after excitation above the band gap the hot carriers relax via scattering with LO phonons followed by SX formation within 200 fs. Ultrafast phonon-mediated relaxation of above band gap excited electrons, slowing down for energies close to the CBM, has been also demonstrated in another 2PPE study by Tisdale *et al.* [Tis08]. Both studies revealed a temperature-independent behaviour of the ultrafast relaxation dynamics up to 300 K which was interpreted as a confirmation of Fröhlich coupling with LO phonons since interaction with lower lying transversal optical phonons leads to a

3.1 Electronic Properties and Excited State Dynamics at the Mixed- and the O-terminated ZnO Surface

slowing down of the relaxation dynamics, as it is the case for low energies. In addition a theoretical study by Zhukov *et al.* confirms the existence of two types of excited electron dynamics: (i) a fast one in the fs regime for high excess energy electrons related to electron-phonon scattering and (ii) ps dynamics for electrons close to the bottom of the CB associated with the reduction of the phonon phase space [Zhu10].

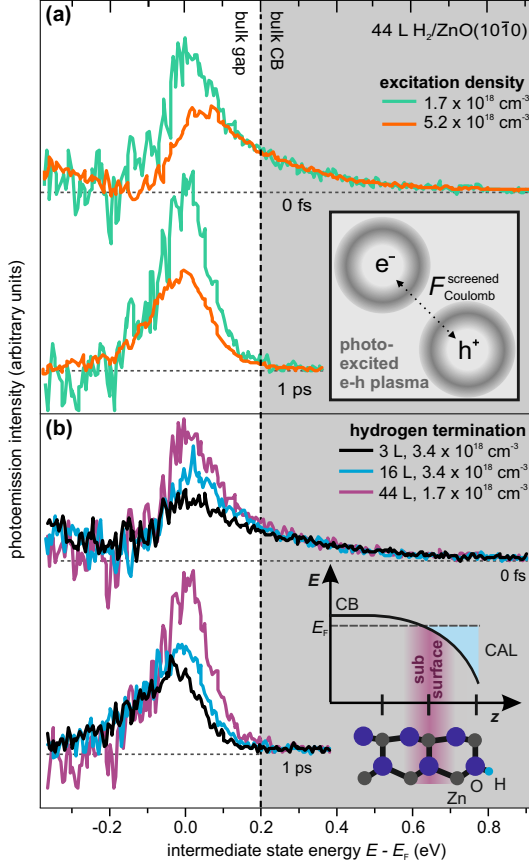


Figure 3.5: Pump-induced 2PPE signals for (a) different excitation densities and (b) different H-dosages, normalized to the hot electron intensity between 0.4 and 0.6 eV to compare intensity changes relative to the single particle excitation density. (a) Higher excitation densities lead to a screening of the Coulomb interaction, as illustrated in the inset, and diminish the SX formation probability. (b) The SX intensity is not decreasing for increased carrier concentration in the CAL, due to higher H-coverages, indicating localization in the subsurface region as visualized in the inset. Adopted from Ref. [Dei14].

The time constants calculated by Zhukov *et al.* will be compared to the time constants experimentally obtained in this work in Section 5.1.2. Above a critical photoinduced carrier density, which was calculated to $1 \times 10^{19} \text{ cm}^{-3}$, the phonon emission rate is expected to decrease significantly with increasing carrier density [Tis08]. The SX lifetime was found to exceed 400 ps and electron-hole recombination, leading to luminescence or Auger-like processes, was suggested as decay channel [Dei14].

Deinert *et al.* demonstrated that the formation probability of SX is reduced by transient screening of the Coulomb interaction at excitation densities close to the Mott density [Dei14]. This result was achieved performing time-resolved 2PPE measurements on the H-doped ZnO surface as a function of the excitation density. Figure 3.5 (a) displays the pump-induced 2PPE signals related to the SX for low (green) and high (orange) excitation densities. For high excitation densities the distance between the excitons becomes smaller than the exciton Bohr radius, leading to a screening of the Coulomb interaction between electron and hole and thus to a reduction of their formation probability, as discussed in Section 2.2.1.

In addition they concluded that the

SX is located in the sub-surface region based on the finding that the SX was stable towards work function changes and enhanced charge carrier density in the CAL, induced by H-adsorption. The fact that the photoemission signal assigned to the SX does not decrease for H₂-dosages up to 44 L, as demonstrated in Figure 3.5 (b), reflects that the SX is neither affected by the change of the surface potential nor by the increased carrier density in the CAL, which might lead to a screening of the Coulomb interaction between electron and hole and with this to a reduction of the exciton formation probability. Moreover the SX could still be observed after exposing the single crystal surface to air [Dei15a]. This extraordinary stability towards air in combination with its stability at room temperature make the SX a promising feature for charge transfer applications, as fabrication processes and device operation usually do not take place in ultrahigh vacuum (UHV) chambers at a temperature of 100 K.

In this thesis the questions, whether such a surface exciton exists as well at the O-polar ZnO(000 $\bar{1}$) surface and if yes, how fast the formation and decay dynamics take place, are examined using time-resolved 2PPE. In addition the question whether the total charge density, consisting of the H-induced (CAL) and the photoinduced (excitation density) electron density, affects the relaxation dynamics of the hot electrons will be pursued. Further problems arising from the discussion above concern the influence of H-adsorption on the electronic structure of the O-terminated surface, e.g. how is the H-induced work function shift on the polar surface affected by the absence of Zn-ions in comparison to the mixed-terminated surface where the O-density is smaller. Another question is related to the behaviour of the CAL intensity as a function of the H₂-dosage, which is not expected to decrease for higher H₂-dosages on the polar surface, as it is the case on the non-polar surface, since no ZnH-bond formation is expected. These problems will be treated in Sections 5.1.1 and 5.1.2.

3.2 Electronic Structure and Excited State Dynamics in SP6 on ZnO

Organic π -conjugated molecules represent a very attractive class of materials for various optoelectronic applications since their electronic and adsorption properties are highly tunable. With the goal to design perfect interfaces for optoelectronics, which are determined by a lot of correlated aspects, such as energy level alignment, interactions between the different materials as well as intermolecular interactions, a huge variety of customized molecules is currently being synthesized.

The spirobifluorene derivative 2,7-bis(biphenyl-4-yl)-2',7'-di-*tert*-butyl-9,9'-spirobifluorene (SP6) is, on the one hand, a promising candidate for the application in OLEDs and organic solid state lasers due to its strong blue luminescence. On the other hand, it is attractive for the study of charge transfer, important e.g. in solar cells, since adsorption on ZnO leads to the necessary type-II energy level alignment [Blu08, Sch04a]. SP6 is a pure hydrocarbon compound consisting of a sexiphenyl backbone which is connected *via* a spirocarbon to a *tert*butyl-substituted fluorene unit. The spirocarbon linkage separates the two π -systems of the sexiphenyl and the fluorene unit. It can be synthesized *via* a palladium-catalyzed cross-coupling reaction of the Suzuki-type using 2,7-dibromo-2',7'-di-*tert*-butyl-9,9'-spirobifluorene [Kim05] and 4-biphenyl-boronic acid [Fal05].

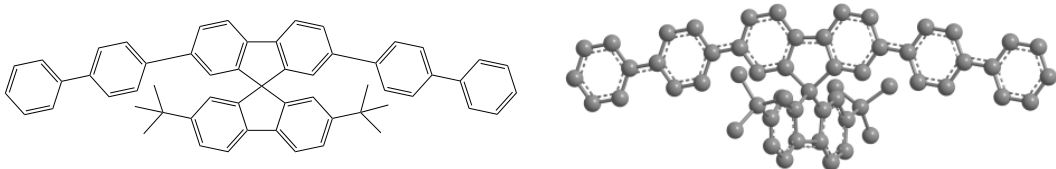


Figure 3.6: Lewis formula and ball and stick model of SP6, showing the carbon atoms only.

As mentioned above the combination of organic and inorganic semiconductors promises new electronic and photonic properties and the great variability of organic molecules provides the possibility of customizing the electronic properties of interfaces. For instance non-radiative energy transfer in an inorganic/organic sandwich structure, consisting of zinc magnesium oxide (ZnMgO)/SP6/ZnO, from the ZnO quantum well to the SP6 film has been observed [Blu09]. In addition, amplified spontaneous emission (ASE) from the SP6 film in a ZnO/SP6/ZnO sandwich structure has been reported, what makes SP6 a promising candidate for the application as active material in organic solid-state lasers [Blu09, Sch04a]. In the following, recent studies on SP6 on ZnO surfaces will be presented as their findings on the energy level alignment at SP6/ZnO interfaces and excited state dynamics in SP6 films on

ZnO are of major interest for this work.

Information on intermolecular as well as molecule-substrate interactions is provided by a recent experimental and theoretical Raman study of SP6 on different substrates, e.g. ZnO(000 $\bar{1}$), by Stähler *et al.* [Stä13]. They observed that the vibrational response of the SP6 molecules is not affected by the substrate and compares well to the DFT calculations of SP6 in the gas phase, revealing that the interaction between the molecules and the employed oxide substrates is weak [Stä13].

The adsorption behaviour of SP6 has been studied by Blumstengel *et al.* by means of atomic force microscopy (AFM) showing that SP6 forms smooth, amorphous films on ZnO surfaces. This is due to the rigid propeller-like structure of the molecules, induced by the spiro-linkage, which prevents crystallization on the sample surface [Blu08]. Furthermore they investigated the electronic structure and the exci-

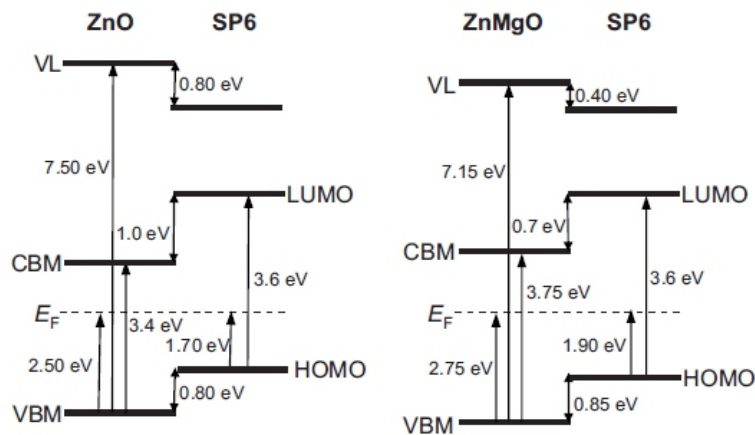


Figure 3.7: Energy level diagrams of SP6/ZnO and SP6/ZnMgO adopted from Ref. [Blu08].

ton dynamics of SP6 on the O-terminated ZnO(000 $\bar{1}$) surface of a ZnO single crystal and on a ZnMgO(000 $\bar{1}$) epilayer using ultraviolet photoelectron spectroscopy (UPS) and time-resolved photoluminescence (PL) spectroscopy. The UPS measurements were carried out for films between 0.2 nm and 3.2 nm thickness, exhibiting work function reductions of 0.8 eV from 5.0 eV to 4.2 eV in the case of SP6/ZnO(000 $\bar{1}$), and 0.4 eV from 4.4 eV to 4.0 eV for SP6/ZnMgO. The energy level diagrams obtained by Blumstengel *et al.* are depicted in Figure 3.7 and exhibit the staggered type-II energy level alignment, where the CBM and the VBM of the inorganic semiconductor lie below the LUMO and HOMO of the molecule [Blu08]. The CBM and LUMO energies have been estimated by adding the optical gaps ($E_{\text{opt}}^{\text{SP6}} = 3.15$ eV, $E_{\text{opt}}^{\text{ZnO}} = 3.34$ eV and $E_{\text{opt}}^{\text{ZnMgO}} = 3.69$ eV), obtained from absorption measurements, and

the exciton binding energies to the VBM and HOMO energies. The exciton binding energy in bulk ZnO ($E_b^{\text{ex}} = 0.06$ eV) is known from the literature [Hüm73] and the exciton binding energy in SP6 was estimated to be similar to the value of 0.45 eV reported for a ladder-type poly(para-phenylene) by Kemerink *et al.* [Kem04].

The PL measurements were performed for SP6 films on ZnMgO for film thicknesses ranging between 1.6 nm and 12 nm for temperatures between 5 K and 280 K. The observed PL lifetime τ and the charge transfer efficiency η_{CT} which describe the electron transfer from the LUMO to the ZnO CB, showed a strong dependence on the film thickness as well as the temperature. Analysis of these measurements using a linear diffusion model yielded a PL lifetime of 300 ps and exciton diffusion lengths of 3.7 nm at 5 K and 10 nm at 300 K [Blu08]. The rate-determining step for the charge separation at the SP6/ZnO interface was found to be the exciton diffusion. The short exciton diffusion lengths in the amorphous SP6 films explain the strong thickness dependence of the PL lifetime and the charge transfer efficiency η_{CT} .

In our group, L. Foglia conducted a comparative study of SP6 films on glass and on the non-polar ZnO(10 $\bar{1}$ 0) surface using time-resolved excited state transmission [Fog15]. Here, the system is excited resonantly with $h\nu_{\text{pump}} = 3.7$ eV and probed

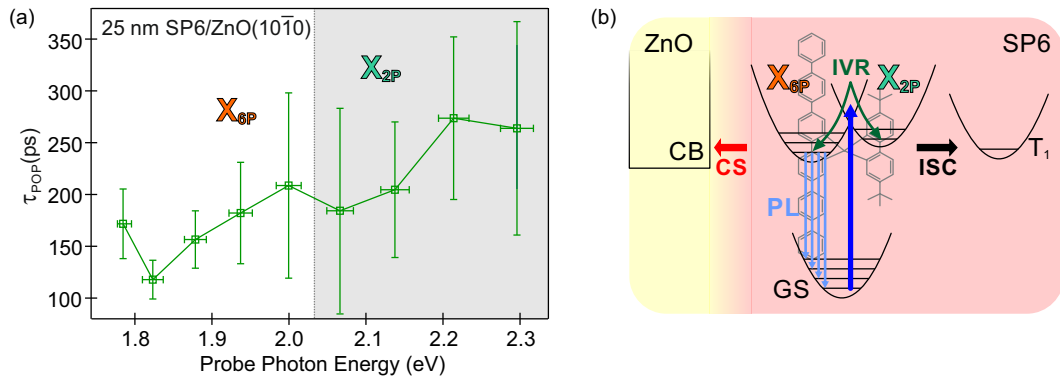


Figure 3.8: (a) τ_{POP} vs. probe photon energies for SP6/ZnO, two resonances X_{6P} and X_{2P} are observed; only X_{6P} is affected by the presence of the ZnO surface. (b) Schematic of the involved electronic processes: Internal vibrational relaxation (IVR), photoluminescence (PL), intersystem crossing (ISC) and charge separation (CS) at the ZnO interface affecting only the X_{6P} population. Adopted from Ref. [Fog15].

by a white light continuum. The time constants are obtained as a function of the probe photon energy from the analysis of the data, which revealed a biexponential decay. In addition a constant offset was observed and related to the existence of a long-lived dark state, exceeding the repetition rate of the laser system. The fast time constant is in the range of several ps and is related to IVR within the excited states. The slow dynamics are on a time scale of 200 ps and were attributed to the decays of two different excited states, X_{6P} and X_{2P} (Figure 3.8 (a)). The X_{6P}

population possesses a shorter lifetime than the X_{2P} population as only the first is affected by charge separation at the ZnO interface.

The observed processes are summed up in Figure 3.8 (b): After resonant excitation with 3.7 eV the system undergoes 1) IVR within the excited states on a timescale of several ps, 2) the X_{6P} population decays on a timescale of ≈ 200 ps *via* 3 competing pathways: photoluminescence (PL), ISC leading to the formation of a long-lived triplet state with a lifetime of several μ s and diffusion of X_{6P} excitons towards the ZnO interface where charge separation (CS) occurs. 3) The X_{2P} population, instead, decays only *via* ISC.

Despite the manifold of studies the energetic positions of the excited states, which are of crucial interest for charge- and energy transfer and the dynamics of the dark state remain unknown. We tackle these open question by time-resolved 2PPE providing not only access to the absolute energies of excited states but also to the dark state dynamics. The triplet state is not necessarily dark for photoemission since electron emission does not underly the strict selection rules which hold for optical spectroscopy, as will be shown in Section 5.2.

3.3 Electronic Structure of Dicyanovinyl-Substituted Oligothiophenes on Au(111)

Oligothiophenes have been extensively investigated over the past 20 years in the context of organic photovoltaic cells (OPVCs), organic light emitting diodes (OLEDs) or organic field effect transistors (OFETs) due to their promising properties, such as high charge carrier mobility and light absorption in the visible range [Vid99, Bar05, Vid00, Spa04]. Oligothiophenes belong to the group of small molecule donor materials and are usually processed by vapour deposition, in contrast to polymers which have to be processed wet chemically. The most intensively studied oligothiophene is α -sexithiophene which was employed in the first organic field effect transistor [Hor96, Var11a, Fic97]. The efficiency of OPVCs depends on several interacting processes such as light absorption, exciton formation, diffusion and dissociation and efficient charge transport towards the electrodes [Poe15]. The absorption strength of organic semiconducting molecules can be enhanced by substituting a donor molecule with an acceptor-group, resulting in so-called donor-acceptor (D-A) or acceptor-donor-acceptor (A-D-A) molecular architectures. The dicyanovinyl-(DCV-)substituted oligothiophenes represent the A-D-A molecules and have significantly smaller HOMO-LUMO gaps than their unsubstituted counterparts, since the DCV-groups are strongly electron withdrawing.

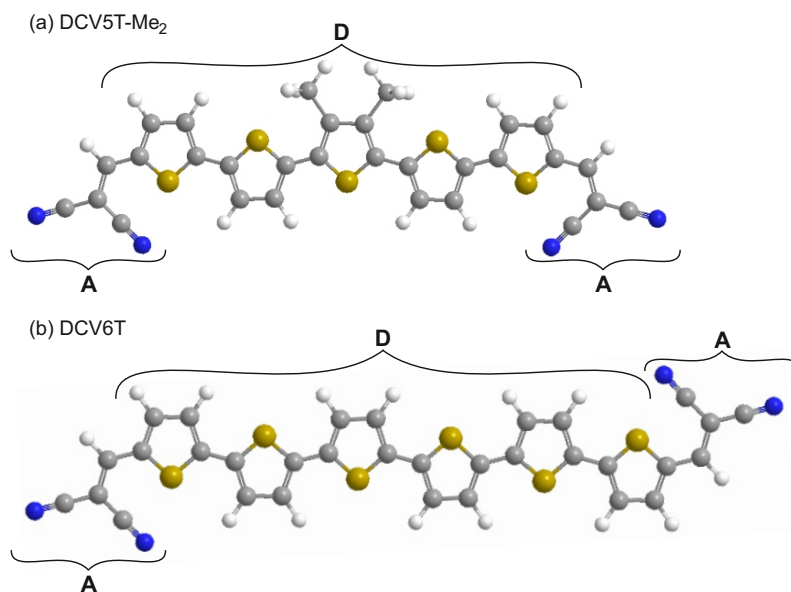


Figure 3.9: Ball and stick model of (a) DCV5T-Me₂ and (b) DCV6T, the carbon atoms are coloured grey, the hydrogen atoms white, the sulfur atoms yellow and the nitrogen atoms blue. The thiophene backbone represents the donor and the dicyanovinyl-groups represent the acceptor part of the molecules.

Figure 3.9 shows the two DCV-substituted oligothiophenes investigated in this work: (a) the dimethylated dicyanovinyl-quinquethiophene (DCV5T-Me₂) and (b) the dicyanovinyl-sexithiophene (DCV6T). The molecules were synthesized by R. Fitzner in the group of P. Bäuerle (Ulm University) from DCV-substituted bromobithiophene and distannylated mono- and bithiophene *via* a Pd-catalysed cross-coupling reaction (Stille-coupling) a detailed description of the synthesis and characterization can be found in [Fit11].

Compound	E_g^{CV} (sol.)	E_g^{opt} (sol.)	E_g^{opt} (film)
DCV5T-Me ₂	1.91 eV	1.99 eV	1.69 eV
DCV6T	1.56 eV	2.00 eV	1.68 eV

Table 3.1: Energy gaps of DCV5T-ME₂ and DCV6T in solution (sol.) and of 30 nm thick films, adopted from Ref. [Fit11, Fit12b].

Table 3.1 presents optoelectronic properties of the two molecules in solution and as 30 nm thick films respectively, which were obtained from absorption spectroscopy and cyclic voltammetry carried out by Fitzner et al. [Fit11, Fit12b]. The gaps measured by means of cyclic voltammetry correspond to the difference between oxidation and reduction potential of the molecules, *i.e.* the difference between the ($N+1$)- and the ($N-1$)-electronic state, and can thus be compared to the transport gaps (EA/LUMO - IP/HOMO) obtained from 2PPE and STS. The gaps from absorption measurements correspond to the optical gaps, the difference between optical and transport gap is discussed in Section 2.2.2. The optical gaps measured in solution are larger compared to the gaps obtained from the films. Moreover Fitzner et al. observed that the absorption and emission spectra of the films exhibited a significant broadening and a red-shift compared to the spectra measured in solution. This was explained by enhanced ordering and intermolecular interaction of the molecules in the bulk [Fit11]. X-ray structure analysis of DCV5T-Me₂ crystals revealed that each molecule in the crystal interacts with 10 neighbouring molecules via 16 well-defined interactions [Fit12b]. For example H-bonds between vinylic or aromatic CH-groups and the N-atoms of adjacent cyanogroups were identified, furthermore dipolar interactions between methyl-H and S atoms and π -stacking contribute to the intermolecular interactions.

Both molecules have been incorporated as donor materials *via* vapour deposition in OPVCs with different architectures and yielded significantly different power conversion efficiencies. A planar heterojunction solar cell with DCV6T as donor

material yielded a power conversion efficiency (PCE) of 2.8 % [Fit11], while a bulk heterojunction solar cell employing DCV5T-Me₂ yielded 6.1 % [Fit11, Fit12b]. More sophisticated solar cell architectures even achieved a PCE of 8.3 % for a single and 9.7 % for a triple junction cell using DCV5T-Me₂ as donor material [Mee14]. This makes DCV5T-Me₂ the world-champion of the evaporated molecular donor materials with a disclosed chemical structure². The question is why these two molecules show such a different solar cell performance, although they exhibit similar optoelectronic properties. Poelking et al. provide an explanation for the high solar cell performance of DCV-substituted molecules by linking molecular order with the energy landscape of the donor/acceptor interface which is influenced by long-range electrostatic effects [Poe15]. These long-range electrostatic effects might be affected by the permanent molecular dipole moment, which is strong in the case of DCV5T-Me₂, due to its C_{2v} symmetry, and cancels out for DCV6T since the DCV-groups point in opposite directions. Another aspect is the film morphology and the degree of order therein. Fitzner et al. compared the solar cell performance and crystal structure of differently alkylated DCV-substituted quarterthiophenes and found that the number of intermolecular interactions correlates with the solar cell efficiency [Fit12a]. While the small structural variations due to alkylation do not significantly change the optoelectronic properties, they have an astonishing influence on the solid state properties which play a major role for exciton diffusion and charge transport, on which in turn the photovoltaic performance relies [Fit12a]. Methyl substitution proved to be a practical method to influence the morphology of donor/acceptor blends in bulk heterojunction solar cells, which leads in this case to an improvement of the device performance [Fit12b].

A theoretical study by Schrader et al. on the charge dynamics in crystalline DCV-substituted oligothiophenes showed that the direction with the highest carrier mobility was not parallel to the direction with the strongest coupling and that pronounced π -stacking even inhibited other transport directions [Sch12b]. Moreover they found that the mobility was higher in the methylated compounds which give rise to more balanced three-dimensional networks of electronic couplings [Sch12c, Sch12b]. Recent X-ray scattering experiments demonstrated that the organic films employed in devices, prepared by vapour deposition in UHV, exhibit well ordered polycrystalline morphologies [Koe12]. Therefore the finding from the theoretical study presented above can be applied to these devices.

In the following sections recent STM and STS studies on the adsorption geometry and electronic structure of DCV5T-Me₂ and DCV6T adsorbed on the Au(111) surface will be presented.

²Another A-D-A quinquethiophene yielded a PCE of 10.1 % in a solution processes device [Kan15]

3.3.1 Adsorption and Electronic Properties of DCV5T-Me₂/Au(111)

The STM and STS investigations introduced in this and the next section were carried out by Z. Yang in the group of I. J. Pascual and K. J. Franke at Freie Universität Berlin [Yan14a, Yan14b, Bog15]. Adsorption of DCV5T-Me₂ on the Au(111) surface leads to the formation of chains and islands on the Au(111) surface for submonolayer coverages [Yan14b]. The chains are stabilized by Au-adatoms which are incorporated *via* coordination bonds with the cyano-groups. In the islands however no such Au-coordination bonds were found, they are stabilized by H-bonds and electrostatic interactions instead. Figure 3.10 (a) shows a STM image of an island, the three coloured spots indicate the molecular positions on which the dI/dV spectra displayed as a function of the bias voltage in Figure 3.10 (b) were taken. Yang et al. found three different resonances, at 1.3, 1.65 and 2.35 V, in the dI/dV spectra depending on the position in the molecule. In order to assign these features to molecular states dI/dV maps at the respective bias voltages were taken and compared to the shape of the Kohn-Sham orbitals, which were calculated at the 6-31G/B3LYP level using the *Gaussian 03* programm package [Fri04].

For example the resonance at 1.3 V is visible at all three positions in the molecule, *i.e.* in all three dI/dV spectra. Taking a look at the Kohn-Sham orbital of the LUMO, Figure 3.10 (c), shows that it is delocalized over the whole molecule and is thus assigned to the resonance at 1.3 eV. In contrast the resonance at 2.35 V is only visible in the red spectrum recorded in the center of the molecule, the dI/dV map taken at a bias of 2.25 V shows that the orbital distribution is located mainly in the center of the molecule which is accordance with the shape of the LUMO+2. According to this assignment procedure the observed resonances were related to the LUMO at 1.3 V, the LUMO+1 at 1.65 V and the LUMO+2 at 2.35 V.

The monolayer structure is the same as in the islands and the islands formed in the second layer are as well stabilized

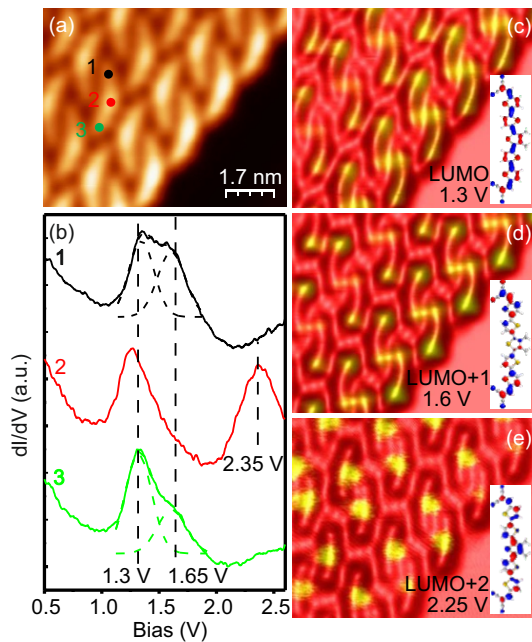


Figure 3.10: (a) STM image of a DCV5T-Me₂ island, (b) dI/dV spectra taken at different points on a molecule in the island, (c)-(e) constant height dI/dV maps of the same island recorded with bias voltages of 1.3, 1.6 and 2.25 V, the insets show the Kohn-Sham LUMO, LUMO+1 and LUMO+2 of DCV5T-Me₂, adopted from Ref. [Bog15].

through intermolecular interactions by the DCV5T-Me₂ molecules. A large scale STM image of the second layer is shown in Figure 3.11 (a). Figure 3.11 (b) shows a

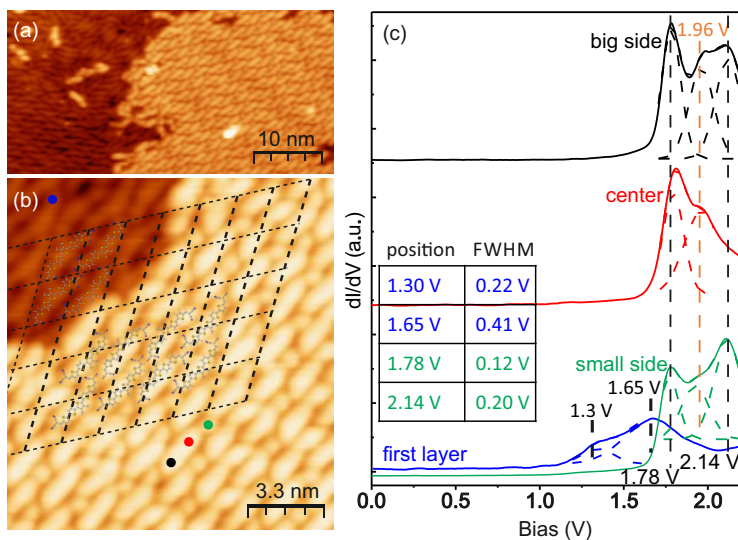


Figure 3.11: (a) Large scale and (b) high resolution STM image of a DCV5T-Me₂ bilayer and (c) dI/dV spectra taken on molecules in the first and the second layer. The energetic position and the FWHM of the peaks are listed in the inset table. The figure is adopted from Ref. [Bog15].

high-resolution STM image of the bilayer film with a grid indicating the orientation of the molecules in the first layer, which are slightly shifted and rotated with respect to the molecules in the second layer. The dI/dV spectra taken on the different positions on the molecule exhibit sharper peaks and resonances shifted to higher bias voltages due to electronic decoupling from the metal surface of the molecules in the second layer [Hei13, Tor08]. Compared to the electronic structure of the islands and the monolayer the LUMO is shifted from 1.3 V to 1.8 V and the LUMO+1 from 1.65 V to 2.1 V. A similar behaviour has been observed for octithiophene (8T) on Au(111), where the binding energy of the HOMO decreased upon increasing the 8T coverage from a submonolayer to a monolayer coverage [Var11b]. In this case monolayer formation lead to a change in the adsorption geometry from planar in the submonolayer to an adsorption geometry where the molecules are tilted with respect to the surface thus strongly enhancing π -stacking. This change of adsorption geometry lead to electronic decoupling of the HOMO and thus to an energetic shift [Var12b].

In addition a resonance peak at 1.96 V is observed which is separated from the LUMO resonance by 180 mV. This amount of energy coincides with the energy of the twist vibration of the thiophene backbone [Yan14a]. Therefore this resonance

has been assigned to a vibronic feature which is excited by the tunneling electrons [Fra12, Bog15].

3.3.2 Adsorption and Electronic Properties of DCV6T/Au(111)

Submonolayer adsorption of DCV6T on the Au(111) surface leads to the formation of three different adsorption regimes, (i) islands, (ii) chains growing across the herringbone reconstruction and (iii) chains which grow in the face centered cubic (fcc) region of the reconstructed Au(111) surface [Yan14a]. The islands (i) and chains (iii) growing in the fcc region of the herringbone reconstructed Au(111) surface are formed *via* intermolecular hydrogen bonding and electrostatic interactions [Yan14a]. In contrast the chains (ii) which grow across the herringbone pattern are stabilized by metal-organic coordination bonds with Au-adatoms, as observed before for DCV5T₂.

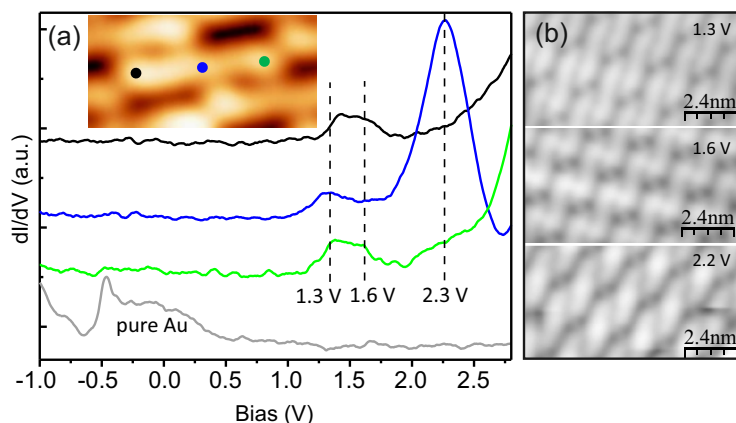


Figure 3.12: (a) dI/dV spectra measured at different locations on the molecule in the island as indicated in the inset. (b) STM images of an island recorded at bias voltages of 1.3 V, 1.6 V and 2.2 V, revealing the distribution of the unoccupied molecular orbitals. Adopted from Ref. [Yan14a].

Figure 3.12 (a) shows dI/dV spectra taken at different positions on a molecule within an island, exhibiting altogether 3 resonances at 1.3, 1.6 and 2.3 V, depending on the position of the STM tip on the molecule. Figure 3.12 (b) displays dI/dV maps recorded at the bias voltages of the resonances showing the distribution of the orbitals. The resonances were assigned to the LUMO at 1.3 V, the LUMO+1 at 1.6 V and the LUMO+2 at 2.3 V [Yan14a]. These energetic positions are similar for DCV6T molecules within all the three adsorption regimes observed, in addition they show a strong similarity to the resonances found for DCV5T-Me₂. For the second layer DCV6T on Au(111) no STM data is available.

3.3 Electronic Structure of Dicyanovinyl-Substituted Oligothiophenes on Au(111)

In order to gain deeper insight into the electronic structure, this work investigates the electronic structure of the two DCV-substituted oligothiophenes on Au(111) as a function of the coverage. Particular focus is on the occupied electronic structure and the electronic structure of higher coverages, which have not been observed in the STS study. Furthermore the excited state dynamics are of particular interest since no time-resolved studies have been reported so far on neither of the two molecules. Time-resolved 2PPE is a powerful method which allows to measure the excited state population after optical excitation at the sample surface. This promises to gain deeper insight into exciton formation and decay dynamics in DCV5T-Me₂ and DCV6T on Au(111) and to reveal whether the difference in solar cell performance is reflected in the excited state dynamics.

3.4 Electronic Structure of the Au(111) Surface

Gold is the noble metal with the highest atomic number in the copper group, the first group of the transition metals. It is very inert and exhibits some extraordinary properties [Hol07] such as the highest (positive) redox potential of all metals ($\epsilon_0 = +1.50$ V for Au/ Au³⁺), the biggest Pauling-electronegativity (EN = 2.4), the most negative electron affinity (EA = -2.31 eV) and, besides mercury and zinc, gold has the highest ionisation energy (IE = +9.22 eV). In contrast to the surrounding metals in the periodic table gold shows halogen analogous behaviour due to the ability of forming a monoanion [Hol07]. Some of these special properties rely on the fact that the valence electrons of gold are liable to powerful relativistic effects, which cause a fairly strong 6s- and a weaker 6p-orbital contraction, and thus a lowering in energy, as well as an expansion of the 5d orbitals, which experience an energetic exaltation [Hol07].

Gold crystallizes in the fcc lattice with a lattice constant of $a = 4.08 \text{ \AA}$ [Kit80], a model of the unit cell is depicted in Figure 3.13 (a). The (111)-surface is obtained by intersecting the coordinate axes of the unit cell at the same axis intercept and is shown in Figure 3.13 (b). The (111)-surface of each unit cell amounts $\sqrt{3}a^2/2 = 14.42$

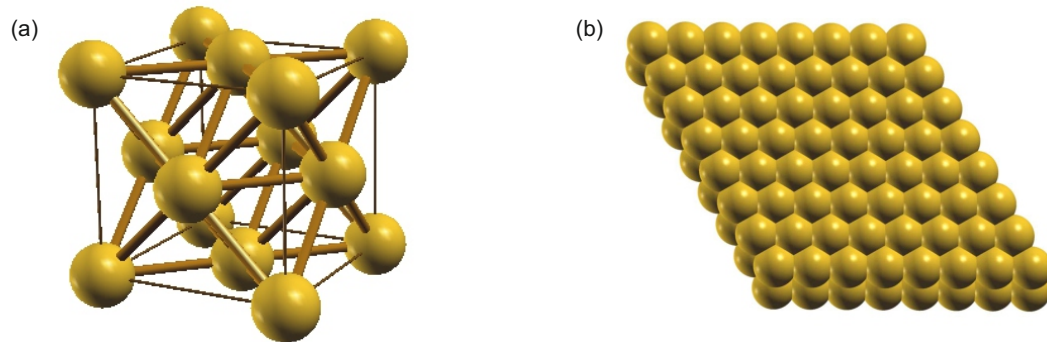


Figure 3.13: (a) Unit cell of the fcc-lattice and (b) the hexagonal Au(111) surface, pictures generated with Xcrysden [Kok03].

\AA^2 and contains two Au atoms. It exhibits a hexagonal structure of the hexagonal close packed (hcp)-type and the expected stacking would be ABABAB...(hcp-like) or ABCABC...(fcc-like).

But the real Au(111) surface appears in a different structure, since the surface undergoes a reconstruction, the so-called herringbone reconstruction. Figure 3.14 (a) shows an STM image of the reconstructed Au(111) surface, exhibiting nicely the herringbone pattern. The reconstructed surface shows a $(n \times \sqrt{3})$ unit cell with $n \approx 22$, containing $2n+2$ surface atoms. The reason for this reconstruction can be found in the competition of two effects [Nar92]:

(i) Surface relaxation: The bond length at the surface is preferred to be smaller than in the bulk. Due to the lack of binding partners at the surface the atoms move towards the bulk, which results in a shortening of the bond lengths.

(ii) The surface atoms prefer staying in registry with the bulk as it is energetically favourable to sit in the minima of the potential, generated by the atoms in the bulk. There exist two different competing sites for the surface atoms, as the fcc-stacking in the direction of the (111) surface may terminate either on a hcp- or a fcc-site, whereas the hcp-site is a little bit higher in energy. The surface bond length can be reduced, by occupying both sites. Thereby alternating domains of hcp- and fcc-like regions, separated by corrugation lines, arise as sketched in Figure 3.14 (b). The atoms, which are located within these transition regions are moved a bit upwards. The corrugation lines form a zig-zag pattern, which are bent by 120° at the domain walls, (dashed lines, which separate the domains of different orientation) forming so-called 'elbows'. In these elbows each second soliton wall exhibits a dislocation (represented by stars in Figure 3.14 (b)), which consists of two atoms, of which one is located within a pentagonal (instead of a hexagonal) coordination sphere and the other one has a coordination number of seven. The elbows play an interesting role

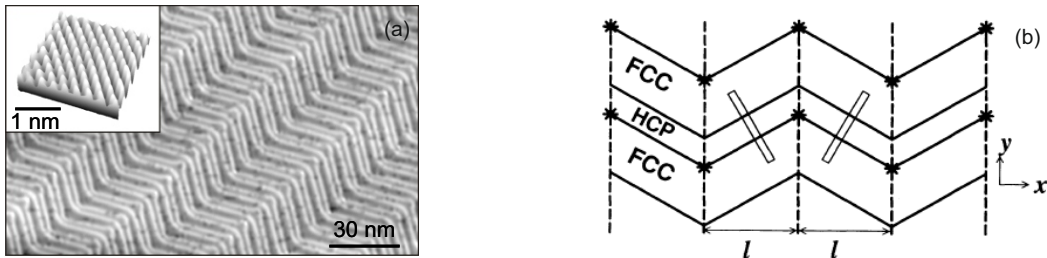


Figure 3.14: (a) STM image of the reconstructed Au(111) surface (image courtesy of E. Varène and Y. Penneç) and (b) scheme of the herringbone reconstruction, adopted from Ref. [Nar92]: The horizontal zigzag line in the sketch depicts the soliton walls, the vertical dashed lines the domain walls and the stars the dislocations. The light solid lines show the $(n \times \sqrt{3})$ subunits.

in the growth of metal overlayers, e.g. Ni and Co are found to assemble at these points [Cha91].

The work function of the Au(111) surface is reported to amount between 5.35 eV [Ren05] and 5.55 eV [Reu96]. The electron configuration of gold is $[\text{Xe}]4f^{14}5d^{10}6s^1$, thus the 4f- and the 5d-orbitals are completely occupied and the only half filled orbital is the 6s-orbital. Due to this electron configuration merely one electron contributes to the metallic properties. The electronic band structure (see fig. 3.15) exhibits a local bandgap between the sp-hybridized conduction band and the first virtual one in [111]-direction ($\Gamma \rightarrow L$). The band structure along the so-called Λ -line (marked

green in fig. 3.15) is observed during photoemission experiments on the Au(111) surface.

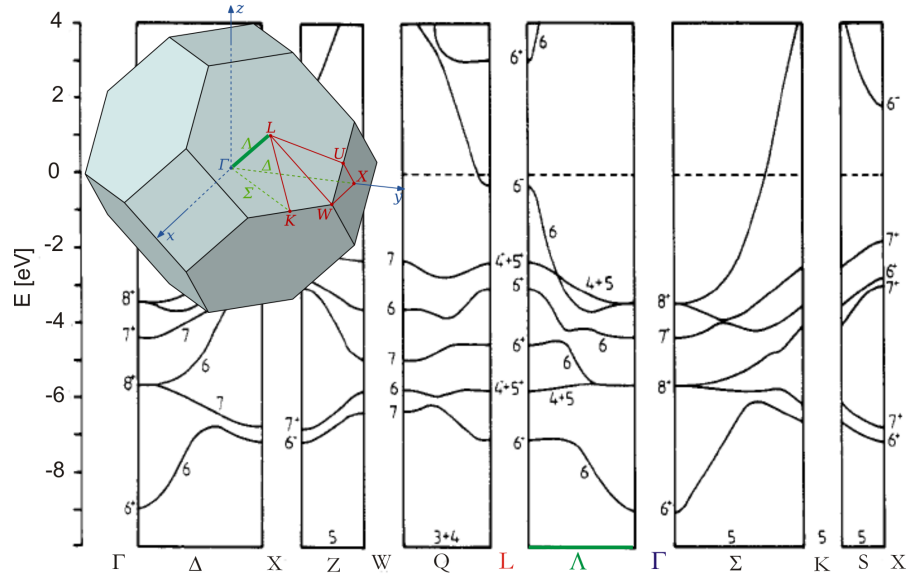


Figure 3.15: Self-consistent relativistic band structure of gold, adopted from Ref. [Eck84], and the Brillouin zone of the fcc-lattice. The Λ -line, along which the sp- and d-bands (6^- , 4^-+5^+ and 6^+) are observed during the photoemission experiments is marked green.

According to DFT calculations, performed by Eckardt et al. in 1984 using Kohn-Sham-type relativistic one-particle equations and the local exchange-correlation potential X_α , the bandgap amounts 3.38 eV (from -0.37 to 3.01 eV) at the L-point and 19.26 eV (from -3.38 to 15.88) at the Γ -point. The values of the L-gap were considered to be too small by 1.2 eV [Eck84], which is not an unusual result since DFT calculations tend to underestimate bandgaps. Within these bandgaps Shockley surface states arise as described before in Section 2.1.1. The surface state in the L-gap of the pristine Au(111) surface lies 0.48-0.49 eV below the Fermi level [Rei01, Nic01], while the surface state of the adsorbate covered Au(111) surface is shifted towards the Fermi level as reported by [For07, Hag10, Var12b]. The d-bands of the Au(111) surface are found at binding energies between -2 and -3 eV relative to the Fermi level [Eck84, Cou86]. The image potential state of the Au(111) surface is located ≈ 0.6 eV below the vacuum level to which it is pinned, i.e. shifts with the work function upon changes of the surface potential [Woo86].

3.5 P3HT: Electronic Structure, Excited State Dynamics and the Influence of Crystallinity

Organic semiconducting materials promise light weight, low cost and flexible devices. Compared to their inorganic counterparts organic semiconductors can be produced and processed energy-efficiently. Semiconducting conjugated polymers gained particular attention compared to small molecular materials due to their solvent processability [Wu10]. Poly(3-hexylthiophene) (P3HT) is a widely investigated semiconducting polymer, which is very attractive for optoelectronic applications due to its high charge carrier mobility. It consists of a polythiophene backbone in which each thiophene unit is hexyl-substituted, either in the regioregular (RR) fashion, *i.e.* always at the same position in the thiophene ring (Figure 3.16 (a)), or of the regiorandom (RRa) type, *i.e.* randomly substituted (Figure 3.16 (b)).

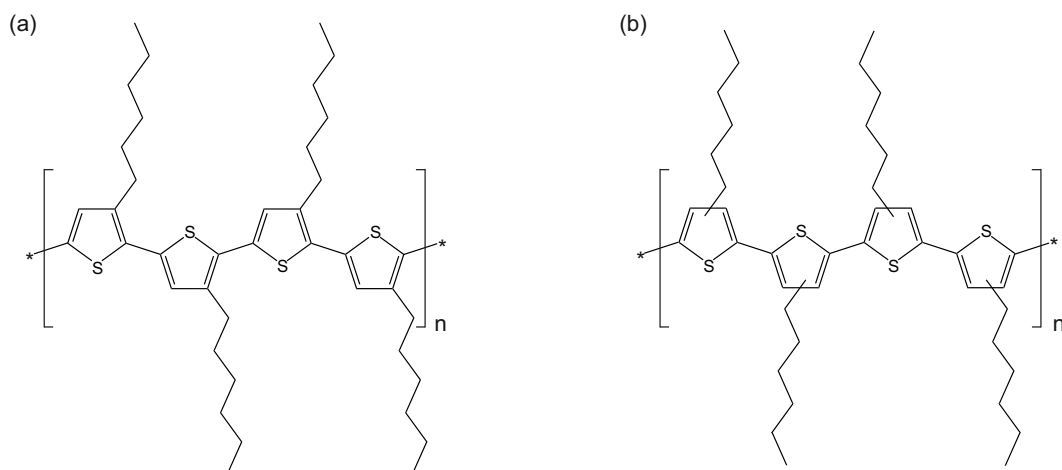


Figure 3.16: Lewis formula of (a) RR-P3HT and (b) RRa-P3HT. In the case of RR-P3HT the hexylchain is located always at the same position in the thiophene ring while it is randomly distributed in RRa-P3HT.

The regioregularity has a strong impact on the packing of the poly(3-hexylthiophene) (P3HT) polymer chains [Mau10]. RR-P3HT forms semicrystalline films consisting of disordered and ordered phases in which the P3HT chains interact strongly and form lamellar crystals, while RRa-P3HT forms disordered amorphous films [Guo09]. The film morphology highly influences the electronic structure, excitation and charge transport properties. For instance Korovyanko *et al.* observed a redshift in the absorption spectra of RR-P3HT compared to RRa-P3HT which they attributed to the superior order in the lamellae [Kor01]. Moreover in RR-P3HT charge transport is much faster and electron and hole transport are nearly balanced compared to RRa-P3HT, since the presence of crystalline regions controls the charge transport

[Mau10, Sch12a]. Besides the regioregularity the formation of crystalline phases in P3HT highly depends on the molecular weight, solvent and synthetic method [Sch12a].

The RR-P3HT investigated in this work has a polymer weight of 10 kg/mol (weight average determined by size exclusion chromatographie) and was synthesized in the group of M. Thelakkat (University Bayreuth) *via* the Grignard metathesis polymerization and is thus of high chemical purity [Wu10, She04]. The preparation of the 50 nm thick RR-P3HT films was carried out by G. Gupta in the group of T. Thurn-Albrecht (University Halle-Wittenberg). Both films were spin-coated on Si-wafers from chloroform solution, subsequently one of the films was heated in nitrogen atmosphere to 230 °C, above the expected melting temperature (≈ 220 °C) and is therefore referred to as melt-crystallized (mc). The non-annealed sample is denoted as-spun (as) and is expected to exhibit a lower degree of crystallinity.

Wu *et al.* investigated the influence of temperature and molecular weight on the equilibrium structures in RR-P3HT of three different molecular weights, 6 kg/mol, 10 kg/mol (the same used in this work) and 22 kg/mol [Wu10]. They observed that

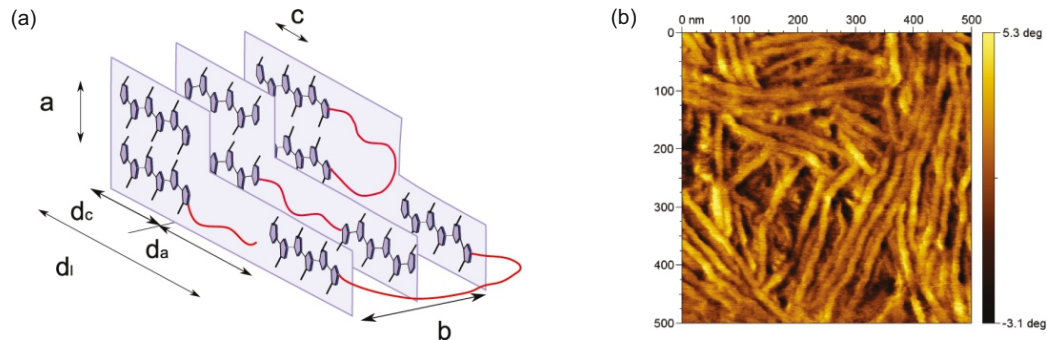


Figure 3.17: (a) Schematic of the microstructure of RR-P3HT: d_c is the thickness of the lamellar crystals and d_a the thickness of the amorphous layer, a , b and c correspond to the crystal lattice parameters. (The scheme is not to scale, the long period d_l is about one order of magnitude larger than the lattice parameters.) (b) AFM image of a P3HT-mc film showing the typical lamellar crystals. Both images are adopted from Ref. [Wu10].

all three polymers form semicrystalline films and that the degree of crystallinity increases with molecular weight. Figure 3.17 (a) shows schematically the typical microstructure of P3HT. The polythiophene backbones form lamellar crystals and interact *via* π -stacking thus leading to delocalization of electronic states across different chains. The ordered crystalline phases are separated by disordered amorphous phases as illustrated by the red lines, the parameters d_c and d_a denote the thickness of the crystalline and the amorphous layers. The parameters a , b and c correspond to the lattice parameters of the orthorhombic unit cell (only measured for the 6 kg/mol P3HT). The scheme shown in Figure 3.17 (a) is not to scale as the long period, $d_l =$

$d_c + d_a$, is about one order of magnitude larger than the lattice parameters. Figure 3.17 (b) shows an AFM image of a P3HT film prepared under the same conditions like the mc-film investigated in this work. Due to heating above the melting temperature and subsequent slow cooling the a -direction is oriented perpendicular to the surface. The image shows the b - c plane, exhibiting the characteristic pattern of the lamellar crystals.

Concerning the optical properties of RR-P3HT thin films, the optical gap amounts to 1.8 - 1.9 eV as reported in several studies employing absorption spectroscopy [Kor01, Sch14, Coo08]. Panzer *et al.* [Pan15] investigated the effect of annealing on thin films prepared from the 22 kg/mol RR-P3HT (studied before by Wu *et al.* [Wu10]). They found two different types of H-aggregates, one with ordered and one with disordered side chains, after heating the film to 250° and cooling down slowly to room temperature. Before annealing however only one type of aggregate was found. In addition they found that the aggregates in the annealed film could be excited separately depending on the photon energy. For photon energies higher than 2 eV only the aggregate which prevails as well in the non-annealed film is excited. Therefore only the aggregate with the ordered side chains should be excited in the measurements presented in this work, since only photon energies > 2 eV have been used, as will be shown in Section 5.4.

The effect of annealing on the electronic structure of RR-P3HT thin films has been investigated as well by means of UPS which is of particular interest for this work as UPS yields IP comparable to those obtained from 2PPE. For instance Kanai *et al.* [Kan10] performed a combined UPS/IPES study on a 17 nm thick RR-P3HT film ($M_w = 25$ -30 kg/mol) on Si. They found that the transport gap decreases upon annealing from 2.6 to 2.4 eV, due to a downward shift of the EA level by 0.2 eV while the IP of 4.7 eV stays constant. Moreover they observed that the peak width are reduced upon annealing at 170 °C. Another UPS study was performed by Frisch *et al.* [Fri11] on a 20 nm thick RR-P3HT ($M_w = 64$ kg/mol) film on poly(ethylenedioxythiophene):poly(styrenesulfonate) (PEDT:PSS). They observed a very small VBM shift of 0.05 eV from 4.55 eV to 4.6 eV upon annealing at 120 °C. The results obtained in this thesis will be compared with the results from Kanai *et al.* since they employed rather light weight P3HT and Si as a substrate. Comparison with the results from Frisch *et al.* have to be handled with caution due to the conducting substrate which potentially influences the film morphology and the electronic structure.

In the following paragraphs information on excited states and their dynamics will be presented as those are of great importance when it comes to the interpretation of the data obtained in this work, as will be discussed in Section 5.4. Several

excited states have been reported to exist in RR-P3HT, e.g. singlet excitons, polaron pairs and polarons (the different species have been introduced before in Section 2.2.2) [Guo09, Kor01, Zha12a, Kan92]. Previous studies yielded controversial results concerning the number and the kind of excited states in RR-P3HT as well as their dynamics. (Triplet formation however, has been consistently reported to occur only in RRa-P3HT [Guo09, Kor01]. Korovyanko *et al.* proposed that the suppression of intersystem crossing in RR-P3HT might be a consequence of enhanced interchain interaction in the crystalline phases [Kor01].) The energetic position and the dynamics of the excited states are influenced by a variety of parameters, such as the molecular weight, the film preparation and morphology, as well as the excitation energy and density used in the measurements. The comparability of the results is therefore questionable, but besides the inconsistencies there are as well a few common tendencies in the reported findings:

1. A significant number of publications find the singlet exciton at a resonance energy between 1.0 and 1.2 eV [Guo09, Kor01, Coo08, Her11, Mül12, Zha12a].
2. A polaron signal around 1.9 eV has been observed in many studies [Kor01, Zha12a, Her11, Mül12] and has been related to delocalized polarons residing in the crystalline phases of the RR-P3HT film [Kor01, Zha12a]. Whereas Guo *et al.* related this resonance to polaron pairs [Guo09].
3. Another polaronic feature, energetically located between the exciton (1-1.2 eV) and the polaron (around 1.9 eV) mentioned before, was observed at resonances between 1.13 and 1.65 eV [Guo09, Kor01, Zha12a, Kan92]. Korovyanko *et al.* and Zhang *et al.* assigned this polaronic resonance to localized polarons inhabiting the disordered phases.

Additional polaronic states have been reported at resonances of 0.1 and 0.4 eV [Kor01] and at 0.5 eV [Kan92] using optical spectroscopy, while X-ray absorption yields a feature related to a polarons 0.8 eV above the VBM [Mül12].

RR-P3HT thin films have been studied as well before by means of 2PPE [Var12c, Soh07]. Varène *et al.* [Var12c] employed PEDT:PSS as a substrate while Sohn *et al.* [Soh07] used a Au-substrate. Both studies report a polaronic state located 0.9 eV [Var12c] and 1.75 eV [Soh07] above the VBM respectively.

As mentioned before a great variety of studies on the excited state dynamics can be found. But unfortunately the reported results are highly contradictory. Only the photoluminescence lifetime was congruently found to take place between 300 - 400 ps and related to the exciton decay *via* electron-hole recombination [Mag97, Kan92, Coo08, Guo09]. Guo *et al.* observed a triexponential exciton decay and assigned the slowest time constant (330 ps) to the recombinative decay.

The formation and decay dynamics of polaron pairs and polarons have been reported to take place on various different time scales. The ability of P3HT to form polarons by itself without the need for a donor-acceptor interface is well known. However there has been a discussion in the past whether polarons are formed immediately after photon absorption or whether they are formed from relaxed singlet excitons [Sak09, Ai06, Mag97, Kor01, Guo09]. But there is convincing evidence that polarons and polaron pairs are formed on an ultrafast timescale from an initial hot exciton population. Guo *et al.* for example observed in a transient absorption study that polarons and polaron pairs are generated in a competitive process directly from hot excitons in RR-P3HT [Guo09].

The decay of polaron pairs was reported to take place on time scales ranging between 0.55 ps [Ai06] and 2.6 ps [Var12c]. The suggested decay mechanisms are geminate recombination to the singlet exciton or the ground state or dissociation into polarons [Guo09, Var12c]. Polaron lifetimes have been reported in a range reaching from several ps [Ai06, Var12c] over several hundred ps [Coo08, Her11] even to μ s [Mül12, Kan92]. The prevailing decay mechanism for polarons is the bimolecular with other polarons [Guo09].

The influence of enhanced order in the polymer films on the excited state dynamics has been studied by Korovyanko *et al.*, who observed slower decay dynamics in RRa-P3HT compared to RR-P3HT [Kor01]. Moreover Laquai *et al.* reported that the PCE of a P3HT:phenyl-C61-butyric acid methyl ester (PCBM) based solar cell was increased by a factor of ten upon annealing the device at 110 °C. This was explained by an enhancement of the hole transport efficiency in the P3HT phase by more than three orders of magnitude [Laq15].

In this thesis the influence of annealing on the electronic structure and the excited state dynamics in RR-P3HT is investigated. 2PPE is a very powerful method to investigate the electronic structure of a material since it provides access not only to occupied but as well to unoccupied states. In addition it allows to measure the lifetimes of excited states. But photoemission is usually not the method of choice to investigate polymers since it is a very surface sensitive technique and polymers, even when they are highly regular and chemically pure, form only semicrystalline films which contain significant fractions of disordered phases. Moreover polymers are usually processed wet chemically which is a problematic precondition for investigations carried out under UHV conditions due to the possible contamination by residual solvent. Therefore RR-P3HT films which were prepared under well defined conditions from polymers of very high regularity and chemical purity were chosen for this 2PPE study.

These films are investigated to find out whether it is possible at all to obtain high

quality 2PPE spectra exhibiting distinct features, since previous 2PPE studies on RR-P3HT films did not yield well resolved spectra [Var12c, Soh07]. Further questions which will be tackled in this work are the influence of enhanced crystallinity, *i.e.* interchain interaction, on the electronic structure and the excited state dynamics in two RR-P3HT films with different degrees of crystallinity. The results will be presented and discussed in Section 5.4.

4 Methods and Experimental Details

This chapter consists of an introduction into two-photon photoemission (2PPE), and the experimental setups used in this work. 2PPE is a very powerful technique to investigate and understand the energy level alignment at interfaces between inorganic substrates and organic adsorbates as well as within molecular or polymer films. In addition time-resolved two-photon photoemission (TR-2PPE) allows to monitor the non-equilibrium dynamics in real time.

This work was carried out in two different research groups, *viz.* Prof. P. Tegeder at Fachbereich Physik, Freie Universität Berlin (FU) Berlin and Dr. J. Stähler at the department of Physical Chemistry, Fritz Haber Institute (FHI) of the Max Planck Society, Berlin. Since the experimental setups are similar the setup at the FHI will be described and the differences with the FU setup will be pointed out. The preparation of the clean single crystal surfaces and the molecular films will be described. Furthermore the quantification of the molecular coverage at each of the setups will be explained.

4.1 Photoelectron Spectroscopy

Photoelectron (or photoemission) spectroscopy (PES) is a well established and widely applied method in surface science which provides a possibility to investigate the electronic structure of atoms, molecules and solid surfaces [Rei07]. The fundamental process of PES is the photoelectric effect which was observed first by Hertz and Hallwachs in 1887 [Her87, Hal87] and formulated by Einstein in 1905 in terms of quantum nature of the photons [Ein05]. Photons with an energy higher than the work function (Φ) of the material emit electrons with the kinetic energy E_{kin}

$$E_{\text{kin}} = h\nu - \Phi + E_{\text{b}}, \quad (4.19)$$

where h is Planck's constant, ν the frequency of light and E_{b} is the binding energy of the occupied electronic state in the sample with respect to E_{F} , as illustrated in Figure 4.1 (a). In fact E_{b} corresponds to the energetic difference between the initial N -electron system and the $(N-1)$ -electron system after photoemission. It is assumed also that the energetic levels are not affected by the ionization. The ionization energy, or IP, can now be approximated to the negative orbital energy which is known as Koopmans' theorem [Koo34]. The work function corresponds to the minimum amount of energy that is needed to excite an electron from the Fermi level into the vacuum: $\Phi = E_{\text{vac}} - E_{\text{F}}$. Accessibility of the particular electronic state is dependent on the photon energy. For instance UPS and X-ray photoelectron spectroscopy

(XPS) enable access to valence and core-regions respectively.

In addition PES provides a possibility to measure the dispersion of electronic states, *i.e.* the energy-momentum relation of the emitted electron, where the parallel component of the wave vector (k_{\parallel}) is conserved during the photoemission process. This special case is known as angle-resolved PES (ARPES) and either demands the use of an angle-resolved analyser (like the Phoibos 100 as described in section 4.2.4) or can be carried by rotating the surface in front of the analyser which changes the emission angle. Figure 4.1 (b) schematically depicts the electron emission process in two dimensions. The parallel component of the wave vector, which is proportional to the electron's momentum is conserved $k_{\parallel} = k'_{\parallel}$, while the perpendicular component k_{\perp} is changed by the work function when passing the surface $k'_{\perp} \neq k_{\perp}$. Therefore

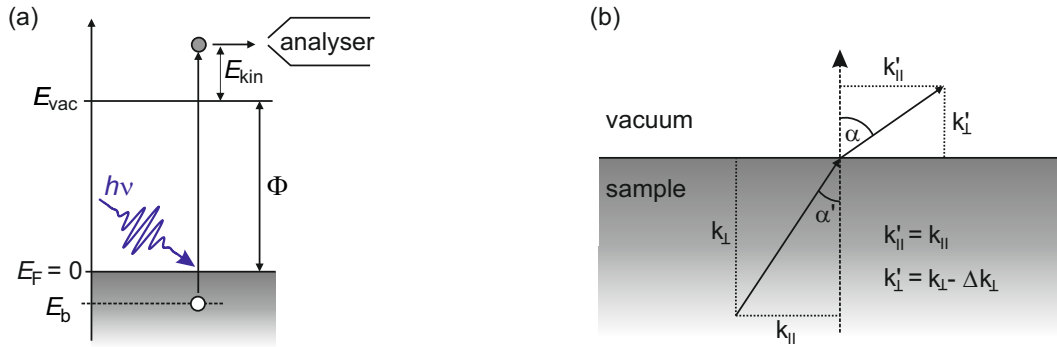


Figure 4.1: (a) Sketch of a photoemission experiment, (b) illustration of the electron emission process: The wave vector component parallel to the surface k^{\parallel} is conserved while and the perpendicular component k^{\perp} changes.

k_{\parallel} can be obtained from E_{kin} and the emission angle α of the photoelectrons with respect to the surface normal [Hen94]

$$k_{\parallel} = \frac{\sqrt{2m_e E_{\text{kin}}}}{\hbar} \sin\alpha \quad (4.20)$$

where m_e is the electron rest mass (not the effective mass of the electron in the solid). The functional relation between the binding energy E_b of a state and the effective mass of electron can be expressed as the following

$$E_b = E_0 + \frac{(\hbar k_{\parallel})^2}{2m^*} \quad (4.21)$$

where m^* is the effective mass of an electron as determined by the strength of the coupling to its surroundings, E_0 is the energy of the photoemitted electrons when the sample surface is oriented perpendicular to the analyser. In practice, a small

bias is applied between the sample and the analyser tip so that the photoelectrons would reach the spectrometer efficiently, essentially the bias lowers the Fermi level of the spectrometer as will be discussed in Section 4.2.4.

4.1.1 Two-Photon Photoemission

PES is a powerful tool for the investigation of the electronic structure of a variety of materials, however yields information about the occupied electronic states only. To study the unoccupied electronic states above the Fermi level inverse photoemission spectroscopy (IPES) is a possibility, in which electrons impact on the surface and populate the unoccupied states. This process emits photons of energy that correspond to the difference between the initial electron energy and the energetic position of the unoccupied state [Bur85]. 2PPE provides a possibility to observe both occupied and unoccupied states. Moreover with TR-2PPE electron dynamics on ultrafast, *i.e.* as - fs, timescale can be investigated, as will be discussed in Section 4.5 [Mii00]. In a 2PPE experiment two, in our case femtosecond, laser pulses with a controllable delay with respect to each other are used to pump and subsequently probe certain electronic states. The first photon excites an electron from an occupied electronic state below E_F to an unoccupied intermediate state which is then emitted into the vacuum by the second photon. The kinetic energy of the photoemitted electrons provides information about the energetic position of the probed state. Since 2PPE is based on a second order non-linear optical process it has four times lower cross section than direct photoemission, thus yielding much lower emission intensities [Fau94]. Therefore the photon energies of pump and probe pulse should be smaller than the work function of the sample to avoid direct photoemission.

In order to assign the features obtained in a 2PPE spectrum to occupied and unoccupied states it is necessary to understand the excitation processes. The dependence of the kinetic energy of the photoemitted electrons on the photon energies in a 2PPE process is illustrated in Figure 4.2 (a) - (c) for one-colour 2PPE (1C-2PPE) and in (d) for two-colour 2PPE (2C-2PPE):

(a) Initial state (E_i)

In the case of photoemission from an occupied initial state (E_i) *via* a virtual intermediate state, the kinetic energy (E_{kin}) of the photoelectron depends on both pump and probe photon energies. Therefore increasing the photon energy by an amount of $\Delta h\nu$ leads to an increase in E_{kin} by $2\Delta h\nu$.

(b) Intermediate state (E_k)

E_{kin} of a photoelectron from a real intermediate state scales with the probe photon energy. In this case, varying the photon energy by $\Delta h\nu$ changes the

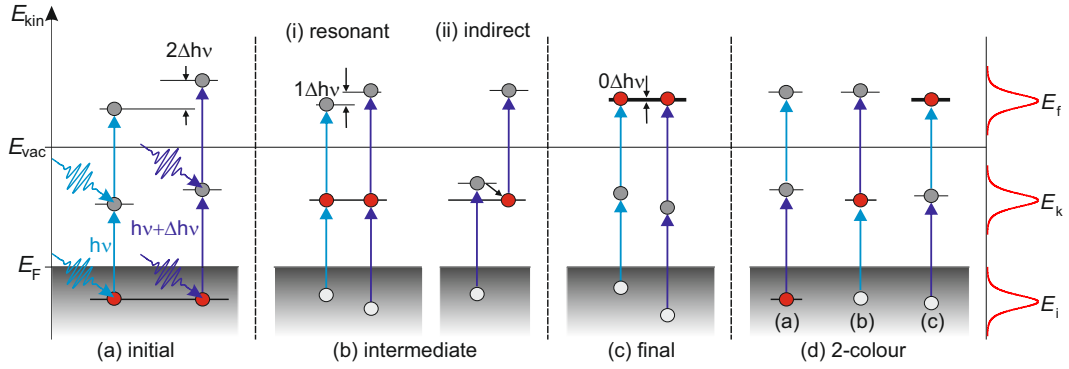


Figure 4.2: 1C-2PPE pump-probe schemes in case of (a) occupied, (b) unoccupied and (c) final states; (d) corresponding 2C-2PPE schemes.

kinetic energy of the emitted electron by $1\Delta h\nu$. The excitation from an occupied initial to an unoccupied intermediate state can occur either resonantly, *i.e.* $h\nu_{\text{pump}} = |E_i - E_k|$ or indirectly as shown in Figure 4.2 (b) (i) and (ii) respectively. In the case of indirect excitation a real intermediate state is populated *via* secondary scattering processes such as electron-electron or electron-phonon scattering.

(c) Final state (E_f)

If unoccupied states above the vacuum level are populated *via* excitation of electrons below the Fermi level a transient negative ion resonance is formed. The kinetic energy of the photoelectron from such a final state is independent of both photon energies, as illustrated in Figure 4.2 (c), since the electron is released *via* an autodetachment process due to the limited lifetime of the final state.

(d) Two-colour 2PPE

The examples above were given only for 1C-2PPE processes for simplicity. Figure 4.2 (d) shows the different 2PPE processes (a) - (c) for the case of 2C-2PPE. A peak in a 2C-2PPE spectrum may even result from two different intermediate states depending on which of the photons acts as the pump or the probe. As recorded a 2C-2PPE spectrum inherently contains 1C-2PPE components. Therefore the 1C-2PPE spectrum has to be subtracted from the 2C-2PPE spectrum to generate a pure signal from the latter.

The energy scale of a 2PPE spectrum is limited by two cutoffs, where the low- and high-energy cutoffs are called secondary and Fermi edge respectively. Figure 4.3 illustrates the origin of the two cutoffs: The secondary edge results from electrons whose kinetic energy is just sufficient to overcome the work function, *i.e.* the lowest

possible kinetic energy while the Fermi edge arises due to photoemission *via* virtual intermediate states of electrons near E_F and possess thus the highest possible kinetic energy. The work function of the sample corresponds to the difference between the

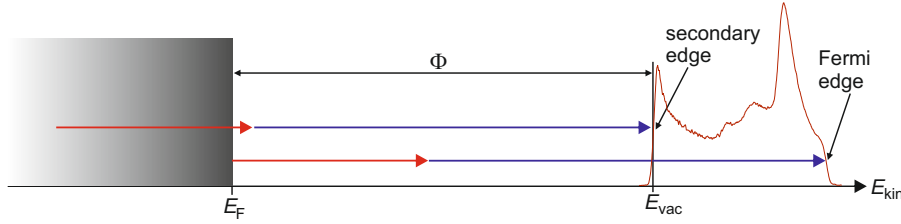


Figure 4.3: Schematic depiction of the origin of the low- and high-energy cutoffs in a 2PPE spectrum.

sum of the photon energies and the width of the spectrum.

$$\Phi_{\text{sample}} = (h\nu_1 + h\nu_2) - (E_{\text{kin}}^{\text{F}} - E_{\text{kin}}^{\text{S}}) \quad (4.22)$$

$E_{\text{kin}}^{\text{F}}$ and $E_{\text{kin}}^{\text{S}}$ are the energetic positions of the Fermi and the secondary edge respectively. Semiconducting materials, like ZnO and P3HT do not possess any density of states at the Fermi level. Hence the Fermi edge is measured on a metallic reference under the same conditions (bias voltage and distance from the analyser, an example is shown in section 5.4).

2PPE spectra can be displayed as a function of different energy scales depending on the origin of the observed states. This allows the parameters required to be accessible directly from the axis. Figure 4.4 illustrates the difference between the possible axes:

(a) Kinetic energy axis (E_{kin})

On the kinetic energy axis the secondary edge is set to 0 while the Fermi edge corresponds to the width of the spectrum which can be read directly from the energy axis. The peak positions in the spectrum correspond to the kinetic energy of the photoemitted electrons with respect to the vacuum level.

(b) Final state axis ($E_{\text{Fin}} - E_{\text{F}}$)

On the final state energy axis the work function can be read directly at the secondary edge while the Fermi edge corresponds to the sum of the photon energies ($h\nu_1 + h\nu_2$). The energetic positions of the peaks correspond to their final state energy relative to the Fermi level. If the peak is due to photoemission from an occupied state, the binding energy is obtained by subtracting both photon energies from the peak position. In case of an intermediate state, its energetic position is obtained by subtracting the probe photon energy from the final state energy of the peak.

The final state energy axis is useful when the origins of the peaks are still unclear or when a spectrum contains peaks originating from occupied and unoccupied states.

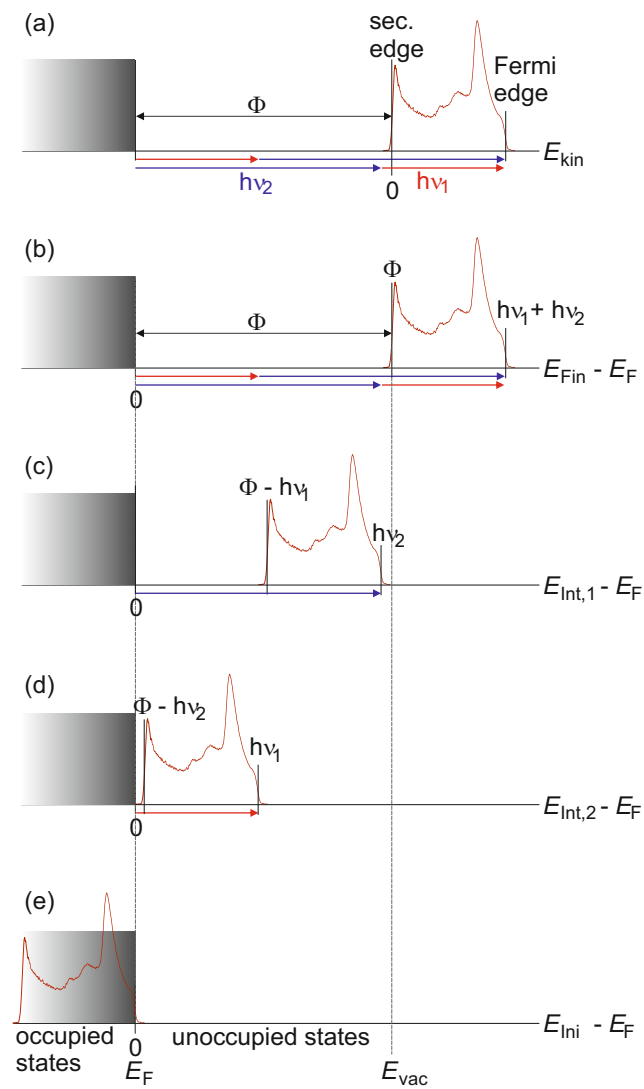


Figure 4.4: Illustration of the different possible energy axes in 2PPE spectra, see text for details.

The Fermi edge is shifted to zero here and the peak positions correspond directly to the binding energies with respect to the Fermi level.

(c) Intermediate state axis ($E_{Int,1} - E_F$)

In 2C-2PPE two different intermediate state axes are possible depending on which of the laser beams acts as the probe pulse. Here the whole spectrum is shifted by $h\nu_1$ compared to the final state axis since $h\nu_1$ and $h\nu_2$ correspond to the probe and the pump pulse respectively. This axis is convenient to read directly the intermediate state energy.

(d) Intermediate state axis ($E_{Int,2} - E_F$)

Here the other intermediate state axis is displayed, which shows the intermediate state energy of an unoccupied state relative to the Fermi level which is probed by $h\nu_2$.

(e) Initial state axis ($E_{Ini} - E_F$)

The initial state axis is useful only when occupied initial states are observed, e.g. in a direct photoemission spectrum.

The Fermi edge is shifted to

4.1.2 Time-Resolved Two-Photon Photoemission

Time-resolved two-photon photoemission provides the possibility to measure the lifetimes of transiently populated intermediate states on time scales as low as tens of fs to hundreds of ps. This is realized by delaying the pump and probe pulses with respect to each other by changing the optical path length of one of the beams. Essentially one of the beams is steered on an electronically controlled delay stage. This provides the possibility to choose the pump beam to arrive first at the sample surface and the probe beam as second. Figure 4.5 (a) shows the three possible scenarios of a TR-2PPE measurement using photon energies in the visible and the UV range. For negative delays the UV pulse impinges on the sample first (pump pulse) while the visible pulse arrives later (probe pulse). At time zero, *i.e.* $\Delta t = 0$ s, both pulses impinge on the sample at the same time and thus can adopt both roles. For positive delays the photoemission signal is due to the vis pulse populating an intermediate state probed by the UV pulse.

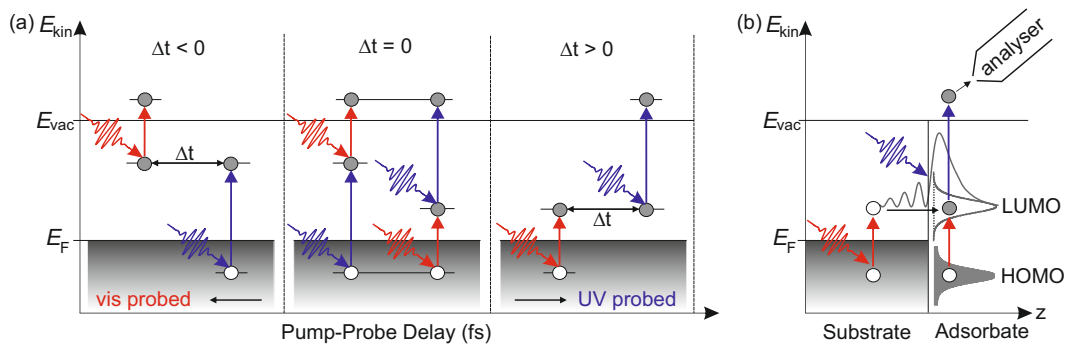


Figure 4.5: (a) Possible pump-probe schemes during a TR-2PPE experiment, (b) population of an unoccupied state *via* an electron from the metal or intramolecularly

Figure 4.5 (b) schematically depicts possible population mechanisms of an unoccupied state of an adsorbate which can occur either from the substrate or an intermolecular transition. In the first case an electron from an occupied state of the substrate is excited into the unoccupied adsorbate state, when probed, this state yields the electron affinity level, *i.e.* the actual LUMO state. Intramolecular excitation from an occupied state within the molecule, e.g. the HOMO, leaves a hole in the initially occupied state forming an exciton. In this case the measured lifetime corresponds to the exciton lifetime and not to that of the LUMO. These two mechanisms can be distinguished by increasing the thickness of the adsorbate film, as electron transition from the substrate is limited by its diffusion length. Furthermore for high adsorbate coverages the electrons which populate intermediate states of adsorbates cannot be probed due to the limited escape depth of the electrons.

In a time-resolved experiment 2PPE spectra are recorded at varying time delays. Plotting these spectra as a function of the intermediate state energy and the pump-probe delay yields a TR-2PPE spectrum as displayed in Figure 4.6. The 2PPE intensity is presented by a false colour-code. This spectrum was measured on H-doped ZnO(000 $\bar{1}$) depicting a long-lived emission signal for positive delays, *i.e.* $h\nu_1 = 3.80$ eV is the pump and $h\nu_2 = 4.65$ eV the probe pulse. For negative delays the pump-probe sequence is *vice versa* as illustrated in Figure 4.6 (top). As mentioned earlier the 1C-2PPE signal needs to be subtracted from the 2C-2PPE signal at each delay point to obtain the pump-induced signal only. There are two possibilities for the background spectra: (i) The background spectrum is taken at negative pump-probe delays, $\Delta t = -30$ ps, where no long-lived emission signal is observed (this procedure was carried out on the data from FHI and was used in the case of the example shown in Figure 4.6). (ii) The other possibility is to subtract the 1C-2PPE spectra from the raw 2C-2PPE signal (this procedure was applied on the data collected at the FU).

Vertical cut of the TR-2PPE spectrum yields spectrally resolved 2PPE signal at certain time delays, as shown on the right side for pump-probe delays of 0 fs and 100 fs. In order to gain deeper insights into the excited state dynamics the TR-2PPE spectrum is integrated over the energetic ranges marked by the grey boxes yielding the cross-correlation (XC)-traces (Figure 4.6 bottom). The black lines correspond to biexponential fits whose derivation is explained below. The red curve represents the XC of the laser pulses which was fitted with a sech^2 envelope.

The population decay can be described analytically with optical Bloch equations which consider as well coherence effects. But in case of non-resonant excitation or dephasing times shorter than the pulse duration coherence effects can be neglected and the optical Bloch equations can be simplified to a set of coupled rate equations [Lou83, Kir08]. In the simplest case the population decay can be treated as a discrete 3-level system consisting of initial, intermediate and final state populations as illustrated in Figure 4.7 (a).

$$\dot{n}_i = -|V_{ik}(t, \tau)|^2 n_i + \Gamma_1 n_k \quad (4.23)$$

$$\dot{n}_k = |V_{ik}(t, \tau)|^2 n_i - |V_{kf}(t, \tau)|^2 n_k - \Gamma_1 n_k \quad (4.24)$$

$$\dot{n}_f = -|V_{kf}(t, \tau)|^2 n_k \quad (4.25)$$

n_x are the population densities of the initial ($x = i$), intermediate ($x = k$) and final state ($x = f$). $|V_{xy}|^2$ is the probability of a transition from $x \rightarrow y$ in the presence of the optical field and τ is the pump-probe delay. Γ_1 is the inelastic scattering rate from the intermediate to the ground state ($k \rightarrow i$) and describes an exponential

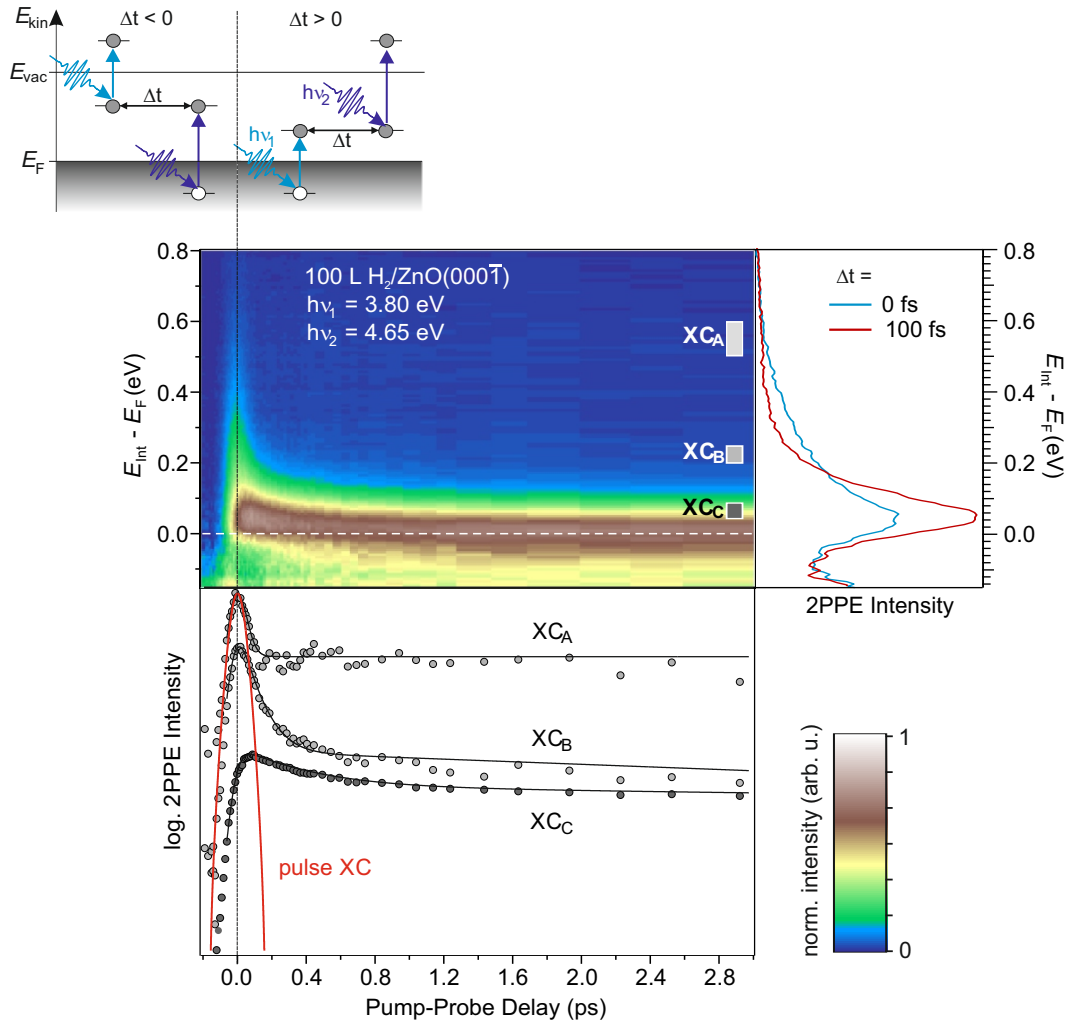


Figure 4.6: Center: Two-dimensional representation of the 2PPE yield of H-doped ZnO(000 $\bar{1}$) as function of intermediate state energy and pump-probe delay recorded with $h\nu_1 = 3.80$ eV and $h\nu_2 = 4.65$ eV. For positive delays $h\nu_1$ is the pump pulse while $h\nu_2$ acts as the probe pulse. The pulse sequence for positive ($\Delta t > 0$) and negative delays ($\Delta t < 0$) is shown in the sketch at the top of the figure. Right: Vertical cuts through the 2D-plot yield the spectrally resolved photoemission intensity, for pump-probe delays of 0 fs and 100 fs. Bottom: Cross correlation (XC) traces obtained from integrating the TR-spectrum over several energetic ranges, which are marked by grey boxes in the 2D-plot. The black lines correspond to fit functions consisting of a biexponential decay convolved with the XC of the laser pulses. The red curve shows the XC of the laser pulses fitted with a sech^2 pulse envelope.

decay of the intermediate state population after the optical excitation is extinguished ($V_{xy}=0$).

If the excitation densities are small enough then the population density of the initial state can be considered as constant and $|V_{kf}(t, \tau)|^2 n_k$ can be neglected. The 2PPE response function for the intermediate state is yielded by integration

$$I_k^{2PPE}(\tau) \propto \int \int dt' dt'' I_1(t') R_k(t'' - t') I_2(t'' - \tau) \quad (4.26)$$

where $I_1(t)$ and $I_2(t)$ denote the transient envelopes of the pump and probe pulses, respectively, $R_k(t)$ represents the response function of the intermediate state. The cross correlation function of both laser pulses is given by [Rul98]

$$I_{XC}(t) = \int dt' I_1(t) I_2(t - t') \quad (4.27)$$

With $I_{XC}(t)$ the 2PPE response function in terms of the pump-probe delay becomes

$$I_k^{2PPE}(\tau) \propto \int dt I_{XC}(t - \tau) R_k(t) \quad (4.28)$$

I_{XC} is obtained from two-photon photoemission from occupied states of a metal surface. The 2PPE process occurs in such case *via* a virtual intermediate state with an infinitely small lifetime therefore the response function of the system is a delta function ($R_k(t) = \delta(t)$). Now Equation (4.28) is reduced to the XC function in Equation (4.27). The response function for a 3-level-system with finite lifetime of the intermediate state is given by

$$R_1(t) = \Theta(t) n_1^{(0)} e^{-\Gamma_1 t} \text{ with } \Gamma_1 = \frac{1}{\tau_1} \quad (4.29)$$

describing the exponential decay of the initial population density $n_1^{(0)} = n_1(t = 0)$ of the intermediate state with a lifetime of τ_1 . $\Theta(t)$ is the Heaviside function.

Most of the systems investigated in this thesis exhibit multiexponential population decays which could not be described analytically by rate equations, since it was not possible to disentangle the following situations: (i) transient populations in several intermediate states which decay monoexponentially but are located so close to each other that they cannot be distinguished or (ii) a population in one excited state which decays in a complex way, e.g. *via* relaxation into energetically close states and other decay channels, leading to a multiexponential behaviour. The XC traces shown in Figure 4.6 were fitted with biexponential decays since the population decay can be approximated here with a 4-level system as shown in Figure 4.7 (b).

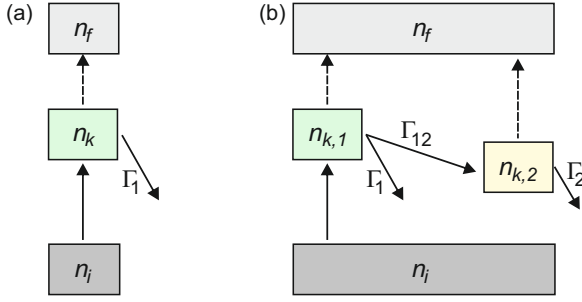


Figure 4.7: Schematic of a 3- and a 4-level system with initial, intermediate and final states. (a) Decay of a 3-level system, after [Kir08]. (b) Decay scheme of a 4-level system: the population $n_{k,1}$ fills the population $n_{k,2}$ with a rate Γ_{12} , while both states are probed and decay with Γ_1 and Γ_2 into the ground state.

The excited electrons in the conduction band are approximated by the intermediate state population ($n_{k,1}$) which relaxes either with Γ_1 into the conduction band minimum or with Γ_{12} into the surface exciton state ($n_{k,2}$). The population of this surface exciton arises due to the relaxation of electrons from the intermediate state $n_{k,1}$ and decays with Γ_2 . While disregarding the optical coupling of the intermediate states by the laser field, the rate equations for

the population densities can be expressed as

$$\dot{n}_1(t) = -(\Gamma_{12} + \Gamma_1)n_1(t) \quad (4.30)$$

$$\dot{n}_2(t) = -\Gamma_2 n_2(t) + \Gamma_{12} n_1(t) \quad (4.31)$$

Summation of these two rate equations yields

$$\dot{n}_1(t) + \dot{n}_2(t) = -\Gamma_1 n_1(t) - \Gamma_2 n_2(t) = -\frac{1}{\tau_1} n_1(t) - \frac{1}{\tau_2} n_2(t) \quad (4.32)$$

From Equations (4.29) and (4.32) the response function of both intermediate states is obtained

$$R_{(1+2)}(t) = \Theta(t) \left[n_1^{(0)} e^{-\Gamma_1 t} + n_2^{(0)} e^{-\Gamma_2 t} \right] \quad (4.33)$$

This biexponential formalism is used here to describe the decay of the hot exciton population in the conduction and their relaxation into the surface excitonic state (for a detailed description of the processes see Section 5.1.2).

4.1.3 2PPE *vs.* Optical Spectroscopy

In Section 5.2.1 results from 2PPE will be compared with the findings from excited state transmission measurements. Therefore it would be appropriate to discuss the differences between these two methods. Optical spectroscopy measures resonances between the electronic states of the system, as sketched in Figure 4.8 (a): After excitation of electrons from S_0 to S_1 the population in the S_1 state is probed by a white light continuum where the colours which are resonant between S_1 and S_2 are absorbed. 2PPE, in contrast, measures the kinetic energy of the emitted electrons

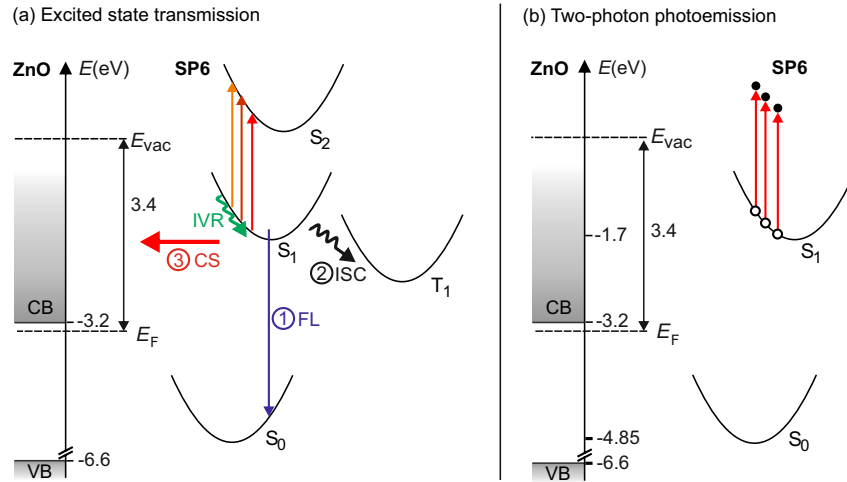


Figure 4.8: Probing of the intermediate state population in (a) excited state transmission and (b) 2PPE.

and allows to determine the energetic position of the intermediate state S_2 with reference to E_F (Figure 4.8 (b)). Both methods yield comparable results when the same pump and probe photon energies are used.

The first excitation process from the ground state (Ψ_i) into the first excited state (Ψ_k) is the same for optical spectroscopy and 2PPE. For this transition the dipole selection rules apply and the transition occurs only when the transition matrix element V_{ik} does not vanish [Hüf95]:

$$V_{ik} = \langle \Psi_i | \mu | \Psi_k \rangle \neq 0 \quad (4.34)$$

here μ is the transition moment operator which depends on the polarization of the laser light. Now the second transition from the intermediate state (Ψ_k) to the final state (Ψ_f) is different for the two methods since the final states diverge ($\Psi_f^{\text{opt}} \neq \Psi_f^{\text{2PPE}}$). In the case of optical spectroscopy the final state is a molecular or crystal resonance and therefore the dipole selection rules apply strictly. In 2PPE however, the final state is an unknown state in the vacuum and is thus not restricted to molecular resonances. Therefore 2PPE provides access to states which would require a forbidden transition in optical spectroscopy. For example if the intermediate state is a triplet state and thus dark for optical spectroscopy, due to the spin forbidden transition between a triplet and a singlet state, it can be probed by 2PPE as the spin can be conserved in the final state.

4.2 Experimental Setup

This chapter provides an overview of the experimental setups and methods which have been employed in this work. As mentioned earlier the 2PPE experiments have been conducted at two different places, but very similar setups. They will be referred to as FHI- and FU-setup in the following and have been described in detail before (FU: [Kir08, Hag09]) (FHI: [Dei11, Weg14]). Both setups consist of mainly two parts, a femtosecond laser system and an UHV chamber and the details of which will be given in the following sections.

4.2.1 The Femtosecond Laser System

The laser system provides the required ultrashort laser pulses tunable over a broad range of wavelengths. The whole laser system is installed on two optical tables placed inside a tent consisting of a base frame which is fixed to the ceiling and plastic curtains reach the floor from the frame. The temperature and humidity of the whole laboratory are controlled by an air conditioning system. Furthermore, there is a flow box in the laser-tent producing a little overpressure such that only a minimal amount of dust is able to enter the tent and to deposit on the optics. The FHI laser system (Figure 4.9) consists of commercially available components from Coherent, such as a pump laser (*Verdi V-18*), a broadband femtosecond oscillator (*Micra*), a regenerative amplifier (*RegA 9050*), a broadband grating stretcher/compressor and an optical parametrical amplifier (OPA) (*vis-OPA 9450*). The FU-setup consisted of the same components but the oscillator was seed based (*MIRA 900B*). (In the meantime at the FHI the *Verdi V-18* pump laser and the *Micra* oscillator have been substituted by a *Vitara* including a *Verdi G* pump laser and an additional *Verdi G* pumping the *RegA 9050*.) *Verdi V-18* is a diode pumped continuous wave laser with a maximum power of 18 W at 532 nm pumping both the oscillator and the amplifier. The *Micra* oscillator contains a Ti:sapphire (titanium doped corundum, $\text{Ti}^{3+} : \text{Al}_2\text{O}_3$) crystal as an active laser medium and provides ultrashort laser pulses at a repetition rate of 80 MHz with a pulse energy of about 6.3 nJ. Before the pulses are amplified in the *RegA* they are stretched up to 50-100 ps in order to reduce their high peak powers protecting the optics in the amplifier from damage. In the *RegA* the stretched pulses are amplified at a repetition rate of 40 - 300 kHz (usually runs at 200 kHz) and subsequently guided back into the stretcher/compressor unit where they are compressed to 40 fs. The setup at FHI typically delivers pulse energies of 5 - 6.7 μJ at a center wavelength of 800 nm (1.55 eV).

The potential of 2PPE relies on the usage of different photon energies. Hence the setup is equipped with a possibility to generate a broad range of photon energies.

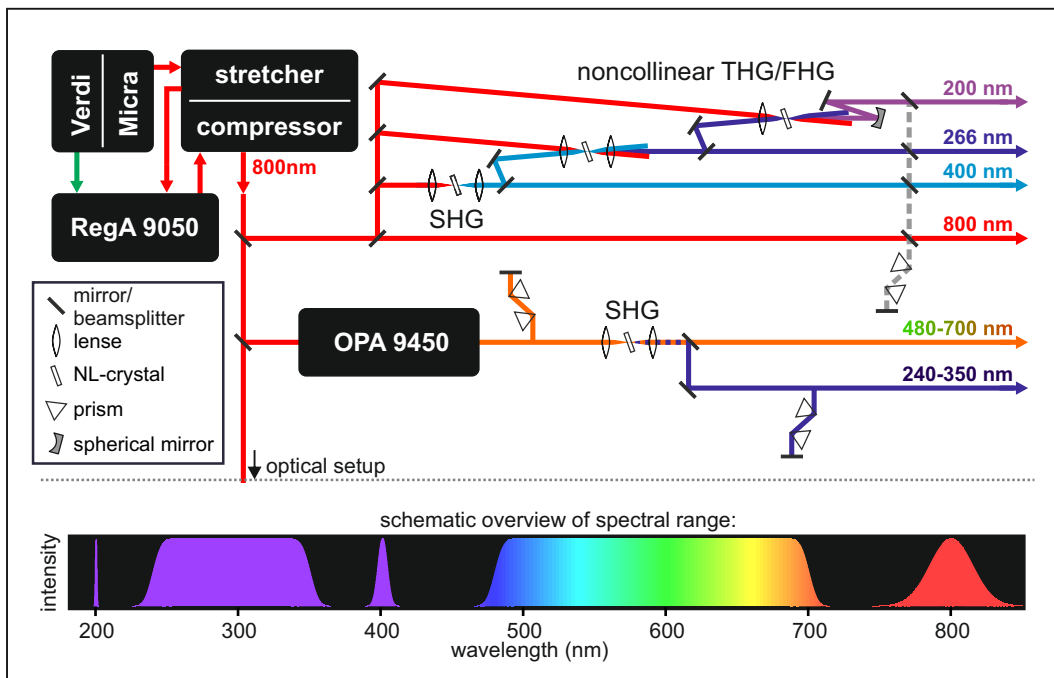


Figure 4.9: Schematic of the laser setup adopted from [Weg14]: The *Coherent* laser system consisting of a *Verdi* pump laser, a *Micra* oscillator, a *RegA 9050* amplifier and a stretcher/compressor unit provides ultrafast laser pulses with a photon energy of 1.55 eV. In the *OPA 9450* visible light of different wavelengths is generated which can be frequency doubled yielding UV light. In addition, second, third and fourth harmonic generation provides access to other UV photon energies.

The fundamental pulses may be used directly, or can be frequency doubled in a β -barium borate (BBO) ($\beta - \text{BaB}_2\text{O}_4$) crystal yielding the second harmonic at 3.1 eV. Third and fourth harmonic generation (THG and FHG) are realized by overlapping the 3.1 eV pulses with a part of the fundamental (1.55 eV) pulses in a BBO where they undergo sum-frequency generation (SFG) yielding the third harmonic of 4.65 eV. The fourth harmonic is generated analogously by adding another part of the fundamental 1.55 eV beam to yield 6.2 eV. The third and fourth harmonic generation is described in detail in [Weg14]. Especially the 6.2 eV beam is suitable for direct photoemission experiments covering the work functions of the currently investigated materials ($\Phi_{\text{Au}(111)} = 5.35$ eV [Ren05], $\Phi_{\text{ZnO}(10\bar{1}0)} = 4.5$ eV and $\Phi_{\text{ZnO}(000\bar{1})} = 5.15$ eV [Oza11]).

A part of the fundamental beam can be used in the OPA providing access to a wide range of wavelength in the visible spectrum. In the OPA the fundamental IR beam splits where 25 % is used to generate white light in a sapphire crystal and the other 75 % is frequency doubled in a BBO crystal to yield a photon energy of 3.1 eV. The white light and the 3.1 eV beam are spatially overlapped in a second BBO crystal. The spectral part of the white light which overlaps with the 3.1 eV beam is amplified. The temporal delay between these two beams can be adjusted using a linear stage which allows continuous tunability over a broad spectral range ($\approx 1.7 - 2.5$ eV). Hence the photon energy can be tuned according to the sample's work function and the energetic positions of the investigated electronic states.

The time resolution of TR-2PPE depends on the pulsewidth of the laser. In the following the comprehension of laser pulses is discussed. In most transparent media the red colour features a higher group velocity than the blue colour. This causes a divergence of the spectral parts of the pulse in time. This effect is called the chirp of a pulse which has to be avoided to obtain short pulses. The chirp can be avoided using a prism compressor which consists of two prisms positioned parallel to each other's bases at an angle of minimum deviation. The laser beam passes the first prism which disperses the constituents such that the longer wavelength components travel a longer optical path through the second prism. After passing the second prism the beam is reflected from a mirror and returns through the two prisms collinearly to the incoming beam. Thereby components of varying wavelengths are brought to a temporal overlap.

4.2.2 Pulse Characterization

In order to analyse the 2PPE data detailed information about the laser pulses, such as photon energy, laser power, pulse duration and spot size is needed. The photon energy is measured with a *Maya200Pro* spectrometer (*OceanOptics*). Note that the energy of the photon is an important parameter that is needed to determine the work function of the sample and the binding energy of the electronic states. A typical laser spectrum is shown in Figure 4.10 (a), where the central photon energy and the bandwidth (FWHM) are obtained from a Gaussian fit (black line). The power of the laser beam is measured with a power meter (*Newport*) just before the beam is coupled into the chamber. In order to calculate the laser fluence, as described in appendix B, the spot size of the laser beam is required. The spot size is measured with a beam profiler (*SP620U*, *Spiricon*) which is placed at a virtual sample position outside the UHV chamber. A typical laser intensity profile is displayed in Figure 4.10 (b) in false colours. The black contours correspond to a 2D gaussian fit from which the FWHM is obtained.

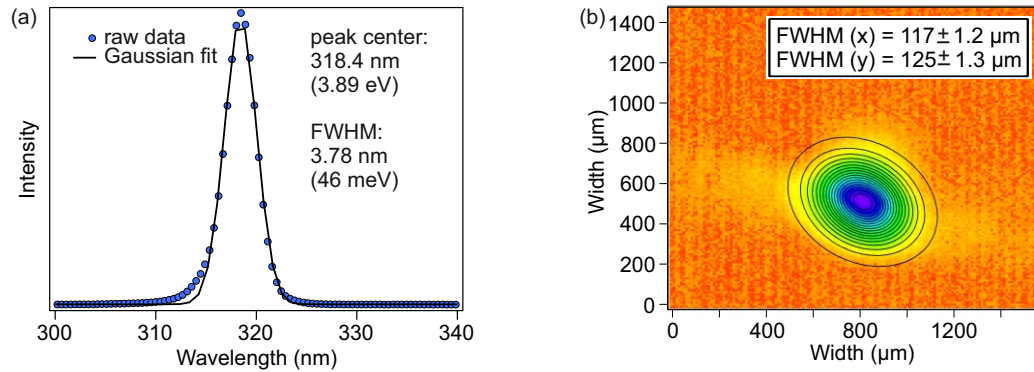


Figure 4.10: (a) An example laser spectrum and (b) the corresponding beam profile in false colours with a 2D Gaussian fit.

The duration of the laser pulses is determined via the XC of the laser pulses, which is usually measured by 2PPE from occupied states of a metal surface. The 2PPE process occurs in such a case *via* a virtual intermediate state with an infinitesimal lifetime. Therefore the measured 2PPE signal ($I_{XC}(t)$) corresponds to the correlation of the transient intensities of pump ($I_1(t)$) and probe ($I_2(t)$) pulses

$$I_{XC}(t) = \int_{-\infty}^{+\infty} dt' I_1(t) I_2(t - t') \quad (4.35)$$

This can be approximated by an autocorrelation of two identical laser pulses under the assumption that pump and probe pulse possess the same pulse duration [Rul98].

4.2.3 The Ultrahigh Vacuum Chamber

The UHV chamber provides a reduced pressure environment that is required for the investigation of surfaces. On the one hand UHV conditions are necessary in order to guarantee clean surfaces since the electronic structure is highly sensitive to surface contamination, e.g. nitrogen, oxygen or water, which would rapidly cover the surface under ambient conditions. On the other hand the mean free path of the photoelectrons decreases with increasing pressure. The UHV chamber sketched in Figure 4.11 is part of the FHI-setup and consists of two levels, the preparation and spectrometer chamber, separated by a gate valve. This helps to avoid contamination of the electron multipliers and optics of the electron analyser during sample preparation. The transfer system is separated from the chamber by a gate valve and provides a possibility to change the samples without breaking the vacuum. The base pressure

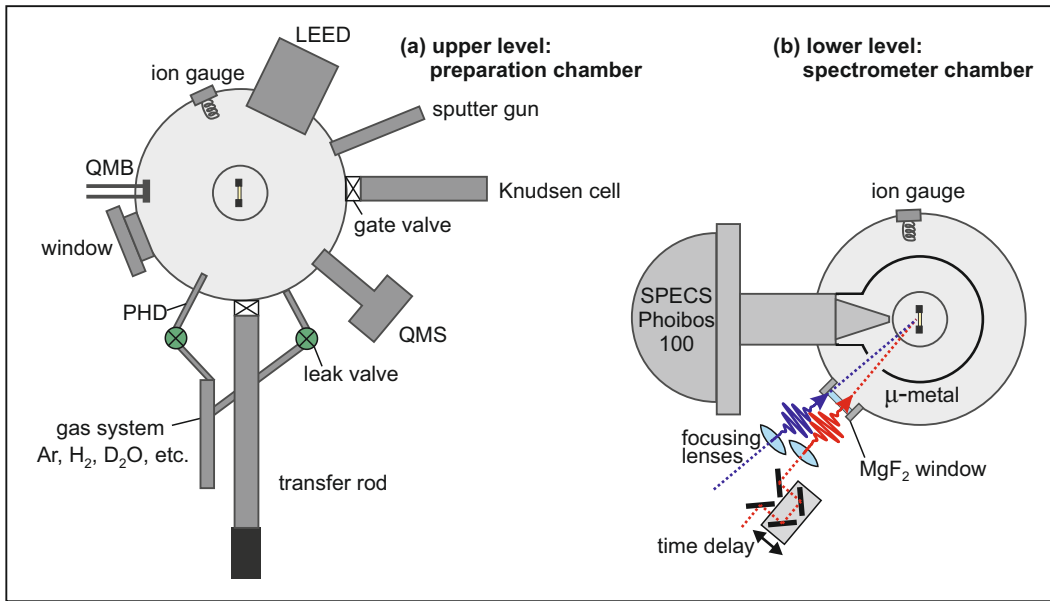


Figure 4.11: Schematic of a horizontal cross section of the UHV chamber consisting of (a) the preparation chamber at the upper level and (b) at the lower level the spectrometer chamber. The sample holder is schematically shown in the center 4.12

of the chamber is $\approx 1 \times 10^{-10}$ mbar and is achieved by several vacuum pumps. The upper level (preparation chamber) is pumped by a high-capacity turbomolecular pump (*HiPace 700*, Pfeiffer Vacuum AG) and the lower level (analyser chamber) by an ion getter pump (*TiTan 200L*, Gamma Vacuum, LLC) apart from an optional titanium sublimation pump (Vacom GmbH). The Knudsen effusion cell and the gas system together with the transfer system are equipped with their own turbo pumps respectively. The pre-vacuum is generated by membrane pumps (*MV2NT*,

Vacuubrand GmbH).

The preparation chamber is equipped with several devices needed for the preparation and characterization of clean single-crystal and adsorbate-covered surfaces. The details of the devices are as follows:

- **Sputter gun (SPECS)** is employed for the preparation of the sample surface during which the surface is first sputtered with argon ions and subsequently annealed. During the sputtering procedure argon is let into the UHV chamber *via* a leak valve and subsequently ionized by the electrons from the sputter gun filament. The Ar^+ ions are accelerated and bombarded onto the sample surface removing the surface atoms by momentum transfer. Since sputtering roughens the sample surface usually an annealing cycle, inducing surface reorganisation, follows to obtain a smooth surface again.
- **Low-energy electron diffraction (LEED)** (*ErLEED 1000-A, SPECS*) provides the possibility to investigate the surface crystal structure of the sample.
- **Quadrupole mass spectrometer (QMS)** (*MKS, Satellite*) has several applications: (i) to quantify the coverage by means of temperature programmed desorption (TPD), (ii) to conduct rest gas analysis (RGA) and to test the purity of the sputter gas and the evaporated molecules and (iii) to detect the mass of helium in leak testing.
- **Knudsen effusion cell** (*Dr. Eberl, MBE components*) contains two water-cooled crucibles in which molecular solids with sublimation temperatures up to 700 °C can be evaporated separately or simultaneously. A copper block with two apertures is attached in front of the crucibles to focus the molecular beam onto the sample. The Knudsen cell is mounted on a linear stage and can be moved into the chamber until the sample is at the focus of the molecular beam. Furthermore, it is equipped with its own turbo pump and separated from the main chamber by a gate valve allowing to refill or exchange the molecules without breaking the vacuum of the UHV chamber.
- **Quartz microbalance (QMB)** (*agilent technologies*) is used to quantify the thickness of molecular films and faces the Knudsen cell such that a part of the molecular beam arrives on to the quartz crystal. The adsorbed molecules change the vibrational frequency of the quartz crystal. The working principle of the quartz crystal microbalance (QMB) is detailed in Section 4.3.2.
- **Pinhole doser (PHD)**: Gaseous, liquid and even solid molecules with evaporation points close to room temperature can be deposited on the sample

surface. In the case of liquids or solids the substances are stored in a glass tube which is attached to the gas system *via* a metal adapter. To evaporate the compounds the glass tube is heated with a heat gun. The gas system is then flooded with the evaporated substance and enters the chamber through the pinhole doser (PHD) (described detailed in [Dei11]).

The spectrometer chamber contains a hemispherical electron analyser (*Phoibos 100, SPECS*) which has been described and characterised in detail before [Dei11], while a brief description is given in Section 4.2.4. A magnesium fluoride (MgF_2) window is installed to couple the laser pulses into the chamber, MgF_2 is transparent from ultraviolet to the infrared spectral region. Also its low refractive index minimizes the dispersion of the laser pulses.

The UHV setup at the FU differs mainly in 3 aspects: (i) upper and lower level are not separated by a gate valve, (ii) the electron analyser is a time-of-flight (TOF) instead of a hemispherical analyser (see Section 4.2.4 for details) and (iii) the LEED is located in the lower level opposite to the TOF.

Both setups use the same sample holder [Hag09] depicted schematically in Figure 4.12. The upper sample holder is attached to the cold finger of the cryostat and consists of copper and is electrically (not thermally) isolated by sapphire plates from the two copper parts which form the intake slits for the sample boat. The sample

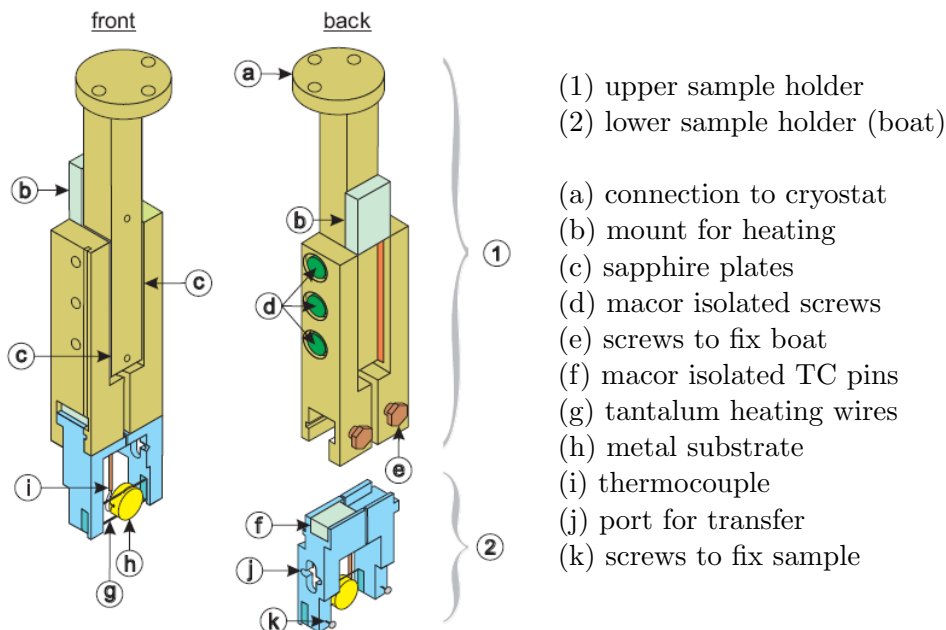


Figure 4.12: Sketch of the sample holder, adopted from [Hag09].

boat consists of two electrically isolated molybdenum parts which connect the two

isolated copper parts of the upper sample holder serving thus as electrodes for the resistive heating. The metal sample is fixed with tantalum (Ta) heating wires in the sample boat. The sample temperature is measured with thermocouple (TC) wires which are connected *via* TC pins to the jacks of the upper part of the sample holder. The ZnO crystals are due to their poor thermal conductivity fixed with grips on a tantalum sheet welded to the heating wires in order to guarantee a homogeneous heating. The cryostat is connected to a manipulator enabling the sample to move in x-, y- and z-direction, as well as to rotate around the z-axis (cryostat axis). The low temperature limit amounts to 77 K when the cryostat is filled with liquid nitrogen (LN₂). A PID temperature controller (*LakeShore 340*) provides a required heating rate. The sample is resistively heated *via* the tantalum wires with which it is fixed to the sample holder. Furthermore, they can be used to ground the sample during sputtering and to apply a bias voltage between sample and analyser during 2PPE measurements.

4.2.4 Electron Analysers

As pointed out earlier the electron analysers are the parts of the two setups which differ the most. The FHI-setup contains a hemispherical analyser (*Phoibos 100*, SPECS) while a custom built TOF spectrometer is included in the FU-setup. Both analysers will be described briefly in the following.

Hemispherical Analyser *Phoibos 100*

The hemispherical analyser *Phoibos 100* is the central part of the experimental setup. It enables a simultaneous measurement of the energetic and the angular distribution of the photoelectrons. Its working principle and characterisation have been described in detail in [Dei11]. In a hemispherical analyser the photoelectrons are spatially selected via electric fields and multiplied by micro-channel-plates (MCP) before illuminating a phosphor screen. The illumination on the phosphor screen is recorded by a camera which is located outside the chamber. The details of the camera are given at the end of the section. The analyser is shown schematically in Figure 4.13 and consists of two parts, *viz.* electrostatic lens system and a hemispherical capacitor. The photoelectrons enter the lens system after passing a working distance of 4 mm. The variable electric field of the lens system allows se-

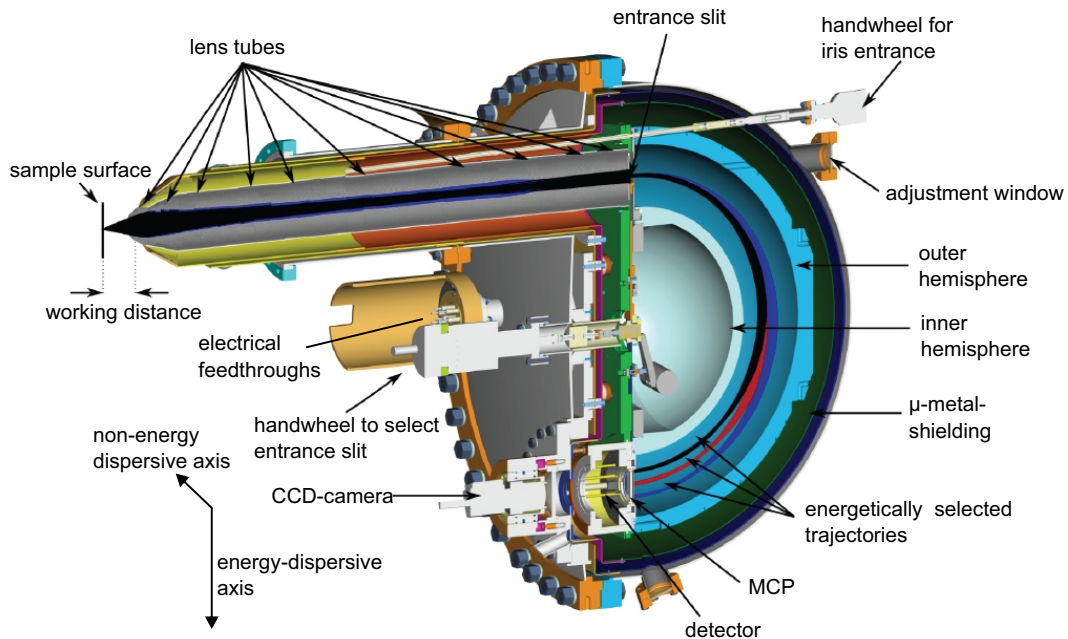


Figure 4.13: Cross section of the hemispherical analyser modified from [Bra09] showing the dispersing trajectories of the photoelectrons along the energy-dispersive axes.

lective projection of the electrons mapping either the spatial position or the angle of emission parallel to the entrance slit onto the 2D detector. The energy range

of mapping can be selected *via* acceleration voltages inside the lens system. The size of the entrance slit defines the transmission *vs.* energy resolution which can be regulated by a magnetically coupled handwheel. Energy selection is realized by the radial electric field ($E(r)$) in the hemispherical capacitor forcing the photoelectrons on elliptic trajectories with different radii according to their kinetic energy. The lens system and the hemispherical capacitors are shielded by μ -metal to prevent distraction of the electrons due to external magnetic fields. The radial electric field ($E(r)$) is given by

$$E(r) = (V_{\text{in}} - V_{\text{out}}) \frac{R_{\text{in}} R_{\text{out}}}{R_{\text{out}} - R_{\text{in}}} \frac{1}{r^2} \quad (4.36)$$

where $V_{\text{in/out}}$ are the voltages of the inner/outer hemisphere and $R_{\text{in/out}}$ are the respective radii. The geometry of this setup leads to a non-energy dispersive axis perpendicular to the energy-dispersive axis which is parallel to the radial direction. Along the energy-dispersive axis of the 2D detector electrons are spatially separated according to their kinetic energy. Depending on the selected working mode the photoelectrons are spatially separated along the non-energy dispersive axis according to either their horizontal spatial position on the sample surface or their emission angle.

After passing the hemispherical capacitor the energetically selected electrons are multiplied by a MCP before illuminating the phosphor screen. The digital picture of the electrons illuminating the phosphor screen is recorded by a highly sensitive CCD-camera (*PCP Sensicam qe*). To obtain from this image a 2D-spectrum, where the kinetic energy is represented as function of the emission angle, the pixel coordinates (m_α, m_E) have to be converted into kinetic energy E and emission angle α . The kinetic energy E_{kin} can be calculated using the following formula [SPEa]:

$$E_{\text{kin}} = E'_{\text{kin}} + DeI \cdot E_{\text{pass}} \cdot M \cdot Ps(m_E - \frac{M_E}{2}) \quad (4.37)$$

Where E'_{kin} and E_{pass} select the energetic range (E'_{kin} defines the center of the spectrum). DeI is the energetic dispersion depending on the radius of the hemisphere and M is the magnification factor of the camera objective. Ps is the pixel size and M_E corresponds to the total range of pixels along the energy-dispersive axis and is aligned such that the image is in the center of the CCD-screen. The conversion to the emission angle (α) from the pixels (m_α) along the non-energy dispersive axis is more complicated since chromatic aberration of the lens system and the hemispherical capacitor lead to a non-linear relation between E'_{kin} and E_{pass} . The image can be unwarped by calculating the trajectories of the electrons and the corresponding iso-angle lines. The pixel (m_α) at energy E_{kin} can be calculated via a second order

polynomial [Weg14]:

$$m_\alpha(E_{\text{kin}}, r) = n_0(\alpha, r) + n_1(\alpha, r)E_{\text{kin}} + n_2(\alpha, r)E_{\text{kin}}^2 \quad (4.38)$$

The coefficients n_i can be calculated from a polynomial expression provided by SPECS [SPEb] and depend on the retarding ratio ($r = E'_{\text{kin}}/E_{\text{pass}}$).

Time-of-Flight Spectrometer

Figure 4.14 shows a schematic drawing of the TOF spectrometer that was used at FU. It consists of a field-free drift tube, a conical tip with an aperture of 3 mm and a MCP detector. The kinetic energy of the photoelectrons is measured indirectly via the time (t) that electrons need to pass the drift distance ($d = \overline{AE}$)

$$E_{kin} = \frac{1}{2}m_e \left(\frac{d}{t} \right)^2 \quad (4.39)$$

where m_e is the electron mass. The drift tube is grounded and free of electromagnetic

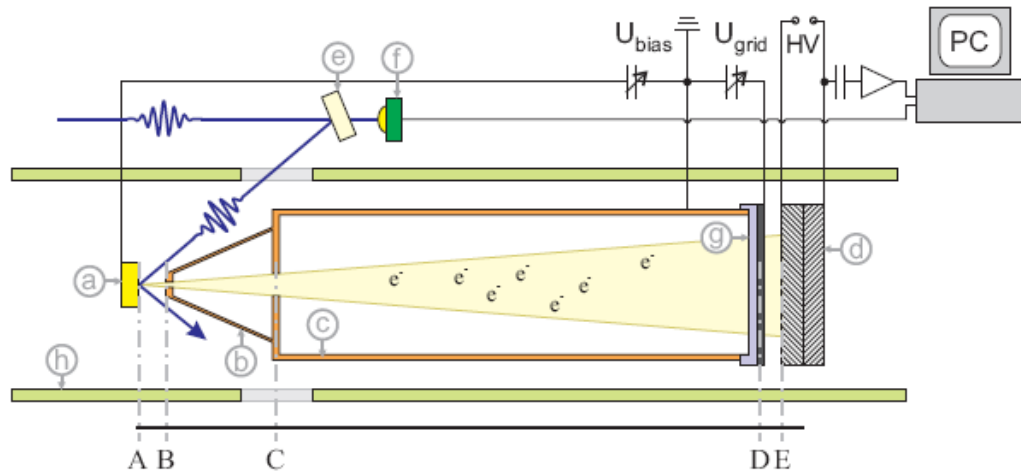


Figure 4.14: Sketch of the time-of-flight spectrometer adopted from [Hag09]. (a) sample, (b) conical TOF-tip, (c) drift tube, (d) micro channel plates, (e) mirror, (f) photodiode, (g) fine-meshed grid, (h) μ -metal casket

fields which may cause deflection, acceleration or deceleration of the photoelectrons. Furthermore the development of electric fields is prevented by keeping the work function of the TOF ($\Phi_{\text{TOF}} = 4.3$ eV) homogenous. This is achieved by coating graphite on both sides of drift tube and tip. Static magnetic fields are shielded by a μ -metal casket, which surrounds the whole spectrometer.

The laser pulses impinge on the sample at an angle of 45° and the photoelectrons enter the drift tube through the aperture of the conical tip. After passing the drift distance of 210 mm they impinge on a fine-meshed copper grid, which terminates the field-free drift region. The electrons are accelerated by a voltage (15 V) between the first and the second grid and thus pass the third grid. The the electrons are accelerated towards the MCPs by a potential difference of ≈ 500 V.

The MCPs consist of 0.5 mm thick glass plates with a diameter of 40 mm, which are veined with microscopic capillaries (10 μm diameter). These capillaries are

oriented at an angle of 8° relative to the surface normal which enables the multiple collisions of photoelectrons inside the glass capillary. This collision produces secondary electrons. The secondary electrons are further accelerated by a high voltage of 2.7 kV, which is applied between the two MCPs. Due to these electron cascades the high voltage decreases for a moment which is detected by a capacitor and a preamplifier. In fact, a time-dependent signal $-\Delta V(t)$ is recorded.

Measuring the Energy *via* the Time

In order to obtain the kinetic energy of the photoelectrons *via* the relation shown in Equation (4.39) the time (t) between the emission and their arrival at the MCPs has to be known. The impact of the electrons on the MCPs is detected but the point of time at which the electrons are emitted cannot be measured directly. Therefore a reference signal for the time measurement is taken from a photodiode which is placed at the RegA output. The measured time (difference between start and arrival signal) is referred to as t' which contains the time (t_0) that light takes to travel from the photodiode to the sample plus the time-of-flight (t)

$$t = t' - t_0 \quad (4.40)$$

Substituting Equation 4.40 in Equation 4.39 yields

$$E_{kin} = \frac{1}{2}m_e \left(\frac{d}{t' - t_0} \right)^2 \quad (4.41)$$

t_0 is determined by a series of spectra taken with different bias voltages. It is assumed that the spectra shift energetically according to the bias voltages. The correct t_0 is obtained by superimposing the spectra taken with different bias voltages under variation of t_0 . The value for t_0 for which all spectra have the same shape is the right one. The energy thus obtained is the kinetic energy relative to the TOF's vacuum level, whereas the kinetic energy with respect to the sample's vacuum level, the final state energy E_{kin}^{fin} , is required. In order to obtain E_{kin}^{fin} relative to the Fermi level the work function difference ($\Delta\Phi = \Phi_{TOF} - \Phi_{sample}$) and the bias voltage (eU_{bias}) have to be taken into account

$$E_{kin}^{fin} = \frac{1}{2}m_e \left(\frac{d}{t' - t_0} \right)^2 - \Delta\Phi + eU_{bias} \quad (4.42)$$

In fact, voltage *vs.* the time-of-flight is measured and is transformed into energy spectra employing Equation 4.42. The measured signal intensity is proportional to the number of electrons (dN) within a certain time frame (bin) (dt), *i.e.* $\Delta V(t) \propto \frac{dN}{dt}$ and subsequently generated energy spectrum should contain the number of events

(dN) occurring in a certain energy range (dE). Therefore the signal has to be converted according to

$$\frac{dN}{dE} = \frac{dN}{dt} \left| \frac{dt}{dE} \right| = \frac{dN}{dt} \frac{(t' - t_0)^3}{m_e d^2} \quad (4.43)$$

Bias Correction

Usually the work function values of sample and analyser differ from each other. Their Fermi levels can be equilibrated by grounding or electrically connecting them. However, their vacuum levels will in general be different as shown schematically in Figure 4.15 (a). This is a great disadvantage if the work function of the sample

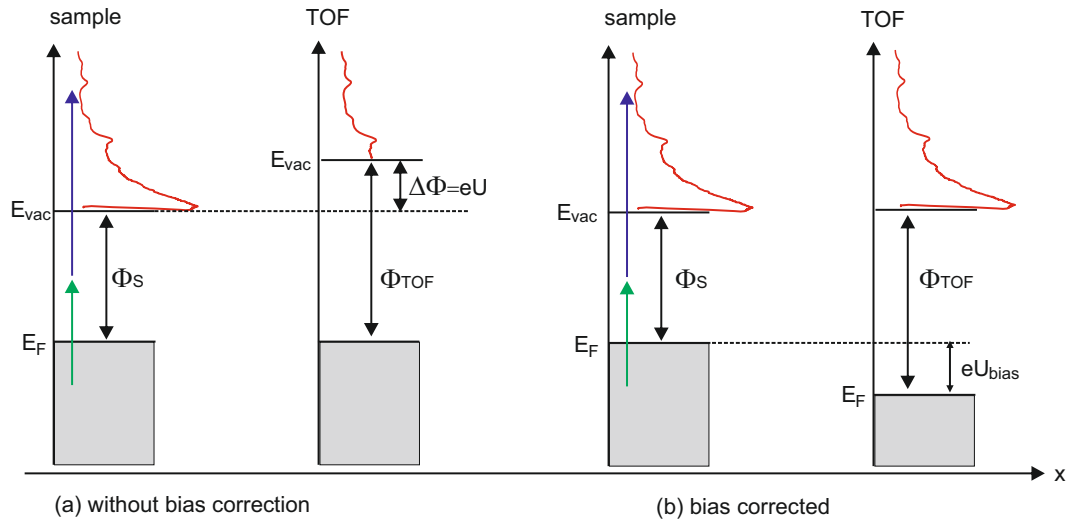


Figure 4.15: Energy diagram for (a) an unbiased sample and (b) a biased sample. (a) The work function difference $\Delta\Phi$ induces an electric field accelerating the emitted electrons. (b) The vacuum levels align due to the applied bias voltage.

is lower than that of the analyser then the slower electrons may not be able to reach the TOF. Thus the spectrum will be lost by the amount of the work function difference ($\Delta\Phi = \Phi_{TOF} - \Phi_{sample}$). By applying a bias voltage (U_{bias}) between the sample and the TOF (Figure 4.15 (b)), the Fermi levels will be shifted by eU_{bias} with respect to one another while the vacuum levels align if the bias is equal to the work function difference. Note that the same principle applies for measurements with a hemispherical analyser.

4.3 Sample Preparation

In the following sections the preparation procedures for the ZnO and Au single crystal samples will be presented. Also the adsorption procedures for solid and gaseous adsorbates will be introduced. Apart from this, the quantification of the adsorbate coverages will be discussed.

4.3.1 Preparation of the O-terminated ZnO Surface and Quantification of the H-Dosage

The single crystal ZnO(000 $\bar{1}$) (*MaTeck GmbH*) sample was prepared by repeated sputtering and annealing cycles until the measures for cleanliness, such as maximal work function ($\Phi = 5.1 - 5.2$ eV, which agrees with the literature 5.15(5) eV [Oza11]) and minimal CAL intensity were satisfied. The sample was sputtered at room temperature for 10 min with argon ions with the following parameters, $p_{\text{Ar}} = 2 \times 10^{-6}$ mbar, 1.0 keV and a sputter current of $\approx 6 \mu\text{A}$. Subsequently the sample was annealed at 950 K for 30 min under oxygen atmosphere, $p_{\text{O}_2} = 1 \times 10^{-6}$ mbar, with a heating rate of $\beta = 30$ K/min (the ZnO sample was mounted on a Ta sheet which was heated resistively guaranteeing a homogeneous heat distribution). The sample was prepared by following the above procedure on a daily basis. All the measurements were performed at temperatures around 100 K.

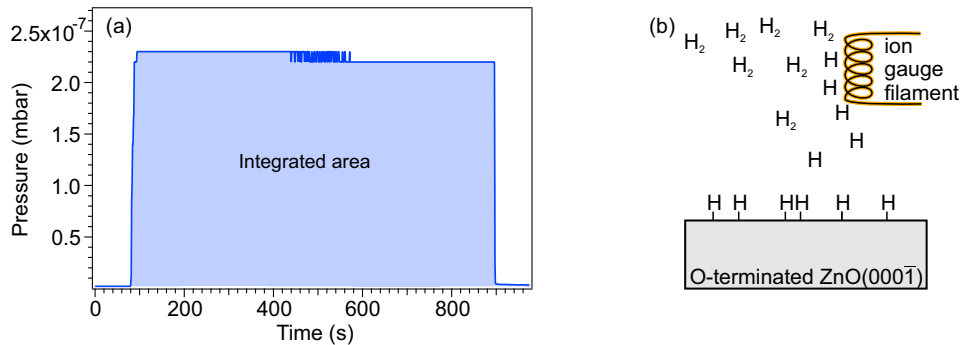


Figure 4.16: (a) Pressure trace taken during H₂ dosing, the dosage can be calculated using the integrated area below the trace (b) illustration of H₂ cracking into atomic hydrogen by the electrons emitted from the filament of the ion gauge.

Hydrogen was dosed *via* the background pressure through a leak valve. The hydrogen dosage was quantified by measuring the pressure and the time as shown in Figure 4.16 (a), where the dosage can be calculated in Langmuir (L) with the integrated area. 1 L is defined as a gas dosage of 1 torr for 1 μs ($1 \text{ L} = 1 \text{ torr} \cdot \mu\text{s}$) under the assumption of a sticking coefficient (S_c) 1. This corresponds to a pressure of 1.33×10^{-6} mbar for 1 s. 1 L hydrogen can be obtained by dosing 4.4×10^{-7} mbar

for 1 s, since the sensitivity of the ion gauge (*Arun Microelectronics Limited*) is 3 times smaller for hydrogen than nitrogen, where the latter is at default setting. Opening a valve for 1 s is not practical with our system, therefore we decided to dose 1 L at a H₂ pressure of 2.2×10^{-7} mbar for 2 s. The H₂-dosage in L is then obtained by dividing the integrated area of pressure *vs.* time curve (Figure 4.16 (a)) by $2 \cdot 2.2 \times 10^{-7}$ mbar·s. During the hydrogen dosage the sample was kept at 100 K and facing the glowing filament of the ion gauge from a distance of ≈ 15 cm. The hot filament enhances dissociation of H₂ as sketched in Figure 4.16 (b).

4.3.2 Preparation of the SP6 Films and Determination of the Film Thickness Using a Quartz Microbalance

ZnO(10 $\bar{1}$ 0) sample was prepared on a daily basis by sputtering for 10 min with Ar⁺ ($p_{\text{Ar}} = 2.0 \times 10^{-6}$ mbar, 0.75 keV at 300 K followed by 30 min annealing at 950 K with a temperature ramp of 30 K/min). The SP6 molecules were evaporated from a Knudsen-cell at a temperature of 580 K onto the sample at 300 K. During the evaporation the QMB was placed behind the sample to quantify the thickness of the SP6 molecules. The thickness on the QMB is proportional to that of the sample, where the proportionality constant is called tooling factor (T).

The working principle of a QMB is based on the piezoelectric properties of quartz. This piezoelectric effect is nearly temperature independent and perpendicular to the prism axis along the a -axis. Therefore it is important to have the crystal either AT-(parallel to the (00 $\bar{1}$)-plain) or BT-cut (parallel to the (023)-plain). Applying pressure or draught to a quartz crystal results in an electrical polarization along the force direction. Conversely under a direct-current voltage a distension or compression occurs. Applying an alternating current voltage with a suitable frequency leads to a resonant vibration of the quartz crystal. The resonance frequency depends on the shape and size of the crystal. The mass of the quartz crystal is changed under absorption of atoms or molecules on the surface and thus the resonance frequency.

In order to determine the mass of the adsorbed material, and thus the film thickness, Sauerbrey equation [Sau59] is employed.

$$\Delta f = -\frac{2(f_0)^2}{A\sqrt{\rho_q\mu_q}}\Delta m \quad (4.44)$$

where	$f_0 =$	resonant frequency (Hz)
	$\Delta f =$	frequency change (Hz)
	$\Delta m =$	mass change (g)
	$A =$	piezoelectrically active crystal area (cm ²)
	$\rho_q =$	2.65 g/cm ³ density of quartz
	$\mu_q =$	2.95×10^{-11} g/cm ² s ² shear modulus for AT-cut crystal

Solving for $\frac{\Delta m}{A}$ with $\sqrt{\rho_q\mu_q} = z_q = 8.8 \times 10^6$ kg m⁻² s⁻¹ Equation 4.44 can be written as

$$\frac{\Delta m}{A} = -\frac{\Delta f z_q}{2(f_0)^2} = \frac{\Delta f (8.8 \times 10^6 \text{ kg m}^{-2} \text{ s}^{-1})}{2(f_0)^2} \quad (4.45)$$

The film thickness (θ) is then given by

$$\theta = \frac{\Delta m T}{A \rho_{\text{Mat}}} \quad (4.46)$$

where ρ_{Mat} is the density of the adsorbed material and T corresponds to the tooling factor which is the ratio between the adsorption rate on the QMB with and without the sample between QMB and evaporator. The Sauerbrey equation holds only for very small frequency changes ($\frac{\Delta f}{f_0} \leq 0.02$) and equally distributed rigid masses. The frequency changes are usually in the range of $\frac{0.2 \text{ kHz}}{5978 \text{ kHz}} = 3.4 \times 10^{-5}$ which is $\ll 0.02$. But of course the large organic molecules such as SP6 are not rigid masses, which introduces a finite error.

In the following an example is given for the determination of the SP6 film thickness. Figure 4.17 shows a QMB trace to determine the tooling factor and the film

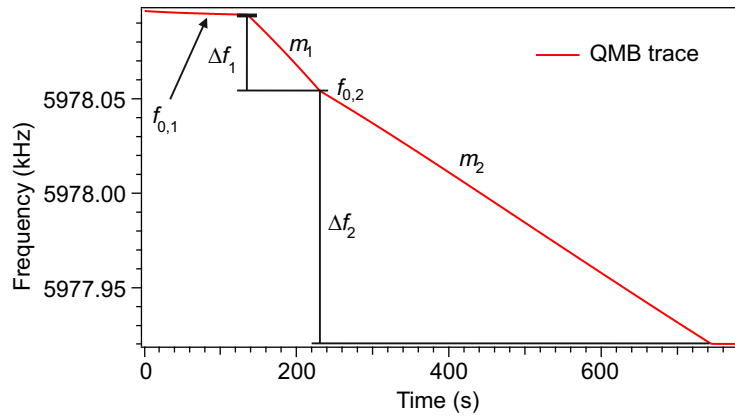


Figure 4.17: QMB trace *vs.* the time for the determination of the tooling factor and the SP6 film thickness.

thickness. The slope, m_1 refers to the frequency change of the quartz crystal without the sample between QMB and evaporator and m_2 is the slope obtained with the sample. The tooling factor is given by

$$T = \frac{m_1}{m_2} = 1.74 \quad (4.47)$$

With T and the density of SP6 ($\rho_{\text{SP6}} = 1.4 \text{ g/cm}^3$, as determined by M. Sparenberg in the group of F. Henneberger (HU Berlin), the film thickness can be calculated from Equation 4.46

$$\theta = \frac{\Delta m T}{A \rho_{\text{SP6}}} \quad (4.48)$$

the start frequency ($f_{0,1}$) and the shift (Δf_2) can be simply read out from the QMB

trace, $\Delta m/A$ can be calculated using Equation 4.45

$$\frac{\Delta m}{A} = \frac{0.13 \text{ kHz}(8.8 \times 10^6 \text{ kgm}^{-2}\text{s}^{-1})}{2(5978.05 \text{ kHz})^2} = 2.46 \times 10^{-5} \text{ kg/m}^2 \quad (4.49)$$

and hence the thickness of film

$$\theta = \frac{2.45 \times 10^{-5} \text{ kgm}^{-2} \cdot 1.74}{1.4 \text{ gcm}^{-3}} = 31 \text{ nm} \quad (4.50)$$

TPD turned out to be not a suitable method to quantify the film thickness, nevertheless it unveils some important information. Figure 4.18 (a) shows TPD traces measured at masses of (m/z) 58 and 78 amu, where the former can be related to a *tert*-butyl group with an additional hydrogen atom and the latter may correspond to a benzene molecule. The signal measured for $m/z = 78$ amu is much lower than that of $m/z = 58$ amu. Both masses are detected at the same temperature indicating that the detected fragments originate from molecules and not from adsorbed fragments. Fragmentation due to dissociation of the molecules may take place during evaporation. In Figure 4.18 (b) the TPD of different coverages SP6/ZnO($10\bar{1}0$) show

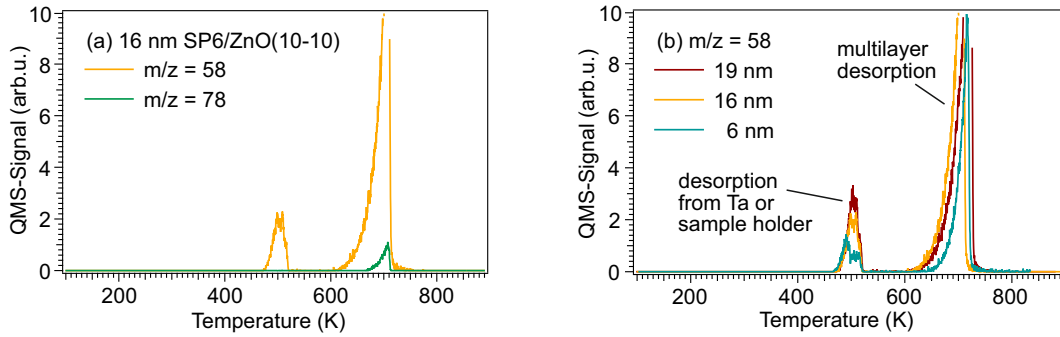


Figure 4.18: (a) TPD of 16 nm SP6/ZnO($10\bar{1}0$) measured with different masses, both of which desorb at the same temperature, (b) TPD traces of different coverages SP6/ZnO($10\bar{1}0$)

that the intensity of both peaks increase with the coverage in a zero order fashion. Essentially, the low temperature signal is from the tantalum sheet or the sample-holder while the high temperature signal originates from multilayer desorption of the SP6 molecules from the ZnO($10\bar{1}0$) surface. A monolayer desorption is not observed here indicating that either the molecules in the monolayer stick to the surface and decompose thermally or that the intermolecular interactions are as strong as the interactions between the SP6 molecules and the ZnO surface such that the whole film desorbs at once. The latter situation is more likely to be the case. A Raman study of SP6 on glass or ZnO revealed that the interaction of the SP6 molecules with the ZnO surface was weak [Stäl13].

In order to understand whether the SP6 molecules decompose thermally during the evaporation nuclear magnetic resonance (NMR) spectra were taken before and after evaporation when dissolved in deuterated benzene. The evaporated molecules were collected from the focussing block which is fixed at the front of the Knudsen cell. Figure 4.19 (a) shows the downfield part of the NMR spectrum with the signals of the aromatic hydrogen atoms which are less screened by the ring current of the π -systems induced by the magnetic field. The signal from the evaporated SP6 molecules (blue-green) is less intense compared to that of the pristine SP6 (before evaporation). Also the solvent (C_6D_6) peak is relatively higher in intensity for the evaporated molecules. This is due to the differences in ratio between solvent and molecules. The solution of the evaporated SP6 molecules is less concentrated than its pristine counterpart. The number and position of the signals from the aromatic hydrogen well agreed across the two samples, *i.e.* both SP6 fractions possess the same chemically equal hydrogen atoms and thus both samples are identical within the detection limits. In Figure 4.19 (b) the upfield part of the NMR spectrum with the signals of the aliphatic hydrogen atoms is depicted. Besides the peaks related to the *tert*-butyl hydrogen atoms there are signals which may be attributed to aliphatic contaminations or water. The peaks next to the *tert*-butyl hydrogens peak are the C^{13} satellites. Another proof that the evaporated molecules are still intact is the ratio between the integrals of the *tert*-butyl hydrogen peak and the peaks between 7.8 - 7.9 ppm, which correspond to 4 aromatic hydrogen atoms. There are 18 H-atoms at the *tert*-butyl-groups, thus the ideal ratio is 18 : 4. In the case of pristine SP6 the ratio amounts to 21.96 : 4.11 and for the evaporated SP6 to 18.76 : 4.00. Notably the ratio from the evaporated SP6 compares very well with the ideal ratio of 18 : 4. This confidently concludes that the SP6 molecules do not decompose during evaporation.

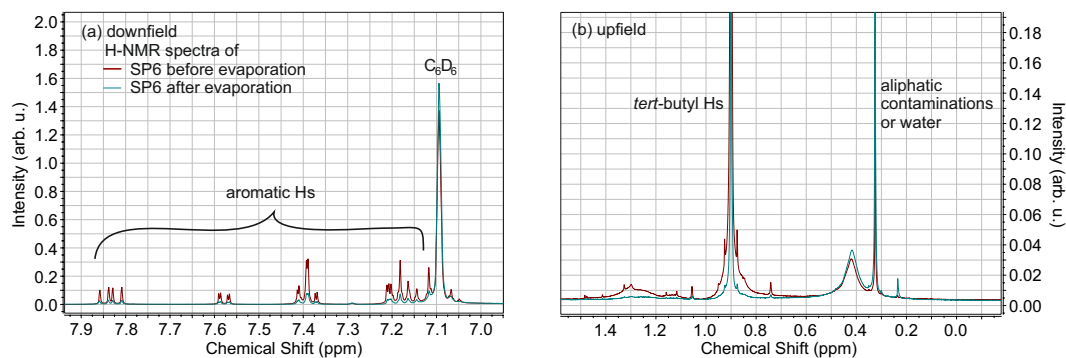


Figure 4.19: (a) Downfield and (b) upfield H-NMR spectra of SP6 before (dark red) and after (blue-green) evaporation.

4.3.3 Preparation of the DCV6T and DCV5T-Me₂ Films on Au(111)

In the following the preparation of the DCV6T and DCV5T-Me₂ films on Au(111) is described. First the preparation and quantification of the DCV6T films will be presented. The knowledge gained during these experiments was later applied in the preparation of the DCV5T-Me₂ films. Usually the molecular coverages were quantified by means of TPD at the FU setup. But in the case of thiophenes this method turned out to be not practical since the molecular monolayer do not desorb intact. Therefore the coverages were quantified by adsorption induced work function changes and the shape of the 2PPE spectra. A detailed discussion about the inapplicability of TPD is given in appendix A.

Before the molecules were evaporated onto the sample surface the Au(111) surface was prepared by sputtering with Ar⁺ ions ($p_{\text{Ar}} \approx 3 \times 10^6$ mbar, 1.5 kV for 10 min) followed by an annealing cycle during which the sample was heated up to 800 K for 20 min with a heating ramp of 60 K/min.

Preparation of the DCV6T Films

The DCV6T molecules were evaporated from a Knudsen cell onto the Au(111) surface. The molecules were heated to 520 K while the Au sample was kept at 300 K. During the initial measurements the DCV6T molecules were evaporated onto the

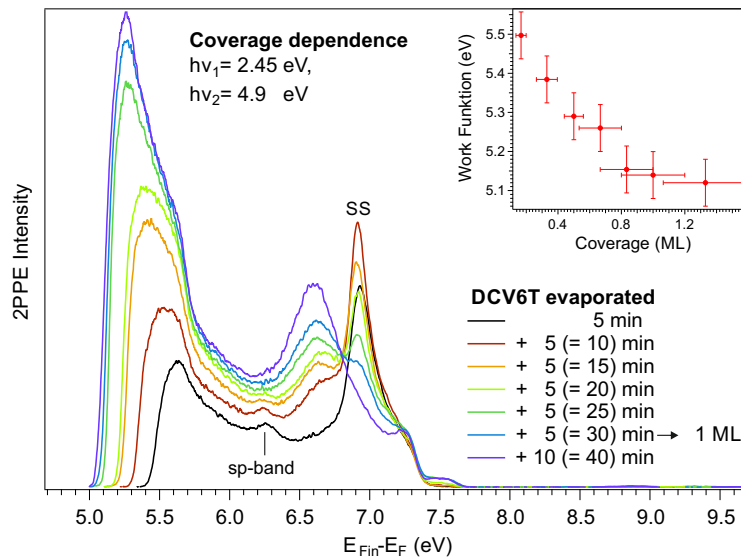


Figure 4.20: Coverage dependent 2PPE spectra measured with $h\nu_1 = 2.45$ and $h\nu_2 = 4.9$ eV. In the inset the work function is plotted as a function of the coverage.

100 K cold Au(111) surface. It is realized that during the evaporation a decomposition product, malonodinitrile, was coadsorbed on the sample surface as an undesired

contamination. This can be easily avoided by evaporating the molecules onto the 300 K sample surface since malonodinitrile desorbs between 180 -300 K. Detailed information is available in appendix A.

In order to quantify the effect of DCV6T coverage, 2PPE measurements were performed as a function of the film thickness. Figure 4.20 shows a series of 2PPE spectra measured with $h\nu_1 = 2.45$ and $h\nu_2 = 4.9$ eV. The work function decreases and the features of the Au(111) surface (sp-band and surface state (SS)) are quenched due to DCV6T adsorption. In the inset of Figure 4.20 the work function is plotted as a function of the DCV6T coverage. It is assumed that the work function decrease saturates at a monolayer (ML) coverage. Therefore the spectrum taken after an evaporation period of 30 min is assigned to a ML coverage. The different film thicknesses were determined according to the ML calibration. This is based on the assumption of a constant evaporation rate, since these depositions were performed in one session (*i.e.* on the same day). The error thereby is estimated to be 20 %.

Higher coverages can be quantified only according to their shape and the excited state lifetime since the work function is more or less constant for coverages ≥ 1 ML. Also, the evaporation rate is not always constant due to the decreasing filling level of the crucible and the irregular heat distribution therein. Therefore a constant evaporation rate is assumed only during evaporation cycles carried out on the same day.

To illustrate this procedure an additional coverage-dependent series of spectra for coverages up to 7 ± 3 ML are depicted in Figure 4.21. The black spectrum has been recorded after a deposition for 4 min and assigned to a coverage of 1.5 ± 0.5 ML since we note a minimum work function and quenched surface state. The other coverages within this series have been determined from this calibration

(for depositions carried out on the same day). At a film thickness of 2 ± 1 ML a very broad feature arises at final state energies between $\approx 5.5 - 6.0$ eV which becomes even more prominent and shifts to lower energies with increasing coverage, while the other molecular features decrease. This feature exhibits an increasing lifetime with

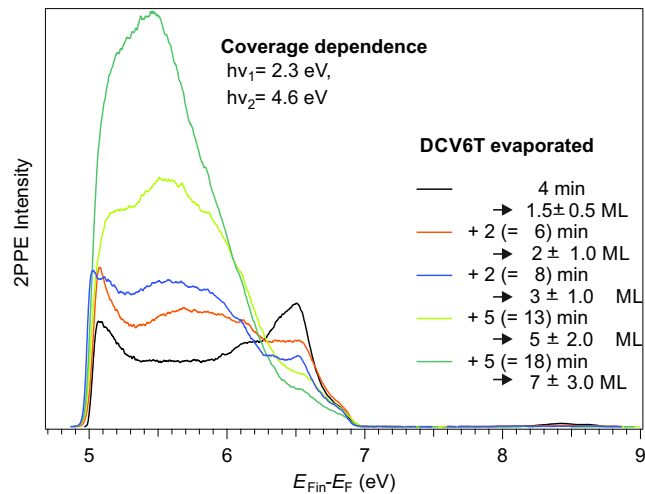


Figure 4.21: 2C-2PPE spectra series measured on different DCV6T coverages on Au(111).

coverage as observed in TR-2PPE. Coverages higher than 7 ± 3 ML can only be distinguished according to the lifetimes measured from the TR-2PPE spectra, mounting the error at least to 30 %.

Preparation of the DCV5T-Me₂ Films

The DCV5T-Me₂ molecules were evaporated from the Knudsen-cell at a temperature of 553°C onto the Au(111) surface which was held at a temperature of 300 K. The coverage was quantified according to the procedure described before in the case of DCV6T, since TPD was not applicable for DCV5T-Me₂ either (see Appendix A for further information). Figure 4.22 displays a series of coverage-dependent 2C-2PPE

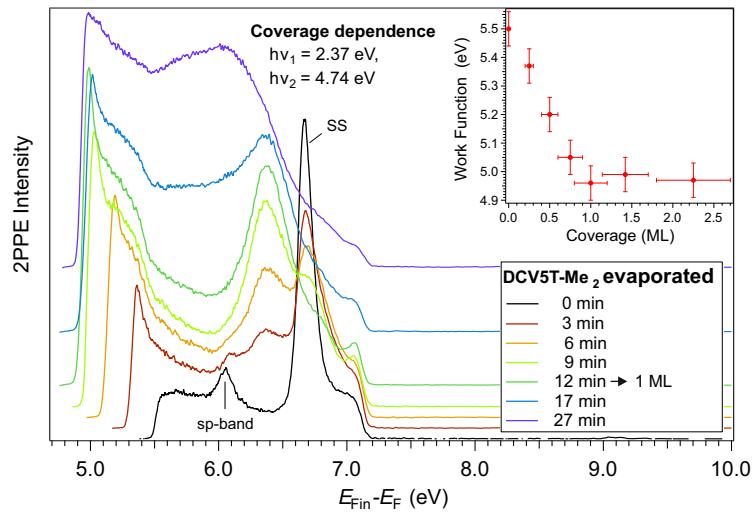


Figure 4.22: Coverage-dependent 2PPE spectra series measured with $h\nu_1 = 2.37$ and $h\nu_2 = 4.74$ eV. In the inset the work function is plotted as a function of the coverage..

spectra recorded with $h\nu_1 = 2.37$ and $h\nu_2 = 4.74$ eV. The black spectrum shows the pristine Au(111) surface with a work function of $\Phi = 5.5$ eV and two characteristic features, namely the sp-band and the surface state (SS). These features are quenched with increasing coverage and the work function shifts to lower values as much as 0.55 eV (see inset of Figure 4.22). After 12 min of evaporation the coverage is assigned to 1 ML (minimal work function and quenched surface state). Based on this calibration the other coverages were determined within an error of 20 %. Higher coverages are determined the same way as described before for DCV6T.

The preparation of the molecular films was carried out using the same experimental parameters, e.g. evaporation and sample temperature, as used during the STM experiments which did not show any decomposed molecules on the Au(111) surface [Yan14b, Yan14a]. This supports the existence of intact DCV5T-Me₂ and

DCV6T molecules on the Au(111) surface.

5 Results

The efficiencies of solar cells and LEDs are determined by similar aspects and processes, such as the film morphology, the energy level alignment at the inorganic/organic and organic/organic interfaces as well as exciton formation, decay and diffusion. A detailed understanding of these fundamental processes is needed in order to improve the performance of LEDs and OPVCs.

In this work the questions of how the molecular levels align at the interface with the substrate and within the film, how and on which times scales excitons form and decay, how the quasiparticles interact and how they are affected by modifications of side conditions are handled. These questions are tackled by 2PPE studies of four model systems which represent different active parts of a solar cell or an LED.

The transparent conductive oxide ZnO is, on the one hand, attractive for the use as active LED medium and thus electronic processes in optically excited ZnO are of interest. On the other hand, it is a promising candidate for transparent electrodes in combination with an organic semiconductor. In this work the spirobifluorene derivative SP6 is used to study charge transfer processes at the ZnO interface. However, bulk SP6 represents a model system for an organic LED or laser medium. The energy level alignment at metal/organic interfaces is investigated using two DCV-substituted oligothiophenes on Au(111). The complexity is further increased by investigating the polymer donor P3HT.

In the following the structure of this chapter is outlined:

In Section 5.1 the influence of H-adsorption on the electronic surface structure of the fully O-terminated ZnO surface is investigated. A comparison with previous results for the mixed-terminated surface allows to study the role of ZnH-bond formation. In addition, the influence of increased electron density at the surface on the relaxation dynamics of hot electrons is investigated.

The model system SP6 on ZnO is studied in Section 5.2 with focus on the dark-state dynamics and the energy level alignment of excited states which have not been observed so far.

In Section 5.3 the influence of a metal surface on the energy level alignment and the excited state dynamics in two DCV-substituted thiophenes adsorbed on the Au(111) surface is investigated.

The influence of the degree of crystallinity on the electronic structure and the excited state dynamics in two different P3HT films is studied in Section 5.4.

5.1 H-induced Metallicity and Excited State Dynamics at the O-terminated ZnO Surface

ZnO is a transparent conductive oxide and therefore very attractive for the application in optoelectronic and light harvesting devices. The stable ZnO surfaces are of particular interest since lots of processes like charge transfer or catalytic processes take place at surfaces and depend highly on the surface electronic structure and morphology. The SX is a promising feature for energy transfer processes at interfaces due to its stability at room temperature and towards air, which are good prerequisites for applications under ambient conditions. Time-resolved 2PPE is a powerful tool to study both, the occupied and unoccupied electronic surface structure, as well as excited state dynamics. Due to its pronounced surface sensitivity it is very suitable to investigate SX dynamics on single crystal surfaces while optical spectroscopy requires high surface-to-volume ratios [Kue13].

As discussed in Section 3.1, previous studies on the effect of H-adsorption on the electronic structure at the O- and the mixed-terminated ZnO surfaces revealed a work function decrease and the formation of a charge accumulation layer right below the Fermi level, *i.e.* surface metallization [Oza11, Dei14]. Moreover a very long-lived and stable surface exciton was observed at the H-doped non-polar ZnO surface in a previous 2PPE study [Dei14]. This work tackles the open questions how the work function change and the CAL intensity develop at the O-terminated ZnO surface in the absence of Zn-ions. In addition the SX formation and decay dynamics and how they are influenced by the photo- and H-induced charge carrier density are of central interest.

In the following sections the influence of hydrogen doping on the surface electronic structure and excited electron dynamics of the polar ZnO(000 $\bar{1}$) surface will be presented and discussed. First static 2PPE measurements of the pristine and the H-doped ZnO(000 $\bar{1}$) surface will be presented in Section 5.1.1. The formation and decay dynamics of the SX exciton are investigated with focus on the ultrafast electron relaxation dynamics after excitation above the band gap. Moreover the influence of charge carrier density at the surface (photo- and H-induced) on the relaxation dynamics at the H-doped non-polar surface are investigated.

The pristine O-terminated ZnO surface exhibits upward surface band bending which switches to downward band bending upon H-adsorption accompanied by a significant decrease of the work function. The CB bends even below the Fermi level giving rise to a CAL right below the Fermi level, often referred to as metallic surface state. Direct photoemission measurements reveal the existence of a state inside the band gap which is related to O- or OH-vacancies according to theoretical and

experimental work as discussed before in Section 3.1 [Fin06, Fog15]. In comparison with the non-polar surface the O-terminated surface behaves in some aspects, such as the work function decrease and CAL formation, qualitatively similar towards H-adsorption. This is striking since the two surfaces are very different in their pristine state: The one is non-polar and atomically flat while the other one has a strong surface dipole and shows a triangular terrace structure. Moreover the mixed-terminated surface includes Zn-ions which form ZnH-bonds and thus introduce additional complexity in the H-adsorption behaviour and the surface potential landscape. Despite all these differences these surfaces can be tuned via H-doping such that their electronic surface structure nearly coincides. However, there are distinct differences related to the absence of Zn-ions at the polar surface. The total work function shift of the O-terminated surface is significantly larger than for the non-polar surface and the CAL intensity saturates for high H₂-dosages and does not decrease. Exciting the H-doped ZnO(000 $\bar{1}$) surface above the band gap leads to ultrafast phonon-mediated relaxation of the hot electrons in the CB followed by the formation of a long-lived surface exciton. A comparison with the relaxation dynamics measured at the non-polar surface and a calculated for bulk ZnO demonstrates that the ultrafast relaxation dynamics *via* phonon-scattering are determined by the bulk electronic structure and are thus similar on both surfaces. The emission intensity from the SX decreases for excitation densities close to the Mott density. This exciton characteristic behaviour confirms that the measured species really is a surface exciton. Moreover it will be shown that with increasing total carrier density the relaxation of low energetic hot electrons slows down due to enhanced screening of the interaction with lower lying phonons.

This work has been performed in close collaboration with C. Richter during his master's thesis and in continuous dialogue with J.-C. Deinert.

5.1.1 Hydrogen Induced Metallicity at the O-terminated ZnO Surface

This section treats the effects of hydrogen adsorption on the electronic structure of the ZnO(000 $\bar{1}$) surface. Hydrogen is a hardly inevitable impurity in most fabrication processes and is even present under UHV conditions, therefore its very desirable to understand its influence on the electronic surface structure of the stable ZnO surfaces. The preparation of the single crystal ZnO surface and the quantification of the hydrogen dosage is described in Section 4.3.1.

In order to investigate the surface band bending on the pristine ZnO(000 $\bar{1}$) surface 2PPE measurements of the VBM region have been performed. Figure 5.1 (a) shows an exemplary 2PPE spectrum (green) of the pristine ZnO(000 $\bar{1}$) surface mea-

sured with a photon energy of $h\nu = 4.65$ eV (the pump-probe scheme is sketched in 5.1 (b)). The spectrum is plotted as a function of the final state energy such that the low-energy electron cutoff corresponds to the work function, $\Phi = 5.2$ eV. The spectrum is dominated by the secondary electron background and a broad feature between final state energies of 5.3 - 6.3 eV. The grey line corresponds to an empirical biexponential fit describing the secondary electron background. Subtracting the fit from the spectrum yields the green background-subtracted spectrum displayed as a function of the initial state energy in the inset of Figure 5.1 (a). The initial energy

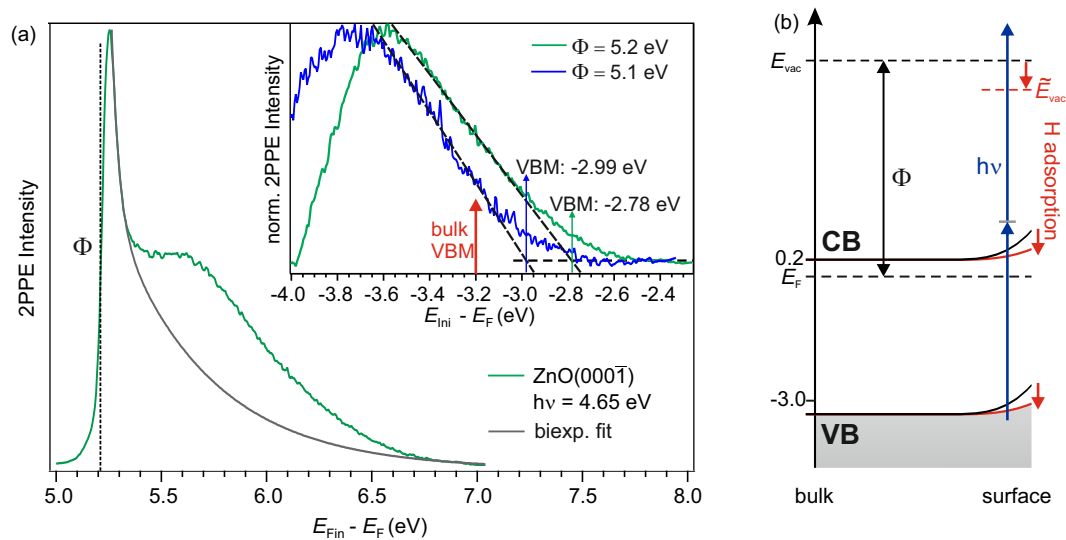


Figure 5.1: (a) Exemplary 2PPE spectrum of the pristine ZnO(000 $\bar{1}$) surface, the low energy electron cutoff corresponds to the work function. The inset shows background subtracted VB spectra taken at different stages of H-uptake exhibiting upward surface band bending. (b) Monochromatic 2PPE process at the pristine (000 $\bar{1}$) surface illustrating H-induced decrease of the work function and surface band bending (red arrows).

axis allows to directly read off the binding energy of the observed feature relative to the Fermi level as described before in Section 4.1.1. The VBM is determined following the established procedure of [Oza11] extrapolating the leading edge of the signal to the baseline, yielding an onset of -2.78 eV for the green spectrum spectrum. This value is higher than the reported value of -3.2 eV for the bulk VBM [Oza11, Dei14]. This can be explained by the strong surface sensitivity of 2PPE making only the upmost ≈ 2 nm of the sample surface accessible and therefore the surface VB is probed here instead of the bulk VB. This upward shift of the surface VBM compared to the bulk value demonstrates upward surface band bending of the investigated surface as illustrated in Figure 5.1 (b).

The inset in Figure 5.1 (a) shows another background-subtracted spectrum (blue) which exhibits the VBM at -2.99 eV and a work function of $\Phi = 5.1$ eV. Compared

to the green spectrum the work function of the blue spectrum is 0.1 eV lower while the VBM is shifted down by 0.21 eV. The two spectra were taken on ZnO surfaces with different degrees of H-doping due to adsorption of residual hydrogen in the UHV chamber. The green spectrum was taken on the pristine surface directly after preparation, while the blue spectrum corresponds to the pristine surface ≈ 1.5 h after the preparation. The residual hydrogen in the UHV chamber is sufficient to dope the ZnO surface with a dosage of ≈ 0.01 L per hour and was used here in order to dope the polar surface with hydrogen. The observed work function and VBM shift illustrate nicely that already small amounts of hydrogen significantly lower the surface potential what leads to a work function decrease and countervails the upward surface band bending as depicted in 5.1 (b). Ozawa et al. observed the VBM on the clean ZnO(000 $\bar{1}$) surface at -2.9 eV, which compares very well with our findings [Oza11].

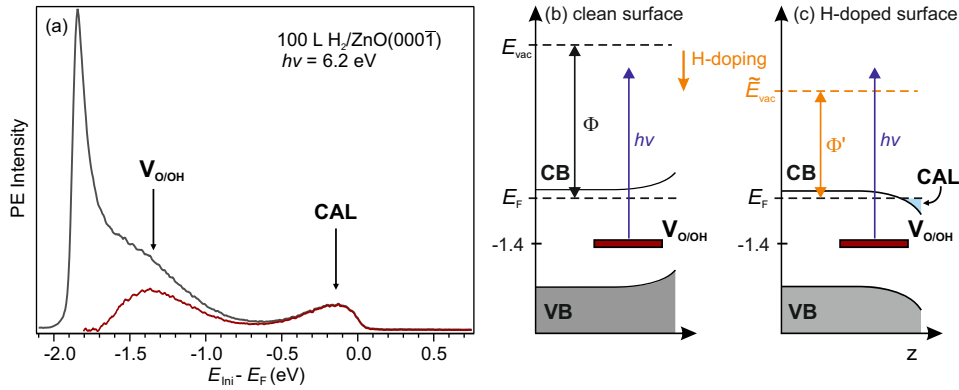


Figure 5.2: (a) Direct photoemission spectrum of 100 L H₂/ZnO(000 $\bar{1}$) showing an additional feature at -1.4 eV which can be related to an O- or OH-defect state, (b) energy level diagram of the pristine and (c) the H-doped ZnO(000 $\bar{1}$) surface illustrating the inverse surface band bending and the work function decrease due to H₂ adsorption which makes it possible to probe the defect state.

For H₂-dosages ≥ 60 L two occupied states have been measured in direct photoemission. Figure 5.2 (a) shows a spectrum (grey) of a 100 L dosage hydrogen on ZnO(000 $\bar{1}$) measured with $h\nu = 6.2$ eV. The corresponding background subtracted spectrum (dark red) clearly exhibits two peaks, one close to E_F (CAL) and one located at -1.4 eV relative to the Fermi level, denoted $V_{O/OH}$. Both lie within the band gap of ZnO, but have very different origin, as will be debated below. As discussed in Section 3.1.1, in gap states are a common feature of ZnO crystals and result from different types of defects. For example O- and OH-vacancies were found to be located 1.8 eV above the VBM, *i.e.* 1.6 eV below the CBM, in a theoretical study [Fin06]. Experimental evidence has been given by luminescence ≈ 1.8 eV below the

CBM [Fog15]. It can, thus, be concluded that the feature at a binding energy of -1.4 eV is due to photoemission from a defect state, either an O- or OH-vacancy. It should be noted that this feature can only be detected in direct photoemission when the work function of the sample is sufficiently low as illustrated in Figures 5.2 (b) and (c): (b) shows an energy level diagram of the pristine surface, where the defect state cannot be probed with 6.2 eV since the work function is too high. In Figure 5.2 (c) the energy level diagram of the H-doped surface is depicted: The work function is reduced significantly, since the OH-bonds formed at the surface reduce the surface dipole, and even lead to downward surface band-bending. Now the work function is low enough so that electrons from the defect state can be photoemitted with a photon energy of 6.2 eV. For the non-polar ($10\bar{1}0$) surface this feature could not be observed clearly, maybe because this surface is less susceptible towards defect states and contains only half the amount of oxygen compared the polar surface, what might decrease the dominance of O-related defect states. The second feature, directly below the Fermi level, is very sensitive to hydrogen adsorption and will be discussed below.

In order to investigate the influence of hydrogen on the electronic surface structure of the polar ZnO surface, the H-dosage has been varied systematically. Figure 5.3 (a) shows a series of direct photoemission spectra taken with $h\nu = 6.2$ eV for different H_2 -dosages. The spectra are plotted as a function of the initial state energy,

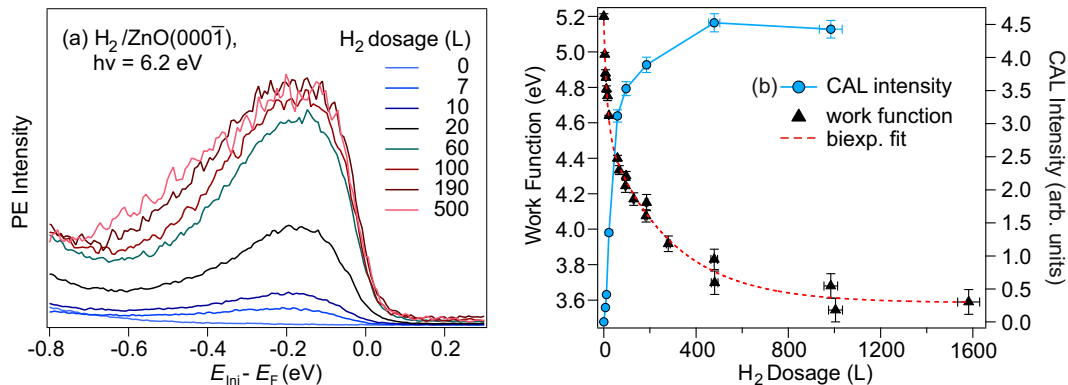


Figure 5.3: (a) Direct photoemission spectra for different hydrogen coverages monitoring the build-up of the CAL at the ZnO(000 $\bar{1}$) surface, (b) CAL intensity increase and work function decrease as function of the H_2 -dosage.

thus the Fermi level corresponds to 0 eV on this axis. Clearly the signal right below the Fermi level emerges with increasing H_2 -dosage with its maximum around -0.2 eV. Analogous to previous studies this signal is assigned to the metallic surface state or CAL [Oza11, Kun03]. Analysis of the CAL intensity as a function of hydrogen dosage shows an increase up to a coverage of ≈ 500 L where it saturates (Figure

5.3 (b)). Concurrent with the CAL intensity increase the work function decreases rapidly during the first 500 L of H₂-dosage and saturates at a work function of 3.6 eV with a maximal decrease of $\Delta\Phi_{\text{max}} = 1.6$ eV. Both effects, the CAL formation and the work function change, can be rationalized by considering the following consequences of H-adsorption:

- (i) H-adsorption leads to the formation of polar hydroxyl-bonds, in which hydrogen has a positive and oxygen a negative partial charge,
- (ii) this decreases the surface dipole
- (iii) thus leading to a work function decrease and downward surface band bending of the CBM below the Fermi level
- (iv) this in turn permits the electrons, donated by the hydrogen, to settle at the CBM which is bent below the Fermi level.

These effects of H-doping on the electronic structure of the O-terminated ZnO surface are qualitatively very similar to the behaviour observed for H-doping of the non-polar ZnO(10 $\bar{1}$ 0) surface. However, as discussed in Section 3.1.2, some distinct differences in the behaviour towards H-adsorption are expected for the polar ZnO surface:

1. A larger work function shift, and thus a stronger decrease of the surface dipole, is expected for the polar surface due to the absence of Zn-ions.
2. The saturation of the work function is expected at higher H₂-dosages due to the higher oxygen density at the polar surface.
3. The CAL intensity is expected to saturate instead of decreasing for higher H-coverages since ZnH-bond formation, which potentially countervail the effects of the OH-bonds, should not occur on the polar surface.

To compare the behaviour of the non-polar ZnO(10 $\bar{1}$ 0) surface with the polar (000 $\bar{1}$) surface towards H-adsorption, the work functions and the CAL intensities of both surfaces are plotted as a function of the H₂-dosage in Figure 5.4 (a). While the work function of the non-polar surface (green triangles, adapted from [Dei15b]) decreases from 4.45 eV to 3.8 eV with a maximal shift of $\Delta\Phi_{\text{max}} = -0.65$ eV the work function of the polar surface (grey triangles) undergoes a reduction from 5.2 - 3.6 eV and thus a total work function shift of $\Delta\Phi_{\text{max}} = -1.6$ eV upon H-adsorption. This yields a 0.95 eV larger total work function shift for the O-terminated ZnO surface with respect to the non-polar surface, confirming thus the first expectation.

Taking a closer look at the evolution of the work functions of the two different surfaces as a function of the H₂-dosage, reveals that the work function of the non-polar surface saturates at H₂-dosages around 500 L. In contrast the work function of the polar ZnO surface saturates at hydrogen dosages of ≈ 1000 L, *i.e.* about the

double amount of hydrogen. This finding can be explained by the different oxygen densities at the two different surfaces: Figure 5.4 (b) shows the surface unit cells of the O-terminated and the mixed-terminated ZnO surface: While the polar surface exhibits 3 O-ions per unit cell, *i.e.* $10.93 \text{ O}^{2-} / \text{nm}^2$, the unit cell of the non-polar surface contains only 1 O-ion, *i.e.* $5.92 \text{ O}^{2-} / \text{nm}^2$. This yields a 1.85 times higher O-density at the polar surface compared to the non-polar surface which is in good agreement with the double amount of hydrogen required for the work function saturation.

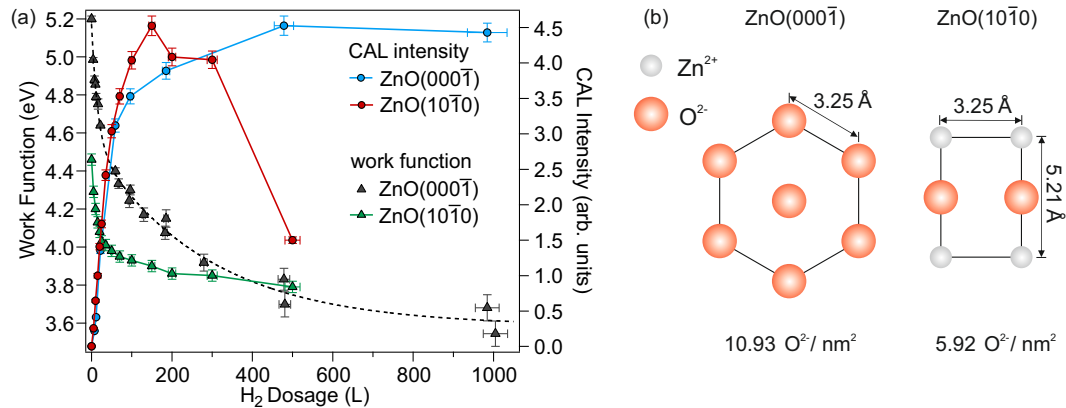


Figure 5.4: (a) Comparison between the polar and the non-polar ZnO surface regarding H-induced work function change and CAL intensity, ZnO(1010) data adopted from [Dei14]. (b) Surface unit cells of the two ZnO surfaces illustrating the different O-ion densities at the respective surfaces.

A striking observation is that both work functions decrease rapidly within the first 30 - 50 L before the work function reduction slows down. In the case of the non-polar surface this behaviour can be explained by the formation of ZnH-bonds setting in when the formation of OH-bonds becomes unfavourable, resulting in a complex mixture at the surface, as discussed in Section 3.1.2. OH-bond formation was found to become less favourable at O-ions located next to already H-terminated oxygen atoms [Dei15b]. Due to the absence of Zn-ions at the polar ZnO surface a linear work function decrease might be expected. But the non-linear behaviour, analogue to the non-polar surface, indicates that a similar complex adsorption mechanism may occur at the polar surface. Most likely OH-bond formation becomes as well less favourable at O-ions adjacent to already H-terminated O-atoms which might reduce the sticking coefficient of the H-atoms. A reduction of the sticking coefficient is expected to slow down the adsorption process and thus the work function decrease.

Now I want to focus on the development of the CAL intensity as function of hydrogen adsorption. In the case of the non-polar surface the CAL intensity decreases for H₂-dosages ≥ 150 L and was explained by the formation of ZnH-bonds which

compensate the effects of the OH-bonds reducing the downward band bending of the CB, thus leading to a reduction of the CAL intensity, as discussed in Section 3.1.2 [Dei15b]. In contrast the CAL intensity at the O-terminated surface increases up to a H₂-dosage of 500 L and stays constant for higher dosages. The saturation of the CAL intensity indicates that the equilibrium coverage under the given experimental conditions, *i.e.* hydrogen background pressure and temperature, is reached at H₂-dosage around 500 L. The observation of a constant CAL intensity in the absence of Zn-ions clearly proves that the reduction of CAL intensity at the non-polar surface can be ascribed to the formation of Zn-H bonds.

In conclusion the polar ZnO(000 $\bar{1}$) surface behaves in some aspects similar to the non-polar ZnO(10 $\bar{1}$ 0) surface upon hydrogen adsorption, despite the absence of Zn-ions at the polar ZnO. The work function decreases from 5.2 - 3.6 eV due to the formation of OH-bonds at the surface which compensate the polarity of the surface thus reducing the surface dipole. The chemisorbed hydrogen donates electrons to the CB leading to the formation of a charge accumulation layer and bending of CB below the Fermi level such that metallic behaviour occurs. For sufficiently low work functions an additional state inside the band gap is detectable in direct photoemission. This state is located 1.6 eV below the CBM and is assigned to a defect state, most likely due to O- or OH-vacancies.

The expected differences in the behaviour of the polar and the non-polar ZnO surface towards H-adsorption proved to be true: 1) The total work function shift is larger at the polar surface, 2) the saturation of the work function is reached at \approx 2 times higher H₂-dosages than for the non-polar surface, in accordance to the 1.85 times higher oxygen density on the polar surface. 3) The CAL intensity was found to saturate for hydrogen dosages \geq 500 L and not to decrease as in the case of the non-polar surface, demonstrating that the formation of ZnH-bonds is responsible for the decrease of CAL intensity at the non-polar surface. For dosages between \approx 100 - 300 L however, H₂-doping even opens up the possibility to tune these two surfaces such that they exhibit both nearly the same electronic surface structure: At a coverage of \approx 300 L both surfaces have similar work functions and exhibit comparable CAL intensities.

In the following section the surface exciton formation and decay dynamics at the H-doped ZnO(000 $\bar{1}$) surface will be discussed.

5.1.2 Surface Exciton Formation and Decay Dynamics at the H-doped Polar ZnO Surface

In this section it is shown that it is possible to generate surface excitons at the polar ZnO surface. The dynamics of SX formation will be discussed with regard to the ultrafast relaxation dynamics of the hot electrons and the influence of the photo- and H-induced carrier density. Moreover the obtained time constants will be compared with the results of a theoretical study and the findings at non-polar surface.

In a time-resolved 2PPE experiment a transient electron population in an intermediate state is generated by photoexcitation with a first laser pulse and is probed after a time delay by a second pulse as described in Section 4.5. Figure 5.5 displays static 2PPE spectra of 100 L H₂/ZnO(000 $\bar{1}$) as a function of the intermediate state energy, which were taken at different time delays with 3.8 and 4.65 eV. As both photon energies can excite the sample above the band gap and also photoemit excited electrons, positive delays describe here excitation with a pump photon energy of $h\nu_{\text{pump}} = 3.8$ eV and probing with $h\nu_{\text{probe}} = 4.65$ eV, for negative delays the pump-probe scheme works vice versa. The blue spectrum was taken at a time delay of -30 ps under equilibrium conditions and is therefore used as background spectrum. The grey spectrum was recorded at a time delay of +50 fs and contains the pump-induced signal, which is presented by the grey coloured area. Subtracting the blue background spectrum from the grey spectrum yields the red difference spectrum, showing only the pump-induced signal. The signal below E_F (0 eV) originates from the CAL.

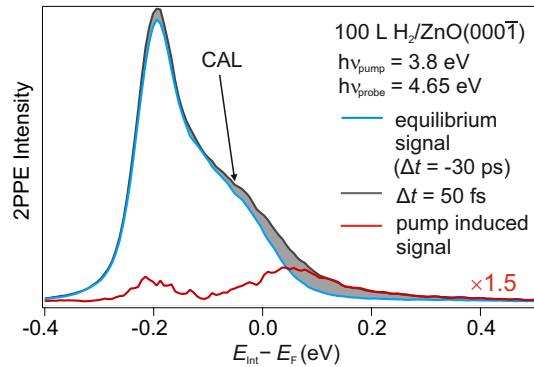


Figure 5.5: 2PPE spectra of the H-doped polar ZnO surface, the signal below E_F (0 eV) originates from the CAL. The pump-induced signal (grey coloured area, red spectrum) is the difference between the equilibrium spectrum (blue) and the spectrum after above gap excitation (grey).

Figure 5.6 (a) shows an exemplary time-resolved 2PPE spectrum of a 100 L H₂-dosage on ZnO(000 $\bar{1}$) measured with 3.8 eV and 4.65 eV. The photoemission intensity is plotted in false colours as a function of the intermediate state energy (left) and the pump-probe delay (bottom). In order to obtain exclusively the pump-induced signal the background spectrum taken at a negative delay of -30 ps, shown in Figure 5.5, was subtracted from the depicted spectrum.

The background subtracted signal exhibits a fast reduction of photoemission intensity at energies between $\approx 0.65 - 0.2$ eV which slows down for lower energies. A

5.1 H-induced Metallicity and Excited State Dynamics at the O-terminated ZnO Surface

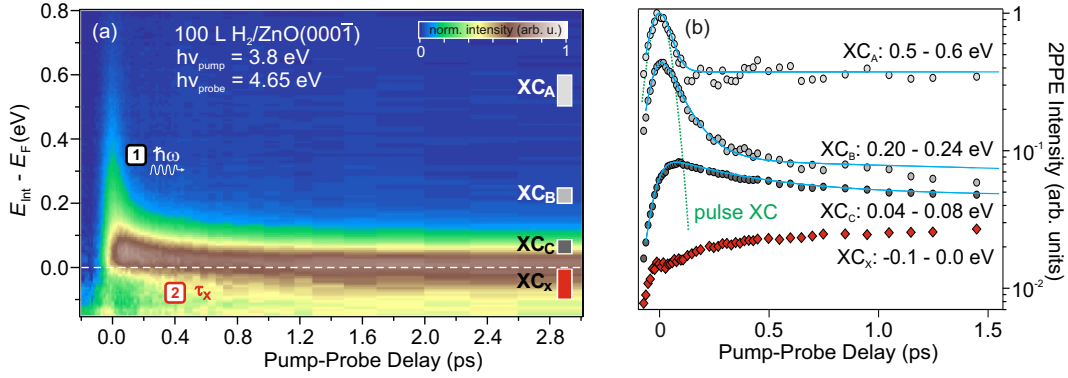


Figure 5.6: (a) Time-resolved 2PPE spectrum of 100 L $\text{H}_2/\text{ZnO}(000\bar{1})$ showing fast electron relaxation dynamics for energies above ≈ 0.1 eV and pump-induced electron density build-up below E_{F} ($E_{\text{int}} = 0$ eV). (b) XC traces for energies above E_{F} , (grey dots) show (1) ultrafast relaxation of the above band gap excited electrons via phonon scattering and formation of a long-lived state. The XC below E_{F} (red diamonds) shows the build up of additional photoelectron intensity (2) which is related to the formation of a surface exciton.

long-lived state is formed just at the Fermi level which shifts even below the Fermi level for longer time delays. This behaviour is very similar to the dynamics observed by Deinert et al. at the H-doped non-polar ZnO surface, who assigned this long-lived signal to a surface excitonic state [Dei14]. Therefore I will refer to this state as SX in the following and will discuss it in detail below.

To obtain quantitative insights into the observed excited state dynamics the time-resolved spectrum was integrated over several energetic ranges as indicated by the grey and red boxes yielding the corresponding XC traces shown in Figure 5.6 (b). The XC traces are plotted logarithmically as a function of the pump-probe delay and are offset for clarity. The green dashed line illustrates the XC of the laser pulses which have an average duration of 70 fs. The cross-correlation trace A (0.5 - 0.6 eV) shows nearly exclusively the fast decay, although all XC traces possess a long-lived component. XC B was obtained by integration between intermediate state energies of 0.20 - 0.24 eV and already clearly exhibits the slowing down of the fast component. This behaviour becomes more intense for lower energies, as demonstrated by XC C (0.04 - 0.08 eV), which indicates as well the relaxation into the long-lived state. Integrating the time-resolved spectrum below the Fermi level yields the red XC trace which differs significantly from the ones obtained by integration at energies above E_{F} : For positive delays the intensity increases with τ_x until it saturates at time delays around 1 ps. Assuming that the long-lived state originates from the surface exciton this rise in intensity corresponds to the build-up of the excitonic population below E_{F} on a timescale of a few hundred fs. The dynamics at negative delays corresponds here to the hot electron dynamics pumped and probed by the

inverted pump-probe process.

In order to fit the grey coloured XC traces the following considerations were taken into account:

The 2PPE intensity $I^{2\text{PPE}}$ as a function of the pump-probe delay is yielded by integration

$$I^{2\text{PPE}}(\Delta t) \propto \int dt F_{\text{XC}}(t - \Delta t) R(t) \quad (5.51)$$

where F_{XC} denotes the cross correlation of the two laser pulses, described by sech^2 pulse envelopes (indicated by the green dashed line in Figure 5.6 (b)), and $R(t)$ the response function of the system. The response function $R(t)$ for positive delays consists of a phenomenological biexponential decay describing the decay of the hot electron population in the CB and the lifetime of the long-lived SX

$$R(t \geq 0) = A e^{-\frac{t}{\tau_1}} + B e^{-\frac{t}{\tau_2}} \quad (5.52)$$

For negative delays the response function is described by the single exponential decay of the hot electrons excited by the reversed pump-probe scheme

$$R(t < 0) = C e^{\frac{t}{\tau_3}} \quad (5.53)$$

The biexponential fit yields a fast time constant τ_1 and a slow time constant τ_2 . The fast time constant can be related to the ultrafast relaxation of the above band gap excited electrons.

As discussed in Section 3.1.3 hot electrons in polar semiconductors such as ZnO relax mainly *via* two mechanisms, electron-electron scattering and electron-phonon scattering which take place on different time scales. Electron-electron scattering can be excluded due to the low electron density in the CB, resulting from the rather low excitation density ($2.86 \times 10^{18} \text{ cm}^{-3}$) employed in this experiment, thus electron-phonon scattering is very efficient. This finding is in good agreement with the strong coupling of electrons with LO phonons in ZnO, well known from literature, both theoretically and experimentally as discussed in Section 3.1.3 [Tis08, Dei14, Zhu10].

The slow time constant τ_2 can be attributed to the lifetime of the long-lived surface exciton, which shows residual intensity even at higher energies and does not decay within the measured 300 ps, thus possessing a lifetime of at least several hundred ps.

In order to analyse the ultrafast relaxation of the photoexcited electrons quantitatively, the fast time constant τ_1 (red dots) obtained from the biexponential fit is plotted as a function of the intermediate state energy in Figure 5.7 (a) and is compared to the values calculated by Zhukov *et al.* [Zhu10]. The dynamics of the

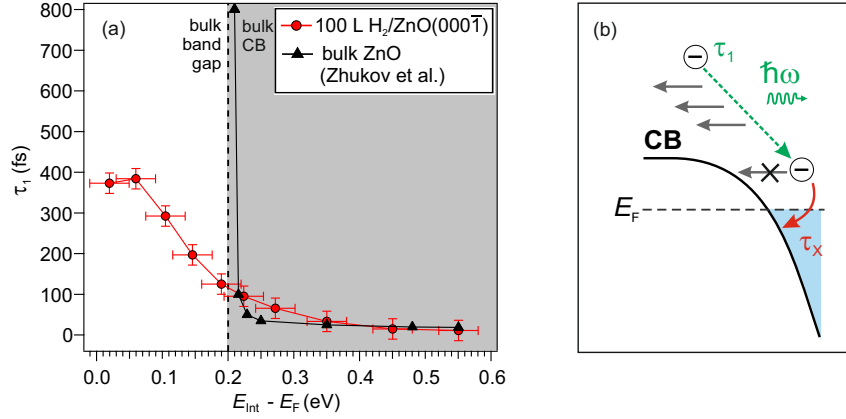


Figure 5.7: a) Comparison of the measured fast time constants (red) with calculated values (black) from ref. [Zhu10] plotted as a function of the intermediate state energy. b) Schematic illustration of the energy-dependent evolution of the relaxation times (green dashed line) prior to SX formation.

hot electrons in the CB is extremely fast (10 - 95 fs) at energies ≥ 0.2 eV, *i.e.* for excitation above the bulk CBM, and slows significantly down towards lower energies. Comparable time constants were observed before by Tisdale *et al.* and Deinert *et al.* for above gap excitation of the mixed-terminated ZnO surface who explained the slowing down of the dynamics for lower energies by the reduction of the phonon phase space [Tis08, Dei14]. Comparison to the calculated lifetimes show that the experimentally derived data compares fairly well in the high energy region down to ≈ 0.22 eV while they diverge for lower energies. The calculated values increase rapidly up to ≈ 1 ps for energies close to the bulk CBM while the experimentally derived time constant slows down to ≈ 400 fs close to the Fermi level. This different behaviour is due to the different preconditions of calculation and experiment: The calculation was performed for bulk ZnO while the experiment was conducted on the H-doped polar ZnO surface with a highly surface sensitive method. In the case of bulk ZnO the electrons at the CBM have no excess energy left to scatter with phonons, leading thus to an increase of their lifetime. In our experiment the situation is different since the surface CBM is not at 0.2 eV but is bent below the Fermi level, as illustrated in Figure 5.7 (b). Therefore the phonon-mediated relaxation of the excited electrons is still possible at lower energies, which explains the slower increase of the time constant down to the Fermi level.

The formation of an intermediate electron population below the Fermi level is an unusual behaviour since usually the electronic levels are filled up to the Fermi level such that no additional pump induced density of states (DOS) can be gener-

ated in this region. To find out whether the long-lived state can be really related to the surface exciton and not to other common effects, as discussed in Section 2.2.1, like small polaron formation or surface band bending effects due to surface photovoltage a test experiment was performed. Small polarons can be excluded since theory predicts them to be unstable in ZnO in accordance with time-resolved THz- and IR-studies who revealed no evidence of small polaron formation [Hen07, Sez15]. In the test experiment the pump induced signal around and below

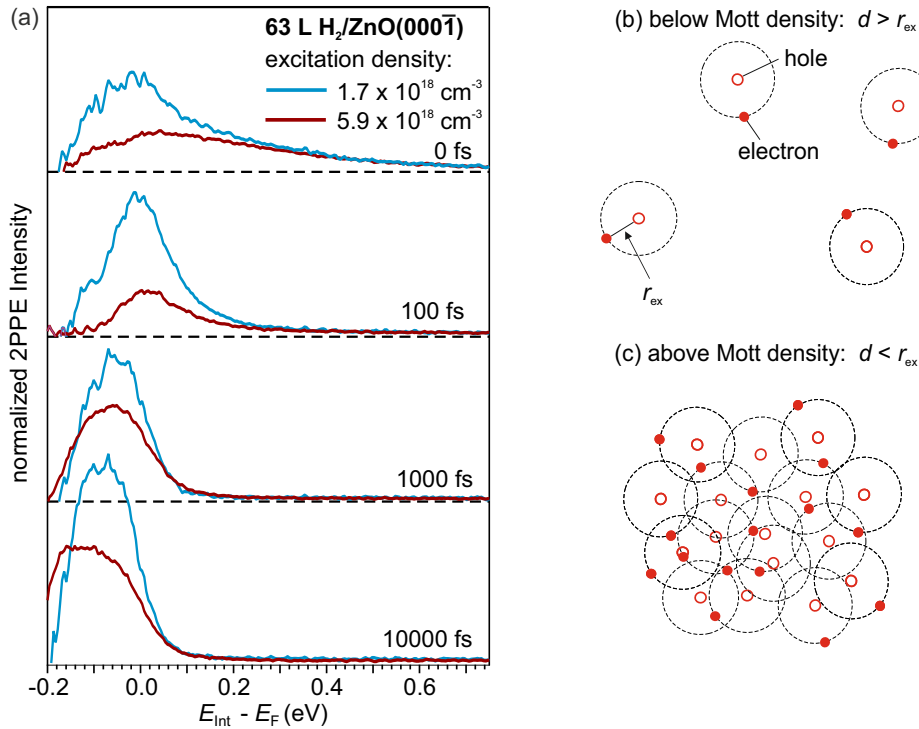


Figure 5.8: (a) Emission signal of the SX for different excitation densities normalized to the pump fluence. The signal intensity decreases for higher excitation densities due to the formation of an electron-hole plasma (c) which screens the attractive Coulomb interaction between electrons and holes thus reducing the exciton formation probability.

the Fermi level is measured as a function of the excitation density. As discussed in Section 2.2.1 surface photovoltage effects are expected to become stronger for higher excitation densities, thus leading to an increase of the signal intensity. In contrast the formation probability of an excitonic species decreases for excitation densities close to the Mott density, resulting thus in a reduction of the observed signal intensity. For excitation densities below the Mott density the distance d between the excitons is larger than the exciton Bohr radius r_{ex} , as illustrated in Figure 5.8 (b). For high excitation densities the distance d between the excitons becomes smaller than r_{ex} (Figure 5.8 (c)) what leads to a screening of the attrac-

tive Coulomb interaction between electrons and holes thus reducing the exciton formation probability. In the test experiment the excitation density is varied by changing the fluence of the pump pulse. The obtained spectra clearly demonstrate the characteristic behaviour of excitons: Figure 5.8 shows the photoemission signal attributed to the surface exciton for an excitation density in the lower Mott density region ($1.7 \times 10^{18} \text{ cm}^{-3}$, blue) and for a higher excitation density ($5.9 \times 10^{18} \text{ cm}^{-3}$, purple) plotted as a function of the intermediate state energy. The signal intensity is normalized to the excitation density and is shown for different time delays.

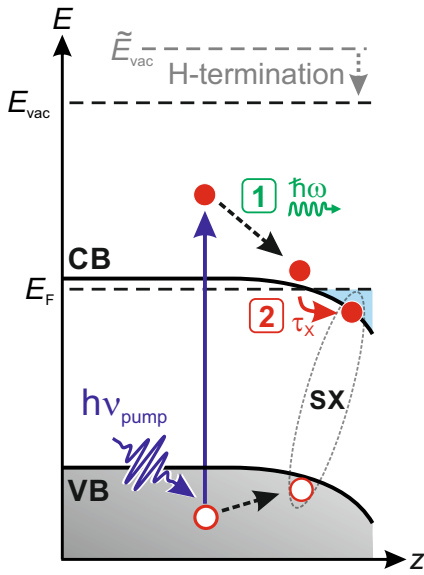


Figure 5.9: Illustration of the relevant processes taking place after photoexcitation of the H-doped polar ZnO surface, modified from [Dei14]. $h\nu_{\text{pump}}$ photoexcites electrons from the VB above the CBM which relax (1) via electron-phonon scattering and (2) surface exciton formation.

The signal derived from the low excitation density (blue) is more intense than the one obtained from the higher excitation density (purple). This demonstrates explicitly that the formation probability of the excitons is reduced by the formation of an electron-hole plasma which screens the attractive Coulomb interaction between electron and hole. Moreover this finding is in accordance with the results of Deinert et al. for the H-doped non-polar ZnO surface [Dei14].

Figure 5.9 summarizes the relevant electronic processes observed after photoexciting the H-doped polar ZnO surface above the band gap. The observed processes and dynamics are comparable to the ones found for the H-doped non-polar ZnO surface: Electrons are photoexcited from the VB above the CBM which relax (1) via electron-phonon scattering and (2) surface exciton formation.

In order to quantitatively compare the ultrafast relaxation dynamics of the excited elec-

trons at the H-doped polar surface with the dynamics observed at the non-polar surface, the time constants obtained for a dosage of 100 L H_2 on both surfaces are plotted as a function of the intermediate state energy in Figure 5.10. This coverage was chosen, as outlined in Section 5.1.1, because at a H_2 -dosage of 100 L the CAL intensity is comparable for both surfaces. The red data points correspond to the time constants obtained for the H-doped polar surface and the green ones to the time constants obtained for the non-polar surface. The results compare well, although for a H_2 -dosage of 100 L already ZnH-bond formation has set

in on the non-polar surface and despite the different work functions of the investigated samples the electron dynamics are in good accordance. This observation leads to the conclusion that the ultrafast relaxation of the hot electrons in the CB is not, or very weakly, affected by the surface potential. This can be explained by the relaxation mechanism of the electrons: they couple via Fröhlich interaction with LO phonons, *i.e.* vibrations of the lattice in which the Zn- and O-ions move in opposite directions. This motion of the ions induces a stronger electric field compared to the compensating polarization of the surrounding electrons, thus leading to a long range interaction between the excited electrons and LO phonons [Tis08].

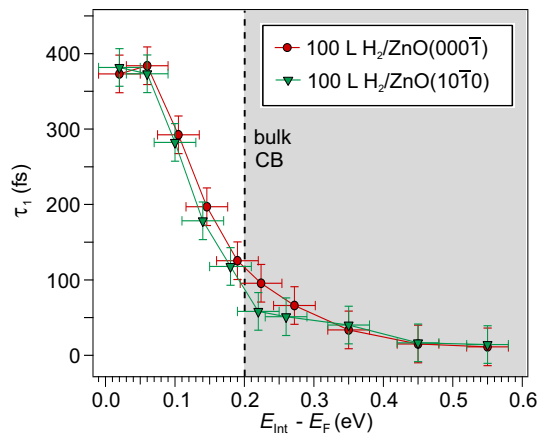


Figure 5.10: Comparison of the fast time constant τ_1 of 100 L H_2 on the $(000\bar{1})$ and the $(10\bar{1}0)$ surfaces.

To evaluate the influence of the total charge carrier density (photo- and H-induced) on the relaxation dynamics the fast time constants, derived from measurements with varying excitation densities and H-coverages on the non-polar ZnO surface, are compared in Figure 5.11. The total charge carrier density is calculated by summing up the photoinduced carrier density, *i.e.* the excitation density, and the H-induced carrier density in the CAL. The latter is estimated according to the maximal surface charge density of 10^{13} cm^{-2} [Oza11], which is related to the CAL intensity maximum at a H_2 -dosage of 150 L, and a CAL thickness of 1 nm. This yields for a H_2 -dosage of 150 L an electron density of 10^{20} cm^{-3} in the CAL. Figure 5.11 (a) displays the fast time constants as a function of intermediate state energy of two data sets recorded with a pump photon energy of 3.8 eV for different total carrier densities in the upper Mott regime. For energies above 0.2 eV the time constants diverge only within the error such that no conclusion can be drawn. For lower energies, however, the time constants measured for a total carrier density of $6.8 \times 10^{19} \text{ cm}^{-3}$ (green), which is above the critical carrier density of 10^{19} cm^{-3} [Tis08], slow down compared to the time constants obtained for the lower carrier density (red). This slowing down of the relaxation dynamics demonstrates that the scattering of low energetic hot electrons with acoustic phonons is screened by the enhanced carrier density. In Figure 5.11 (b) the time constants derived from 2PPE measurements with a pump photon energy of 3.8 eV are compared to time constants adopted from Deinert *et al.* [Dei15b] which were gained using a pump photon energy of 4.2 eV. These time

5.1 H-induced Metallicity and Excited State Dynamics at the O-terminated ZnO Surface

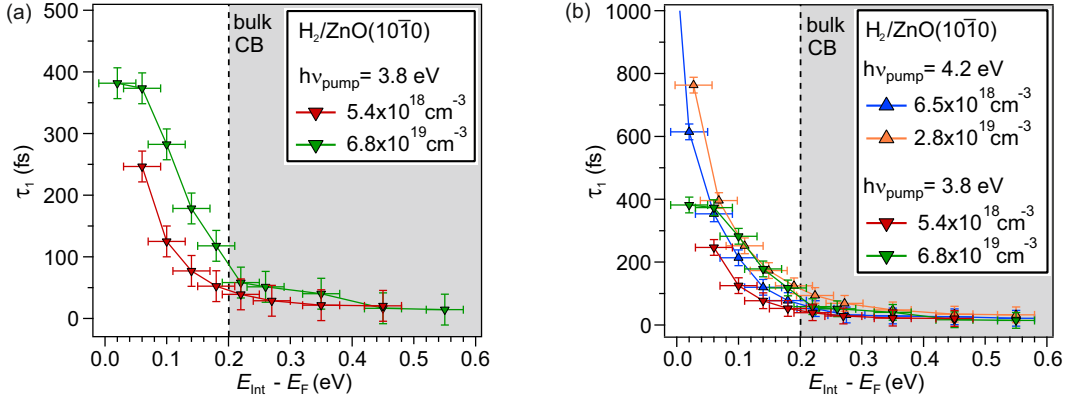


Figure 5.11: Comparison between the time constants for different total carrier densities and (a) same and (b) different pump photon energies

constants exhibit the same tendency, that the dynamics slow down at energies below 0.2 eV with increasing carrier density. But the photon energy seems to have an effect as well: The time constants for carrier densities of $2.8 \times 10^{19} \text{ cm}^{-3}$ (orange) and $6.8 \times 10^{19} \text{ cm}^{-3}$ (green) coincide very well although the latter is expected to be slower due to the higher carrier density. Apparently the relaxation dynamics slow down for higher pump photon energies, indicating that the excess energy of the hot electrons affects the relaxation dynamics at lower energies. This may be explained by the following consideration: With a higher pump photon energy hot electrons with higher excess energies are generated. Due to the higher excess energies these hot electrons need more scattering events with LO phonons to reach the CBM. The hot electron population with low excess energies at the CBM is in turn emptied by scattering with acoustic phonons on a slower time scale than the scattering with LO phonons. When higher pump photon energies are used the population at the CBM is refilled for a longer time with more electrons from higher states, thus leading to a slowing down of the relaxation dynamics. In addition, this observation agrees well with results from Zhukov *et al.* who found that the higher the excess energy of the hot electrons, the longer it takes them to reach the CBM [Zhu10].

Summary

In the following the results presented and discussed in this chapter are summarized. The pristine O-terminated ZnO-surface exhibits upward surface band bending. H-adsorption reduces the surface potential and thus the work function decreases and the upward surface band bending is reversed, such that the CBM shifts below the Fermi level. The chemisorbed hydrogen donates electrons to the CB leading to the formation of a charge accumulation layer right below the Fermi level. For sufficiently low work functions an additional state inside the band gap is detectable in direct

photoemission. This state is located 1.6 eV below the CBM and is assigned to a defect state, most likely due to O- or OH-vacancies.

The polar ZnO surface behaves towards H-doping in some aspects qualitatively very similar to the non-polar surface, despite the absence of Zn-ions and the lower stability. For example, both surfaces exhibit a reduction of the work function and the formation of a CAL due to band bending below the Fermi level. But quantitatively there are distinct differences, such as the significantly higher total work function decrease at the polar ZnO surface and the saturation of the CAL intensity for H₂-dosages above 500 L. This proves that the formation of ZnH-bonds at the non-polar surface is responsible for the decrease of CAL intensity for H₂-dosages higher than 150 L.

The investigation of the hot electron relaxation and SX formation and decay dynamics on the H-doped polar ZnO surface reveals ultrafast relaxation of the above band gap (3.4 eV) excited electrons slowing down for lower energies, followed by the formation of a long-lived surface excitonic feature. Measurements under variation of the excitation density clearly demonstrate the exciton characteristic Mott physics: the observed emission signal decreases with increasing excitation density, which leads to a screening of the attractive Coulomb interaction between electron and hole reducing thus the formation probability of excitons. The ultrafast relaxation times are in good accordance with the calculated values by Zhukov et al. as well as with experimentally derived results for the non-polar ZnO surface [Zhu10, Tis08, Dei14]. A comparison with the findings obtained for the H-doped non-polar surface, studied before by Deinert et al., shows astonishing coincidence in consideration of the different surface electronic structure and composition and morphology. This behaviour is explained by the strong Fröhlich-type interaction of electrons and phonons prevailing over other scattering mechanisms, such as electron-electron scattering. Moreover it was demonstrated that the relaxation dynamics of the low energetic hot electrons slows down for high charge carrier densities screening the scattering with lower lying phonons.

5.2 Exciton Formation and Decay Dynamics in SP6 Films on ZnO

SP6 is a promising material for applications in OLEDs and organic solid state lasers due to its strong luminescence [Sch04b, Sch05]. The Also the SP6/ZnO interface is attractive for the study of charge transfer from molecular excitons to the conduction band of ZnO, as demonstrated by Blumstengel *et al.* [Blu08, Blu09].

In the following sections the results of our time-resolved 2PPE study of SP6 films on the non-polar ZnO(10 $\bar{1}$ 0) surface are presented and discussed. The ultrafast exciton formation and decay dynamics are treated in Section 5.2.1. The TR-2PPE measurements reveal an ultrafast decay on a time scale of 300 fs directly after photoexcitation most likely due to polarization effects resulting from exciton formation. In addition two slower decay times, in the range of several ps and hundreds of ps, are observed and related to internal vibrational relaxation within the excited state and the decay of the population in the excited state. The time scales of the two slow processes agree surprisingly well with the values resulting from the analysis of the transient transmission traces [Fog15]. In order to find an explanation why photoemission and optical spectroscopy yield here the same excited state dynamics a time-dependent diffusion model was developed and described in Section 5.2.1. It could be shown that the charge separation at the ZnO interface has no strong influence on the dynamics in a 21 nm thick SP6 film, although optical spectroscopy probed as well bulk contributions.

Furthermore an electron emission signal was observed which exhibits no dependence on neither the photon energy nor the pulse duration. This signal could be revealed as emission from the long-lived dark state indicated by the excited state transmission data as described in Section 5.2.2. We were able to show with a set of specialized time-resolved experiments that electron emission results here from excitation energy transfer between two long-lived, most likely triplet, states in a triplet-triplet annihilation process. In addition our 2PPE results provided the possibility to calculate the energetic positions of the ground state S_0 , the first excited state S_1 and the triplet state T_1 .

5.2.1 Ultrafast Dynamics of Excited States in SP6 Films

In order to investigate the excited state dynamics and the electronic structure in SP6 films on ZnO(10 $\bar{1}$ 0), time-resolved (TR) 2PPE measurements have been performed. Figure 5.12 (b) shows a background subtracted time-resolved 2PPE spectrum of a 21 nm thick SP6 film on ZnO(10 $\bar{1}$ 0) which was measured with a resonant pump photon energy of $h\nu_{\text{pump}} = 3.86$ eV and probed as well resonantly with $h\nu_{\text{probe}} = 1.93$ eV, as known from the excited states transmission data (presented in Section 3.2). The 2PPE intensity is plotted as a function of the kinetic energy (E_{kin}) and the pump-probe delay. The 2PPE intensity is represented by a false colour code, where dark blue corresponds to zero intensity and white to maximal intensity. The maximum photoemission intensity is at the low-energy cutoff and decreases towards higher energies. This intense 2PPE signal at the low-energy cutoff seems to exhibit the slowest dynamics while for higher energies the dynamics seem to decrease.

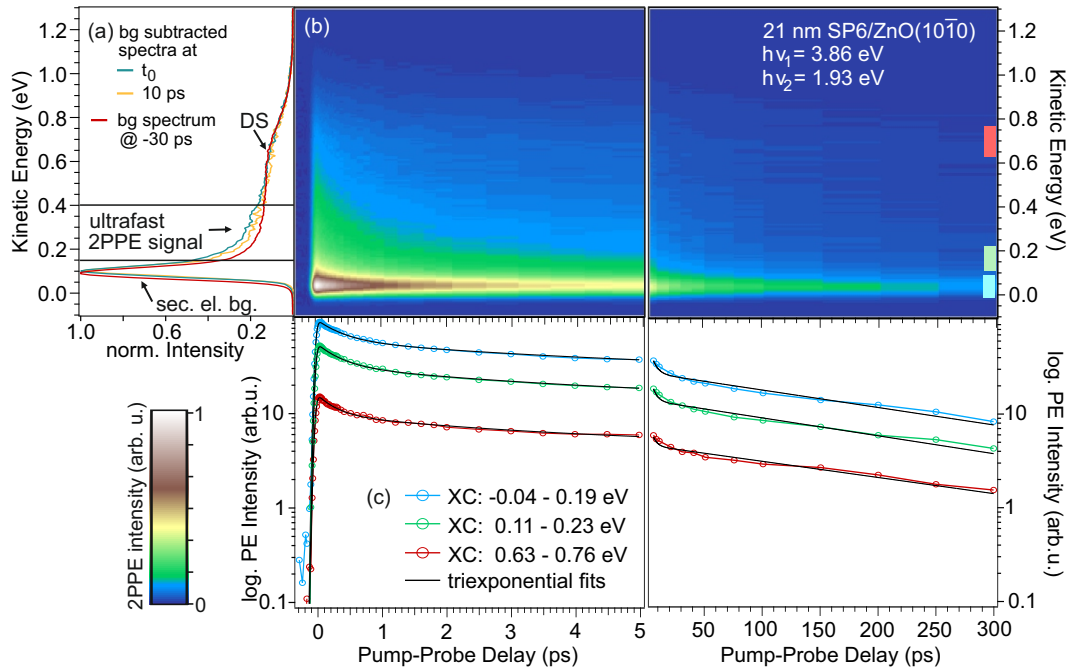


Figure 5.12: (a) Comparison of 2PPE spectra for different time delays. The intensities are normalized to point out the 2PPE signal showing ultrafast dynamics, since the spectra are dominated by long-lived background signals: The secondary electron background (sec. el. bg.) and a signal labeled DS which will be discussed below. (Note that the photoemission intensity of the background signals is amplified for the applied pump probe scheme and is therefore still visible in the background subtracted spectra.) (b) Background subtracted TR-2PPE spectrum of 21 nm SP6/ZnO(10 $\bar{1}$ 0): the 2PPE intensity is plotted as a function of the kinetic energy and the pump-probe delay. (c) Cross-correlation traces obtained from integrating the TR-spectrum over the energetic ranges marked by the coloured boxes in (b), the black lines correspond to triexponential fits.

To take a closer look at the spectral signature vertical cuts at time delays of 0 ps (blue) and 10 ps (yellow) are plotted as a function of the kinetic energy (Figure 5.12 (a)). The spectra are compared to the background spectrum taken at -30 ps with the reversed pump-probe scheme (*i.e.* 1.93 eV pumped and 3.86 eV probed) which has been subtracted as well from the data shown in Figure 5.12 (b). All spectra are normalized to the maximum intensity of the secondary electron background in order to emphasize the signal which exhibits ultrafast dynamics. (Note that the photoemission intensity of the DS signal is amplified for the applied pump probe scheme ($h\nu_{\text{pump}} = 3.86$ eV, $h\nu_{\text{probe}} = 1.93$ eV) and is thus still present after background subtraction.) The spectra exhibit an intense photoemission intensity at the low-energy cutoff, after a rapid intensity decrease up to $E_{\text{kin}} \approx 0.2$ eV the spectrum is dominated by a broad photoemission signal up to $E_{\text{kin}} \approx 1$ eV. The spectra are divided into three parts according to the observed features. (i) 0 - 0.15 eV: The most intense photoemission signal at the low-energy cutoff is related to the secondary electron background (sec. el. bg.). (ii) The signal between 0.15 eV and 0.4 eV is labeled ultrafast 2PPE signal and is subject of the following analysis and discussion. (iii) The broad feature up to 1 eV, labeled DS, will be further investigated in the next section.

In order to gain deeper insight into the dynamics the time-resolved spectrum was integrated over different energetic ranges, e.g. in the red, green and blue marked energy windows, yielding the XC-traces plotted on a logarithmic intensity scale as a function of the pump-probe delay in Figure 5.12 (c). The intensity of the XC-traces rises on an ultrafast timescale and decreases on a timescale of a few hundred ps. The XC traces can be described with triexponential decays convolved with Gaussian shape pulse envelopes, shown by the black lines in Figure 5.12 (c).

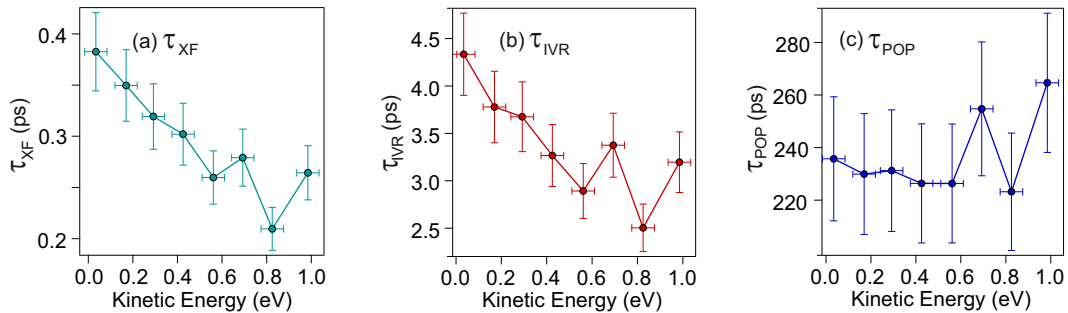


Figure 5.13: Time constants yielded by triexponential fitting of 8 XC-traces obtained from the TR-2PPE spectrum of 21 nm SP6/ZnO shown in Figure 5.12 (b). The time constants are plotted as a function of the kinetic energy and range from a time scale of several hundred fs to several hundred ps.

To analyse the dynamics quantitatively as a function of the kinetic energy, the XC-traces yielded by integrating the TR-spectrum over 8 contiguous energy windows were fitted with the triexponential fit function. The three time constants obtained from the fits, τ_{XF} , τ_{IVR} and τ_{POP} , are plotted as a function of the kinetic energy in Figure 5.13. τ_{XF} is with several hundred femtoseconds (fs) the fastest time constant. The next slower time constant, τ_{IVR} , is in the range of a few picoseconds (ps) while the slowest one, τ_{POP} , is on a time scale of a few hundred ps. While τ_{XF} and τ_{IVR} get faster for higher energies, τ_{POP} stays almost constant up to an energy of 0.6 eV and increases for higher energies. All three time constants exhibit a dip at a kinetic energy of 0.8 eV.

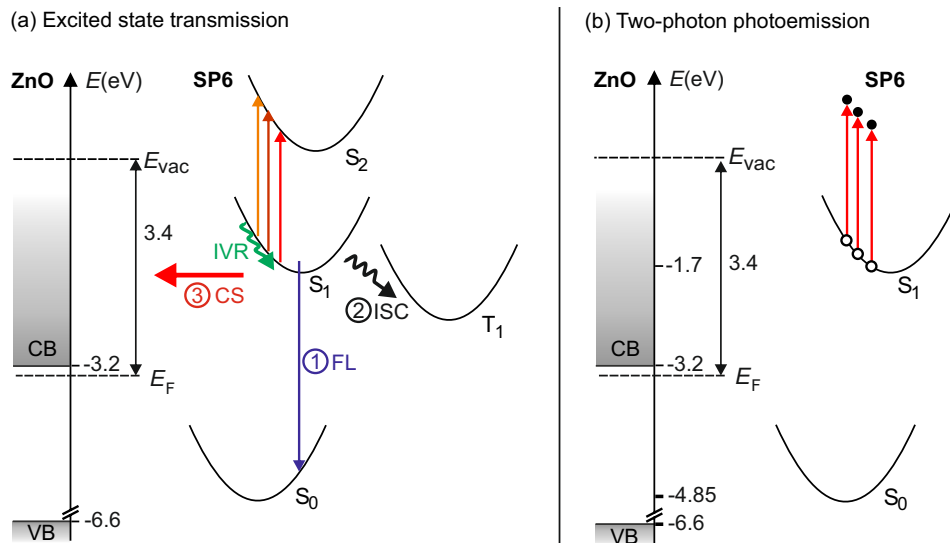


Figure 5.14: (a) Excited state transmission probes resonances between excited states: The differently coloured arrows illustrate photons with different photon energies. In addition the electronic processes observed after photoexcitation are illustrated. (b) During the probing step in 2PPE the population in the excited state is excited above the vacuum level by the probe pulse (red arrows) yielding thus absolute energies.

In order to compare the 2PPE results with the time constants obtained from excited state transmission, presented in Section 3.2, the differences of these two methods have to be pointed out. Excited state transmission probes resonances between excited states as sketched in Figure 5.14 (a) and underlies thus the dipole selection rules for optical transitions. The time constants obtained from excited state transmission depend on the probe photon energy. In contrast, in a photoemission experiment electrons are emitted and thus the second transition does not have to match a molecular resonance, as discussed before in Section 4.1.3. In the sim-

plest picture, 2PPE vertically projects the electronic structure and probes thus the absolute energies of the excited electrons as illustrated in Figure 5.14 (b). The time constants resulting from a time-resolved 2PPE experiment depend on the kinetic energy of the photoemitted electrons.

In order to compare the results yielded by the two different methods the same probe photon energies have to be used. Here a probe photon energy of 1.93 eV was used in the 2PPE measurements and thus the results can be compared with the time constants obtained from excited state transmission at 1.94 eV. The excited state transmission data revealed for a probe photon energy of 1.94 eV two time constants: $\tau_{\text{IVR}} \approx 4$ ps and $\tau_{\text{POP}} \approx 200$ ps [Fog15, Fog14]. These time constants were related to the following processes, as illustrated in Figure 5.14 (a) and discussed before in Section 3.2: τ_{IVR} is attributed to internal vibrational relaxation (IVR) occurring after resonant excitation from the ground state to the first excited state within S_1 . τ_{POP} corresponds to the total S_1 population decay decaying *via* three competing pathways: (1) fluorescence (FL), (2) the formation of a long-lived, most probably triplet state *via* intersystem crossing (ISC) and (3) diffusion towards the ZnO interface, followed by charge separation (CS).

The time constants obtained from 2PPE adopt comparable values of 3.8 ± 0.4 ps and 230 ± 23 ps to the ones from excited state transmission for kinetic energies between 0.2-0.3 eV, as shown in Figure 5.13 (b) and (c). Therefore the two ps time constants are related to IVR within the S_1 and to the overall S_1 population decay, according to the results from excited state transmission [Fog15, Fog14]. Now the energetic position of the S_1 state can be estimated by subtracting the probe photon energy (1.93 eV) from the kinetic energy (averaged to 0.25 eV) yielding for the S_1 an energetic position of 1.7 eV below the vacuum level. The groundstate energy can be estimated by subtracting the energy difference between the S_1 and the ground state S_0 , which amounts to 3.15 eV according to luminescence measurements [Blu08, Fog14]. With this the ground state (S_0) is estimated to be located 4.85 eV below the vacuum level, as depicted in Figure 5.14 (b).

The additional fast time constant τ_{XF} yielded by the analysis of the TR-2PPE experiments (Figure 5.13 (a)) amounts to several hundred fs and has not been observed in excited state transmission. This ultrafast time constant is probably related to electronic processes, such as polarization effects, or very fast vibrations due to the exciton formation process.

The comparability of 2PPE and excited state transmission can be tested as well by plotting the data obtained from the respective experiments. In Figure 5.15 a XC trace from the time-resolved 2PPE spectrum (integrated in an energetic range of 0.11 - 0.23 eV, as the fit of this XC yielded results comparable to those from excited

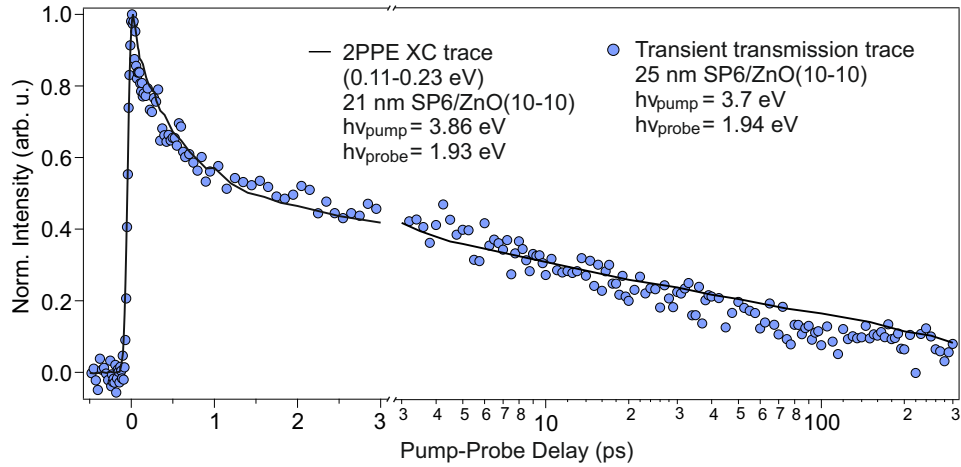


Figure 5.15: Comparison of a 2PPE cross-correlation with a transient transmission trace normalized to maximal intensity: The traces agree very well, demonstrating that in this case both techniques probe the same excited state dynamics, although photoemission is very surface sensitive and can access only the dynamics in the upmost few nm, while optical spectroscopy probes the dynamics of the whole film.

state transmission) shown in Figure 5.12 (b) and an excited state transmission trace from L. Foglia are plotted as a function of the pump-probe delay. The traces are normalized to the maximum intensity and compare very well, demonstrating that both methods probe here the same dynamics although photoemission is very surface sensitive while optical spectroscopy is able to probe the dynamics of the whole film. In order to explain this observation a simple numerical model of the exciton diffusion as function of time was developed and will be explained in the following.

The exciton diffusion length was adopted from Blumstengel *et al.* who analysed their time-resolved photoluminescence data with a linear diffusion model yielding an exciton diffusion length of $L_D = 3.7$ nm (T = 5 K) and a PL lifetime of $\tau_0 = 300$ ps [Blu08]. With the exciton diffusion length L_D and the PL lifetime τ_0 the diffusion constant D is given by

$$D = \frac{L_D^2}{\tau_0} = \frac{(3.7 \text{ nm})^2}{300 \text{ ps}} = 0.0456 \text{ nm}^2/\text{ps} \quad (5.54)$$

The time steps in the model were set to 1 ps as it is significantly shorter than τ_0 and the exciton lifetime of 230 ps, as measured with 2PPE. The diffusion length L'_D for 1 ps can be calculated as follows

$$L'_D = \sqrt{0.0456 \text{ nm}^2/\text{ps} \cdot 1 \text{ ps}} = 0.2135 \text{ nm} \quad (5.55)$$

The section size $\Delta\theta$ has to be larger than L'_D to avoid that excitons diffuse in the next but one section, therefore a section size of 0.5 nm was chosen. The model

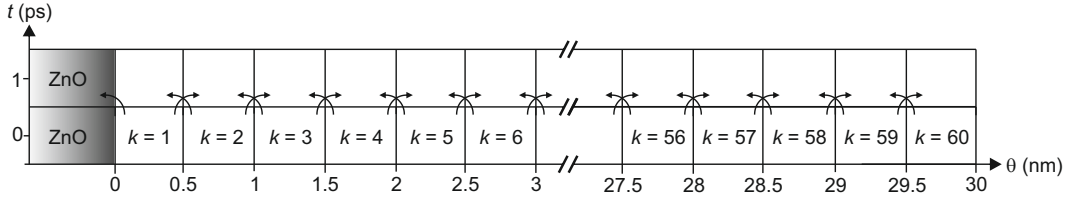


Figure 5.16: Schematic of the time-dependent diffusion model: The SP6 film has a thickness of 30 nm, which is divided into sections of $\Delta\theta = 0.5$ nm, thus yielding 60 sections ($k = 1 - 60$). The singlet excitons can move only between neighbouring sections in both directions, the y-axis indicates the temporal evolution in 1 ps time steps.

system shown in Figure 5.16 describes a SP6 film on ZnO with a thickness of 30 nm, *i.e.* the maximum distance from the ZnO interface (θ_{\max}) amounts 30 nm. This 30 nm thick film is divided into 60 sections, numbered $k = 1 - 60$, with a section size of $\Delta\theta = 0.5$ nm. In the model the singlet excitons diffuse to the neighbouring sections in both directions except at the SP6/ZnO and the SP6/vacuum interface: The excitons which reach the ZnO interface are separated, so there is a loss channel, while possible separation mechanisms at the SP6/vacuum interface are neglected.

The exciton diffusion length for 1 ps L'_D is inserted into the model and illustrated by the green boxes shown in Figure 5.17. The red arrows illustrate the diffusion between the sections while the green arrows depict the diffusion within a section. Actually the excitons cover in 1 ps an average distance of L'_D either towards the ZnO or towards the vacuum interface, but in this model it is assumed that each exciton moves L'_D in one of the directions within 1 ps. Therefore half of the excitons within L'_D is assumed to diffuse towards the ZnO interface and the other half towards the vacuum interface. The diffusion of the excitons in the white boxes between the green boxes can be neglected as they do not leave the section. The exciton population n_{S_1}

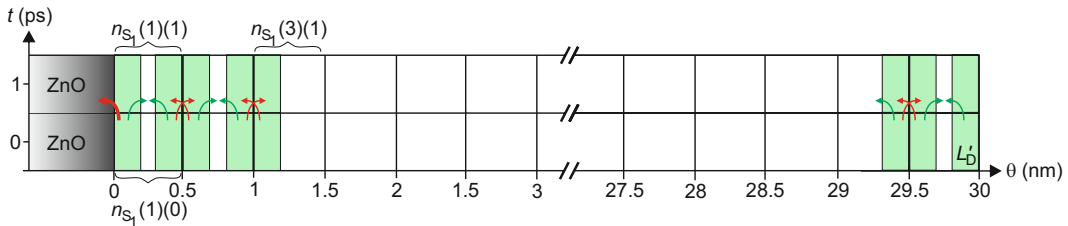


Figure 5.17: Schematic of the diffusion model including the exciton diffusion length: The distance which an exciton can move during a time step of 1 ps is illustrated by the green areas, the excitons reaching the ZnO interface dissociate while dissociation at the vacuum interface is neglected.

in each $\Delta\theta = 0.5$ nm thick section is defined by the section number ($k = 1 - 60$) and the time (t), e.g. the population in the first section next to the ZnO interface: $n_{S_1}(k = 1)(t = 0)$. The temporal evolution of the population in this layer is described by:

$$\begin{aligned} n_{S_1}(1)(t+1) &= n_{S_1}(1)(t) - \left(2 \cdot \frac{1}{2} \cdot \frac{L'_D}{\Delta\theta} n_{S_1}(1)(t) \right) \\ &+ \left(\frac{1}{2} \cdot \frac{L'_D}{\Delta\theta} n_{S_1}(2)(t) \right) \\ &- \beta_{ISC} \cdot n_{S_1}(1)(t) - \beta_{FL} \cdot n_{S_1}(1)(t) \end{aligned} \quad (5.56)$$

where β_{ISC} is the amount of singlet excitons which form triplet excitons *via* inter-system crossing and β_{FL} is the amount of excitons which is lost due to electron-hole recombination under the emission of photons, *i.e.* fluorescence. For the SP6 sections ($k = 2 - 59$) between the ZnO and the vacuum interface the temporal evolution writes as

$$\begin{aligned} n_{S_1}(k)(t+1) &= n_{S_1}(k)(t) - \left(2 \cdot \frac{1}{2} \cdot \frac{L'_D}{\Delta\theta} n_{S_1}(k)(t) \right) \\ &+ \left(\frac{1}{2} \cdot \frac{L'_D}{\Delta\theta} n_{S_1}(k+1)(t) \right) \\ &+ \left(\frac{1}{2} \cdot \frac{L'_D}{\Delta\theta} n_{S_1}(k-1)(t) \right) \\ &- \beta_{ISC} \cdot n_{S_1}(k)(t) - \beta_{FL} \cdot n_{S_1}(k)(t) \end{aligned} \quad (5.57)$$

And the population at the SP6/vacuum interface ($k = 60$) as a function of time is described by

$$\begin{aligned} n_{S_1}(60)(t+1) &= n_{S_1}(60)(t) - \left(\frac{1}{2} \cdot \frac{L'_D}{\Delta\theta} n_{S_1}(60)(t) \right) \\ &+ \left(\frac{1}{2} \cdot \frac{L'_D}{\Delta\theta} n_{S_1}(59)(t) \right) \\ &- \beta_{ISC} \cdot n_{S_1}(60)(t) - \beta_{FL} \cdot n_{S_1}(60)(t) \end{aligned} \quad (5.58)$$

The start population at $t = 0$ ps ($n_{S_1}(k)(0)$) is shown in Figure 5.18 (b) and is given by

$$n_{S_1}(k)(0) = N_{\max} \cdot e^{-(\alpha(\theta_{\max} - \Delta\theta \cdot k))} \quad (5.59)$$

where $N_{\max} = 22708$ is the maximum number of excitons in the upmost 0.5 nm section ($n_{S_1}(60)(0)$), calculated from the excitation density (as explained in Appendix B) under the assumption that each absorbed photon generates one exciton. $\alpha = 0.04$ nm⁻¹ corresponds to the absorption coefficient of SP6 as measured by Blumstengel *et al.* [Blu08] and θ_{\max} is maximal distance from the ZnO interface, *i.e.* the total

SP6 film thickness, of 30 nm. β_{ISC} and β_{FL} are chosen such that the populations in the upmost sections (58 - 60) have decayed to $\approx 1/e$ within the measured lifetime of 230 ps.

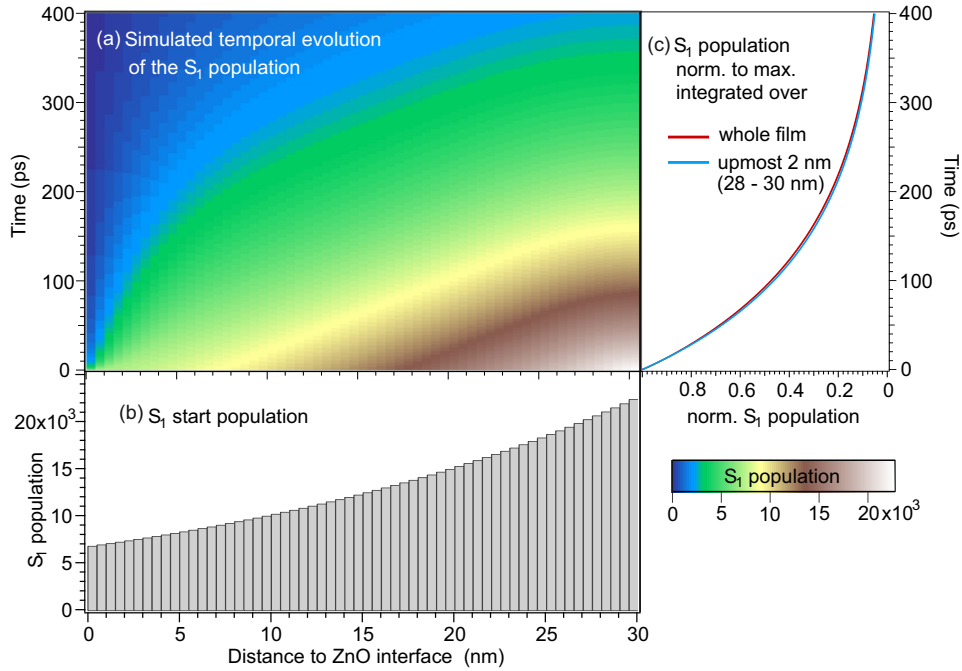


Figure 5.18: (a) Simulated temporal evolution of the S_1 start population, (b) S_1 start population as a function of the film thickness and (c) comparison of the S_1 population dynamics averaged over the whole SP6 film and at the surface: the two normalized curves coincide very well demonstrating that the overall S_1 population dynamics is not strongly affected by the exciton dissociation at the ZnO interface.

Figure 5.18 (a) shows the temporal evolution of the S_1 population within 400 ps, the number of excitons is illustrated by a colour code. To model the dynamics probed in the 2PPE experiment the 2D presentation of the S_1 population was integrated over the upmost 1.5 nm (section 58 - 60) since photoemission is very surface sensitive due to the finite escape depth of electrons [Sea79]. In contrast the dynamics probed in excited state transmission is modeled by averaging over the whole film, which is not entirely true since optical spectroscopy is as well depth dependent. The obtained traces are normalized to the maximum and plotted as a function of time in Figure 5.18 (c). Both traces coincide nearly perfectly demonstrating that the decay dynamics of the S_1 population averaged over the whole SP6 film is very similar to the dynamics in the topmost nanometers of the SP6 film. The model reproduced the same behaviour which was found by comparing the time-resolved 2PPE data with the excited state transmission data shown before in Figure 5.15.

Now I want to get back to the photoemission feature observed in the TR-2PPE

data which was labeled DS. Figure 5.19 shows again the spectra depicted before in Figure 5.12 (a). Here 3 spectra taken at different pump-probe delays are displayed as a function of the kinetic energy and are normalized to maximum intensity. The spectra recorded at positive delays originate from 3.86 eV pumping and 1.93 eV probing while the spectrum taken at -30 ps results from the reversed pump-probe scheme.

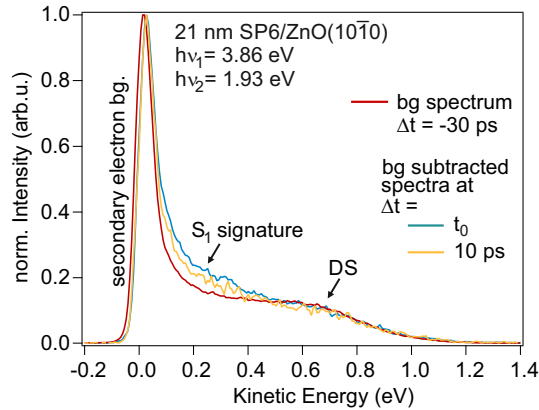


Figure 5.19: Comparison of 2PPE spectra taken at different time delays. The intensities are normalized to the maximum intensity. The ratio between the secondary electron background and the DS signature stays nearly constant for the different time delays (the spectra nearly coincide at these signals). This indicates that both features have similar dynamics in the observed time range. In contrast the ratio between the ultrafast 2PPE signal (S_1) intensity with the background signals changes as a function of pump-probe delay and is not present in the background spectrum (red) taken at -30 ps with the reversed pump-probe scheme.

The secondary electron background and the signal labeled DS coincide nearly perfectly for all three spectra whereas the S_1 signature exhibits dynamics on a ps timescale, as analysed and discussed above. This almost constant intensity ratio of the secondary electron background and the DS signal indicates that both features possess similar dynamics, at least within the investigated time range and for this photon energy combination (a different behaviour is observed for a longer timescale, *i.e.* hundreds of ps to ns, in an autocorrelation experiment presented and discussed in Section 5.2.2). The DS feature can be most probably related to the dark state indicated before in excited state transmission, as discussed before in Section 3.2 [Fog15, Fog14]. This long-lived dark state appeared as a constant offset in the excited state transmission data exceeding the repetition rate of the laser system. In the following section the dynamics and origin of this state will be investigated and discussed.

5.2.2 Triplet-Triplet Annihilation Leading to Electron Emission

In this section the dynamics of the long-lived background signal, which has been observed in the time-resolved 2PPE measurements (labeled DS in Figure 5.12, Section 5.2.1), and as a constant offset in the excited state transmission data by L. Foglia [Fog14] will be investigated and discussed. This feature has been labeled DS before and is most likely related to a triplet state, as it is dark for optical spectroscopy, and will thus be referred to as triplet (T) in the following.

To find out whether the observed signal is really due to a long-lived state which exceeds the repetition rate of the laser system the intensity of the observed electron emission signal is investigated as a function of the pulse duration. In a 2PPE process

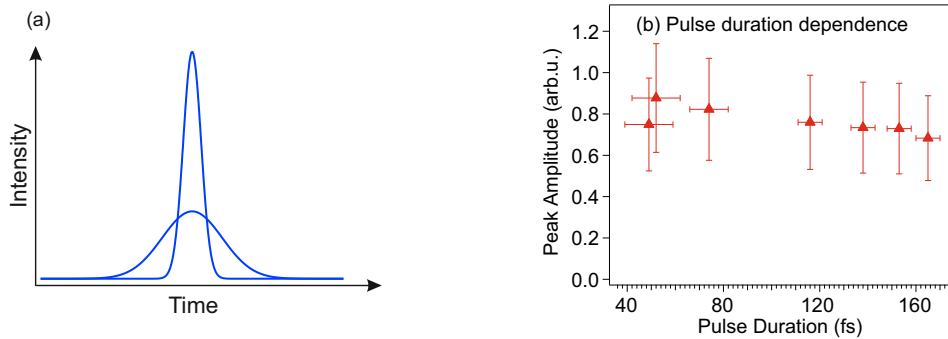


Figure 5.20: (a) Schematic of two laser pulses with different duration but same integral, (b) emission intensity as a function of the pulse duration, demonstrating that the emission signal is not due to a 2PPE process.

the peak intensity highly depends on the pulse duration. Figure 5.28 (a) shows two Gaussian pulses with the same integral but different pulse durations: Overlapping two short pulses leads to a signal with a higher intensity compared to the signal intensity resulting from a 2PPE process with longer pulses. A 20 nm thick SP6 film on ZnO(10 $\bar{1}$ 0) was measured with a photon energy of 3.1 eV under variation of the pulse duration. Figure 5.28 (b) displays the peak amplitudes of the most prominent peak of the triplet signature as a function of the pulse durations, showing clearly that the observed signal is not affected by the variation of the pulse duration. This behaviour demonstrates that the detected electrons are not emitted *via* a 2PPE process, *i.e.* are not pumped and probed within 2 laser pulses. This corroborates the suggestion that the triplet state is so long-lived that it exceeds the repetition rate. The time delay between the laser pulses amounts 5 μ s at a repetition rate of 200 kHz which was used in the pulse duration as well as in the TR-2PPE and the excited state transmission experiments. This demonstrates that the lifetime of the triplet is longer than 5 μ s.

In order to investigate the lifetime of the triplet state the pump-probe delay

needs to be varied on a μs timescale. This can be achieved in a ‘static’ time-resolved

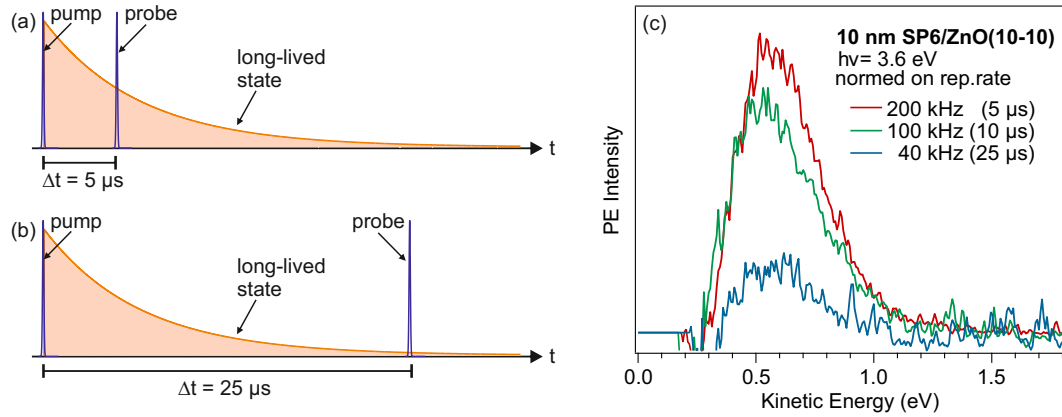


Figure 5.21: Sketch of the overlap of the laser pulses with the dark state population for (a) 200 kHz and (b) 40 kHz, (c) the repetition rate dependent spectra of 10 nm SP6/ZnO(10 $\bar{1}$ 0) measured with 3.6 eV show that the emission intensity strongly depends on the population in the long-lived state.

experiment under variation of the repetition rate. Figure 5.21 (a) and (b) illustrate the idea behind this experiment: the first laser pulse acts as the pump pulse and populates the triplet while the second laser pulse probes the population of this state. Decreasing the repetition rate e.g. from 200 kHz to 40 kHz leads to an increase of the time interval between the laser pulses from 5 μs (Figure 5.21 (a)) to 25 μs (Figure 5.21 (b)). Increasing the time interval between the laser pulses leads to a decrease of the overlap between the probe pulse and the population in the triplet state. Thus, a lower signal intensity in the spectrum is expected. This experiment has been performed on a 10 nm SP6 film on ZnO(10 $\bar{1}$ 0) with a photon energy of 3.6 eV. The spectra recorded with different repetition rates are displayed in Figure 5.21 (b) as function of the kinetic energy (the secondary electron background has been subtracted from these spectra to point out the triplet signature). These spectra clearly show a decrease in signal with decreasing repetition rate. This behaviour indicates that the observed signal strongly depends on the population in the long-lived triplet state and that the lifetime of this state exceeds 25 μs .

As the observed signal can be related to a long-lived unoccupied intermediate state, the signal position in the spectrum should depend on the probe photon energy. Figure 5.22 (a) sketches the pump-probe scheme for the case of an unoccupied intermediate state: The first laser pulse populates the intermediate state and the second pulse photoemits the electrons from this state. Therefore the peak position in the spectrum should depend on the probe photon energy and should shift with

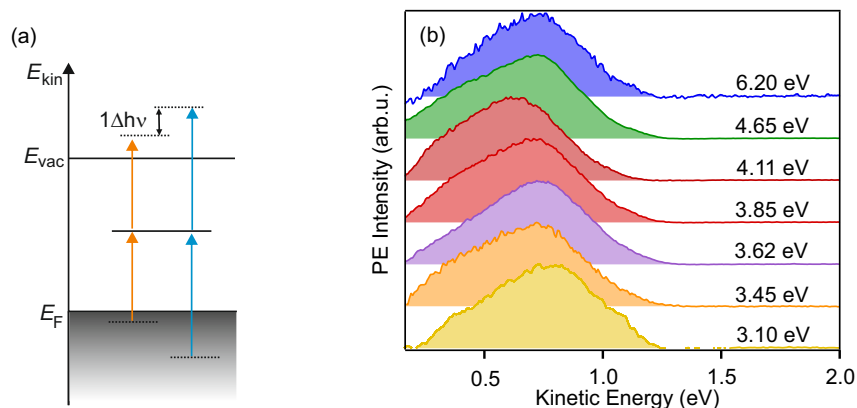


Figure 5.22: (a) 2PPE pump-probe scheme for the case of an unoccupied intermediate state: The peak position in the spectrum shifts with the photon energy difference $\Delta h\nu$, (b) photon energy dependent spectra series of 20 nm SP6/ZnO(10 $\bar{1}$ 0): The kinetic energy of the emission signal does not shift with $\Delta h\nu$.

$1 \times \Delta h\nu$. Figure 5.22 (b) displays a photon energy dependent spectra series (after background subtraction) measured on ≈ 20 nm thick SP6 films on ZnO(10 $\bar{1}$ 0) as a function of the kinetic energy. The spectra reveal that the signal does not shift with the photon energy difference. Although varying the photon energy from 3.1 - 6.2 eV should shift the signal by 3.1 eV it stays at the same energetic position. Such behaviour is usually observed for final states. But this is not the case here, because a two-photon process would be required to populate a final state at this energetic position. (And the absence of a real 2PPE process has been demonstrated before in the pulse duration dependent experiment, Figure 5.20). This demonstrates that the photon energy information put into the system *via* the laser pulses gets lost in an intermediate step which acts as an energy filter, so that the emitted electrons possess the same kinetic energy. The electrons emitted from the long-lived triplet state are emitted by a fixed amount of energy rather than the laser photons, whose varied photon energies did not show an effect on the kinetic energy of the emitted electrons.

This observation leads to the question where this fixed amount of energy originates from and how much energy it amounts to. A fixed amount of energy hints at a system immanent property like a molecular resonance. Thinking about the transfer of an intrinsic amount of energy in an optically excited system which consists of a molecular film on a semiconductor surface, exciton recombination or excitation energy transfer appear to be probable processes. Figure 5.23 shows the scenario of two neighbouring SP6 molecules: Molecule A is excited at $t = 0 \mu\text{s}$ by a first laser pulse, undergoes internal vibrational relaxation within the S_1 , which in turn decays on a

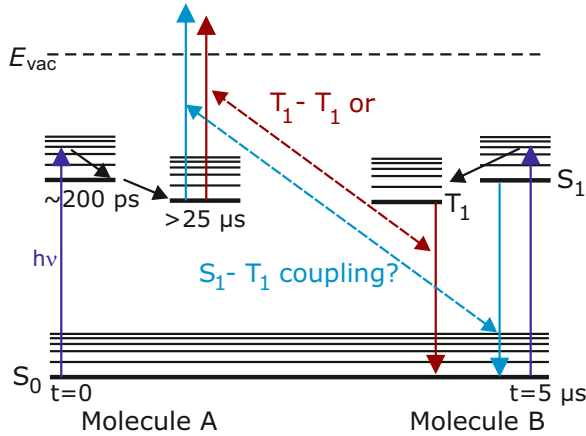


Figure 5.23: Jablonski diagram of two neighbouring SP6 molecules A and B illustrating possible excitation transfer processes: singlet-triplet or triplet-triplet coupling.

their different lifetimes into account: e.g. in the case of singlet-triplet interaction the ps dynamics are included in the process while in the case of triplet-triplet interaction only μs dynamics should be observable.

In order to disentangle these processes *via* the lifetime of the involved states a time-resolved experiment autocorrelation experiment is performed. In an autocorrelation (AC) experiment pump and probe pulse possess the same photon energy and therefore the same pump-probe scheme applies for negative and positive delays, thus yielding a symmetric signal. In this experiment, each laser pulse excites the system generating singlet and triplet populations which then can interact with each other. Figure 5.24 (a) illustrates the experiment for the case of triplet-triplet interaction: First, the pump pulse generates population in the long-lived state and after the delay time, which varies between several fs up to 3 ns, the probe pulse does the same. The generated triplet populations can interact with each other in the time range where they overlap, as illustrated by the orange coloured area.

In order to be able to interpret the data from the autocorrelation experiment the expected AC-traces were simulated. This is done by correlating the singlet and triplet population functions which are obtained from a simplified model sketched in Figure 5.24 (b) Here n_{S_1} corresponds to the singlet and n_{T_1} to the triplet population, $\Gamma_1 = \frac{1}{\tau_1}$ is the fluorescence rate, $\Gamma_{12} = \frac{1}{\tau_{12}}$ relates to the intersystem crossing rate and $\Gamma_2 = \frac{1}{\tau_2}$ to the triplet decay rate. The population n_{S_1} depends on the fluorescence ($\Gamma_1 = \frac{1}{\tau_1}$) and the intersystem crossing rate ($\Gamma_{12} = \frac{1}{\tau_{12}}$) and is described by the following equation:

$$\dot{n}_{S_1} = -(\Gamma_1 + \Gamma_{12})n_{S_1} = -\left(\frac{1}{\tau_1} + \frac{1}{\tau_{12}}\right)n_{S_1} \quad (5.60)$$

time scale of 200 ps *via* fluorescence, triplet formation and diffusion towards the ZnO interface. Molecule B is excited after 5 μs by the second laser pulse and undergoes the same relaxation processes like molecule A. When these two molecules interact with each other they can be either both in the triplet state or B is in the singlet and A in triplet state because the singlets of A should have already decayed after 5 μs. We can distinguish between the different coupling mechanisms taking

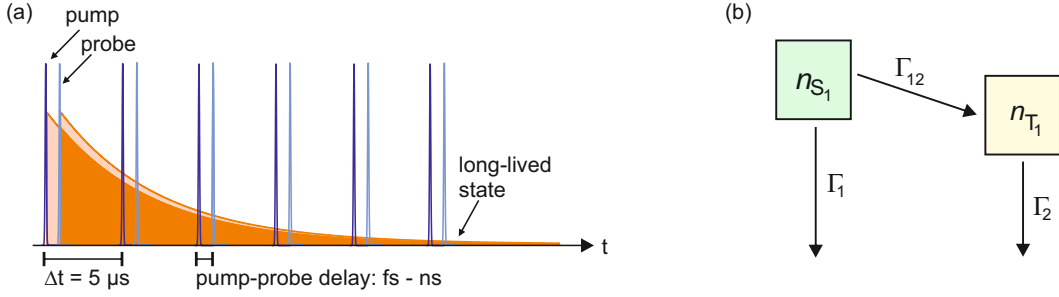


Figure 5.24: (a) Schematic of the autocorrelation experiment for the case of triplet-triplet interaction: Both, pump and probe, pulses generate triplet populations which can interact with each other as illustrated by the orange coloured area. (b) Simplified model describing the singlet and triplet population decays.

with $\frac{1}{\tau_1} + \frac{1}{\tau_{12}} = \frac{1}{\tau_{S_1}}$ this writes as

$$\dot{n}_{S_1} = -\frac{1}{\tau_{S_1}}n_{S_1} \quad (5.61)$$

The solution is already given by

$$n_{S_1}(t) = n_{S_1}(0)e^{-t\left(\frac{1}{\tau_1} + \frac{1}{\tau_{12}}\right)} = n_{S_1}(0)e^{-t/\tau_{S_1}} \quad (5.62)$$

The rate equation for the triplet population n_{T_1} writes as

$$\dot{n}_{T_1} = \frac{1}{\tau_{12}}n_{S_1} - \frac{1}{\tau_2}n_{T_1} = \Gamma_{12}n_{S_1} - \Gamma_2n_{T_1} \quad (5.63)$$

The complete solution of the differential equation 5.63 can be found in Appendix C yielding

$$n_{T_1}(t) = n_{T_1}(0)e^{\frac{-t}{\tau_2}} + n_{S_1}(0)\frac{\frac{1}{\tau_{12}}}{\frac{1}{\tau_2} - \frac{1}{\tau_{S_1}}}\left(e^{\frac{-t}{\tau_{S_1}}} - e^{\frac{-t}{\tau_2}}\right) \quad (5.64)$$

The obtained solutions can be plotted after inserting values for the time constants. From the time-resolved 2PPE and the excited states transmission it is known that the population decay of S_1 amounts ≈ 200 ps, with $\frac{1}{\tau_{S_1}} = \frac{1}{\tau_1} + \frac{1}{\tau_{12}}$ and the assumption that $\tau_1 \approx \tau_{12}$, τ_1 and τ_{12} are approximated to 400 ps. The triplet lifetime (τ_2) is approximated to 40 μs . This yields for

$$n_{S_1} = A * e^{\frac{-x}{200 \text{ ps}}} \quad (5.65)$$

and for

$$n_{T_1} = B * e^{\frac{-x}{40 \mu s}} - C * \frac{1}{\frac{1}{200 \text{ ps}} - \frac{1}{40 \mu s}} \left(e^{\frac{-x}{200 \text{ ps}}} - e^{\frac{-x}{40 \mu s}} \right) \quad (5.66)$$

which can be simplified to

$$n_{T_1} = B * e^{\frac{-x}{40 \mu s}} - C * 0.5 * \left(e^{\frac{-x}{200 \text{ ps}}} - e^{\frac{-x}{40 \mu s}} \right) \quad (5.67)$$

The amplitude A was set to 1 and the amplitudes $B = C$ were set such that both decay functions yield the same integral, since the number of singlet and triplet excitons is assumed to be in the same order of magnitude in this model. The case of triplet-singlet interaction is modeled by correlating n_{S_1} with n_{T_1} and *vice versa*, as both processes should happen in the autocorrelation experiment and correlation is not a commutative mathematical operation. Triplet-triplet coupling is simulated by autocorrelating n_{T_1} .

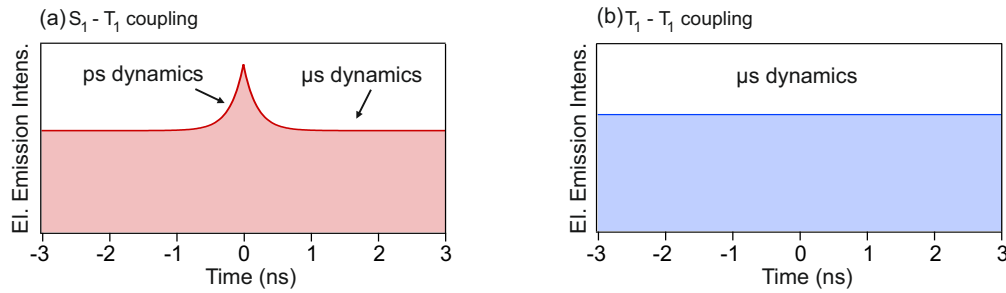


Figure 5.25: Modeled autocorrelation traces for (a) triplet-singlet and (b) triplet-triplet coupling

Figure 5.25 (a) depicts the AC-trace of the singlet-triplet coupling and exhibits an intensity loss within several hundred ps around t_0 since the S_1 population decay takes part in this process. Figure 5.25 (b) shows the simulated autocorrelation trace for triplet-triplet interaction, which is a constant line in the time range of -3 - 3 ns.

This autocorrelation experiment has been conducted as well experimentally on a 20 nm thick SP6 film on ZnO(10 $\bar{1}$ 0) with $h\nu_{\text{pump}} = h\nu_{\text{probe}} = 3.85$ eV in a delay range from -0.5 - 3.0 ns, which technical is the limit due to the length of the delay stage. The autocorrelation spectrum is presented in Figure 5.26 (a) and exhibits a little increase in intensity around t_0 . In order to disentangle whether this intensity decrease really originates from the signal of the long-lived state, vertical cuts were taken at different time delays, as illustrated by the coloured lines in the 2D spectrum, and biexponential background fits were subtracted from the spectra. The biexponential background fits and the corresponding spectra are shown in Figure 5.26 (b),

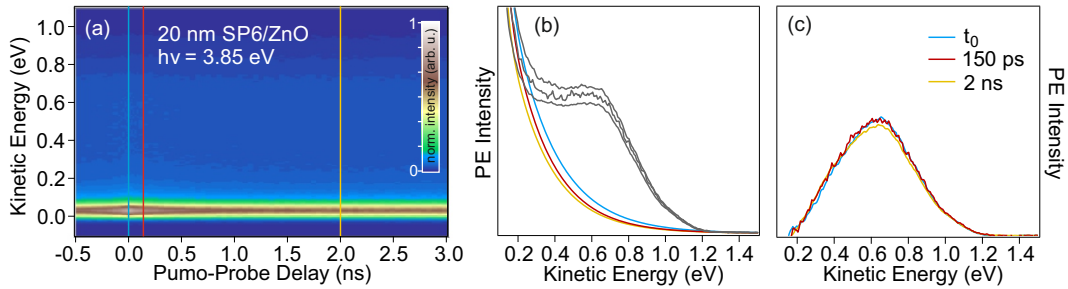


Figure 5.26: (a) 2D-spectrum of the autocorrelation measurement, the coloured lines mark the delay times at which the vertical cuts, yielding the spectra shown in (b) and (c), are taken. (b) Spectra taken at t_0 , 150 ps and 2 ns time delay (grey) and the corresponding background fits which are subtracted yielding the background subtracted spectra shown in (c). Only the secondary electron background changes as a function of the pump-probe delay while the actual signal stays constant.

demonstrating that the signal intensity of the secondary background decreases with increasing time delay. The background subtracted spectra for different time delays, depicted in Figure 5.26 (c), clearly show that the signal intensity of the long-lived triplet state is not affected within 200 ps around t_0 . This observation suggests that the long-lived signal is due to triplet-triplet interaction.

This process is known as triplet-triplet annihilation (TTA) in the literature [Kel64, Rei12, Sta07] and often leads to delayed fluorescence (DF), as discussed in Section 2.2.2. If the higher excited singlet state S_n lies energetically above

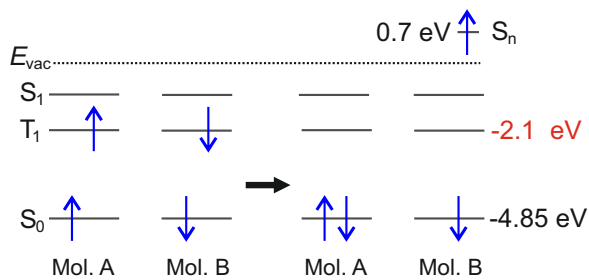


Figure 5.27: Schematic of the suggested triplet-triplet annihilation process: Two molecules A and B, both in the triplet state interact with each other such that the excitation energy of molecule A is transferred to molecule B which gets excited to a higher lying singlet state above the vacuum level, thus leading to the observed electron emission.

the vacuum level electron emission might occur as well as described by Friedlein for the case of singlet-singlet annihilation in thin perylene films [Fri09]. Figure 5.27 schematically depicts the TTA process suggested for the investigated system:

Two neighbouring molecules A and B both in the triplet state interact with each other such that molecule A ends up in the ground state and molecule B in a higher excited singlet state above the vacuum level, leading to electron emission. Under

the assumption that the transferred amount of energy corresponds to the energetic difference between S_0 and T_1 , the triplet should be located right between S_0 and S_n , *i.e.* 2.1 eV below the vacuum level.

As TTA is a bimolecular process the resulting signal intensity should depend quadratically on the triplet concentration, as observed before for the DF intensity [SR08]. To study the dependence of the electron emission on the laser fluence spectra were taken on a 25 nm thick SP6 film on ZnO(10 $\bar{1}$ 0) under variation of the power of the 3.6 eV laser beam. Figure 5.28 displays the peak amplitudes of the most prominent feature of the emission signal as a function of the laser power. The power law fit yields neither a linear nor a quadratic fluence dependence, but instead an exponent of 1.5. This behaviour which deviates from the expected quadratic dependence may be explained by the following consideration which was originally formulated by Hoffmann *et al.* for a DF study [Hof11]. Under steady state conditions, which are suitable here as the triplet can be considered as a quasi stationary state during measurements with a repetition rate of 200 kHz, the rate equation of the triplet concentration $[T]$ writes as

$$\frac{d[T]}{dt} = k_{\text{ISC}} - k_{\text{D}}[T] - k_{\text{TTA}}[T]^2 = 0 \quad (5.68)$$

Where k_{ISC} is the triplet formation rate by ISC from the singlet, k_{D} is the sum of other decay rates, e.g. phosphorescence or triplet quenching rate and k_{TTA} is the rate constant for bimolecular TTA. If the triplet population decays predominantly *via* TTA (which is a plausible assumption since a significant electron emission signal is observed), *i.e.* $k_{\text{TTA}} \gg \gg k_{\text{D}}$, so that the other decay channels can be neglected Equation 5.68 becomes

$$k_{\text{ISC}} - k_{\text{TTA}}[T]^2 = 0 \quad (5.69)$$

From this follows

$$[T] = \sqrt{\frac{k_{\text{ISC}}}{k_{\text{TTA}}}} \quad (5.70)$$

As mentioned before, the intensity I_{Em} of electron emission signal is a result of bimolecular TTA and thus quadratically dependent on the triplet concentration

$$I_{\text{Em}} \propto k_{\text{ISC}}[T]^2 \quad (5.71)$$

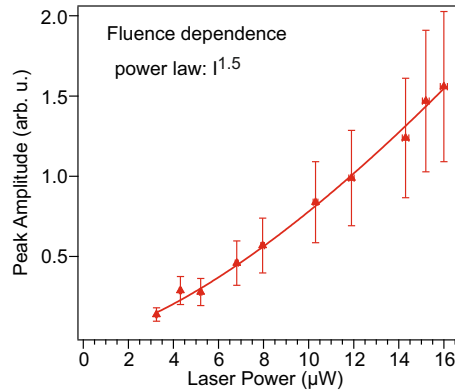


Figure 5.28: Dependence of the electron emission signal, due to TTA, on the incident laser light: The peak amplitudes of the most prominent peak are plotted as a function of the laser power.

inserting Equation 5.70 yields for this limiting case a linear relation between emission signal intensity and triplet formation rate and thus the triplet concentration

$$I_{\text{Em}} \propto k_{\text{ISC}} \left(\sqrt{\frac{k_{\text{ISC}}}{k_{\text{TTA}}}} \right)^2 \propto k_{\text{ISC}} \quad (5.72)$$

Taken this consideration into account it is possible that the exponent of 1.5 describes a situation which lies in between the two limiting cases of quadratic and linear dependence.

Other decay channels besides TTA are e.g. triplet quenching at defect sites or charge separation at the ZnO interface. As all these decay channels are diffusion controlled they should be influenced by enhancing the diffusion, e.g. by increasing the temperature. Thus, the electron emission signal resulting from TTA is expected to

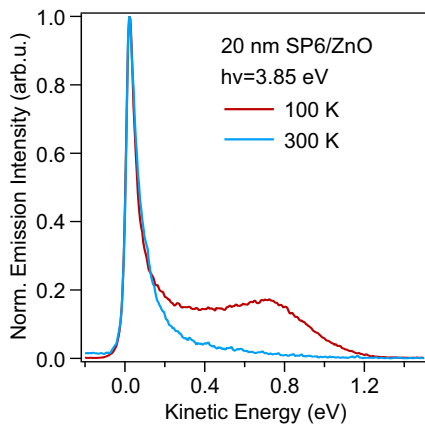


Figure 5.29: Spectra of 20 nm SP6 on ZnO measured at liquid nitrogen temperature (100 K) and at room temperature (300 K): The emission signal due to TTA is only observable at low temperatures.

exhibit a temperature behaviour, *i.e.* to decrease upon increasing the sample temperature. To test this, spectra were taken at temperatures of 100 K and 300 K on 20 nm SP6 on ZnO(10 $\bar{1}$ 0) as shown in Figure 5.29. Comparing the two spectra, normalized to maximum intensity, clearly shows that the electron emission signal due to TTA has completely vanished at 300 K and only the secondary electron background is left. Hoffmann *et al.* observed the same temperature dependent behaviour for the intensity of the delayed fluorescence in poly(*p*-phenylene) derivatives [Hof11]. The disappearance of the electron emission signal at room temperature is thus consistent with the increased triplet diffusion leading to enhanced triplet quenching at defect sites

and/or charge separation at the ZnO interface.

To further investigate the possibility of triplet dissociation at the SP6/ZnO interface, as observed for the singlet excitons in this system [Blu08, Fog15], the distance to the ZnO interface is decreased by lowering the coverage. Figure 5.30 (a) displays a coverage dependent spectra series of SP6 on ZnO measured with an excitation photon energy of 3.6 eV, where the electron emission intensity is plotted logarithmically as a function of the kinetic energy. The electron emission signal resulting from TTA is significantly lower for a SP6 coverage of 6 nm, demonstrating the influence of CS at the SP6/ZnO interface on the triplet lifetime. At a distance of 20 nm from the ZnO interface, triplet quenching due to CS does not significantly affect the life-

times of triplets close to the SP6/vacuum interface anymore, as the emission signal saturates.

To obtain more information on the electron emission signature the secondary electron background is described by an empirical background fit, blue curve in Figure 5.30 (b), which is subtracted from the original spectrum (yellow), yielding the red background subtracted spectrum. This background subtracted spectrum can be fitted with a function consisting of three Gaussians (black). This fine structure may be due to vibronic replica as observed before by Arnold *et al.* [Arn79] in an electron emission signal due to interaction of trapped charge-transfer states and free electrons in crystalline tetracene. They attributed the structure of the signal to a sequence of molecular vibrational states. This is as well plausible explanation for the fine structure observed here spectra since all three peaks exhibit the same behaviour towards variations of the repetition rate and the photon energy indicating that they have the same origin.

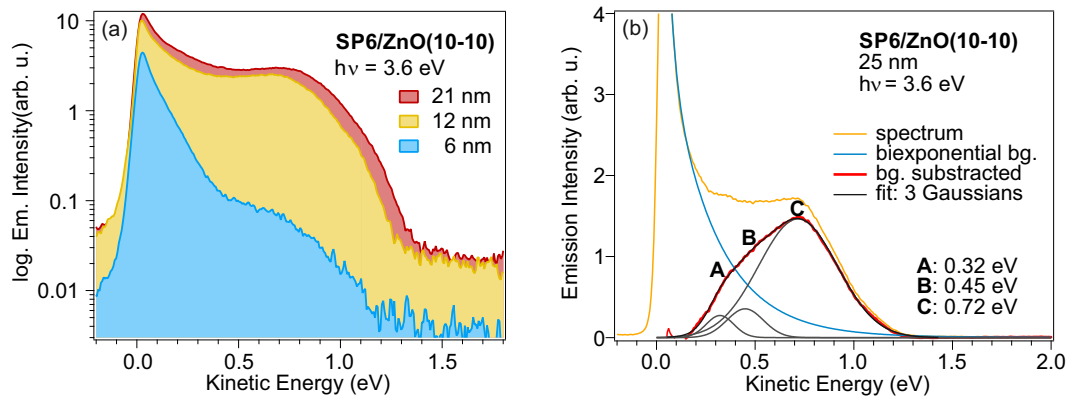


Figure 5.30: (a) The coverage dependent spectra series of SP6/ZnO(10 $\bar{1}$ 0) measured with 3.6 eV shows an increase of the signal with the coverage up to 20 nm. (b) Illustration of the subtraction of a biexponential background fitted to the secondary electron background and fitting of the corresponding background subtracted spectrum with a fit function consisting of three Gaussians.

Summary

Time-resolved 2PPE measurements of 20 nm SP6 on ZnO(10 $\bar{1}$ 0) reveal an ultrafast time constant, τ_{XF} , in addition to the slower time constants, τ_{IVR} and τ_{POP} , observed as well in excited state transmission by L. Foglia [Fog15, Fog14]. In Figure 5.31 the photoinduced processes observed in SP6 films on ZnO(10 $\bar{1}$ 0) are summarized. The system is excited from the ground state S_0 to a higher vibrational level of the first excited state S_1 and subsequently undergoes internal vibrational relaxation (IVR) within the S_1 state on a time scale of a few picoseconds. The S_1 population decays within ≈ 200 ps *via* three competing pathways: (1) electron-hole recombination, *i.e.* fluorescence (FL), (2) formation of the long-lived triplet state by intersystem crossing (ISC) and (3) diffusion towards the ZnO interface, where charge separation (CS) takes place. It is shown that the broad emission signal in the 2PPE spectra,

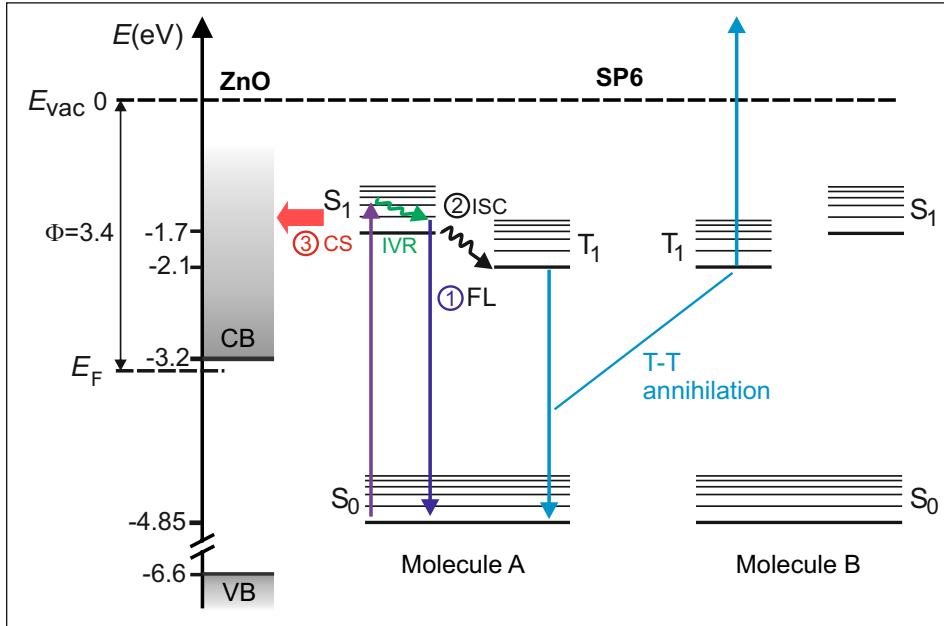


Figure 5.31: Jablonski diagram of the observed processes in SP6/ZnO: After resonant excitation from the ground state, S_0 , to the first excited state, S_1 , the system relaxes vibrationally on a timescale of $\tau_{IVR} \approx 4$ ps. The S_1 population decays within ≈ 200 ps *via* three competing pathways: (1) fluorescence (FL), (2) formation of the long-lived triplet state (ISC) and (3) diffusion towards the ZnO interface, where charge separation (CS) takes place.

independent of the probe photon energy and the pulse duration, originates from emission of a very long-lived triplet state, exceeding 25 μ s. The conclusion that the observed emission signal does not result from a two-photon process leads to the conjecture that electron emission occur here most likely *via* intermolecular excitation energy transfer instead of photoemission by the laser light. This assumption is

corroborated by the result of an autocorrelation experiment, thus leading to the conclusion that triplet-triplet annihilation between two neighbouring molecules is the process which underlies the observed electron emission signal. In addition, the absolute energies of the ground state as well as the singlet and the triplet state are obtained from the 2PPE measurements.

5.3 Electronic Structure and Excited State Dynamics in DCV-substituted Oligothiophenes on Au(111)

Dicyanovinyl-substituted oligothiophenes are very attractive molecules for the application as donor materials in organic solar cells because they absorb light in the visible range and exhibit high charge carrier mobility. The methylated DCV-substituted quinquethiophene DCV5T-Me₂ yields up to now the highest PCE among the known molecular donor materials processed by vapour-deposition [Poe15]. Although the optical gap of DCV6T was reported to be similar to the one of DCV5T-Me₂ its solar cell performance is much lower which was explained by enhanced molecular interactions due to methyl-substitution [Fit12a, Fit11, Fit12b].

In this work the electronic structures of DCV5T-Me₂ and DCV6T adsorbed on Au(111) are studied by means of 2PPE in collaboration with Z. Yang, I. N. Pascual and K. J. Franke (FU Berlin) who investigated the adsorption and electronic properties of the two systems with STM and STS, as presented before in Section 3.3. The 2PPE study is focused especially on the occupied molecular states and the electronic structure of multilayer coverages which have not been observed in STS. Moreover the excited state dynamics are of particular interest since so far no time-resolved studies have been reported on DCV5T-Me₂ and DCV6T, thus nothing is known about the excited state dynamics in these materials.

Merging 2PPE results obtained in this work with those from STM/STS we are able to draw a rather complete picture of the electronic structure as a function of the coverage [Yan14b, Yan14a, Bog15]. The energy level alignment at the organic/metal interface reveals a decreased HOMO-LUMO gap due to interaction with the metal. The gap increases again in the second layer when the molecules are electronically decoupled from the surface. Time-resolved 2PPE measurements demonstrate that the excited state dynamics in DCV5T-Me₂ are faster than in DCV6T. This observation may be explained with the enhanced intermolecular interactions in DCV5T-Me₂ promoting exciton and charge carrier transport according to Fitzner *et al.* [Fit12b]. In addition the relaxation and decay processes occurring within the first 2 ps are more efficient in DCV5T-Me₂ which might be due to stronger coupling to vibrational states.

5.3.1 Coverage-Dependent Electronic Structure of DCV5T-Me₂ on Au(111)

In this section the electronic structure of DCV5T-Me₂ on Au(111) interface and as a function of the coverage is investigated. The preparation and quantification of the molecular films is described in Section 4.3.3. In order to investigate the energy level alignment at the DCV5T-Me₂/Au(111) interface, 2PPE measurements under variation of the photon energy have been performed. Figure 5.32 (a) shows an exemplary 1C-2PPE spectrum of a submonolayer coverage DCV5T-Me₂ on Au(111) measured with a photon energy of $h\nu = 4.8$ eV. The spectrum is plotted as a function of the final state energy above the Fermi level such that the secondary electron cutoff corresponds to the work function of the system, $\Phi = 5.4$ eV, which is reduced by ≈ 50 meV compared to the bare Au(111) surface. The features in the low energy region, *i.e.* at final state energies between 6.4 and 7.6 eV, can be related to occupied states of the Au(111) substrate, namely to emission from the d-bands which are located between ≈ -2.0 and -3.0 eV [Hei79, Eck84].

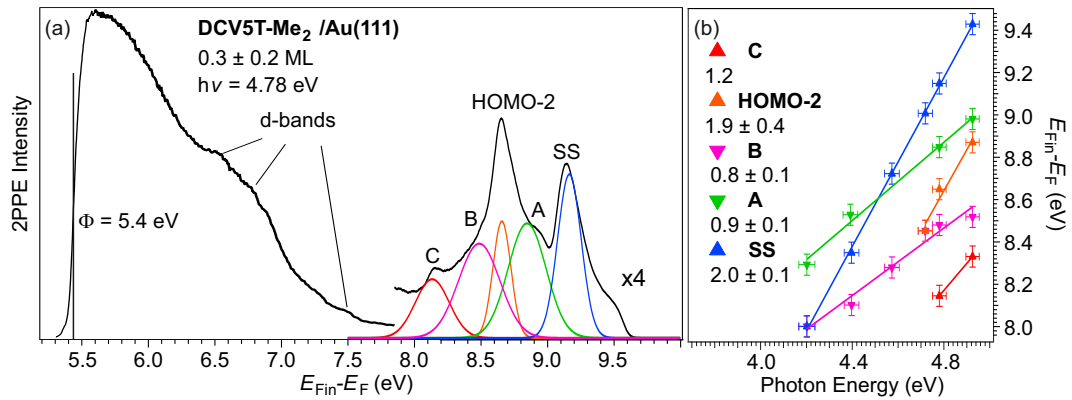


Figure 5.32: (a) 1C-2PPE spectrum of 0.3 ML DCV5T-ME₂/Au(111), (b) peak positions as a function of the photon energy: A slope of 1 is characteristic for photoemission from unoccupied electronic states while a slope of 2 indicates photoemission from occupied states.

At higher energies there are five features located very close to each other. This part of the spectrum was fitted with five gaussians as depicted in Figure 5.32 (a). In order to distinguish between occupied and unoccupied states the peak maxima are plotted as a function of the photon energy in Figure 5.32 (b). As described before in Section 4.1.1 a slope of 1 indicates photoemission from an unoccupied state while a slope of 2 demonstrates photoemission from an initially occupied state. According to this analysis two occupied and three unoccupied states are found here. The peaks related to occupied states are labeled SS and HOMO-2, since the first originates from photoemission from the surface state of the Au(111) surface, which

is located 0.48 eV below the Fermi level [Nic01]. The second feature is related to a low-lying occupied molecular state with a binding energy of -1.0 eV. This occupied state is assigned to the HOMO-2 since HOMO and HOMO-1 appear for a monolayer coverage at higher binding energies, as will be shown below. The states labeled A, B and C yield slopes of ≈ 1 and are thus related to unoccupied states located 4.0 eV (A), 3.6 eV (B) and 3.4 eV (C) above the Fermi level. Feature C is only observable for two photon energies here, but further photon energy dependent measurements on a higher coverage yielded more data points, as will be shown below (Figure 5.34). The origin of peaks A, B and C will be discussed at the end of the section.

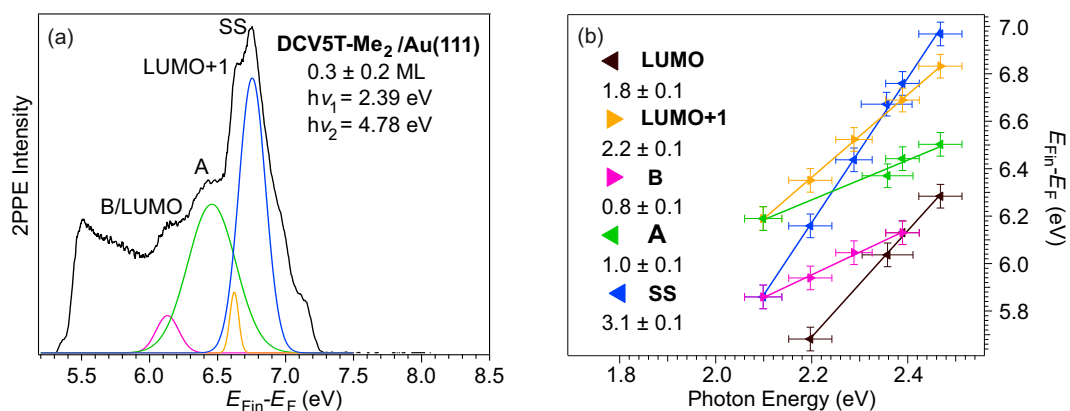


Figure 5.33: (a) 2C-2PPE spectrum of 0.3 ML DCV5T-ME₂/Au(111) showing 2 additional features, (b) the photon energy dependent peak positions demonstrate that the two additional peaks are due to unoccupied states and can be attributed to the LUMO and LUMO+1.

To obtain more information on the submonolayer electronic structure 2C-2PPE spectra were measured on the same sample, since the use of different photon energies promises to reveal additional electronic states. Figure 5.33 (a) displays an exemplary 2C-2PPE spectrum measured with photon energies of $h\nu_1 = 2.39$ eV and $h\nu_2 = 4.78$ eV. This spectrum shows exclusively the 2PPE signal originating from a two-color process, since the 1C-2PPE spectra have been subtracted. This is usually the case for the 2C-2PPE spectra shown in the following sections if not mentioned otherwise. The spectrum exhibits a lot of strongly overlapping features located close to each other. In Figure 5.33 (b) the energetic positions of the observed features are plotted as a function of $h\nu_1$, *i.e.* the photon energy of the visible laser pulse. This graph illustrates nicely that the peaks overlap strongly and intersect upon shifting with the photon energy. Since $h\nu_1 = 1/2 h\nu_2$ a slope of 1 indicates that the observed emission signal originates from an unoccupied state which is pumped by the UV-pulse ($h\nu_2$) and probed by the vis-pulse ($h\nu_1$). A slope of 2 suggests the reversed pump probe scheme, *i.e.* probed by the $h\nu_2$ and pumped by $h\nu_1$. Photoemission from

an occupied state is then demonstrated by a slope of 3, since the peak position in the spectrum shifts with $3 \times \Delta h\nu_1$. In addition to the peaks A, B and SS, which have been observed before in the 1C-2PPE spectrum (Figure 5.32 (a)) two new features are observed. Both peaks yield a slope of ≈ 2 indicating that they are probed by the UV-pulse and are thus located 1.3 eV and 1.8 eV above the Fermi level. These states are related to the LUMO and LUMO+1 according to STS measurements conducted by Yang *et al.* who found the LUMO at 1.3 V and the LUMO+1 at 1.65 V [Yan14a, Yan14b, Bog15]. Especially the values for the LUMO coincide very well.

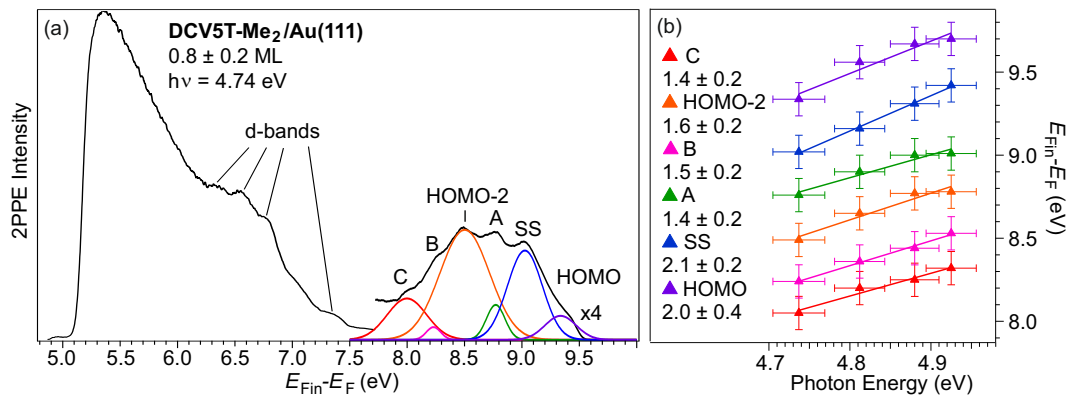


Figure 5.34: (a) 1C-2PPE spectrum of 0.8 ML DCV5T-ME₂/Au(111) and (b) peak positions as a function of the photon energy revealing that the additional feature close to E_F is due to emission from the highest occupied molecular orbital at -0.1 eV.

In order to further investigate the electronic structure as a function of coverage photon energy-dependent measurements were conducted on a coverage of 0.8 ± 0.2 ML DCV5T-Me₂ on Au(111). Figure 5.34 (a) displays a 1C-2PPE spectrum of 0.8 ± 0.2 ML DCV5T-Me₂/Au(111) recorded with a photon energy of 4.74 eV. The work function is decreased to $\Phi = 5.1$ eV upon DCV5T-Me₂ adsorption due to the push back effect and a decrease of the surface dipole as described in Section 2.1.1. Besides the d-band features located at final state energies between 6.2 eV and 7.5 eV, a broad signal is observed between 7.5 - 9.5 eV. This signal contains 6 peaks whose energetic positions are plotted as a function of the photon energy in Figure 5.34 (b). The peak at 9.05 eV is related to the SS; the signal intensity of this peak is decreased compared to the lower coverage. Four of the remaining five peaks yield equivocal slopes between 1 and 2. According to the results obtained for the submonolayer coverage these features are assigned to the states A, B, C and the HOMO-2. In addition to the five features observed before the spectrum contains an additional peak very close to the Fermi edge. Plotting its energetic position as a function of the photon energy (Figure 5.34 (b)) yields a slope of 2. This indicates that this feature can be related to photoemission from an occupied molecular state

5.3 Electronic Structure and Excited State Dynamics in DCV-substituted Oligothiophenes on Au(111)

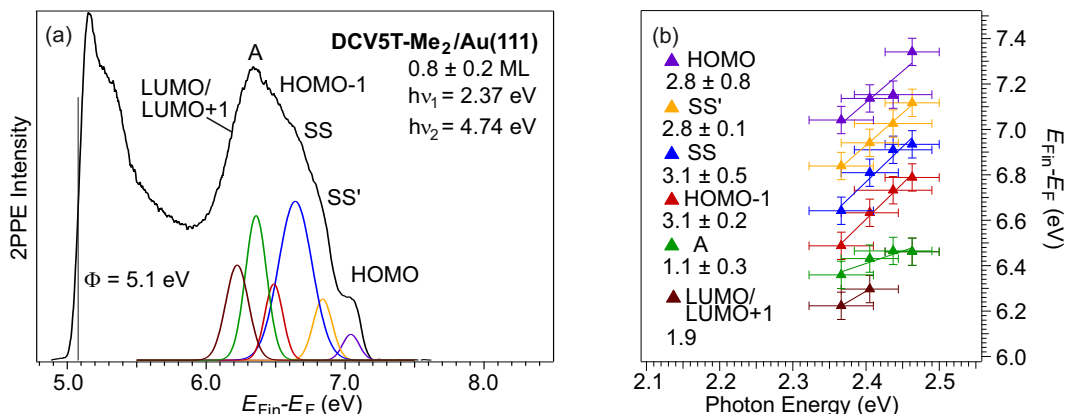


Figure 5.35: (a) 1C-2PPE spectrum of 0.8 ± 0.2 ML DCV5T-ME₂/Au(111), (b) peak positions as function of the photon energy.

0.1 eV below the Fermi level, which is assigned to the HOMO.

The newly discovered HOMO feature is more pronounced in the corresponding 2C-2PPE spectrum shown in Figure 5.35 (a). The features overlap strongly in this spectrum so that they can hardly be distinguished. In the secondary electron background close to the low energy cutoff a shoulder emerges indicating the excitonic signature which increases with the coverage until it dominates the complete spectrum as will be shown below. The signal between final state energies of 6 eV and 7.2 eV has been fitted with six Gaussians as depicted in Figure 5.35 (a). In Figure 5.35 (b) the peak positions are displayed as a function of $h\nu_1$, revealing four occupied states and two unoccupied states of which one is probed by the UV- and the other one by the vis-pulse. Among the occupied states are the HOMO, HOMO-2 and the SS observed before. The additional two occupied states correspond to states at binding energies of -0.6 and -0.3 eV. The first one is related to the HOMO-1 and the latter to the emission signal from the adsorbate covered surface state SS'. It is known that adsorption of atoms and molecules can lead to an energetic shift of the Shockley surface state as described before in Section 2.1.1. The unoccupied state probed by the UV-pulse is located 1.5 eV above the Fermi level and might be due to a superposition of the LUMO and LUMO+1. But this feature appears only as a shoulder in two spectra, therefore this assignment has to be treated with caution. The other unoccupied state probed by the vis-pulse corresponds to the peak A, which has been observed before.

To further track the evolution of the electronic structure upon increasing coverage 2PPE measurements have been performed on a coverage of 3 ± 1 ML DCV5T-Me₂ on Au(111). Figure 5.36 shows a 1C-2PPE spectrum (a) and the corresponding 2C-2PPE (b) spectrum of 3 ML DCV5T-Me₂ on Au(111). The 1C-2PPE spectrum was

recorded with a photon energy of 4.56 eV and is displayed as a function of the final state energy. Besides the features related to emission from the d-bands only three further features are visible. The very broad feature at a final state energy of 6.15 eV corresponds according to photon energy dependent measurements (not shown here) to an unoccupied state at 1.6 eV and is most likely related to a superposition of LUMO or LUMO+1 as observed before for the ML coverage. The two features at higher energies can be assigned to the peaks A and B. Both peaks appear to be broader than at lower coverages and peak A is shifted from 4.0 to 4.25 eV above the Fermi level while peak B is still located at 3.6 eV.

The 2C-2PPE spectrum of 3 ± 1 ML DCV5T-Me₂/Au(111) (Figure 5.36 (b)) is dominated by the excitonic feature which is probed by the UV-pulse, as will be shown below in the TR-2PPE spectra, and thus located around 0.8 eV above the Fermi level. The shoulder at 5.9 eV can be related to the LUMO at 1.3 eV. The other two features can be assigned as well to unoccupied states at 1.8 and 1.95 eV according to STS measurements by Yang *et al.* [Yan14a, Bog15]. They demonstrated that the LUMO shifts from 1.3 V to 1.8 V and the LUMO+1 from 1.65 V to 2.15 V going from the ML to the second layer due to electronic decoupling from the metal surface. Therefore the two unoccupied states are assigned to the shifted LUMO* and LUMO+1* of the second layer. A similar behaviour has been observed for octithiophene on Au(111), where the HOMO was electronically decoupled from the surface due to a change of the adsorption geometry induced by increasing the coverage from a submonolayer to a monolayer coverage, as discussed in Section 3.3.1 [Var11b].

To sum up the obtained molecular states they are listed in the energy level diagram shown in Figure 5.37 for (a) a submonolayer, (b) a monolayer and (c) a

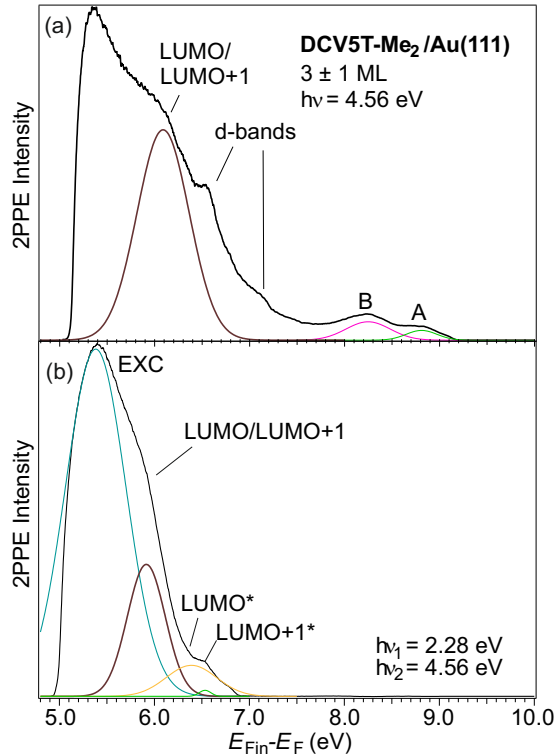


Figure 5.36: (a) UV spectrum and (b) 2C-2PPE spectrum of 3 ML DCV5T-Me₂/Au(111).

5.3 Electronic Structure and Excited State Dynamics in DCV-substituted Oligothiophenes on Au(111)

multilayer coverage DCV5T-Me₂ on Au(111). The energy levels are displayed here relative to the vacuum level, *i.e.* the LUMO levels correspond to the EA levels and the HOMO levels to the respective IP. The red-coloured states were obtained from the 2PPE measurements presented above, while the green-coloured levels were adopted from the STS results presented in Section 3.3.1 [Yan14b, Yan14a, Bog15]. Comparing the submonolayer- and the monolayer coverage the work function shifts

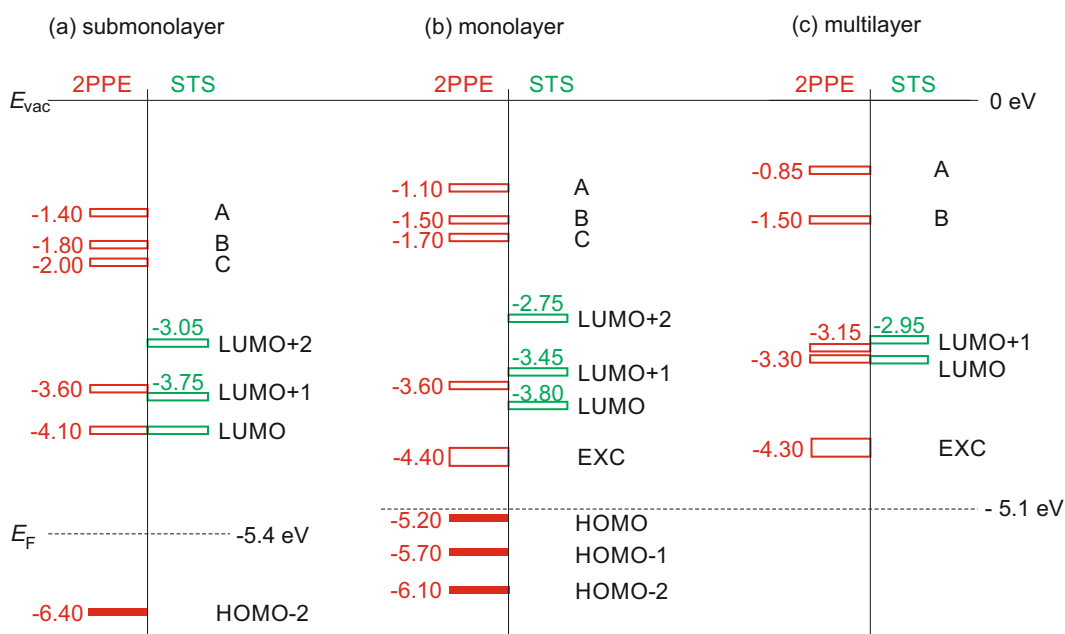


Figure 5.37: Energy level diagrams of (a) submonolayer, (b) monolayer and (c) multilayer coverages DCV5T-Me₂/Au(111). The HOMO levels and the red-coloured LUMOs result from the 2PPE measurements, while the green ones are adopted from the STS experiments [Yan14b, Yan14a, Bog15]. Note that no occupied states are observable at higher coverages most likely due to the enhanced signal intensity of the excitonic state which superposes the other signals.

by 0.3 eV, thus shifting the EA and IP levels as well by 0.3 eV. The HOMO and HOMO-1 appear only at a monolayer coverage while they could not be observed for the submonolayer coverage, most likely due to a photoemission intensity too weak to be resolved besides the other intense features. Since the HOMO is located very close to the Fermi level this is most probably a case of Fermi level pinning as introduced in Section 2.1.2. In the multilayer regime none of the occupied states was observable most probably due to the significantly enhanced photoemission intensity from the excitonic feature which dominates the spectra for coverages ≥ 3 ML and superposes all the other less intense features. For the monolayer coverage a HOMO-LUMO gap, *i.e.* a transport gap, of 1.4 eV is obtained which is by 0.5 eV smaller than the gap measured with cyclic voltammetry for the molecules in solution [Fit12b]. This

reduced HOMO-LUMO gap with respect to the 'free' molecule in solution indicates that the molecular levels are shifted towards the Fermi level due to interaction with the metal substrate as discussed in Section 2.1.2. In the second layer the LUMO and LUMO+1 are shifted upwards by 0.5 eV demonstrating electronic decoupling from the metal surface. The exciton binding energy amounts to 0.6 eV for the monolayer coverage and increases to 1.0 eV for the multilayer coverage. The latter compares well to the exciton binding energy of 0.9 eV obtained for 1 ML sexithiophene on Au(111) [Var11a].

The origin of the unoccupied states A, B and C has not been tackled so far. In a system consisting of a metal substrate and an organic semiconducting adsorbate layer different kinds of unoccupied states are possible:

- (i) Image potential states (IPS), as were found on tetracene and pentacene surfaces [Zhu09].
- (ii) Interface states (IS), which were observed before at organic/metal interfaces [Hag10, Mar14].
- (iii) Charge transfer (CT) excitons, as witnessed before at the surfaces of tetracene and pentacene [Yan09, Zhu09].
- (iv) Energetically higher located unoccupied molecular states (LUMO+ n).

These states can be at least partially distinguished since the first two examples, (i) and (ii), possess characteristic properties: Both types of unoccupied states are expected to exhibit a parabolic dispersion parallel to the surface and in addition image potential states are pinned to the vacuum level. Thus the first possibility, (i) the image potential states, can be ruled out since the energetic positions of A, B and C stay constant relative to the Fermi level, *i.e.* do not shift with the vacuum level, when the DCV5T₂ coverage is increased from the submonolayer to the monolayer regime.

In order to identify whether one of the states shows a dispersion, 1C-2PPE spectra of 2 ± 0.5 ML DCV5T-Me₂ on Au(111) were recorded as a function of the emission angle. Figure 5.38 (a) shows the spectra series, measured with a photon energy of $h\nu = 4.3$ eV, plotted as function of the final state energy. For this photon energy and coverage only peaks A, B and the HOMO-1 are visible. The peak positions are plotted as a function of the angle in Figure 5.38 (b) demonstrating clearly that none of the investigated states shows a dispersion. With this result the second possibility, (ii) the interface states, can be excluded as well. The possibilities still left are (iii) the CT states and (iv) the higher lying unoccupied molecular orbitals. The charge transfer excitons observed before at vacuum interfaces with tetracene and pentacene

5.3 Electronic Structure and Excited State Dynamics in DCV-substituted Oligothiophenes on Au(111)

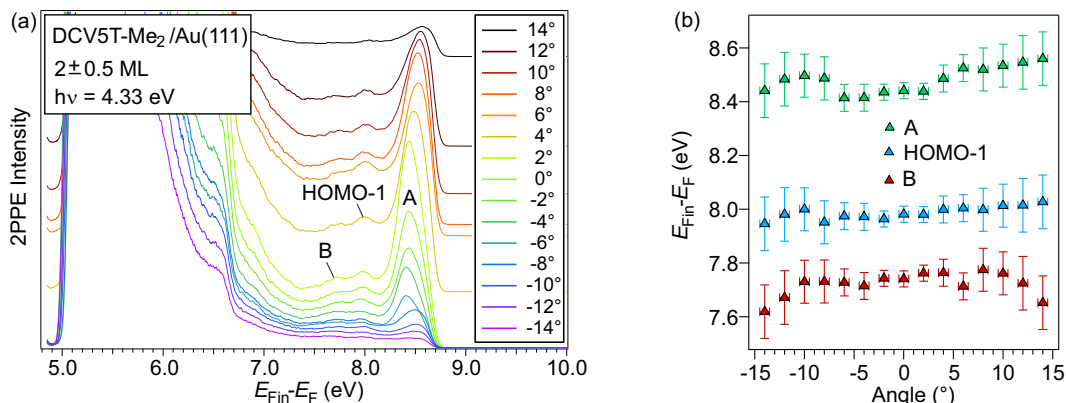


Figure 5.38: (a) 2C-2PPE spectra series of 2 ML DCV5T-Me₂/Au(111) and (b) peak maxima as a function of the angle: None of the studied states shows a dispersion.

appeared always in the vicinity of IPS [Yan09, Zhu09]. Since no IPS was observed here the states A, B and C originate most likely from higher lying LUMO+*n* levels and not from charge transfer states at the molecule/vacuum interface.

In the next section the electronic structure of DCV6T on Au(111) will be investigated accordingly.

5.3.2 Coverage-Dependent Electronic Structure of DCV6T/Au(111)

In the following the electronic structure as a function of DCV6T coverage on Au(111) is investigated with focus on occupied states, energetically higher located unoccupied states and the electronic structure of the multilayer regime, which have not been observed by STS. For DCV6T adsorbed on Au(111) an electronic structure similar to the one of DCV5T-Me₂ is expected according to adsorption measurements of both molecules yielding comparable optical gaps [Fit11, Fit12b, Yan14a]. In addition the LUMO levels from STS measurements agree very well [Yan14a].

Figure 5.39 (a) shows an exemplary 1C-2PPE spectrum of 1.4 ± 0.4 ML DCV6T on Au(111) recorded with a photon energy of 4.6 eV. The spectrum is displayed as a function of the final state energy where the low energy cutoff corresponds to the work function, which amounts here to $\Phi = 5.1$ eV. Besides the features related to the d-bands of the Au(111) surface there are three peaks located at final state energies between 8 eV and 9 eV which are labeled A, B and HOMO-1. This already anticipates the peak assignment, which is based on the one hand on the slopes yielded by the plot of the peak positions as a function of the photon energy, shown in Figure 5.39 (b), and on the other hand on the electronic structure found for the related DCV5T-Me₂. The features A and B yield slopes of ≈ 1 indicating that those are due to unoccupied states located 4.1 eV and 3.7 eV above the Fermi level. These

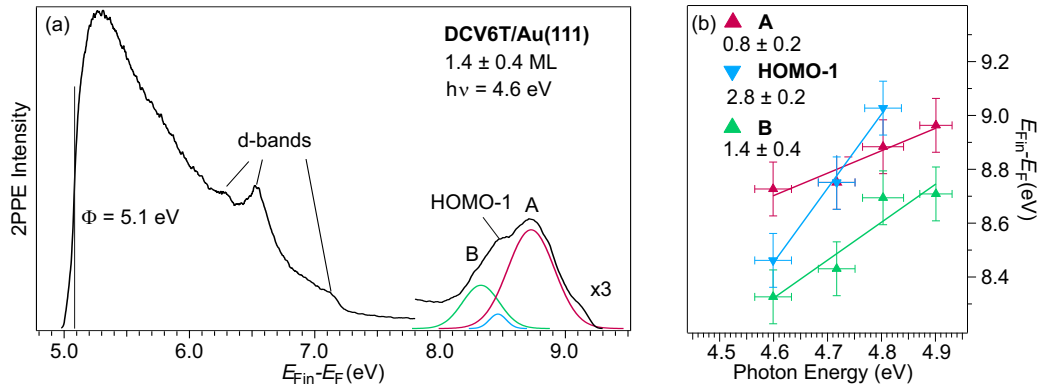


Figure 5.39: (a) 1C-2PPE spectrum of 1.4 ML DCV6T/Au(111), (b) peak positions as function of the photon energy.

energetic positions remind strongly of features A and B observed for DCV5T-Me₂ (A: 4.0 eV, B: 3.6 eV) and are thus named after them. The slope of the third peak amounts to 2.8 instead of 1 or 2. This deviant behaviour can be explained with the deficient quality of the data; the features overlap strongly and none of the recorded spectra shows all three peaks separated from each other. Since 2.8 is closer to 2 than to 1 it can be assumed that this feature is due to photoemission from an occupied state located 0.6 eV below the Fermi level which may be related to the HOMO-1, in accordance to the HOMO-1 of DCV5T-Me₂.

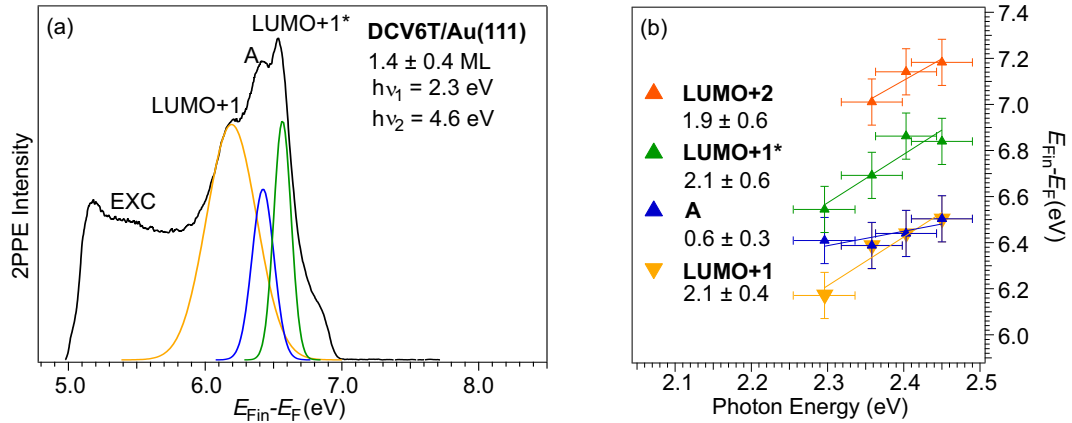


Figure 5.40: (a) 2C-2PPE spectrum of 1.4 ML DCV6T/Au(111), (b) peak positions as function of the photon energy.

Figure 5.40 (a) shows the corresponding 2C-2PPE spectrum measured with $h\nu_1 = 2.3$ eV and $h\nu_2 = 4.6$ eV. The spectrum exhibits as well strongly overlapping peaks but three peak maxima are clearly visible here. Although this spectrum shows three peaks at final state energies between 6 eV and 6.7 eV the positions of four peaks

are displayed as a function of the photon energy in Figure 5.40 (b). This is because none of the recorded spectra shows all four peaks simultaneously. Three of the peaks yield slopes of ≈ 2 indicating that they result from unoccupied states probed by the UV pulse and are thus located 1.6 eV, 2.0 eV and 2.3 eV above the Fermi level. According to the unoccupied states derived from STS measurements the states at 1.6 eV and 2.3 eV are assigned to the LUMO+1 and LUMO+2 [Yan14b, Yan14a, Bog15]. The unoccupied state at 2.0 eV might be related to the LUMO+1* of the second layer shifted to higher binding energies due to electronic decoupling from the metal surface, as discussed for DCV5T-Me₂ and in Section 2.1.2. The fourth feature is related to peak A (4.1 eV), although yielding a slope of 0.6, according to the 1C-2PPE spectrum shown in Figure 5.39 (a). Close to the secondary electron cutoff the broad excitonic feature emerges which increases in intensity for higher coverages as shown below in Figure 5.41 (b).

In order to investigate the electronic structure of the multilayer coverage, 2PPE measurements on 4 ± 1 ML DCV6T on Au(111) have been performed. Figure 5.41 (a) displays a 1C-2PPE spectrum measured with $h\nu = 4.6$ eV as a function of the final state energy. The work function decreases by 0.1 eV to 5.0 eV in comparison to the 1.4 ML coverage. The peaks A and B are broadened and shift by 0.1 eV to higher binding energies of 4.2 eV and 3.7 eV upon adsorption of additional DCV6T. Figure 5.41 (b) shows the corresponding 2C-2PPE spectrum recorded with $h\nu_1 = 2.3$ eV and $h\nu_2 = 4.6$ eV. A broad feature rises at a final state energy of 5.5 eV and is related to the exciton located 0.9 eV above the Fermi level, *i.e.* probed by $h\nu_2$, as will be shown below in TR-2PPE spectra. This feature dominates the spectrum, so that the other features appear only as shoulders of this intense peak. The feature at a final state energy of 5.9 eV could be either due to an occupied state 1.0 eV below the

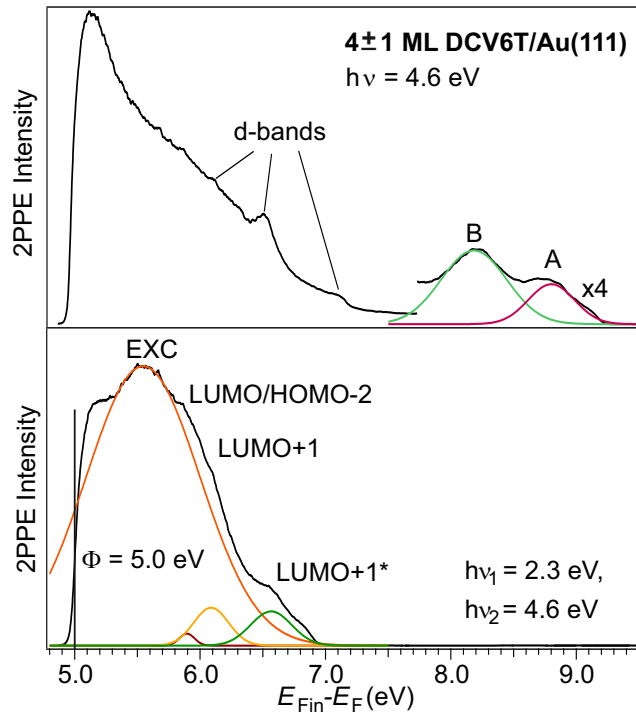


Figure 5.41: (a) 1C-2PPE and (b) 2C-2PPE spectra of a multilayer DCV6T/Au(111)

Fermi level, most probably the HOMO-2, or to an unoccupied state at 1.3 eV, *i.e.* the LUMO of the monolayer according to the STS measurements [Yan14a]. Since both energetic positions are in accordance with the electronic structure observed so far it might as well be a superposition of both states. The two other features can be related to the LUMO+1 at 1.6 eV and the multilayer LUMO+1* at 2.0 eV as observed before in the case of DCV5T-Me₂.

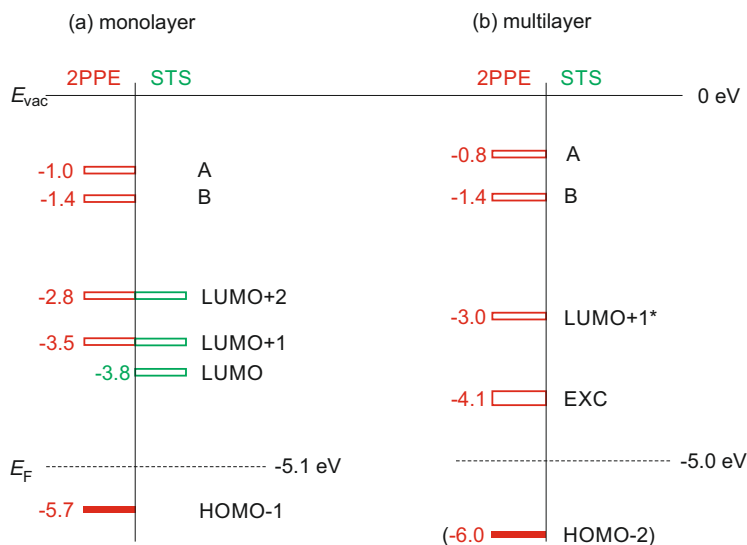


Figure 5.42: Energy level diagram of (a) a monolayer and (b) a multilayer coverage DCV6T on Au(111).

The electronic structure is summed up in an energy level diagram shown in Figure 5.42 (a) for the monolayer and (b) the multilayer coverage with respect to the vacuum level. For the monolayer coverage a fairly complete picture of the electronic structure of DCV6T on Au(111) was obtained merging 2PPE and STS results. Four unoccupied states were measured of which two are assigned to the LUMO+1 and the LUMO+2 in accordance with STS measurements [Yan14a]. The other two unoccupied states A and B originate most likely from higher lying unoccupied molecular orbitals following the interpretation for DCV5T-Me₂ on Au(111) in Section 5.3.1 [Bog15]. The HOMO could not be observed here, but due to the striking similarity to DCV5T-Me₂ the possibility is high that it is located very close to the Fermi level as it is the case for DCV5T-Me₂. Under this assumption the HOMO-LUMO gap of the ML would amount to 1.4 eV, which is by 0.18 eV lower than the gap derived from cyclic voltammetric measurements [Fit11]. This can be explained by the stabilization of the molecular levels due to interaction with the metal surface as described before in Section 2.1.2. Here no exciton binding energy is obtained since for the ML coverage no exciton is observed and in the case of the multilayer the position of the

LUMO is unknown. With increasing coverage the LUMO+1 state shifts to higher binding energies due to the decoupling from the metal surface, as observed before for DCV5T-Me₂. At coverages of $\approx 3 - 4$ ML a broad feature emerges whose signal intensity increases with the coverage and can be related to an excitonic state, as will be treated in detail in Section 5.3.4.

The electronic structure observed for DCV6T is very similar compared to the electronic structure of DCV5T-Me₂, which is in agreement with the results obtained from absorption spectroscopy and STS [Fit11, Fit12b, Yan14a]. In the next two sections the excited state dynamics as function of the coverage will be presented and discussed.

5.3.3 Excited State Dynamics in DCV5T-Me₂ on Au(111)

In this section the excited state dynamics of different coverages of DCV5T-Me₂ on Au(111) will be investigated by means of TR-2PPE. The excited state dynamics of the DCV-substituted thiophenes are of great interest since up to now no time-resolved experiments have been reported. Especially the question whether the different solar cell efficiencies yielded by the molecules are reflected in the dynamics is crucial. First TR-2PPE spectra of two different coverages will be presented and the influence of the metal substrate on the dynamics will be discussed. Then the dynamics measured on a thick DCV5T-Me₂ film will be debated.

To investigate the excited state dynamics as a function of the DCV5T-Me₂ film thickness time-resolved 2PPE measurements were performed on different coverages. Figure 5.43 shows time-resolved 2PPE spectra of (a) 10 ± 3 ML and (b) 20 ± 5 ML measured with photon energies of $h\nu_1 = 2.28$ eV and $h\nu_2 = 4.56$ eV. The photoemission signal observed here for positive delays originates from initially unoccupied intermediate states pumped with $h\nu_1$ and probed with $h\nu_2$. The signal originating from monochromatic 2PPE processes was subtracted, as explained before in Section 4.5. The intermediate state energy relative to the Fermi level is plotted as a function of the pump-probe delay and the signal intensity is illustrated by a false colour code (white corresponds to 100 % and dark blue to 0 % intensity). The electrons are excited above the optical gap and relax on a femtosecond time-scale into a broad long-lived state, which can be related most probably to an excitonic state and will be referred to as such from now on. The broad long-lived feature has a maximum around 0.8 eV and dominates the spectra of both coverages. This can be observed as well in Figure 5.43 (c) where 2PPE spectra taken on different coverages and a pump-probe delay of $t = 0$ ps are displayed as a function of the intermediate state energy. Comparing the 2PPE spectra taken on 4 ± 1 , 10 ± 3 and 20 ± 5 ML DCV5T-Me₂ on Au(111) reveals that the dominance of the excitonic feature over

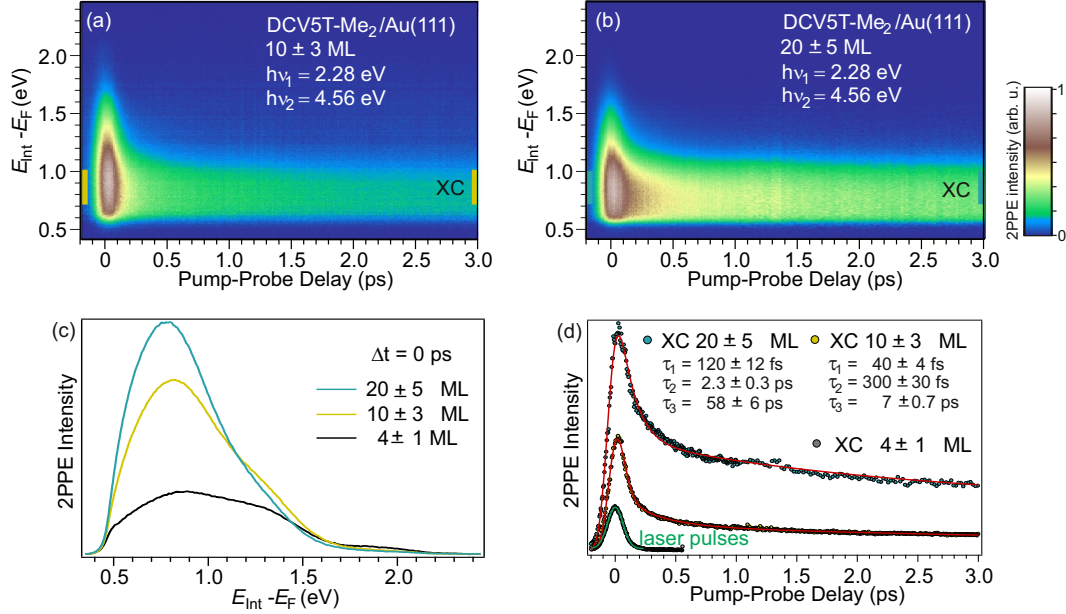


Figure 5.43: Time-resolved 2PPE spectra of (a) 10 ML and (b) 20 ML DCV5T-Me₂/Au(111), (c) spectra taken at $t = 0$ and (d) corresponding XC-traces.

the other features increases as a function of the coverage. Taking a closer look at the time-resolved spectra depicted in Figure 5.43 (a) and (b), which are both plotted in the same time interval from -0.2 to 3 ps, suggests that the long-lived state has a longer lifetime in the 20 ML than in the 10 ML film. This assumption is confirmed comparing the corresponding XC-traces. Figure 5.43 (d) shows the XC-traces obtained by integrating the time-resolved spectra over an energy range from 0.7 - 1.0 eV, as indicated by the coloured bars in the respective spectra. The XC-trace of the 4 ML coverage (grey dots) shows no lifetime within the experimental resolution, in contrast to the XC-traces of the 10 ML (yellow dots) and the 20 ML coverage (blue dots). These XC-traces can be described with a triexponential decay convolved with the XC of the laser pulses which is depicted by the green Gaussian curve. The fit yields time constants of $\tau_1 = 40 \pm 4$ fs, $\tau_2 = 300 \pm 30$ fs and $\tau_3 = 7 \pm 0.7$ ps for the 10 ML coverage, which was measured up to a time delay of 10 ps. For the 20 ML coverage, which was measured for a longer time range up to 50 ps, time constants of $\tau_1 = 120 \pm 12$ fs, $\tau_2 = 2.3 \pm 0.3$ ps and $\tau_3 = 58 \pm 6$ ps were obtained. The time constants clearly demonstrate an increase of the lifetime as a function of the coverage. A coverage-dependent lifetime indicates the existence of two different decay channels: an extrinsic channel depending on the interaction with the substrate and an intrinsic decay channel, which consists of processes such as recombination and/or relaxation into other states. The lifetime converges to the intrinsic decay rate for

high coverages when the excited state population in the upmost layers, probed by 2PPE, is not affected anymore by the substrate, as discussed in Section 2.2.2. Such an increase of lifetime as function of the distance to the metal surface has been observed before for C_{60} and 6T on Au(111) [Dut05, Var12a].

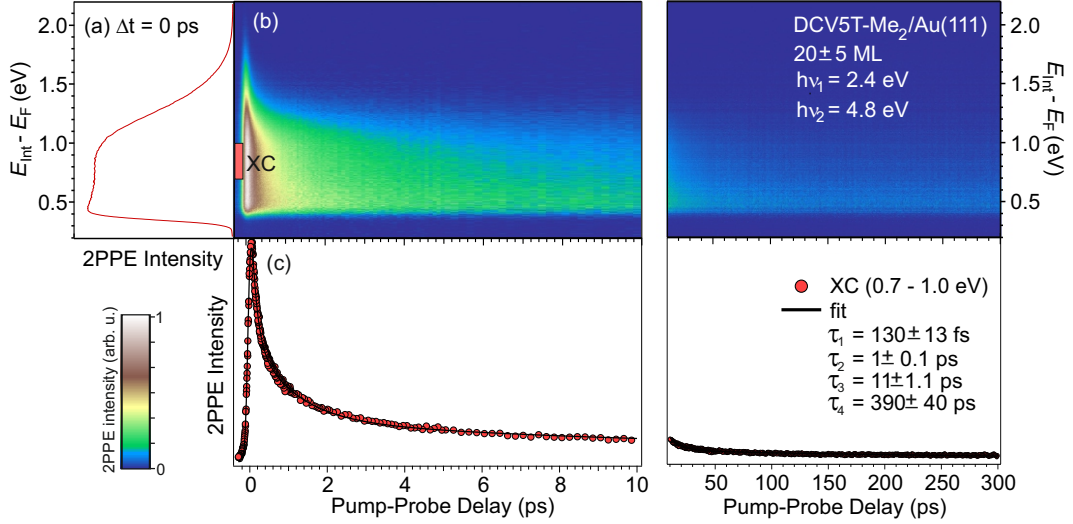


Figure 5.44: (a) 2PPE spectrum of 20 ML DCV5T-Me₂ at $t = 0$ ps, (b) time-resolved spectrum and (c) the XC-trace, described by a quadruple exponential decay.

To gain deeper insight into the excited state dynamics of a high coverage DCV5T-Me₂ on Au(111) a 20 ± 5 ML film was measured with a pump photon energy of $h\nu_1 = 2.4$ eV and a probe photon energy of $h\nu_2 = 4.8$ eV for pump-probe delays up to 300 ps. The resulting time-resolved spectrum is depicted in Figure 5.44 (b). The intermediate state energy is plotted as a function of the pump-probe delay, in the left part from -0.2 to 10 ps and in the right part from 10 - 300 ps. The spectrum is dominated by the broad excitonic feature with a maximum at an intermediate state energy of ≈ 0.8 eV. The XC trace displayed in Figure 5.44 (c) as a function of the pump-probe delay, analogous to the time-resolved spectrum in two parts, was obtained by integrating the time-resolved spectrum between 0.7 and 1.0 eV. It exhibits a rapid decay within the first 2 ps during which $\approx 2/3$ of the excited state population decays. After that the decay slows down significantly and a small amount of the initial population exhibits a lifetime of several hundred ps. The XC trace was fitted with an empirical fit function consisting of a quadruple exponential decay convolved with the XC of the laser pulses. The obtained time constants amount to $\tau_1 = 130 \pm 13$ fs, $\tau_2 = 1 \pm 0.1$ ps, $\tau_3 = 11 \pm 1.1$ ps and $\tau_4 = 390 \pm 40$ ps. Since the spectrum shows no structure it is not possible to energetically separate the involved states and to disentangle the involved processes. Therefore the

time constants obtained from the fit cannot be assigned to certain decay processes explicitly. In addition no time-resolved measurements of the investigated thiophene have been reported so far in the literature, therefore no information on e.g. the photoluminescence lifetime is available. With an excitation energy of 2.4 eV it should be possible to excite more than one excitonic state since the absorption spectrum of a 30 nm thick film shows absorption between 1.7 eV (optical gap) and 2.8 eV which is attributed to the transitions from the ground state (S_0) to the first (S_1) and the second excited states (S_2) [Fit12b]. This might be a reason for the broad signal and the multiexponential decay.

Processes which may take place on fs time scales are for instance polarization due to the exciton formation process or electron transfer from the S_2 to the S_1 . The latter process has been reported to take place within several hundred fs when higher vibronic levels of the S_2 are excited in $C_{60}/Au(111)$ [Dut05]. The time constant of 1 ps could be related to internal vibrational relaxation within the excited states due to excitation of higher vibronic levels. This assumption is supported by the strong coupling of excited electrons to vibrational states which has been observed in STS measurements on the second DCV5T-Me₂ layer on Au(111), as described in Section 3.3.1 [Yan14a, Bog15]. The long lifetimes of 11 and 390 ps might be related to polaron or trap states into which the excitonic state might decay, to electron-hole recombination and/or diffusion towards the metal interface.

The next section focuses on the excited state dynamics in DCV6T on Au(111) and the dynamics of the two molecules will be compared.

5.3.4 Excited State Dynamics in DCV6T on Au(111)

The excited state dynamics in DCV6T on Au(111) are investigated as a function of the distance to the metal surface analogous to DCV5T-Me₂/Au(111). Figure 5.45 displays time-resolved spectra of two different coverages, 3 ± 1 ML and 5 ± 2 ML, DCV6T on Au(111). The observed signal intensity corresponds to emission from unoccupied states which were pumped with a photon energy of 2.3 eV and probed by 4.6 eV photons. The emission signal in the time-resolved spectrum of a 3 ± 1 ML thick DCV6T film on Au(111), shown in Figure 5.45 (a), exhibits a slightly asymmetric shape while the spectrum recorded on a 5 ± 2 ML coverage looks clearly asymmetric towards positive delays. This reveals that in this coverage regime the excited state starts to retain a measurable lifetime. The corresponding XC-traces are displayed in Figure 5.45 (c) as a function of the pump-probe delay and are fitted with a biexponential decay convolved with the XC of the laser pulses which corresponds to the black curve. The biexponential fit yields lifetimes of $\tau_1 = 53 \pm 6$ fs, $\tau_2 = 325 \pm 33$ fs for the 5 ML coverage and for the 3 ML coverage a bit

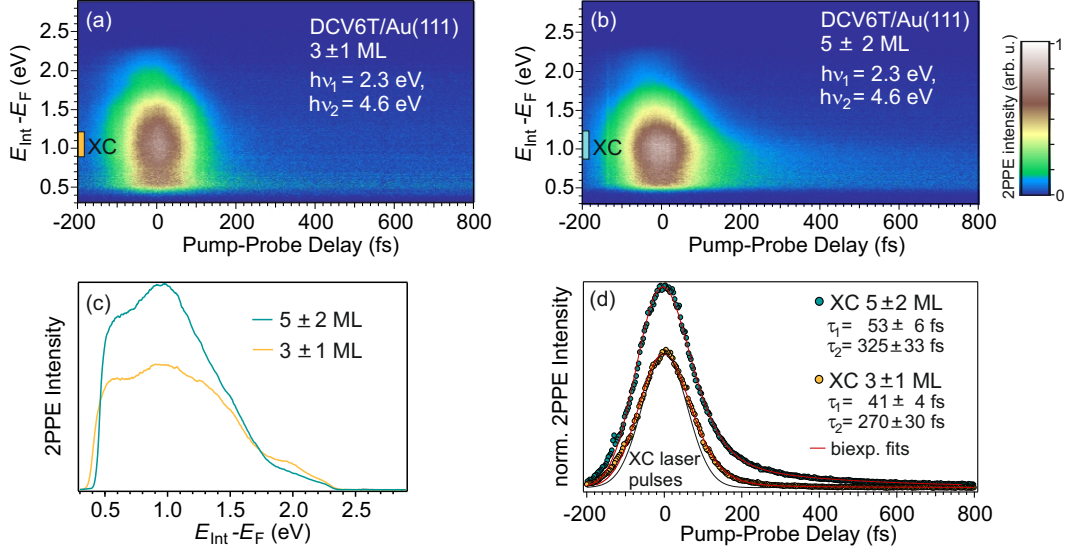


Figure 5.45: Time-resolved 2PPE spectra of (a) 3 ML and (b) 5 ML DCV6T on Au(111), (c) the corresponding spectra at $t = 0$ ps and (d) XC-traces.

shorter time constants of $\tau_1 = 41 \pm 4$ fs and $\tau_2 = 270 \pm 30$ fs. The time constants obtained from the biexponential fits indicate the evolution of a yet short lifetime. In Figure 5.45 (b) the 2PPE spectra of 3 and 5 ML DCV6T on Au(111) taken at zero pump-probe delay are displayed as a function of the intermediate state energy. The broad emission signal increases with the coverage and has a maximum around 0.9 eV above the Fermi level. So far the behaviour of the excited state dynamics as a function of the coverage is similar to DCV5T-Me₂.

In order to study the excited state dynamics of a higher DCV6T coverage time-resolved measurements on a 20 ± 5 ML thick film were carried out with a pump photon energy of $h\nu_1 = 2.4$ eV and a probe energy of $h\nu_2 = 4.8$ eV. Figure 5.46 (b) shows the resulting time-resolved spectrum as a function of the intermediate state energy and the pump-probe delay from -0.2 - 10 ps. The spectrum is as well dominated by a broad emission signal with its maximum at 0.7 eV, as can be seen as well in the 2PPE spectrum taken at $t = 0$ ps in Figure 5.46. The peak maximum is here 0.2 eV lower in energy compared to the peak maximum at low coverages; this decrease in binding energy indicates the stabilization of the exciton due to polarization of the neighbouring molecules, as observed before for C₆₀/Au(111) by Dutton *et al.* [Dut05]. The signal intensity in the time-resolved spectrum decreases only very slowly within the measured 10 ps. The XC-trace, displayed below in Figure 5.46 (c) was described with a triexponential decay, yielding time constants of $\tau_1 = 200 \pm 20$ fs, $\tau_2 = 1.4 \pm 0.2$ ps and $\tau_3 = 70 \pm 7$ ps. The third time constant

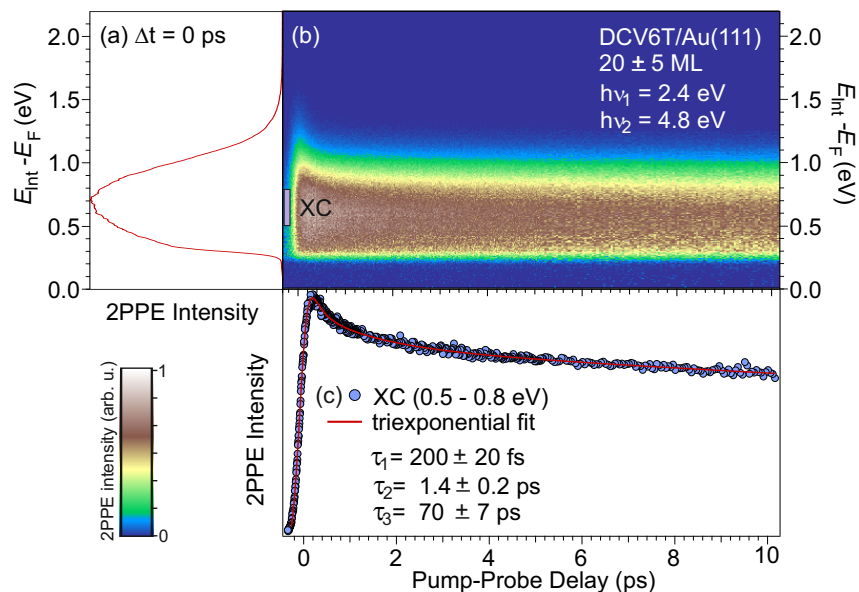


Figure 5.46: (a) 2PPE spectrum of a 20 ML thick DCV6T film on Au(111) recorded at $t = 0$ ps, (b) time-resolved spectrum measured up to a pump-probe delay of 10 ps and (c) XC-trace described by a triexponential empirical fit function.

exceeds the measured time range and a further slowing down of the decay can be assumed. This would require a fourth component to describe the overall decay as it is the case for DCV5T-Me₂. Due to the broad emission signal which does not allow to disentangle different states no unambiguous assignment can be made for the obtained time constants. The possible decay and relaxation mechanisms taking place on the respective time scales have been discussed before in Section 5.3.3.

In the following paragraph the dynamics of the two DCV-substituted thiophenes will be compared in order to find out whether the obtained results reflect the better solar cell performance of DCV5T-Me₂ compared to DCV6T.

To compare the dynamics of the two molecules the XC-traces of the 20 ± 5 ML thick DCV5T-Me₂ and DCV6T films are plotted as a function of the pump-probe delay and normalized to the maximum signal intensity in Figure 5.47. The striking difference between these two XC-traces are the different amplitudes. Whereas for DCV5T-Me₂ the intensity drops by more than 2/3 within the first two ps only a small decrease in intensity is observed for DCV6T. This indicates that the ultrafast decay processes are much more efficient in the case of DCV5T-Me₂. This might be due to a stronger coupling to vibrational states. In order to compare the time constants the DCV5T-Me₂ XC-trace was fitted in a time range between -0.2 and 10 ps (before normalization) with the triexponential decay function employed before to fit the

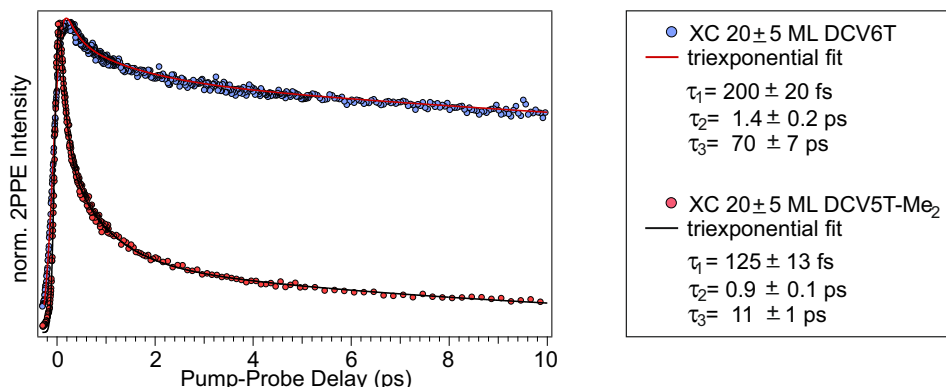


Figure 5.47: Comparison of the normalized XC-traces of 20 ML thick DCV5T-Me₂ and DCV6T films on Au(111) in a time interval between -0.2 to 10 ps, both fitted with the same triexponential decay function: The dynamics in DCV6T is significantly slower than in DCV5T-Me₂.

DCV6T XC-trace. The time constants obtained with this fit are in good accordance with the first three time constants yielded before by the quadruple exponential fit (which was used to fit the complete XC-trace up to a pump-probe delay of 300 ps). A comparison of the time constants reveals that especially the third component is significantly slower in the DCV6T film than in DCV5T-Me₂. This ps lifetime might be related to the exciton or polaron lifetime, which is considerably faster in DCV5T-Me₂. This may have several reasons such as a faster recombination rate or faster exciton diffusion, or charge carrier transport in the case of polarons, away from the surface towards the metal interface where charge transfer occurs. A faster electron-hole recombination rate seems unlikely due to the very similar optical properties of the two molecules known so far. In DCV5T-Me₂ crystals a greater number of intermolecular interactions, which are known to promote the exciton mobility, was found and employed as an explanation for the superior performance of solar cells containing DCV5T-Me₂ [Fit12b, Fit12a, Sch12b]. In a solar cell efficient diffusion allows excitons to travel fast to the donor/acceptor interface where the charges are separated, resulting thus in a high photon to electron conversion.

Summary

In the following the findings on the electronic structure and excited state dynamics in DCV5T-Me₂ and DCV6T on Au(111) are concluded. The electronic structure, from the submonolayer to the multilayer regime, of the DCV-substituted thiophenes on Au(111) was found to be very similar and in good accordance with STS measurements [Yan14a, Bog15]. At submonolayer coverages hybridization of the molecular states with the metal surface leads to a decrease of the HOMO-LUMO gap, which

opens up again in the second layer when the molecules are electronically decoupled from the surface. Time-resolved 2PPE measurements demonstrate coverage dependent excited state lifetimes indicating interaction with the metal surface which is quenched for higher coverages. In addition TR-2PPE revealed that the dynamics in DCV6T films is slower than in DCV5T-Me₂ films. This can be explained by a more efficient exciton and carrier diffusion in DCV5T-Me₂ films due to enhanced intermolecular interactions *via* the methyl-groups which are correlated with the solar cell efficiency [Fit12b, Fit12a, Sch12b]. To obtain a complete picture of the elementary electronic processes in these systems further investigations using time-resolved optical spectroscopy such as transient absorption or time-resolved photoluminescence would be attractive since they promise information about e.g. the recombination lifetime.

5.4 Electronic Properties of P3HT Films and the Influence of Crystallinity

P3HT is a semiconducting conjugated polymer which has been investigated extensively due to its high carrier mobility and easy processibility. The film morphology of π -conjugated polymers is known to have a significant impact on the electronic structure, charge carrier transport and exciton diffusion and dissociation [Pan15].

In this work the influence of annealing on the electronic structure and excited state dynamics in RR-P3HT films is investigated. As previous 2PPE studies of RR-P3HT films did not yield well resolved spectra [Var12c, Soh07] we aim to demonstrate that 2PPE is a good method to study as well highly defined polymer films. In the following sections a comparative 2PPE study of two P3HT films with different degrees of crystallinity is presented.

Direct photoemission measurements demonstrate that the IP is not influenced by enhanced crystallinity. In contrast the optical gap increases upon annealing, as the CBM shifts upwards. Further 2PPE experiments reveal the existence of additional three unoccupied electronic states. One of the states can be related to the exciton while the second feature is most likely due to polaron pairs and/or polarons. The third unoccupied state might be due to a higher lying unoccupied band or an excitonic state and is shifted to lower energies for the annealed sample. Moreover the peak width of the features was found to decrease upon annealing. Compared to previous 2PPE measurements on RR-P3HT films the spectra obtained in this work are of good quality and allow to determine the electronic structure of the two samples.

Time-resolved 2PPE measurements reveal multiexponential decays for both excited states. The exciton decay takes place on a slower time scale than the polaron pair and/or polaron decay. Comparing the dynamics of the two different films shows that the decay dynamics are faster in the mc-sample than in the as-sample. This can be explained by the larger fraction of crystalline phases which are known to control and promote the transport properties in P3HT.

5.4.1 Electronic Structure of P3HT Films with Different Degrees of Crystallinity

In the following section the electronic structure of two P3HT films with different degrees of crystallinity is investigated by means of 2PPE. The high purity RR-P3HT was synthesized in the group of M. Thelakkat (University Bayreuth) [Wu10]. The 50 nm thick P3HT films were prepared in the group of T. Thurn-Albrecht (University Halle-Wittenberg), as described before in Section 3.5 [Wu10]. One of the films was heated in nitrogen atmosphere above the melting point after spin-coating and is thus referred to as melt-crystallized (mc) while the non-annealed film is denoted as-spun (as). The P3HT-mc film is expected to exhibit a higher degree of crystallinity as a result of annealing than the P3HT-as film. The measurements were carried out at room temperature. To create electric contact, required for the application of a bias voltage and to prevent charging, a Ta clip was used to connect the polymer film with the sample holder. The photoemission features observed in the spectra can be described by Gaussians and although the picture of molecular orbitals may still be appropriate for this rather short polymer (39 repeating units), I will employ the concept of bands as commonly used for polymers.

In order to study the occupied electronic structure of the two P3HT samples, direct photoemission spectra were recorded with a photon energy of $h\nu = 6.2$ eV.

Figure 5.48 displays three direct photoemission spectra plotted as a function of the binding energy. The yellow spectrum corresponds to the P3HT-mc film and the blue one to the P3HT-as film. These spectra are normalized to the maximal photoemission intensity and exhibit both a similar shape. Besides the secondary electron background a broad photoemission signal dominates the spectra. The black spectrum was taken on a metallic sample used as reference to define the Fermi level. The work function of the samples can be determined after

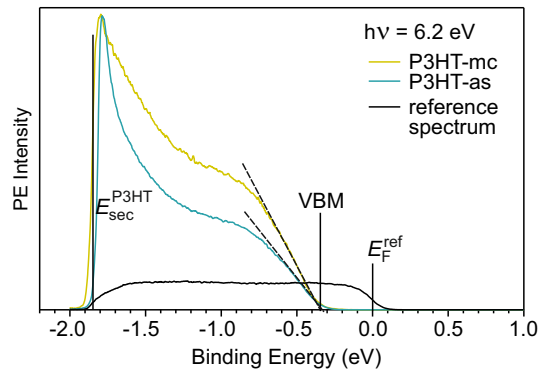


Figure 5.48: Direct photoemission spectra of P3HT-mc and -as, and a reference spectrum for the determination of the Fermi level.

$$\Phi = h\nu - (E_F^{\text{ref}} - E_{\text{sec}}^{\text{P3HT}}) \quad (5.73)$$

This yields for P3HT-mc a work function of $\Phi_{\text{mc}} = 4.35$ eV and for the P3HT-as film a workfunction of $\Phi_{\text{as}} = 4.37$ eV, which is a negligible difference since it is within

the work function error of 0.03 eV.

The broad feature in the photoemission spectra shown in Figure 5.48 can be related to photoemission from the valence band (VB). The valence band maxima (VBM) of both samples are found at a binding energy of 0.33 eV below the Fermi level of the reference sample, thus yielding an IP of 4.7 eV. This demonstrates that the occupied electronic structure is not affected by the samples' different degrees of crystallinity. In comparison with literature the IP coincides perfectly to the IP of 4.7 eV observed by Kanai *et al.* who found as well that the IP was not affected by annealing [Kan10]. The IP measured by Frisch *et al.* [Fri11] shifted from 4.55 eV to 4.6 eV upon annealing which compares well with our results although they used another substrate, as discussed before in Section 3.5.

Further investigations of the electronic structure of the P3HT-mc and -as films were carried out employing 2PPE. Figure 5.49 displays 1C-2PPE spectra of the (a) P3HT-mc and (b) P3HT-as films plotted as a function of the final state energy. The spectra were recorded with a photon energy of 4.15 eV. Qualitatively the spectra of both films look very similar, both exhibit two rather broad peaks labeled A and CB. An additional low intensity feature, labeled C, is observed at higher final state energies for both films. A clear difference between the spectra taken on the two different samples is that the peaks A and CB are more pronounced in the case of the mc-film and feature C is located ≈ 0.25 eV lower in energy than for the as-film. The

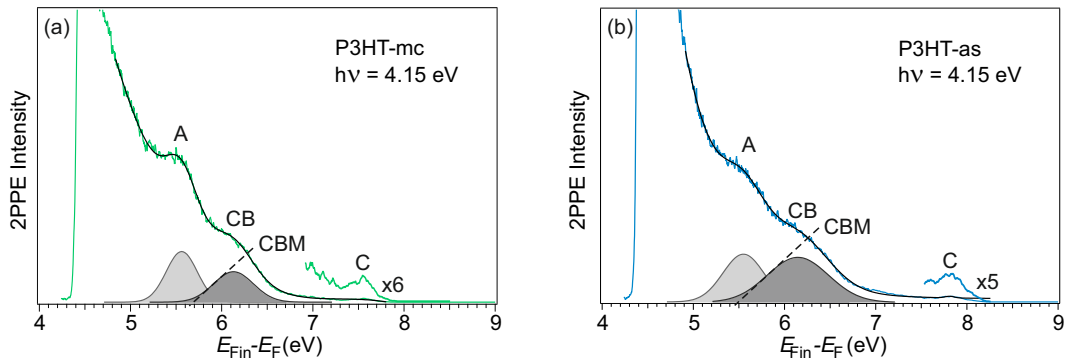


Figure 5.49: 1C-2PPE spectra of (a) P3HT-mc and (b) P3HT-as films .

black lines correspond to fits which consist of three Gaussians and an exponential background, they describe the features A and CB well but the low intensity feature C cannot be fitted satisfactorily. The Gaussian shaped peaks obtained from the fits are plotted below the spectra, revealing that the peak width in the case of the mc-film are narrower than for the as-sample. This is in accordance with the findings of Kanai *et al.* [Kan10] who observed as well a decrease of the peak width upon annealing.

The feature labeled CB is related to the conduction band of P3HT, as will be discussed below, and the CBM is determined by extrapolating the rising edge of the Gaussian to the baseline. This yields CBM at final state energies of 5.65 eV for P3HT-mc and 5.5 eV for P3HT-as, *i.e.* intermediate state energies of 2.85 eV and 3.0 eV below the vacuum level. This upward shift of the CBM upon annealing is here due to the decrease of the peak width, while the peak maximum stays at the same energetic position. Note that the energetic positions of the unoccupied electronic states obtained here from 2PPE can not be compared to those from IPES from reference [Kan10]. IPES measures an $(N+1)$ -electron state while 2PPE measures in this case an N -electron state as the unoccupied states are populated *via* intermolecular excitations and not through electron transfer from the substrate to the adsorbate.

In order to be able to assign the observed features to occupied or unoccupied states, photon energy dependent measurements were performed. Figure 5.50 (a) displays a 1C-2PPE spectra series measured on the P3HT-mc film as a function of the final state energy. In the spectrum recorded with a photon energy of 4.15 eV the features A and CB are visible very clearly while they have vanished in the 4.4 eV spectrum. In Figure 5.50 (b) the peak positions are plotted as a function of

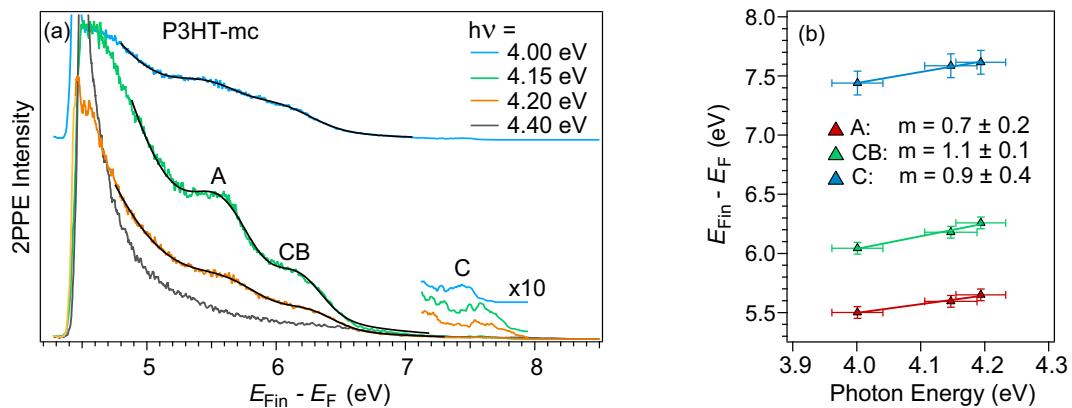


Figure 5.50: (a) Photon energy dependent 1C-2PPE spectra series taken on P3HT-mc, (b) peak maxima plotted as a function of the photon energy, indicating that all three features originate from unoccupied intermediate states.

the photon energy, yielding a slope around 1 in all three cases. This indicates that all three the peaks can be assigned to unoccupied states or bands. As mentioned before CB is related to the conduction band with its minimum 2.85 eV below the vacuum level. This assignment is based on the energetic position of the CBM which is located 1.85 eV above the VBM. This value corresponds to the optical gap and compares well with the literature value around 1.8 - 1.9 eV [Kor01, Sch14, Co08].

The features A and C can be related to unoccupied intermediate states located 2.95 eV (A) and 0.95 eV (C) below the vacuum level. Feature A is thus located 1.75 eV above the VBM and is most likely due to polaron pairs and/or polarons, according to previous studies which found the resonance related to polaron pairs [Guo09] or delocalized polarons residing in the crystalline phase of the P3HT film at 1.9 eV [Kor01, Zha12a]. Feature C might originate from an energetically higher unoccupied band or excitonic state, according to Müller *et al.* [Mül12] who measured with X-ray absorption an excitonic state 3.1 eV above the VBM.

In the case of P3HT-as, the CBM is shifted to lower energies by 0.15 eV, thus yielding an optical gap of 1.7 eV. The downward shift of the CBM is due to the broader peak width characteristic for the lower degree of crystallinity in the as-sample. The energetic position of state A which is most likely due to polaron pairs or polarons is the same for both samples. Whereas the third feature C, related to either a higher lying unoccupied band or exciton, is shifted upwards by 0.15 eV compared to the mc-film, and is thus located 0.7 eV below the vacuum level for the as-film.

In order to further investigate the electronic structure of the P3HT films 2C-2PPE spectra of both films are compared and the 2C-2PPE signal as a function of the pump-probe delay is studied (Figure 5.51). Figure 5.51 (a) compares 2C-2PPE

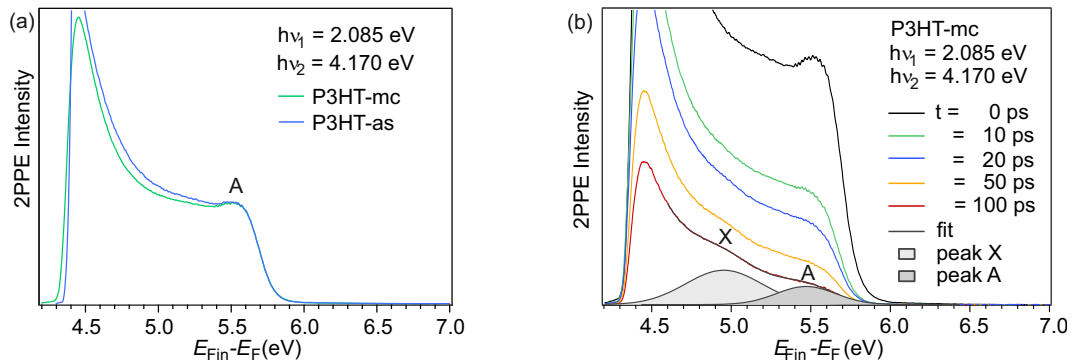


Figure 5.51: (a) 2C-2PPE spectra of the P3HT-mc and the P3HT-as film, (b) spectra taken at different time-delays on the melt-crystallized film: at longer time-delays an additional feature X becomes visible at 5.0 eV

spectra recorded with photon energies of 2.9 eV and 4.17 eV on the two respective films. Both spectra look qualitatively very similar showing a feature at a final state energy of 5.55 eV. This emission signal is more pronounced in the spectrum taken on the mc-film and can be, according to the energetic position, related to state A which was observed before in the 1C-2PPE spectra. Another feature is hidden between peak A and the secondary electron background and becomes visible at longer time delays (Figure 5.51 (b)).

Figure 5.51 (b) shows a series of 2C-2PPE spectra which were measured on the P3HT-mc film at different time delays with a pump photon energy of $h\nu_1 = 2.09$ eV and a probe photon energy of $h\nu_2 = 4.17$ eV. The black spectrum corresponds to the spectrum taken at zero pump-probe delay shown before in Figure 5.51 (a). The 2PPE emission intensity of feature A decreases rapidly within the first 10 ps. Whereas the spectra taken at time delays of 10 ps (green) and 20 ps (blue) do not exhibit any pronounced structure and look like photoemission from a continuum of states, a structure becomes visible again at a time delay of 50 ps (yellow). At a pump-probe delay of 100 ps (red spectrum) clearly two broad features are observable which can be fitted with a function consisting of two Gaussians and an exponential background, as illustrated by the grey line. The fit yields peak positions at final state energies of 4.95 eV and 5.55 eV which corresponds to intermediate state energies of 3.55 and 2.95 eV below the vacuum level, due to probing with 4.17 eV photons.

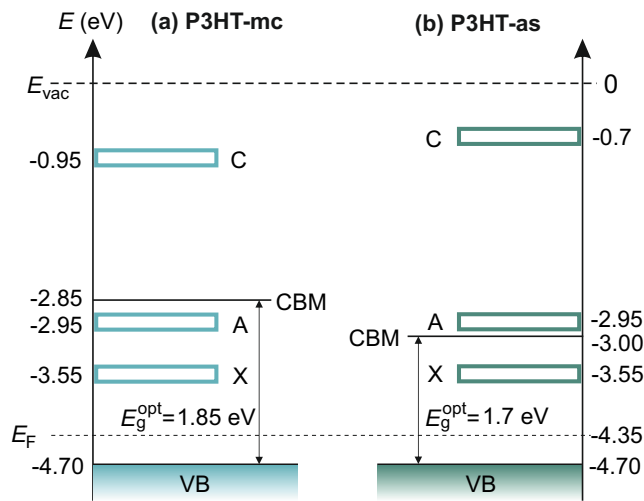


Figure 5.52: Energy level diagram of (a) P3HT-mc and (b) P3HT-as films.

The observed states are summed up in an energy level diagram shown in Figure 5.52 (a) for the P3HT-mc and (b) for the P3HT-as film. The optical gaps amount to 1.85 eV for P3HT-mc and to 1.7 eV for P3HT-as. State X is assigned to an excitonic state 1.15 eV above the VBM and state A originates most likely from polaron pairs or polarons. Feature C may be related to an energetically higher excitonic level or unoccupied band.

In conclusion the different degrees of crystallinity of the two P3HT samples only weakly influences their electronic structure. Compared to spectra from previous 2PPE studies of RR-P3HT films, the 2PPE spectra obtained in this work show a larger number and more distinct features [Var12c, Soh07]. This confirms that the investigated polymer films possess a very well defined structure. In the next section the dynamics of the excited states A and X will be further investigated.

This confirms that the feature at higher energies corresponds to state A. The feature at lower energies, labeled as X, is located 1.15 eV above the VBM and is thus attributed to the singlet exciton which was observed before at resonances between 1.0 and 1.2 eV [Guo09, Kor01, Co08, Her11, Mü12, Zha12a].

The observed states are summed up in an energy level diagram shown in Figure 5.52 (a) for the P3HT-mc and (b) for the P3HT-as film.

5.4.2 Influence of Crystallinity on the Excited State Dynamics in P3HT Films

From the spectra taken at different time delays (Figure 5.51 (b)), it is known that the excited state populations in X and A are still observable at a pump-probe delay of 100 ps. In order to investigate the influence of the different degrees of crystallinity on the excited state dynamics, time-resolved 2PPE measurements on the mc- and the as-P3HT films were performed.

Figure 5.53 (a) shows the background subtracted (*i.e.* 1C-2PPE signals have been subtracted as discussed before in Section 4.5) time-resolved data measured on the mc-P3HT film with a pump photon energy of $h\nu_1 = 2.09$ eV and a probe photon energy of $h\nu_2 = 4.18$ eV. In the 2D-spectrum the data is plotted as a function of the intermediate state energy with respect to the Fermi level and as a function of the pump-probe delay, the photoemission intensity is illustrated by a false colour code. The spectrum is divided into two parts, the first part includes a pump-probe delay in the range of -0.3 - 10 ps and the second part is reaching from 10 ps to 300 ps. The time-resolved spectrum shows a very broad 2PPE emission signal in which the features X and A are not well resolved. But a closer look at the signal at later delay times reveals that the signal between $\approx 1 - 1.5$ eV decays faster than the signal between $\approx 0.5 - 1$ eV. The secondary electron background signal at energies below 0.5 eV exhibits an even longer lifetime.

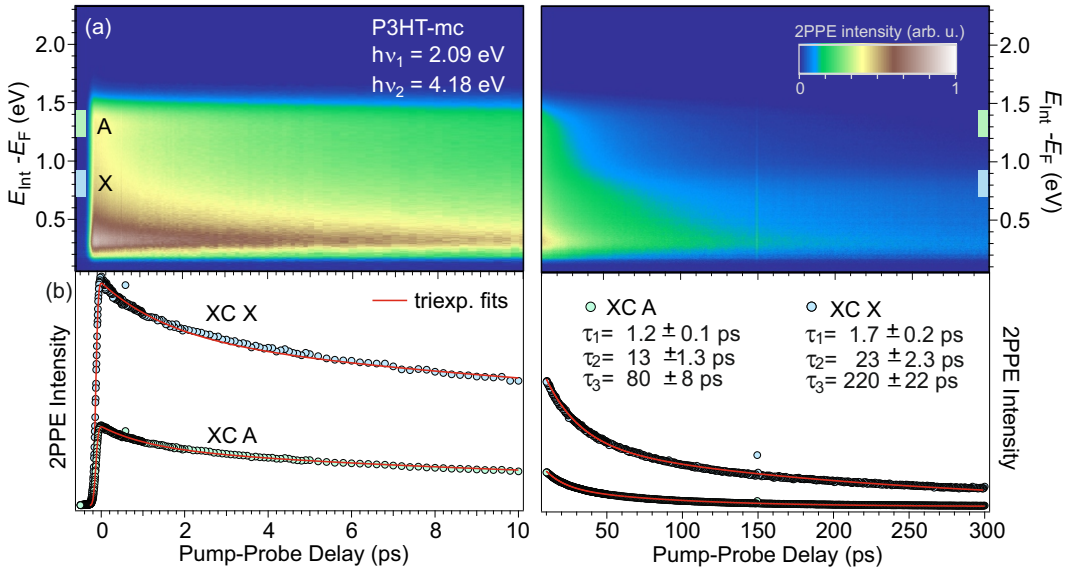


Figure 5.53: (a) Time-resolved 2PPE spectrum of P3HT-mc, (b) XC-traces integrated around the peak maxima of A and X with triexponential fits.

In order to gain deeper insights into the decay dynamics of the investigated

excited states the time-resolved spectrum was integrated around the peak maxima of the states A and X, as illustrated by the light green and blue boxes. The obtained XC-traces are displayed as a function of the pump-probe delay in Figure 5.53 (b). The XC-traces are described by empirical fit functions consisting of a triexponential decay convolved with the cross-correlation of Gaussian shaped pulse envelopes. The fits yield three time constants for each XC-trace, a fast one τ_1 in the range of 1-2 ps, a slower one τ_2 which amounts to 10-20 ps and a slow time constant τ_3 in the range of 100-200 ps. Comparing the time constants obtained for X and A confirms the observation that the population decay of state X is slower than those of state A.

Due to the broad and overlapping 2PPE signals the excited states cannot be separated energetically so that the obtained time constants cannot be assigned unambiguously. In addition, divergent time scales for the same processes are reported in literature, as discussed in Section 3.5, making it even more difficult to relate the time constants to distinct processes.

State X is related to the singlet exciton 1.15 eV above the VBM, the time constants obtained from the fit amount to $\tau_1 = 1.7 \pm 0.2$ ps, $\tau_2 = 23 \pm 2.3$ ps and $\tau_3 = 220 \pm 22$ ps. A triexponential exciton decay has been observed before by Guo *et al.* in transient absorption measurements [Guo09]. They attributed the slowest decay constant (330 ps) to electron-hole recombination, while for the faster time constants no assignment was reported. According to the reported luminescence decay ranging from 300 - 400 ps [Mag97, Kan92, Co08] the slow decay of 220 ± 22 ps is most likely connected to the recombinative decay of excitons. The fast time constant $\tau_1 = 1.7 \pm 0.2$ ps might originate from internal vibrational relaxation within the excited state due to excitation of higher vibronic levels.

Fitting the XC-trace of state A, which is most probably related to polaron pairs and/or polarons, yields time constants of $\tau_1 = 1.2 \pm 0.1$ ps, $\tau_2 = 13 \pm 1.3$ ps and $\tau_3 = 80 \pm 8$ ps. All three time constants are faster than those obtained for the excitonic state but they are still in the same order of magnitude. According to literature where the decay of polaron pairs *via* recombination and dissociation into polarons was found to take place on a time scale ranging from 0.5 ps [Ai06] to 2.6 ps [Var12c] the fast decay of 1.2 ± 0.1 ps might be related to the decay of polaron pairs. The slower decay times (τ_2 and τ_3) might be due to geminate recombination of polaron pairs and/or recombination of negative polarons with positive polarons located on adjacent polymer chains. The XC-traces of the exciton and the polaron exhibit the same instantaneous risetime corroborating the observation by Guo *et al.* that polarons can form directly after photon absorption and not only from relaxed singlet excitons [Guo09].

In order to investigate the influence of the different degrees of crystallinity on

the excited state dynamics time-resolved 2PPE measurements have been performed as well on the P3HT-as film. Figure 5.54 (a) shows a time-resolved 2PPE spectrum

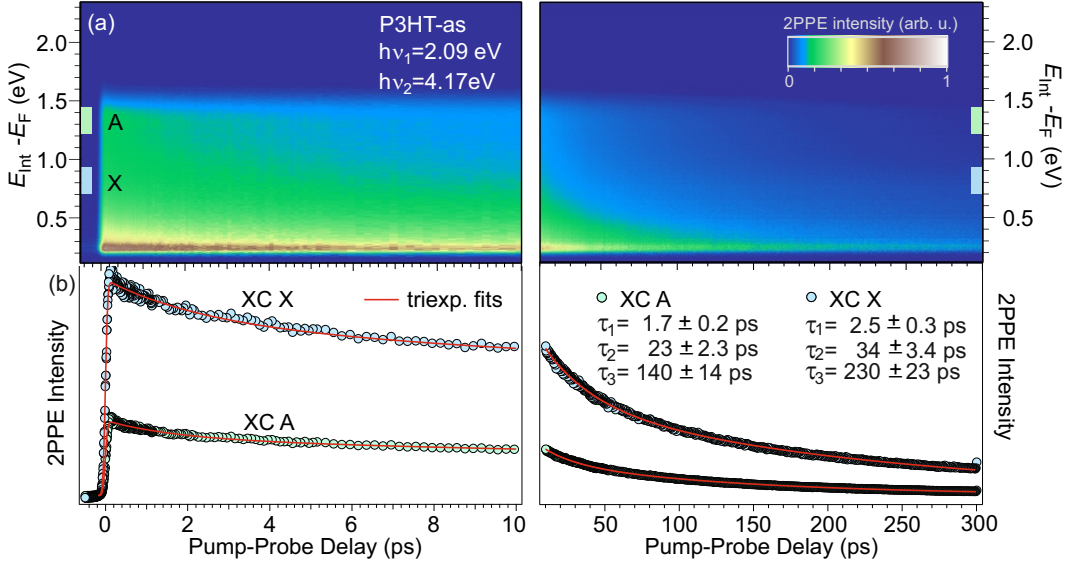


Figure 5.54: (a) Time-resolved 2PPE spectrum of P3HT-as, (b) XC-traces integrated around the peak maxima of A and X with triexponential fits.

of the P3HT-as film as a function of the pump-probe delay, recorded with photon energies of $h\nu_1 = 2.09$ eV and $h\nu_2 = 4.17$ eV. The time-resolved spectrum looks qualitatively very similar to the spectrum measured on the mc-film: It shows as well a broad emission signal which decays faster between 1.0 - 1.5 eV than between 0.5 - 1.0 eV and below intermediate state energies of 0.5 eV the hot electron dynamics decay even slower. The time-resolved 2PPE spectrum was integrated around the maxima of states A and X, yielding the XC-traces displayed as a function of the pump-probe delay in Figure 5.54, where the red lines correspond to triexponential fits. The time constants obtained for the polaronic state A are, like in the case of the mc-film, faster than those obtained for the exciton. Again, the electronic processes leading to the triexponential decay cannot be disentangled, therefore the same possible processes as for P3HT-mc might be considered.

Comparing the time constants obtained for the two different films, listed in Table 5.1, reveals that the decay dynamics in the P3HT-as film are slower than in the P3HT-mc film. Only the slowest decay (τ_3) of the excitonic state X, which is attributed to electron-hole recombination, is in good agreement for both films. In case of the other time constants, especially those related to polaron decay, the faster dynamics observed for the mc-film can be explained by the enhanced crystallinity which is known to promote charge transport.

	P3HT-mc		P3HT-as	
	X	A	X	A
τ_1 (ps)	1.7 ± 0.2	1.2 ± 0.1	2.5 ± 0.3	1.7 ± 0.2
τ_2 (ps)	23 ± 2.3	13 ± 1.3	34 ± 3.4	23 ± 2.3
τ_3 (ps)	220 ± 22	80 ± 8	230 ± 23	140 ± 14

Table 5.1: Time constants yielded by triexponential fits describing the decay of the excited states X and A.

Summary

To investigate the influence of the film morphology on the electronic structure and excited state dynamics, the results obtained for an annealed and a non-annealed P3HT film were compared. The optical gap increases upon annealing due to a narrowing of the peak width thus leading to an upward shift of the CBM in the case of the mc-film. In contrast the IP of both films stay unaffected which is in good agreement with the literature [Kan10]. The 2PPE measurements reveal the existence of two excited states which are related to the exciton and polaron pairs and/or polarons. Another unoccupied feature which might be related to an energetically higher unoccupied band or exciton is shifted to lower energies in case of the mc-sample. Compared to previous 2PPE measurements on P3HT the spectra obtained in this work are well-resolved and exhibit distinct features which allow to determine the electronic structure. In conclusion the electronic structure at the surface of the P3HT films is only weakly affected by the annealing process.

Time-resolved 2PPE measurements reveal exciton and polaron lifetimes in the range of 100 - 200 ps, whereas the exciton exhibits a slower decay than the polaronic feature. Both states decay in a multiexponential fashion whose underlying processes could not be disentangled explicitly. Moreover the decay dynamics proceed faster in the mc-film than in the as-film, except for the slow exciton decay which is related to electron-hole recombination and is in accordance for both films. The faster decay in the mc-sample can be explained by the enhanced crystallinity in the annealed film which is known to control and promote the transport properties in this polymer.

6 Summary and Conclusions

This work focuses on fundamental processes relevant for light harvesting and generation. Both conversion mechanisms, photon-to-electron and electron-to-photon, are influenced by similar mechanisms such as exciton formation, decay and diffusion as well as charge and energy transfer processes at interfaces. Those in turn are highly affected by e.g. the energy level alignment at the active inorganic/organic and organic/organic interfaces and the film morphology. The questions of how the molecular levels align at the interface with the substrate and within the film, how and on which times scales excitons form and decay, how the quasiparticles interact and how they are affected by modifications of side conditions are treated in this thesis.

These questions were tackled by 2PPE investigations of four model systems which represent different active parts of a solar cell or an LED. For instance the conductive transparent oxide ZnO is a promising candidate as active medium in LEDs and also as transparent electrode material for OPVCs when combined with an organic semiconductor. Here the spirobifluorene derivative SP6 was used to study charge transfer processes at the interface with ZnO. In addition, bulk SP6 represents a model system for an organic LED medium. The energy level alignment at an interface between a metallic electrode and an organic donor material was studied using DCV-substituted oligothiophenes on Au. The fourth model system is the polymer donor material P3HT, in which the influence of the film morphology on the electronic structure and the excited state dynamics was investigated.

In the following the findings for the different model systems are summarized:

H-induced Metallicity and Excited State Dynamics at the O-terminated ZnO Surface

On the fully O-terminated ZnO surface the adsorption of hydrogen leads to a switching of the upward surface band bending to downward band bending and the work function decreases significantly. In addition, the formation of a CAL at the surface was observed which saturates for higher coverages. This strongly suggests that the CAL reduction observed for the non-polar surface is due to ZnH-bond formation. With increasing charge carrier density at the surface, both photo- and H-induced, the ultrafast electron-phonon scattering which is a prerequisite for surface exciton formation is screened, thus leading to a slower formation of the surface exciton.

On this basis time-resolved 2PPE investigations on the fully Zn-terminated surface seem to be an interesting experiment as this surface is known to exhibit a completely different electronic surface structure. For instance no CAL is formed

since hydrogen acts as an electron acceptor in the ZnH-bond. Therefore it would be very interesting to find out whether an excitonic species, e.g. the bulk exciton or another kind of surface exciton, is at all observable at this surface.

Exciton Formation and Decay Dynamics in SP6 Films on ZnO

In addition to the picosecond dynamics which were observed before in excited state transmission and were related to internal vibrational relaxation and the excited states' population decay *via* competing pathways [Fog15], an ultrafast decay was discovered in 2PPE which may be attributed to polarization effects due to the exciton formation process. The picosecond dynamics agree well with those from excited state transmission, although 2PPE probes only the surface whereas excited state transmission probed also bulk contributions. This is due to the slow exciton diffusion in the amorphous film. The long-lived triplet state decays *via* triplet-triplet annihilation which leads here to the emission of electrons. This triplet state has a lifetime of tens of μs which can be efficiently reduced by increasing the temperature and thus the diffusion towards the ZnO surface or other quenching sites. A reduction of the film thickness showed the same effect. In addition the 2PPE measurements allowed to uncover the energy level alignment at the SP6/ZnO interface.

Based on these findings it would be interesting to conduct further time-resolved photoluminescence measurements to find out whether delayed fluorescence, which is often a consequence of triplet-triplet annihilation, occurs as well in this system.

Electronic Structure and Excited State Dynamics in DCV-substituted Oligothiophenes on Au(111)

The 2PPE measurements of DCV-substituted oligothiophenes on Au(111) revealed, in accordance with previous STS measurements, that the energy level alignment of the molecular monolayer is influenced by the metal surface and changes in the multilayer regime. The excited state dynamics exhibit a dependence on the coverage demonstrating that charge transfer at the metal interface is an efficient decay channel. In addition, the excited state dynamics are faster in the case of the molecule which is known to possess a larger number of intermolecular interactions thus promoting the exciton diffusion.

On the basis of these results further investigations using time-resolved optical spectroscopy seem promising as they provide the possibility to measure the photoluminescence lifetimes and thus allow a deeper insight into the processes after optical excitation.

Electronic Properties of P3HT Films and the Influence of Crystallinity

In contrast to previous 2PPE studies on P3HT films well-resolved spectra were obtained confirming the outstanding chemical purity and quality of these films. Two long-lived states, related to the exciton and to polaron pairs and/or polarons, have been observed. The excited state dynamics were found to be faster in the film with the higher degree of crystallinity, thus reflecting the superior transport properties. Both the electronic structure and the excited state dynamics are only weakly affected by the different film morphologies of these two P3HT films.

Further 2PPE investigations could be performed using lower pump photon energies since a recent study revealed the existence of two kinds of aggregates in annealed P3HT films [Pan15]. These aggregates can be excited separately with photon energies lower than 2 eV.

In conclusion these results provide a deeper insight into the complex interplay between the various decay pathways of optically excited states. Understanding these processes in detail opens up the possibility to selectively utilize and influence decay channels in order to optimize device performances. The challenges thereby are to reinforce the desired processes while unwanted loss channels have to be minimized. For instance, the solar cell efficiency can be improved by enhancing the exciton diffusion such that the excitons have not decayed before reaching the active interfaces. This can be achieved e.g. by external modifications like the temperature or by increasing the internal arrangement of the film *via* annealing or the use of sophisticated molecular designs. In systems where triplet-triplet annihilation results in delayed fluorescence the enhancement of this process promises greater photon yields. This represents an additional way, besides enhancing phosphorescence with heavy atoms, to exploit triplets for light generation.

A Mass Spectra and TPD of DCV6T & DCV5T-Me₂

At the FU setup the coverage was usually quantified by temperature programmed desorption (TPD). Thereby the adsorbate covered surface is heated with a constant heating rate in front of the quadrupol mass spectrometer (QMS) which detects one or more characteristic fragments of the desorbing molecules as function of the temperature. To determine the characteristic fragment masses of the DCV6T molecules, needed for the TPD, the molecules are evaporated from the Knudsen cell into the UHV chamber while a mass spectrum is taken. The quadrupol mass spectrometer (QMS) is able to detect cations with a mass to charge ratio up to $m/z = 200$ amu. For the TPD analysis usually the largest fragments available are chosen since the smaller fragments, $m/z \leq 50$ amu, may originate not only from the investigated molecules but from residual solvents or other organic impurities. Figure A.1 displays an exemplary mass spectrum of DCV6T, evaporated at 520 K, where the QMS intensity is plotted as a function of the mass to charge ratio m/z . Here the fragment with a mass of 66 amu seems to be the fragment of choice for the TPD study. It can be assigned to malononitrile (C₃H₂N₂) which is a decomposition product of the dicyanovinyl groups, the question is whether this compound is formed during evaporation or in the QMS.

The masses 39, 38, 27 and 26 are most probably decomposition products of the dicyanovinyl groups, too, and can be assigned to the fragments C₂HN⁺, C₂N⁺, hydrogen cyanide (HCN⁺) and a single cyano group (CN⁺).

In order to perform a TPD experiment the DCV6T molecules were evaporated onto the cold, ≈ 100 K, Au(111) sample, which was then moved

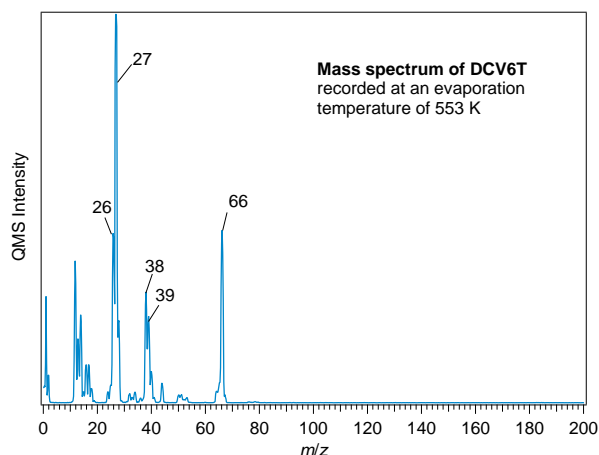


Figure A.1: Mass spectrum of DCV6T.

in front of the QMS and heated up to detect fragments of the desorbing molecules. A representative TPD spectrum of $m/z = 66$ amu is shown in Figure A.2. The temperature domain at which the signal occurs is striking, since the expected desorption temperature for a molecule of that size is much higher (≥ 500 K). This already indicates that malonodinitrile is most likely not formed due to electron bombardment

by the QMS or during the desorption from the surface, but that it is formed during evaporation and coadsorbed on the surface.

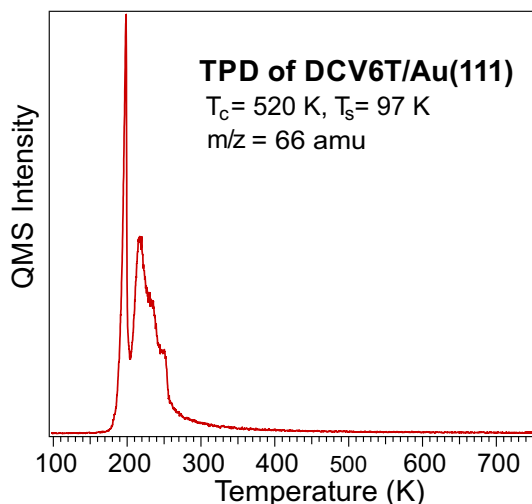


Figure A.2: TPD of DCV6T/Au(111) evaporated on the cold surface.

molecules decompose during evaporation producing malonodinitrile which sticks on the cold but not on the warm surface. Thus the desorption peaks observed in the TPD spectrum shown in Figure A.2, can be related to the malondionitrile desorption between ≈ 180 and 300 K and not to the desorption of DCV6T.

The TPD experiment has been repeated with the sample temperature changed to 300 K during evaporation, since at this temperature malononitrile is already desorbed, *i.e.* should not stick on the surface in the first place. In Figure A.3 (a) TPD spectra of the masses 27 amu and 66 amu are shown. There is no significant QMS signal of the fragment mass $m/z = 66$ amu at temperatures between 180 and 250 K, this confirms the suggestion that malonodinitrile is not generated during DCV6T desorption or electron bombardment in the QMS. In fact part of the DCV6T

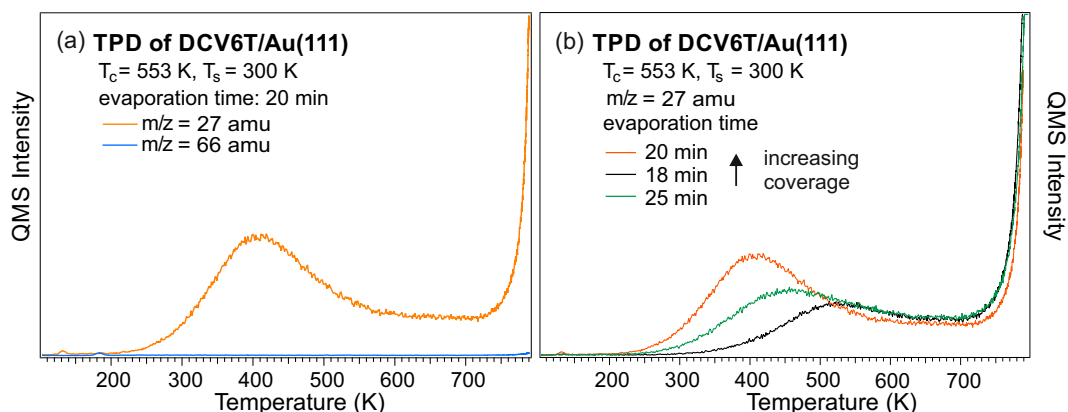


Figure A.3: TPDs of DCV6T/Au(111) evaporated on the Au(111) surface held at 300 K.

Since the detection of the fragment mass of 66 amu does not carry any information on the desorption of the DCV6T molecules another mass was tested in TPD experiments, namely the mass of 27 amu which corresponds most likely to hydrogen cyanide (HCN⁺). The desorption signal of this mass does not vanish when the molecules are adsorbed on the warm surface, but the features are not separated

from each other and the shape of the signal does not allow for exact TPD analysis. The rising signal up to the maximal temperature indicates that the molecules stick strongly on the sample surface and do not desorb completely. This behaviour is expected since gold is highly thiophilic and photoemission experiments showed that the Au(111) surface is not clean after being heated up to 800 K during the TPD experiment. Figure A.3 (b) shows TPD spectra of $m/z = 26$ amu for different coverages, but unfortunately the signal behaves neither proportionally to the film thickness nor to the evaporation period what makes this fragment inapplicable for further TPD experiments as well. Since TPD is not practicable for this system and the evaporation time is not a useful parameter either, the film thickness has to be determined otherwise as described in Section 4.3.3.

For DCV5T-Me₂ the situation concerning the applicability of TPD was found to be the same like for DCV6T. Figure A.4 shows a mass spectrum taken during the evaporation of DCV5T-Me₂ at a temperature of 553 K. Here as well malonodinitrile with a mass of 66 amu is observed, but since it does not show a significant desorption signal when the sample is held at 300 K during the deposition of DCV5T-Me₂, the same

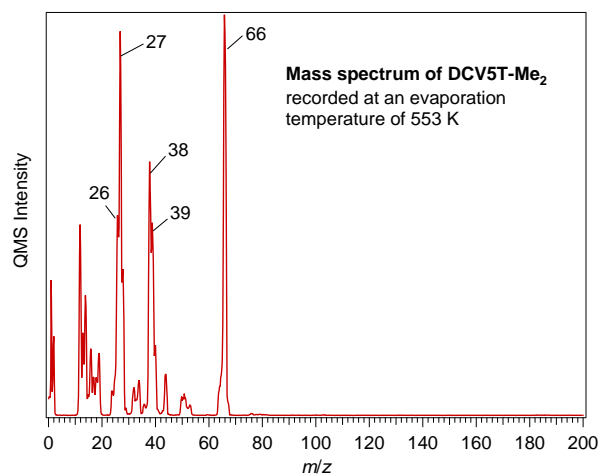


Figure A.4: Mass spectrum of DCV5T-Me₂ adsorbed on the Au(111) surface at 300 K.

conclusion can be drawn like for DCV6T, namely that malonodinitrile is already produced during evaporation and not during the desorption or in the QMS.

The masses 39 , 38 , 27 and 26 amu may be assigned to the same fragments of the dicyanovinyl groups as described above for DCV5T-Me₂. Figure A.5 (a) shows TPD spectra of DCV5T-Me₂ for the masses 26 and 39 amu. Only the fragment mass of 26 amu which is related to a single cyano group shows a significant signal which rises at temperatures towards 800 K indicating that the molecules do not desorb completely and stick on the surface instead. In Figure A.5 (b) TPD spectra of different coverages DCV5T-Me₂/Au(111) are shown but again the integrals of the QMS signals do not behave proportionally neither to the film thickness nor to the evaporation period. Therefore the same procedure to quantify the coverage was carried out like for DCV6T, as described in Section 4.3.3.

The DCV5T-Me₂ and DCV6T films were prepared under the same experimental

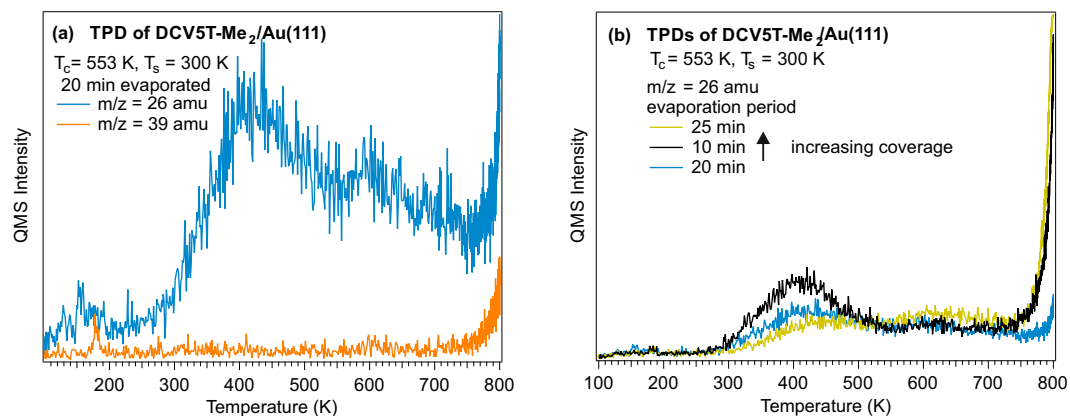


Figure A.5: TPDs of DCV5T-Me₂/Au(111).

conditions, *i.e.* same evaporation and sample temperature, like the samples investigated by means of STM by Yang et al. who did not observe any decomposed molecules on the surface [Yan14b, Yan14a]. This finding assures that the 2PPE measurements have been conducted on intact molecules.

B Calculation of the Excitation Density

The absorption of light is described by an exponential decay from the surface into the bulk after the Beer-Lambert law cite:

$$I(z) = I_0 \cdot e^{(-\alpha z)} \quad (\text{B.74})$$

here I_0 is the intensity of the absorbed light at the surface, α is the absorption coefficient which is a material specific constant and z is the thickness of the light absorbing material. The penetration depth, l_0 , is the lengths over which the absorption decays by 1/e

$$l_0 = \frac{1}{\alpha} \quad (\text{B.75})$$

The excitation density is given by

$$N_0 = \frac{fl}{l_0 \hbar \omega} \cdot \left| \left(\frac{2}{1 + \sqrt{\epsilon_{\text{opt}}}} \right)^2 \right| \quad (\text{B.76})$$

where fl corresponds to the laser fluence, *i.e.* the energy per m², the second term accounts for the surface reflectivity and ϵ_{opt} is the dielectric constant of the photoexcited material. In order to calculate the fluence of the incident laser light it has to be taken into account that after the power is measured the laser beam has to pass two mirrors and a MgF₂ window before it reaches the sample surface. For a photon energy of 3.8 eV the reflectivity of a Al-mirror is $\approx 90\%$ and the transmittance of the MgF₂ window is $\approx 95\%$, thus the prefactor for the laser power P is $0.9^2 \cdot 0.95 = 0.77$. For the calculation of the illuminated area A of the sample surface the incidence angle of 45° has to be taken into account since it leads to an elliptical distortion of the laser spot, the laser spot area on the surface is thus given by

$$A = \pi \cdot a \cdot b = \pi \cdot \sqrt{2} \cdot \left(\frac{\text{FWHM}(x) \cdot \text{FWHM}(y)}{2} \right) \quad (\text{B.77})$$

Since we are working with a pulsed laser source the repetition rate (usually 200 kHz) has to be included in the calculation. With this the fluence writes as

$$\begin{aligned} fl &= \frac{P}{A \cdot \text{rep. rate}} = \frac{P \cdot 0.77 \cdot 2 \cdot 2}{\pi \cdot \sqrt{2} \cdot \text{FWHM}(x) \cdot \text{FWHM}(y) \cdot \text{rep. rate}} \\ &= \frac{P \cdot 0.77 \cdot \sqrt{8}}{\pi \cdot \text{FWHM}(x) \cdot \text{FWHM}(y) \cdot \text{rep. rate}} \end{aligned} \quad (\text{B.78})$$

Excitation Density in ZnO

The absorption coefficient α of ZnO is for photon energies ≥ 3.3 eV $\alpha_{\text{ZnO}} = 2 \cdot 10^5 \text{ cm}^{-1}$ [Jel98], with this a penetration depth of $l_0 = 1/\alpha_{\text{ZnO}} = 50 \text{ nm}$ is obtained. The optical dielectric constant ϵ_{opt} depends on the photon energy and amounts to $\epsilon_{\text{opt}}^{3.8 \text{ eV}} = 4 + i1.8$ for the pump photon energy of 3.8 eV and to $\epsilon_{\text{opt}}^{4.64 \text{ eV}} = 2 + i1.5$ for the 4.65 eV probe photon energy [Jel98]. So the fluence of a laser pulse with a photon energy of 3.8 eV, a spot size of $118 \times 101 \mu\text{m}$ and a power of $P = 710 \mu\text{W}$ and a repetition rate of 200 kHz can be calculated after

$$fl = \frac{710 \mu\text{W} \cdot 0.77 \cdot \sqrt{8}}{\pi \cdot 118 \mu\text{m} \cdot 101 \mu\text{m} \cdot 200 \text{ kHz}} = 0.207 \text{ J/m}^2 \quad (\text{B.79})$$

and with this the excitation density writes as

$$N_0 = \frac{0.207 \text{ J/m}^2}{l_0 \hbar \omega} \cdot \left| \left(\frac{2}{1 + \sqrt{4 + i1.8}} \right)^2 \right| = 2.86 \cdot 10^{18} \text{ cm}^{-3} \quad (\text{B.80})$$

Excitation Density in SP6

The absorption coefficient of SP6 for a photon energy of 3.6 eV amounts to $\alpha_{\text{SP6}} = 4 \cdot 10^5 \text{ cm}^{-1}$ this yields a penetration depth of $l_0 = 1/\alpha_{\text{SP6}} = 25 \text{ nm}$ [Blu08]. Since the optical dielectric constant of SP6 is not known it was set to 1. With this approximation the excitation density for a laser pulse with a photon energy of 3.6 eV and a fluence of 0.013 J/m^2 is given by

$$N_0 = \frac{0.013 \text{ J/m}^2}{l_0 \hbar \omega} \cdot 1 = 8.96 \cdot 10^{23} \text{ m}^{-3} \quad (\text{B.81})$$

The start population for the diffusion model was calculated for a spot area of $2561 \mu\text{m}^2$. The percentage of the absorbed photons in the upmost 0.5 nm layer of the SP6 film is given by

$$1 - e^{-\frac{0.5 \text{ nm}}{25 \text{ nm}}} = 0.0198 \quad (\text{B.82})$$

Thus 1.98 % of $896 \ 000 \text{ photons}/\mu\text{m}^2 = 17741 \text{ photons}/\mu\text{m}^2$ are absorbed in the upmost 0.5 nm layer. The volume of the illuminated are is given by $V = 2561 \mu\text{m}^2 \cdot 0.5 \text{ nm} = 1.28 \mu\text{m}^3$ and with this the number of absorbed photons amounts to $17741 \text{ photons}/\mu\text{m}^2 \cdot 1.28 \mu\text{m}^3 = 22708$.

C Differential Equation Solution

In order to simulate the autocorrelation experiment described in Section 5.2.2 the population and decay functions of the singlet and the triplet states have to be calculated. This is done by solving the differential equations resulting from the simplified rate equation model shown in Figure C.1. Here n_{S_1} corresponds to the singlet and n_{T_1} to the triplet population, $\Gamma_1 = \frac{1}{\tau_1}$ is the electron-hole recombination, *i.e.* fluorescence, rate, $\Gamma_{12} = \frac{1}{\tau_{12}}$ relates to the intersystem crossing rate and $\Gamma_2 = \frac{1}{\tau_2}$ to the triplet decay rate. The population n_{S_1} depends on the fluorescence ($\Gamma_1 = \frac{1}{\tau_1}$) and the intersystem crossing rate ($\Gamma_{12} = \frac{1}{\tau_{12}}$):

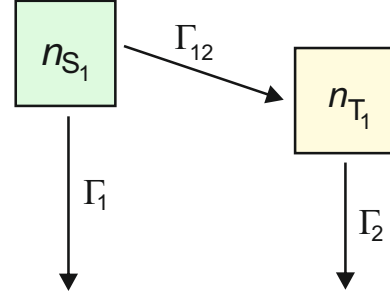


Figure C.1: Simplified model describing the singlet and triplet population decays.

$$\dot{n}_{S_1} = -(\Gamma_1 + \Gamma_{12})n_{S_1} = -\left(\frac{1}{\tau_1} + \frac{1}{\tau_{12}}\right)n_{S_1} \quad (\text{C.83})$$

with $\frac{1}{\tau_1} + \frac{1}{\tau_{12}} = \frac{1}{\tau_{S_1}}$ this writes as

$$\dot{n}_{S_1} = -\frac{1}{\tau_{S_1}}n_{S_1} \quad (\text{C.84})$$

The solution is already given by

$$n_{S_1}(t) = n_{S_1}(0)e^{-t\left(\frac{1}{\tau_1} + \frac{1}{\tau_{12}}\right)} = n_{S_1}(0)e^{-t/\tau_{S_1}} \quad (\text{C.85})$$

The rate equation for the triplet population n_{T_1} writes as

$$\dot{n}_{T_1} = \frac{1}{\tau_{12}}n_{S_1} - \frac{1}{\tau_2}n_{T_1} = \Gamma_{12}n_{S_1} - \Gamma_2n_{T_1} \quad (\text{C.86})$$

A first order differential equation of the form

$$y' + a(x)y = r(x) \quad (\text{C.87})$$

is solved by the whole solution

$$y = y_S + y_H \quad (\text{C.88})$$

with y_H being the whole solution of the homogeneous differential equation

$$y' + a(x)y = 0 \quad (\text{C.89})$$

and y_S being a special solution of the inhomogeneous differential equation

$$y' + a(x)y = r(x) \quad (\text{C.90})$$

Bringing equation C.86 in the same form according to Equation C.87 yields

$$\frac{d}{dt}n_{T_1}(t) + \Gamma_2 n_{T_1}(t) = \Gamma_{12} n_{S_1}(t) \quad (\text{C.91})$$

With this y_H writes as

$$\frac{d}{dt}n_{T_1}(t) + \Gamma_2 n_{T_1}(t) = 0 \quad (\text{C.92})$$

$$\frac{d}{dt}n_{T_1}(t) = -\Gamma_2 n_{T_1}(t) \quad (\text{C.93})$$

and the solution is given by

$$n_{T_1}(t)_H = n_{T_1}(0)e^{-\Gamma_2 t} = n_{T_1}(0)e^{\frac{-t}{\tau_2}} \quad (\text{C.94})$$

In order to solve y_S the following formula can be applied

$$y_S = e^{-A(x)} \int r(x)e^{A(x)} dx \quad (\text{C.95})$$

which yields

$$\begin{aligned} n_{T_1}(t)_S &= e^{-\Gamma_2 t} \int \Gamma_{12} n_{S_1}(t) e^{\Gamma_2 t} dt \quad \text{with equation C.85} \\ &= e^{-\Gamma_2 t} \Gamma_{12} \int n_{S_1}(0) e^{-\Gamma_{S_1} t} e^{\Gamma_2 t} dt \\ &= e^{-\Gamma_2 t} \Gamma_{12} n_{S_1}(0) \int e^{-\Gamma_{S_1} t} e^{\Gamma_2 t} dt \\ &= e^{-\Gamma_2 t} \Gamma_{12} n_{S_1}(0) \int e^{(-\Gamma_{S_1} + \Gamma_2)t} dt \\ &= e^{-\Gamma_2 t} \Gamma_{12} n_{S_1}(0) \left[\frac{1}{(-\Gamma_{S_1} + \Gamma_2)} e^{(-\Gamma_{S_1} + \Gamma_2)t} \right]_0^t \\ &= e^{-\Gamma_2 t} n_{S_1}(0) \frac{\Gamma_{12}}{(-\Gamma_{S_1} + \Gamma_2)} (e^{(\Gamma_2 - \Gamma_{S_1})t} - 1) \\ &= n_{S_1}(0) \frac{\Gamma_{12}}{(-\Gamma_{S_1} + \Gamma_2)} (e^{(\Gamma_2 - \Gamma_{S_1} - \Gamma_2)t} - e^{-\Gamma_2 t}) \\ &= n_{S_1}(0) \frac{\Gamma_{12}}{(-\Gamma_{S_1} + \Gamma_2)} (e^{-\Gamma_{S_1} t} - e^{-\Gamma_2 t}) \end{aligned}$$

Adding up the solutions for y_H and y_S yields the solution for $n_{T_1}(t)$

$$\begin{aligned}n_{T_1}(t)_H + n_{T_1}(t)_S &= n_{T_1}(0)e^{-\Gamma_2 t} + n_{S_1}(0) \frac{\Gamma_{12}}{(-\Gamma_{S_1} + \Gamma_2)} (e^{-\Gamma_{S_1} t} - e^{-\Gamma_2 t}) \\ &= n_{T_1}(0)e^{\frac{-t}{\tau_2}} + n_{S_1}(0) \frac{\frac{1}{\tau_{12}}}{\frac{1}{\tau_2} - \frac{1}{\tau_{S_1}}} (e^{\frac{-t}{\tau_{S_1}}} - e^{\frac{-t}{\tau_2}})\end{aligned}$$

References

- [Ai06] X. Ai, M. C. Beard, K. P. Knutsen, S. E. Shaheen, G. Rumbles, & R. J. Ellingson. *Photoinduced Charge Carrier Generation in a Poly(3-hexylthiophene) and Methanofullerene Bulk Heterojunction Investigated by Time-Resolved Terahertz Spectroscopy*. *Journal of Physical Chemistry B* **110**, (2006) 25462 . 57, 162
- [Ams15] P. Amsalem, G. Heimel, M. Oehzelt, & N. Koch. *The interface electronic properties of organic photovoltaic cells*. *Journal of Electron Spectroscopy and Related Phenomena* **204**, (2015) 177. 7, 12
- [Arn79] S. Arnold, M. Pope, & T. K. T. Hsieh. *Double Quantum External Photoelectric Effect in Crystalline Tetracene*. *Physica Status Solidi B* **94**, (1979) 263. 26, 132
- [Bar05] G. Barbarella, M. Melucci, & G. Sotgiu. *The Versatile Thiophene: An Overview of Recent Research on Thiophene-Based Materials*. *Advanced Materials* **17**, 13, (2005) 1581. 43
- [Bec01] T. Becker, S. Hövel, M. Kunat, C. Boas, U. Burghaus, & C. Wöll. *Interaction of hydrogen with metal oxides: the case of the polar ZnO(0001) surface*. *Surface Science Letters* **486**, (2001) L502. 33
- [Bis11] M. Biswas, Y. S. Jung, H. K. Kim, K. Kumar, G. J. Hughes, S. Newcomb, M. O. Henry, & E. McGlynn. *Microscopic origins of the surface exciton photoluminescence peak in ZnO nanostructures*. *Physical Review B* **83**, (2011) 235320. 36
- [Bla99] R. Blachnik, J. Chu, R. R. Galazka, J. Geurts, J. Gutowski, B. Hönerlage, D. Hofmann, J. Kossut, R. Lévy, P. Michler, U. Neukirch, T. Story, D. Strauch, & A. Waag. *Landolt-Börnstein, New Series III/41B, Semiconductors: II-VI and I-VII Compounds; Semimagnetic Compounds*. Springer, Heidelberg, (1999). 30, 31
- [Blu06] S. Blumstengel, S. Sadofev, C. Xu, J. Puls, & F. Henneberger. *Converting Wannier into Frenkel Excitons in an Inorganic/Organic Hybrid Semiconductor Nanostructure*. *Physical Review Letters* **97**, 23, (2006) 237401. 2
- [Blu08] S. Blumstengel, S. Sadofev, C. Xu, J. Puls, R. L. Johnson, H. Glowatzki, N. Koch, & F. Henneberger. *Electronic coupling in organic-inorganic*

- semiconductor hybrid structures with type-II energy level alignment*. Physical Review B **77**, (2008) 085323. VIII, 3, 39, 40, 41, 113, 117, 118, 120, 131, 174
- [Blu09] S. Blumstengel, S. Sadofev, J. Puls, & F. Henneberger. *An Inorganic/Organic Semiconductor "Sandwich" Structure Grown by Molecular Beam Epitaxy*. Advanced Materials **21**, (2009) 4850. 39, 113
- [Bog15] L. Bogner, Z. Yang, M. Corso, R. Fitzner, P. Bäuerle, K. J. Franke, J. I. Pascual, & P. Tegeder. *Electronic structure and excited states dynamics in a dicyanovinyl-substituted oligothiophene on Au(111)*. Physical Chemistry Chemical Physics **17**, (2015) 27118. IX, 46, 47, 48, 135, 138, 140, 141, 145, 146, 150, 153
- [Bow83] M. Bowker, H. Houghton, K. C. Waugh, T. Giddings, & M. Green. *Crystal plane dependence of adsorption and reaction on zinc oxide*. Journal of Catalysis **84** (1), (1983) 252. 30
- [Bra09] T. Braun. *Entwicklung und Charakterisierung einer Elektronenlinse für abbildende Photoelektronenspektroskopie*. Dissertation, Freie Universität Berlin (2009). IX, 79
- [Bur85] G. Burns. *Solid State Physics*. Academic Press, Inc., Orlando/Florida, (1985). 61
- [Cha91] D. D. Chambliss, R. J. Wilson, & S. Chiang. *Nucleation of ordered Ni islands arrays on Au(111) by surface lattice dislocations*. Physical Review Letters **66**, (1991) 1721. 51
- [Cha11] W.-L. Chan, M. Ligges, A. Jailaubekov, L. Kaake, L. Miaja-Avila, & X.-Y. Zhu. *Observing the Multiexciton State in Singlet Fission and Ensuing Ultrafast Multielectron Transfer*. Science **334**, (2011) 1541 . 25
- [Cha12a] W.-L. Chan, M. Ligges, & X.-Y. Zhu. *The energy barrier in singlet fission can be overcome through coherent coupling and entropic gain*. Nature Chemistry **4**, (2012) 840. 25
- [Cha12b] W.-L. Chan, J. R. Tritsch, & X.-Y. Zhu. *Harvesting Singlet Fission for Solar Energy Conversion: One- versus Two-Electron Transfer from the Quantum Mechanical Superposition*. Journal of the American Chemical Society **134**, (2012) 18295 . 25

- [Coo08] S. Cook, A. Furube, & R. Katoh. *Analysis of the excited states of regioregular polythiophene P3HT*. Energy & Environmental Science **1**, (2008) 294. 55, 56, 57, 158, 160, 162
- [Cou86] R. Courths, H. G. Zimmer, A. Goldmann, & H. Saalfeld. *Electronic structure of gold: An angle-resolved photoemission study along the Γ line*. Physical Review B **34**, (1986) 3577. 52
- [Cri01] X. Crispin, V. Geskin, A. Crispin, J. Cornil, R. Lazzaroni, W. R. Salaneck, & J.-L. Bredas. *Characterization of the Interface Dipole at Organic/ Metal Interfaces*. Journal of the American Chemical Society **124**, (2001) 8131. 11
- [Dei10] C. Deibel, Th. Strobel, & V. Dyakonov. *Role of the Charge Transfer State in Organic Donor-Acceptor Solar Cells*. Advanced Materials **22**, (2010) 4097. 23
- [Dei11] J.-C. Deinert. *Zeit- und winkelaufgelöste Zweiphotonen-Photoemissionspektroskopie: Aufbau und Charakterisierung des Experiments anhand der Cu(111)- und der D₂O/Cu(111)-Oberfläche*. Diplomarbeit, Freie Universität Berlin (2011). 71, 77, 79
- [Dei14] J.-C. Deinert, D. Wegkamp, M. Meyer, C. Richter, M. Wolf, & J. Stähler. *Ultrafast Exciton Formation at the ZnO(10 $\bar{1}$ 0) Surface*. Physical Review Letters **113**, 5, (2014) 057602. VIII, X, 3, 34, 36, 37, 96, 98, 102, 105, 106, 107, 109, 112
- [Dei15a] J.-C. Deinert. *Zinc oxide surfaces and interfaces: Electronic structure and charge carrier dynamics*. Dissertation, Technische Universität Berlin (2015). 38
- [Dei15b] J.-C. Deinert, O. T. Hofmann, M. Meyer, P. Rinke, & J. Stähler. *Local aspects of hydrogen-induced metallization of the ZnO(10 $\bar{1}$ 0) surface*. Physical Review B **91**, (2015) 235313. VIII, 16, 30, 31, 34, 35, 101, 102, 103, 110
- [Dev96] J.T. Devreese. *Encyclopedia of Applied Physics, Vol. 14*. Wiley-VCH Publishers, Inc., (1996) 383. 20
- [Dex53] D. L. Dexter. *A Theory of Sensitized Luminescence in Solids*. Journal of Chemical Physics **21**, (1953) 836 . 26
- [Die04] U. Diebold, L. V. Koplitz, & O. Dulub. *Atomic-scale properties of low-index ZnO surfaces*. Applied Surface Science **237**, 1-4, (2004) 336. 31

- [Dul02] O. Dulub, L. A. Boatner, & U. Diebold. *STM study of the geometric and electronic structure of ZnO(0001)-Zn, (000 $\bar{1}$)-O, (10 $\bar{1}$ 0), and (11 $\bar{2}$ 0) surfaces.* Surface Science **519**, 3, (2002) 201. 31, 32
- [Dut05] G. Dutton, D. P. Quinn, C. D. Lindstrom, & X.-Y. Zhu. *Exciton dynamics at molecule-metal interfaces: C₆₀/Au(111).* Physical Review B **72**, (2005) 045441. 23, 149, 150, 151
- [Ech78] P. M. Echenique & J. B. Pendry. *The existence and detection of Rydberg states at surfaces.* Journal of Physics C **11**, (1978) 2065. 10
- [Eck84] H. Eckardt, L. Fritsche, & J. Noffke. *Self-consistent relativistic band structure of the noble metals.* Journal of Physics F **14**, (1984) 97. IX, 52, 136
- [Ein05] A. Einstein. *Über einen die Erzeugung und Verwandlung des Lichtes betreffenden heuristischen Gesichtspunkt.* Annalen der Physik **17**, (1905) 132. 59
- [Fal05] A. Falcou, F. Meyer, A. Parham, & H. Becker. *Organic electroluminescent elements with spirobifluorene derivative-containing hole-blocking layers.* PCT Int. Appl., WO 2005011334 A1 20050203, (2005) . 39
- [Fau94] T. Fauster. *Two-photon photoemission.* Progress in Surface Science **46**, (1994) 177. 61
- [Fau02] T. Fauster. *Elektronen nahe Metalloberflächen.* Physik in unserer Zeit **33**, (2002) 68. 9, 10
- [Fic97] D. Fichou, M.-P. Ulade-Fichou, G. Horowitz, & F. Demanze. *Thermal and optical characterization of high purity α -octithiophene.* Advanced Materials **9**, 1, (1997) 75. 43
- [Fin06] K. Fink. *Ab initio cluster calculations on the electronic structure of oxygen vacancies at the polar ZnO(000 $\bar{1}$) surface and on the adsorption of H₂, CO, and CO₂ at these sites.* Physical Chemistry Chemical Physics **8**, 13, (2006) 1482. 32, 33, 97, 99
- [Fit11] R. Fitzner, E. Reinhold, A. Mishra, E. Mena-Osteritz, H. Ziehlke, C. Körner, K. Leo, M. Riede, M. Weil, O. Tsaryova, C. Uhrich A. Weiß, M. Pfeiffer, & P. Bäuerle. *Dicyanovinyl-Substituted Oligothiophenes: Structure-Property Relationships and Application in Vacuum-Processed Small-Molecule Organic Solar Cells.* Advanced Functional Materials **21**, (2011) 897. 4, 44, 45, 135, 143, 146, 147

- [Fit12a] R. Fitzner, C. Elschner, M. Weil, C. Uhrich, C. Körner, M. Riede, K. Leo, M. Pfeiffer, E. Reinhold, E. Mena-Osteritz, & P. Bäuerle. *Interrelation between Crystal Packing and Small - Molecule Organic Solar Cell Performance*. *Advanced Materials* **24**, (2012) 675. 45, 135, 153, 154
- [Fit12b] R. Fitzner, E. Mena-Osteritz, A. Mishra, G. Schulz, E. Reinhold, M. Weil, C. Körner, H. Ziehlke, C. Elschner, K. Leo, M. Riede, M. Pfeiffer, C. Uhrich, & P. Bäuerle. *Correlation of π -Conjugated Oligomer Structure with Film Morphology and Organic Solar Cell Performance*. *Journal of the American Chemical Society* **134**, (2012) 11064. 4, 44, 45, 135, 141, 143, 147, 150, 153, 154
- [Fog14] L. Foglia, L. Bogner, J. Stähler, & M. Wolf. *Exciton trapping in vibrationally excited organic molecules near a ZnO surface*. arXiv:1412.0597, (2014) . 117, 122, 123, 133
- [Fog15] L. Foglia. *Ultrafast dynamics and energy loss channels at a hybrid inorganic/organic interface*. Dissertation, Technische Universität Berlin (2015). IX, 3, 33, 41, 97, 100, 113, 117, 122, 131, 133, 166
- [Fon04] V. A. Fonoberov & A. A. Balandin. *Radiative lifetime of excitons in ZnO nanocrystals: The dead-layer effect*. *Physical Review B* **70**, (2004) 195410. 36
- [For03] F. Forster, G. Nicolay, F. Reinert, D. Ehm, S. Schmidt, & S. Hüfner. *Surface and interface states on adsorbate covered noble metal surfaces*. *Surface Science* **532-533**, (2003) 160. 8, 9
- [For07] F. Forster, A. Bendounan, F. Reinert, V.G. Grigoryan, & M. Springborg. *The Shockley-type surface state on Ar covered Au(111): High resolution photoemission results and the description by slab-layer DFT calculations*. *Surface Science* **601**, (2007) 5595. 9, 52
- [För48] T. Förster. *Zwischenmolekulare Energiewanderung und Fluoreszenz*. *Annalen der Physik* **437**, (1948) 55 . 25
- [Fra12] K. J. Franke & J. I. Pascual. *Effects on electron-vibration coupling in transport through single molecules*. *Journal of Physics: Condensed Matter* **24**, (2012) 394002. 48
- [Fri04] M. J. Frisch, G. W. Trucks, H. B. Schlegel, G. E. Scuseria, M. A. Robb, J. R. Cheeseman, J. A. Montgomery, T. Vreven Jr., K. N. Kudin, J. C.

- Burant, J. M. Millam, S. S. Iyengar, J. Tomasi, V. Barone, B. Men-
nucci, M. Cossi, G. Scalmani, N. Rega, G. A. Petersson, H. Nakatsuji,
M. Hada, M. Ehara, K. Toyota, R. Fukuda, J. Hasegawa, M. Ishida,
T. Nakajima, Y. Honda, O. Kitao, H. Nakai, M. Klene, X. Li, J. E. Knox,
H. P. Hratchian, J. B. Cross, V. Bakken, C. Adamo, J. Jaramillo, R. Gom-
perts, R. E. Stratmann, O. Yazyev, A. J. Austin, R. Cammi, C. Pomelli,
J. W. Ochterski, P. Y. Ayala, K. Morokuma, G. A. Voth, P. Salvador, J. J.
Dannenberg, V. G. Zakrzewski, S. Dapprich, A. D. Daniels, M. C. Strain,
O. Farkas, D. K. Malick, A. D. Rabuck, K. Raghavachari, J. B. Foresman,
J. V. Ortiz, Q. Cui, A. G. Baboul, S. Clifford, J. Cioslowski, B. B. Ste-
fanov, G. Liu, A. Liashenko, P. Piskorz, I. Komaromi, R. L. Martin, D. J.
Fox, T. Keith, M. A. Al-Laham, C. Y. Peng, A. Nanayakkara, M. Challa-
combe, P. M. W. Gill, B. Johnson, W. Chen, M. W. Wong, C. Gonzalez,
& J. A. Pople. *Gaussian03, Revision C0.2*. Inc., Wallingford, CT, (2004).
46
- [Fri09] S. Friedlein. *Two-photon photoionization by singlet-singlet annihilation
in polycrystalline, thin perylene films*. Applied Physics A **95**, (2009) 315.
26, 27, 129
- [Fri11] J. Frisch, A. Vollmer, J. P. Rabe, & N. Koch. *Ultrathin polythiophene films
on an intrinsically conducting polymer electrode: Charge transfer induced
valence states and interface dipoles*. Organic Electronics **12**, (2011) 916
. 55, 157
- [Fri15] S. Friede, S. Kuehn, S. Sadofev, S. Blumstengel, F. Henneberger, &
T. Elsaesser. *Nanoscale transport of surface excitons at the interface be-
tween ZnO and a molecular monolayer*. Physical Review B **91**, (2015)
121415(R). 36
- [Güd05] J. Güdde & U. Höfer. *Femtosecond time-resolved studies of image-
potential states at surfaces and interfaces of rare-gas adlayers*. Progress
in Surface Science **80**, 3-4, (2005) 49. 10
- [Güd06] J. Güdde, W. Berthold, & U. Höfer. *Dynamics of Electronic Transfer Pro-
cesses at Metal/Insulator Interfaces*. Chemical Reviews **106**, 10, (2006)
4261. 9
- [Gre13] M. A. Green. *Improved value for the silicon free exciton binding energy*.
AIP Advances **3**, (2013) 112104. 30

- [Gre15] Martin A. Green, Keith Emery, Yoshihiro Hishikawa, Wilhelm Warta, , & Ewan D. Dunlop. *Solar cell efficiency tables (version 46)*. Progress in Photovoltaics: Research and Applications **23**, (2015) 805. 1
- [Guo09] J. Guo, H. Ohkita, H. Benten, & S. Ito. *Near-IR Femtosecond Transient Absorption Spectroscopy of Ultrafast Polaron and Triplet Exciton Formation in Polythiophene Films with Different Regioregularities*. Journal of the American Chemical Society **131**, (2009) 16869. 53, 56, 57, 159, 160, 162
- [Haa71] D. Haarer & G. Castro. *Exciton induced photoemission in anthracene*. Chemical Physics Letters **12**, (1971) 277 . 26
- [Hag09] S. Hagen. *Isomerization behavior of photochromic molecules in direct contact with noble metal surfaces*. Dissertation, Freie Universität Berlin (2009). IX, 71, 77, 82
- [Hag10] S. Hagen, Y. Luo, R. Haag, M. Wolf, & P. Tegeder. *Electronic structure and electron dynamics at an organic molecule/metal interface: interface states of tetra-tert-butylimine/Au(111)*. New Journal of Physics **12**, (2010) 125022. 9, 10, 52, 142
- [Hal87] W. Hallwachs. *Über den Einfluss des Lichtes auf electrostatisch geladene Körper*. Annalen der Physik **269**, (1887) 301. 59
- [Hei79] P. Heimann, H. Miosga, & H. Neddermeyer. *Photoemission from Au single crystals. Location of transitions in k space along lines of high symmetry*. Solid State Communications **29**, (1979) 463. 136
- [Hei13] G. Heimel, S. Duhm, I. Salzmann, A. Gerlach, A. Strozecka, J. Niederhausen, C. Bürker, T. Hosokai, I. Fernandez-Torrente, G. Schulze, S. Winkler, A. Wilke, R. Schlesinger, J. Frisch, B. Bröker, A. Vollmer, B. Detlefs, J. Pflaum, S. Kera, K. J. Franke, , N. Ueno, J. I. Pascual, F. Schreiber, & N. Koch. *Charged and metallic molecular monolayers through surface-induced aromatic stabilization*. Nature Chemistry **5**, (2013) 187. 13, 47
- [Hel15] <http://www.heliatek.com/en/press/press-releases> Heliatek (last accessed, October 27th, 2015). 1
- [Hen94] M. Henzler & W. Göpel. *Oberflächenphysik des Festkörpers*. B. G. Teubner Stuttgart, 2. Auflage, (1994). 60

- [Hen07] E. Hendry, M. Koeberg, & M. Bonn. *Exciton and electron-hole plasma formation dynamics in ZnO*. Physical Review B **76**, 4, (2007) 045214. 18, 19, 108
- [Her87] H. Hertz. *Über einen Einfluss des ultravioletten Lichtes auf die elektrische Entladung*. Annalen der Physik **267**, (1887) 983. 59
- [Her11] D. Herrmann, S. Niesar, C. Scharsich, A. Koehler, M. Stutzmann, & E. Riedle. *Role of Structural Order and Excess Energy on Ultrafast Free Charge Generation in Hybrid Polythiophene/Si Photovoltaics Probed in Real Time by Near-Infrared Broadband Transient Absorption*. Journal of the American Chemical Society **133**, (2011) 18220. 56, 57, 160
- [Hüf95] S. Hüfner. *Photoelectron Spectroscopy*. Springer, Heidelberg, (1995). 70
- [Hüm73] K. Hümmer. *Interband Magnetoreflexion of ZnO*. Physica Status Solidi B **56**, (1973) 249. 41
- [Hof11] S. T. Hoffmann, J.-M. Koenen, U. Scherf, I. Bauer, P. Strohrriegel, H. Bässler, & A. Köhler. *Triplet-Triplet Annihilation in a Series of Poly(p-phenylene Derivatives)*. Journal of Physical Chemistry B **115**, (2011) 8417. 2, 26, 27, 130, 131
- [Hol07] A. F. Holleman, E. Wiberg, & N. Wiberg. *Lehrbuch der Anorganischen Chemie*. Walter de Gruyter, Berlin, 102. Auflage, (2007). 50
- [Hor96] G. Horowitz, F. Garnier A. Yassar, R. Hajlaoui, & F. Kouki. *Field-effect transistor made with a sexithiophene single crystal*. Advanced Materials **8**, 1, (1996) 52. 43
- [Jan09] A. Janotti & C. G. Van de Walle. *Fundamentals of zinc oxide as a semiconductor*. Reports on Progress in Physics **72**, 12, (2009) 126501. 30, 31
- [Jel98] G. Jellison & L. Boatner. *Optical functions of uniaxial ZnO determined by generalized ellipsometry*. Physical Review B **58** (7), (1998) 3586. 174
- [Kal02] J. Kalinowski, W. Stampor, J. Mężyk, M. Cocchi, D. Virgili, V. Fattori, & P. Di Marco. *Quenching effects in organic electrophosphorescence*. Physical Review B **66**, (2002) 235321. 24
- [Kan92] G. S. Kanner, X. Wei, B. C. Hess, L. R. Chen, & Z. V. Vardeny. *Evolution of Excitons and Polarons in Polythiophene from Femtoseconds to Milliseconds*. Physical Review Letters **69**, (1992) 538. 56, 57, 162

- [Kan10] K. Kanai, T. Miyazaki, H. Suzuki, M. Inaba, Y. Ouchi, & K. Seki. *Effect of annealing on the electronic structure of poly(3-hexylthiophene) thin film*. Physical Chemistry Chemical Physics **12**, (2010) 273 . 5, 55, 157, 158, 164
- [Kan15] B. Kan, M. Li, Q. Zhang, F. Liu, X. Wan, Y. Wang, W. Ni, G. Long, X. Yang, H. Feng, Y. Zuo, M. Zhang, F. Huang, Y. Cao, T. P. Russell, & Y. Chen. *A Series of Simple Oligomer-like Small Molecules Based on Oligothiophenes for Solution-Processed Solar Cells with High Efficiency*. Journal of the American Chemical Society **137**, (2015) 3886. 45
- [Kel64] R. E. Kellogg. *Radionless Intermolecular Energy Transfer. IV. Triplet-Triplet Annihilation*. The Journal of Chemical Physics **41**, (1964) 3046. 26, 129
- [Kem04] M. Kemerink, S. F. Alvaro, P. Müller, P. M. Koenraad, H. W. M. Salemink, J. H. Wolter, & R. A. J. Janssen. *Scanning tunneling spectroscopy on organic semiconductors: Experiment and model*. Physical Review B **70**, (2004) 045202. 41
- [Kim05] Y.-H. Kim, H.-S. Kim, & S.-K. Kwon. *Synthesis and Characterization of Highly Soluble and Oxygen Permeable New Polyimides Based on Twisted Biphenyl Dianhydride and Spirobifluorene Diamine*. Macromolecules **38**, (2005) 7950. 39
- [Kin11] P. D. C. King & T. D. Veal. *Conductivity in transparent oxide semiconductors*. Journal of Physics: Condensed Matter **23**, 33, (2011) 334214. 30
- [Kir08] P. S. Kirchmann. *Ultrafast Electron Dynamics in Low-Dimensional Materials*. Dissertation, Freie Universität Berlin (2008). 66, 69, 71
- [Kit80] C. Kittel. *Einführung in die Festkörperphysik*. R. Oldenbourg Verlag, München, Wien, 5. Auflage, (1980). 50
- [Kli10] C. Klingshirn, J. Fallert, H. Zhou, J. Sartor, C. Thiele, F. Maier-Flaig, D. Schneider, & H. Kalt. *65 years of ZnO research - old and very recent results*. Physica Status Solidi B **247**, 6, (2010) 1424. 30
- [Knu03] M. Knupfer. *Exciton binding energies in organic semiconductors*. Applied Physics A **77**, (2003) 623. 21
- [Koc06] S. W. Koch, M. Kira, G. Khitrova, & H. M. Gibbs. *Semiconductor excitons in new light*. Nature Materials **5**, 7, (2006) 523. 18

- [Koc07] N. Koch. *Organic Electronic Devices and Their Functional Interfaces*. ChemPhysChem **8**, (2007) 1438. 7, 29
- [Koc12] N. Koch. *Electronic structure of interfaces with conjugated organic materials*. Physica Status Solidi (RRL) **7**, (2012) 227 . 12, 13
- [Koe12] C. Koerner, C. Elschner, N. C. Miller, R. Fitzner, F. Selzer, E. Reinold, P. Bäuerle, M. F. Toney, M. D. McGehee, K. Leo, & M. Riede. *Probing the effect of substrate heating during deposition of DCV4T:C60 blend layers for organic solar cells*. Organic Electronics **13**, (2012) 623. 45
- [Kok03] A. Kokalj. *Computer graphics and graphical user interfaces as tools in simulations of matter at the atomic scale*. Computational Materials Science **28**, (2003) 155. 50
- [Koo34] T. Koopmans. *Über die Zuordnung von Wellenfunktionen und Eigenwerten zu den Einzelnen Elektronen Eines Atoms*. Physica **1**, (1934) 104. 59
- [Kor01] O. J. Korovyanko, R. Österbacka, X. M. Jiang, Z. V. Vardeny, & R. A. J. Janssen. *Photoexcitation dynamics in regioregular and regiorandom polythiophene films*. Physical Review B **64**, (2001) 235122. 53, 55, 56, 57, 158, 159, 160
- [Kro11] L. Kronik & Y. Shapira. *Surface photovoltage spectroscopy of semiconductor structures: at the crossroads of physics, chemistry and electrical engineering*. Surface and Interface Analysis **31**, (2011) 954 . 20
- [Kue13] S. Kuehn, S. Friede, S. Sadofev, S. Blumstengel, F. Henneberger, & T. Elsaesser. *Surface excitons on a ZnO(000 $\bar{1}$) thin film*. Applied Physics Letters **103**, (2013) 191909. 36, 96
- [Kun02] M. Kunat, St. Gil Girol, Th. Becker, U. Burghaus, & Ch. Wöll. *Stability of the polar surfaces of ZnO: A reinvestigation using He-atom scattering*. Physical Review B **66**, 8, (2002) 081402. 32
- [Kun03] M. Kunat, U. Burghaus, & Ch. Wöll. *Adsorption of hydrogen on the polar O-ZnO surface: a molecular beam study*. Physical Chemistry Chemical Physics **5**, (2003) 4962. 33, 100
- [Kur05] M. Kurtz, J. Strunk, O. Hinrichsen, M. Muhler, K. Fink, B. Meyer, & C. Wöll. *Active Sites on Oxide Surfaces: ZnO-Catalyzed Synthesis of Methanol from CO and H₂*. Angewandte Chemie, International Edition **44**, (2005) 2790. 30

-
- [Lag63] J. Lagois & K. Hümmer. *Experimental and Theoretical Effects of Surface Layers and Spatial Dispersion on the Free Exciton Reflectance of ZnO*. Physica Status Solidi B **72**, (1963) 393. 36
- [Lan71] N. D. Lang & W. Kohn. *Theory of Metal Surfaces: Work Function*. Physical Review B **3**, (1971) 1215. 11
- [Laq09] F. Laquai, Y.-S. Park, J.-J. Kim, & T. Basché. *Excitation Energy Transfer in Organic Materials: From Fundamentals to Optoelectronic Devices*. Macromolecules Rapid Communications **30**, (2009) 1203. 26
- [Laq15] F. Laquai, D. Andrienko, R. Mauer, & P. W. M. Blom. *Charge Carrier Transport and Photogeneration in P3HT:PCBM Photovoltaic Blends*. Macromolecules Rapid Communications **36**, (2015) 1001. 57
- [Lou83] R. Loudon. *Quantum Theorie of Light*. Oxford University Press, New York, (1983). 66
- [Lüt10] H. Lüth. *Solid Surfaces, Interfaces and Thin Films*. Springer-Verlag, Berlin Heidelberg, (2010). 14, 16
- [Mag97] L. Magnani, G. Rumbles, I. D. W. Samuel, K. Murray, S. C. Moratti, A. B. Holmes, & R. H. Friend. *Photoluminescence studies of chain interactions in electroluminescent polymers*. Synthetic Metals **84**, (1997) 899 . 56, 57, 162
- [Mar14] M. Marks, A. Schöll, & U. Höfer. *Formation of metal-organic interface states studied with 2PPE*. Journal of Electron Spectroscopy and Related Phenomena **195**, (2014) 263. 142
- [Mau10] R. Mauer, M. Kastler, & F. Laquai. *The Impact of Polymer Regioregularity on Charge Transport and Efficiency of P3HT:PCBM Photovoltaic Devices*. Advanced Functional Materials **20**, (2010) 2085. 53, 54
- [MB78] M. E. Michel-Beyerle, R. Haberkorn, J. Kinder, & H. Seidlitz. *Direct Evidence for the Singlet-Triplet Exciton Annihilation in Anthracene Crystals*. Physica Status Solidi B **85**, (1978) 45 . 26
- [Mee14] R. Meerheim, C. Körner, & K. Leo. *Highly efficient organic multi-junction solar cells with a thiophene based donor material*. Applied Physcs Letters **105**, (2014) 063306. 45
- [Mer68] R.E. Merrifield. *Diffusion and Mutual Annihilation of Triplet Excitons in Organic Crystals*. Accounts of Chemical Research **1**, (1968) 129. 26, 27

- [Mii00] T. Mii & H. Ueba. *Theory of time-resolved two-photon photoemission spectroscopy from metal surfaces*. Journal of Luminescence **87-89**, (2000) 898. 61
- [Mül12] K. Müller, M. Richter, S. Philip, M. Kunst, & D. Schmeißler. *Excited States in P3HT and P3HT/PCBM Blends*. BioNanoScience **2**, (2012) 42. 56, 57, 159, 160
- [Mor09] H. Morkoç & Ü. Özgür. *Zinc Oxide*. Wiley-VCH, Weinheim, (2009). 30
- [Mot38] N. F. Mott. *Note on the contact between a metal and an insulator or semiconductor*. Mathematical Proceedings of the Cambridge Philosophical Society **34**, (1938) 568. 14
- [Mot68] N. F. Mott. *Metal-Insulator Transition*. Reviews of Modern Physics **40**, (1968) 677 . 18
- [Mun10] M. Muntwiler & X.-Y. Zhu. *Dynamics at Solid State Surfaces and Interfaces Vol.1: Current Developments*. Wiley-VCH Verlag GmbH & Co. KGaA, Weinheim, (2010) 325. 18, 21, 24
- [Nar92] S. Narasimhan & D. Vanderbilt. *Elastic Stress Domains and the Herringbone Reconstruction on Au(111)*. Physical Review Letters **69**, (1992) 1564. IX, 50, 51
- [Nea06] J. B. Neaton, Mark S. Hybertsen, & Steven G. Louie. *Renormalization of Molecular Electronic Levels at Metal-Molecule Interfaces*. Physical Review Letters **97**, (2006) 216405. 13
- [Nic01] G. Nicolay, F. Reinert, S. Hüfner, & P. Blaha. *Spin-orbit splitting of the L-gap surface state on Au(111) and Ag(111)*. Physical Review B **65**, (2001) 033407. 52, 137
- [Oeh14] M. Oehzelt, N. Koch, & G. Heimel. *Organic semiconductor density of states controls the energy level alignment at electrode interfaces*. Nature Communications **5:4174**, (2014) 1. 13
- [Ono98] M. Ono & M. Kotani. *Time-resolved measurement of excitonic electron emission from a fluoranthrene crystal*. Chemical Physics Letters **295**, (1998) 493. 26, 27
- [Oza10] K. Ozawa & K. Mase. *Metallization of ZnO(10 $\bar{1}$ 0) by adsorption of hydrogen, methanol, and water: Angle-resolved photoelectron spectroscopy*. Physical Review B **81**, 20, (2010) 205322. VIII, 34

- [Oza11] K. Ozawa & K. Mase. *Comparison of the surface electronic structures of H-adsorbed ZnO surfaces: An angle-resolved photoelectron spectroscopy study*. Physical Review B **83**, 12, (2011) 125406. 3, 33, 34, 73, 85, 96, 98, 99, 100, 110
- [Pan15] F. Panzer, M. Sommer, H. Bäessler, M. Thelakkat, & A. Köhler. *Spectroscopic Signature of Two Distinct H-Aggregate Species in Poly(3-hexylthiophene)*. Macromolecules **48**, (2015) 1543. 5, 55, 155, 167
- [Poe15] C. Poelking, M. Tietze, C. Elschner, S. Olthof, D. Hertel, B. Baumeier, F. Würthner, K. Meerholze, K. Leo, & D. Adrienko. *Impact of mesoscale order on open-circuit voltage in organic solar cells*. Nature Materials **14**, (2015) 434. 43, 45, 135
- [Pow15] B. J. Powell. *Theories of phosphorescence in organo-transition metal complexes - From relativistic effects to simple models and design principles for organic light-emitting diodes*. Coordination Chemistry Reviews **295**, (2015) 46 . 24, 25
- [Rei01] F. Reinert, G. Nicolay, S. Schmidt, D. Ehm, & S. Hüfner. *Direct measurements of the L-gap surface states on the (111) face of noble metals by photoelectron spectroscopy*. Phys. Rev. B **63**, (2001) 115415. 52
- [Rei07] F. Reinert & S. Hüfner. *Photoemission Spectroscopy with Very High Energy Resolution: Studying the Influence of Electronic Correlations on the Millielectronvolt Scale*. Lecture Notes Physics **715**, (2007) 13. 59
- [Rei12] S. Reineke & Marc A. Baldo. *Recent progress in the understanding of exciton dynamics within phosphorescent OLEDs*. Physica Status Solidi A **209**, (2012) 2341. 25, 129
- [Ren05] V. De Renzi, R. Rousseau, D. Marchetto, R. Biagi, S. Scandolo, & U. des Pennino. *Metal Work-Function Changes Induced by Organic Adsorbates: A Combined Experimental and Theoretical Study*. Physical Review Letters **95**, (2005) 046804. 51, 73
- [Reu96] C. Reuß, W. Wallauer, & T. Fauster. *Image States of Ag on Au(111)*. Surface Review and Letters **3**, (1996) 1547. 51
- [Ric08] J.-P. Richters, T. Voss, L. Wischmeier, I. Rückmann, & J. Gutowski. *Influence of polymer coating on the low-temperature photoluminescence properties of ZnO nanowires*. Applied Physics Letters **92**, (2008) 011103. 36

- [Roh05] M. Rohleder, W. Berthold, J. Güdde, & U. Höfer. *Time-Resolved Two-Photon Photoemission of Buried Interface States in Ar/Cu(100)*. Physical Review Letters **94**, (2005) 017401. 10
- [Rul98] C. Rullière. *Laser Spectroscopy*. Springer, Berlin, (1998). 68, 74
- [Sak09] A. Sakamoto & M. Takezawa. *Picosecond time-resolved infrared absorption study on photoexcited dynamics of regioregular poly(3-hexylthiophene)*. Synthetic Metals **159**, (2009) 809 . 57
- [Sau59] G. Sauerbrey. *Verwendung von Schwingquarzen zur Wägung dünner Schichten und zur Mikrowägung*. Zeitschrift für Physik **155**, (1959) 206. 87
- [Sch38] W. Schottky. *Halbleitertheorie der Sperrschicht*. Naturwissenschaften **26**, (1938) 843. 14
- [Sch04a] D. Schneider, T. Rabe, T. Riedl, T. Dobbertin, M. Kröger, E. Becker, H.-H. Johannes, W. Kowalsky, T. Weimann, J. Wang, & P. Hinze. *Laser threshold reduction in all-spiro guest-host system*. Applied Physics Letters **85**, (2004) 1659. 3, 39
- [Sch04b] D. Schneider, T. Rabe, T. Riedl, T. Dobbertin, O. Werner, M. Kröger, E. Becker, H.-H. Johannes, W. Kowalsky, T. Weimann, J. Wang, P. Hinze, A. Gerhard, P. Stoössel, & H. Vestweber. *Deep blue widely tunable organic solid-state laser based on a spirobifluorene derivative*. Applied Physics Letters **84**, 23, (2004) 4693. 113
- [Sch05] D. Schneider, T. Rabe, T. Riedl, T. Dobbertin, M. Kröger, E. Becker, H.-H. Johannes, W. Kowalsky, T. Weimann, J. Wang, & P. Hinze. *Organic solid-state lasers based on sexiphenyl as active chromophore*. Journal of Applied Physics **98**, (2005) 043104. 113
- [Sch11] A. Schleife, C. Rödl, F. Fuchs, K. Hannewald, & F. Bechstedt. *Optical Absorption in Degenerately Doped Semiconductors: Mott Transition or Mahan Excitons?* Physical Review Letters **107**, 23, (2011) 236405. 19
- [Sch12a] C. Scharsich, R. H. Lohwasser, M. Sommer, U. Asawapirom, U. Scherf, M. Thelakkat, D. Neher, & A. Köhler. *Control of Aggregate Formation in Poly(3-hexylthiophene) by Solvent, Molecular Weight, and Synthetic Method*. Journal of Polymer Science Part B: Polymer Physics **50**, (2012) 442 . 54

- [Sch12b] M. Schrader, R. Fitzner, M. Hein, C. Elschner, B. Baumeier, K. Leo, M. Riede, P. Bäuerle, & D. Andrienko. *Comparative Study of Microscopic Charge Dynamics in Crystalline Acceptor-Substituted Oligothiophenes*. Journal of the American Chemical Society **134**, (2012) 6052. 45, 153, 154
- [Sch12c] Manuel Schrader, Christian Körner, Chris Elschner, & Denis Andrienko. *Charge transport in amorphous and smectic mesophases of dicyanovinyl-substituted oligothiophenes*. J. Mater. Chem. **22**, (2012) 22258. 45
- [Sch14] M. Schulze, M. Hänsel, & P. Tegeder. *Hot Excitons Increase the Donor/Acceptor Charge Transfer Yield*. Journal of Physical Chemistry C **118**, (2014) 28527. 55, 158
- [Sea79] M. P. Seah & W. A. Dench. *Quantitative Electron Spectroscopy of Surfaces: A Standard Data Base for Electron Inelastic Mean Free Paths in Solids*. Surface and Interface Analysis **1**, (1979) 2. 121
- [Sez15] H. Sezen, H. Shang, F. Bebensee, C. Yang, M. Buchholz, A. Nefedov, S. Heissler, C. Carbogno, M. Scheffler, P. Rinke, & C. Wöll. *Evidence for photogenerated intermediate hole polarons in ZnO*. Nature Communications **6**: 6901, (2015) 1. 20, 108
- [Sha96] J. Shah. *Ultrafast Spectroscopy of Semiconductors and Semiconductor Nanostructures*. Springer Series in Solid-State Sciences 115, Springer Science + Business Media, New York, (1996). 19
- [She04] E. E. Sheina, J. Liu, M. C. Iovu, D. W. Laird, & R. D. McCullough. *Chain Growth Mechanism for Regioregular Nickel-Initiated Cross-Coupling Polymerizations*. Macromolecules **37**, (2004) 3526. 54
- [Sho39] W. Shockley. *On the Surface States Associated with a Periodic Potential*. Physical Reviews **56**, (1939) 317. 8
- [Soh07] Y. Sohn & J. T. Stuckless. *Characteristics of Photoexcitations and Interfacial Energy Levels of Regioregular Poly(3-hexylthiophene-2,5-diyl) on Gold*. ChemPhysChem **8**, (2007) 1937. 5, 56, 58, 155, 160
- [Spa04] H. Spanggaard & F. C. Krebs. *A brief history of the development of organic and polymeric photovoltaics*. Solar Energy Materials and Solar Cells **83**, (2004) 125 . 43
- [SPEa] SPECS. *SpecsLab, Juggler and CCD Acquire Software for 2D and 3D Detect*. 80

- [SPEb] SPECS GmbH (Hrsg.): *PHOIBOS Hemispherical Energy Analyzer Series*. Version 2.2. Specs GmbH, (2008). 81
- [SR08] T. N. Singh-Rachford & F. N. Castellano. *Pd(II) Phtalocyanine-Sensitized Triplet-Triplet Annihilation from Rubrene*. Journal of Physical Chemistry A **112**, (2008) 3550. 26, 27, 130
- [Stä13] Julia Stähler, Oliver T. Hofmann, Patrick Rinke, Sylke Blumstengel, Fritz Henneberger, Yilei Li, & Tony F. Heinz. *Raman study of 2,7-bis(biphenyl-4-yl)-2',7'-ditertbutyl-9,9'-spirobifluorene adsorbed on oxide surfaces*. Chemical Physics Letters **584**, (2013) 74. 40, 89
- [Sta07] W. Staroske, M. Pfeiffer, K. Leo, & M. Hoffmann. *Single-Step Triplet-Triplet Annihilation: An Intrinsic Limit for the High Brightness Efficiency of Phosphorescent Organic Light Emitting Diodes*. Physical Review Letters **98**, (2007) 197402. 129
- [Sun05] C. K. Sun, S. Z. Sun, K. H. Lin, K. Y. J. Zhang, H. L. Liu, S. C. Liu, & J. J. Wu. *Ultrafast carrier dynamics in ZnO nanorods*. Applied Physics Letters **87**, (2005) 023106. 19
- [Tam32] I. Tamm. *Über eine mögliche Art der Elektronenbindung an Kristalloberflächen*. Journal of Physics F **76**, (1932) 849. 8
- [Tis08] W. A. Tisdale, M. Muntwiler, D. J. Norris, E. S. Aydil, & X.-Y. Zhu. *Electron Dynamics at the ZnO(10 $\bar{1}$ 0) Surface*. Journal of Physical Chemistry C **112**, (2008) 14682. 36, 37, 106, 107, 110, 112
- [Tor08] I. F. Torrente, K. J. Franke, & J. I. Pascual. *Spectroscopy of C60 single molecules: the role of screening on energy level alignment*. Journal of Physics: Condensed Matter **20**, (2008) 184001. 47
- [Var11a] E. Varene, I. Martin, & P. Tegeder. *Optically Induced Inter- and Intrafacial Electron Transfer Probed by Two-Photon Photoemission: Electronic States of Sexithiophene on Au(111)*. Journal of Physical Chemistry Letters **2**, (2011) 252. 43, 142
- [Var11b] E. Varene, Y. Pennec, & P. Tegeder. *Assembly and electronic structure of octithiophene on Au(111)*. Chemical Physics Letters **515**, (2011) 141. 47, 140
- [Var12a] E. Varene, L. Bogner, C. Bronner, & P. Tegeder. *Ultrafast Exciton Population, Relaxation, and Decay Dynamics in Thin Oligothiophene Films*. Physical Review Letters **109**, (2012) 207601. 23, 149

- [Var12b] E. Varene, L. Bogner, S. Meyer, Y. Pennec, & P. Tegeder. *Coverage-dependent adsorption geometry of octithiophene on Au(111)*. Physical Chemistry Chemical Physics **14**, (2012) 691. 9, 47, 52
- [Var12c] E. Varene & P. Tegeder. *Polaron dynamics in thin polythiophene films studied with time-resolved photoemission*. Applied Physics A **107**, (2012) 13. 5, 56, 57, 58, 155, 160, 162
- [Var12d] J. B. Varley, A. Janotti, C. Franchini, & C. G. Van de Walle. *Role of self-trapping in luminescence and p-type conductivity of wide-band-gap oxides*. Physical Review B **85**, (2012) 081109(R). 20
- [Ver11] M. A. M. Versteegh, T. Kuis, H. T. C. Stoof, & J. I. Dijkhuis. *Ultrafast screening and carrier dynamics in ZnO: Theory and experiment*. Physical Review B **84**, 3, (2011) 035207. 18
- [Ver12] M. A. M. Versteegh, A. J. van Lange, H. T. C. Stoof, & J. I. Dijkhuis. *Observation of preformed electron-hole Cooper pairs in highly excited ZnO*. Physical Review B **85**, 19, (2012) 195206. 19
- [Vid99] C. Videlot & D. Fichou. *Influence of molecular orientation on the photovoltaic properties of octithiophene*. Synthetic Metals **102**, 1-3, (1999) 885. 43
- [Vid00] C. Videlot, A. El Kassmi, & D. Fichou. *Photovoltaic properties of octithiophene-based Schottky and p/n junction cells: Influence of molecular orientation*. Solar Energy Materials and Solar Cells **63**, 1, (2000) 69. 43
- [Wan05a] H. T. Wang, B. S. Kang, F. Ren, L. C. Tien, P. W. Sadik, D. P. Norton, S. J. Pearton, & J. Lin. *Hydrogen-selective sensing at room temperature with ZnO nanorod*. Applied Physics Letters **86**, 24, (2005) 243503. 30
- [Wan05b] Y. Wang, B. Meyer, X. Yin, M. Kunat, D. Langenberg, F. Traeger, A. Birkner, & Ch. Wöll. *Hydrogen Induced Metallicity on the ZnO(10 $\bar{1}$ 0) Surface*. Physical Review Letters **95**, 26, (2005) 266104. 33, 34
- [Weg14] D. Wegkamp. *Ultrafast electron dynamics and the role of screening*. Dissertation, Freie Universität Berlin (2014). IX, 71, 72, 73, 81
- [Wes90] J. Wessel. *Biexcitonic Autoionization in Naphtalene Trimer Clusters*. Physical Review Letters **64**, (1990) 2046 . 26, 27

- [Wil03] H. Wilmer, M. Kurtz, K. V. Klementiev, O. P. Tkachenko, W. Grunert, O. Hinrichsen, A. Birkner, S. Rabe, K. Merz, M. Driess, C. Wöll, & M. Muhler. *Methanol synthesis over ZnO: A structure-sensitive reaction?* Physical Chemistry Chemical Physics **5**, (2003) 4736. 30
- [Wöl07] C. Wöll. *The chemistry and physics of zinc oxide surfaces*. Progress in Surface Science **82**, 2-3, (2007) 55. 31
- [Wol96] M. Wolf, E. Knoesel, & T. Hertel. *Ultrafast dynamics of electrons in image-potential states on clean and Xe-covered Cu(111)*. Physical Review B **54**, (1996) R5295. 10
- [Woo86] D. P. Woodruff, W. A. Royer, & N. V. Smith. *Empty surface states, image states, and band edge on Au(111)*. Physical Review B **34**, (1986) 764. 52
- [Wu10] Z. Wu, A. Petzold, T. Henze, T. Thurn-Albrecht, R. H. Lohwasser, M. Sommer, & M. Thelakkat. *Temperature and Molecular Weight Dependent Hierarchical Equilibrium Structures in Semiconducting Poly(3-hexylthiophene)*. Macromolecules **43**, (2010) 4646. IX, 53, 54, 55, 156
- [Yag08] T. Yago, Y. Tamaki, A. Furube, & R. Katoh. *Self-trapping limited exciton diffusion in a monomeric perylene crystal as revealed by femtosecond transient absorption microscopy*. Physical Chemistry Chemical Physics **10**, (2008) 4435. 26
- [Yan07] Y. Yang, B. K. Tay, X. W. Sun, J. Y. Sze, Z. J. Han, J. X. Wang, X. H. Zhang, Y. B. Li, & S. Zhang. *Quenching of surface-exciton emission from ZnO nanocombs by plasma immersion ion implantation*. Applied Physics Letters **91**, (2007) 071921. 36
- [Yan09] Q. Yang, M. Muntwiler, & X.-Y. Zhu. *Charge transfer excitons and image potential states on organic semiconductor surfaces*. Physical Review B **80**, (2009) 115214. 142, 143
- [Yan14a] Z. Yang. *Structural and Electronic Properties of Thiophene-based Supramolecular Architectures on Metal Surfaces*. Dissertation, Fachbereich Physik, Freie Universität Berlin (2014). IX, 4, 46, 47, 48, 93, 135, 138, 140, 141, 143, 145, 146, 147, 150, 153, 172
- [Yan14b] Z. Yang, M. Corso, R. Robles, C. Lotze, R. Fitzner, E. Mena-Osteritz, P. Bäuerle, K. J. Franke, & J. I. Pascual. *Orbital Redistribution in Molecular Nanostructures Mediated by Metal-Organic Bonds*. ACS Nano **8**, (2014) 10715. 46, 93, 135, 138, 141, 145, 172

- [Yos12] S. R. Yost, E. Hontz, S. Yeganeh, & T. Van Voorhis. *Triplet vs Singlet Energy Transfer in Organic Semiconductors: The Tortoise and the Hare*. The Journal of Physical Chemistry C **116**, (2012) 17369. 25, 26
- [Yos14] S. R. Yost, J. Lee, M. W. B. Wilson, T. Wu, D. P. MacMahon, R. R. Parkhurst, N. J. Thompson, D. N. Congreve, A. Rao, K. Johnson, M. Y. Sfeir, M. G. Bawendi, T. M. Swager, R. H. Friend, M. A. Baldo, & T. Van Voorhis. *A transferable model for singlet-fission kinetics*. Nature Chemistry **6**, (2014) 492. 25
- [Zau07] Y. Zaushitsyn, K. G. Jespersen, L. Valkunas, V. Sundström, & A. Yartsev. *Ultrafast dynamics of singlet-singlet and singlet-triplet exciton annihilation in poly(3-2' methoxy-5'octyl)thiophene films*. Physical Review B **75**, (2007) 195201. 26, 27
- [Özg05] Ü. Özgür, Ya. I. Alivov, C. Liu, A. Teke, M. a. Reshchikov, S. Doğan, V. Avrutin, S.-J. Cho, & H. Morkoç. *A comprehensive review of ZnO materials and devices*. Journal of Applied Physics **98**, 4, (2005) 041301. 31, 36
- [Zha12a] W. Zhang, R. Hu, D. Li, M.-M. Huo, X.-C. Ai, & J.-P. Zhang. *Primary Dynamics of Exciton and Charge Photogeneration in Solvent Vapor Annealed P3HT/PCBM Films*. Journal of Physical Chemistry C **116**, (2012) 4298. 56, 159, 160
- [Zha12b] Z. Zhang & Jr. J. T. Yates. *Band Bending in Semiconductors: Chemical and Physical Consequences at Surfaces and Interfaces*. Chemical Reviews **112**, (2012) 5520 . 14, 15
- [Zhu09] X.-Y. Zhu, Q. Yang, & M. Muntwiler. *Charge-Transfer Excitons at Organic Semiconductor Surfaces and Interfaces*. Accounts of Chemical Research **42**, (2009) 1779 . 24, 142, 143
- [Zhu10] V. P. Zhukov, P. M. Echenique, & E. V. Chulkov. *Two types of excited electron dynamics in zinc oxide*. Physical Review B **82**, 9, (2010) 094302. X, 37, 106, 107, 111, 112

References

Acknowledgement

Zuerst möchte ich mich bei Petra Tegeder dafür bedanken, dass sie mir die Möglichkeit gegeben hat meine Doktorarbeit in ihrer Gruppe anzufangen und auch nach ihrem Umzug nach Heidelberg stets erreichbar für mich und meine Belange geblieben ist. Ebenso großer Dank gebühren Julia Stähler und Martin Wolf, dafür dass sie mich am Fritz-Haber-Institut aufgenommen haben und mir ermöglicht haben an meine bisherige Arbeit anzuknüpfen. Darüber hinaus danke ich Julia für ihre engmaschige Betreuung und ihre vielen hilfreichen Anregungen.

I would like to acknowledge all the scientists with whom I had the possibility to collaborate with. In particular I would like to thank Zechao Yang, Nacho Pascual and Katharina Franke (Freie Universität Berlin) for the fruitful cooperation on the thiophenes. Roland Fitzner und Peter Bänderle (Universität Ulm) danke ich dafür, dass sie mir ihre DCV-substituierten Thiophene zur Verfügung gestellt haben. Furthermore I would like to thank Gaurav Gupta and Thomas Thurn-Albrecht (Universität Halle-Wittenberg) for the preparation of the P3HT films. Mino Sparenberg (AG Henneberger, HU Berlin) danke ich dafür, dass er mich mit der Spiroverbindung SP6 versorgt hat. Außerdem danke ich dem DFG-Schwerpunktprogramm 1355 und dem Sonderforschungsbereich 951 der DFG, die diese Arbeit mitfinanziert haben und mir darüber hinaus einen Rahmen für wissenschaftlichen Austausch geboten haben.

Ich danke meinen ehemaligen Kollegen von der FU, Chris, Stephan, Erwan, Michael S. und Michael M., Felix, Rocío und Laurenz für eine angenehme Arbeitatmosphäre und Dietgard für ihre Hilfe bei administrativen Dingen. Besonders danke ich Chris der mich vor vielen Jahren mit dem experimentellen Aufbau vertraut gemacht hat und stets für Fragen jeglicher Art zur Verfügung stand. Von der Universität Heidelberg danke ich Frau Neuner und Friedrich Maaß, die sich um die Weiterleitung meiner Unterlagen gekümmert haben.

Ebenso danke ich allen meinen Kollegen am FHI, vor allem der Electron Dynamix Gruppe. Besonders danke ich Jan, der mich in den Aufbau am FHI eingeführt hat und mit dem ich viele Stunden im Labor verbracht habe und dessen ZnO Expertenwissen ich jederzeit anzapfen konnte. Clemens danke ich ebenfalls für die vielen gemeinsamen Stunden im Labor; ohne Euch wäre es bestimmt weniger unterhaltsam gewesen! Besonderer Dank gebührt auch Laura, mit der ich viele erhellende Gespräche über SP6 und ZnO geführt habe, im Büro oder an der frischen Luft. I want to thank Sesha particularly for critical review of part of this thesis and for helpful discussions about P3HT. Meinen neuen Büronachbarn Alex und Joachim danke ich für die freundliche Aufnahme. Natürlich könnte ich jetzt zu jedem einzelnen einen Satz schreiben, aber machen wir's kurz: Danke Selene, Marc, Lutz, Daniel, Lukas und Sarah für gemeinsame Mittagessen, Gespräche zwischen Tür und Angel

und unterhaltsame Kaffeepausen. Des Weiteren danke ich allen Mitarbeitern der Abteilung PC, die einem das Leben in administrativen und technischen Belangen erleichtern, Albrecht, Marcel, Manuel, Daria, Waruno, Frau Ziebarth und allen die ich an dieser Stelle vergessen habe.

Ich danke ‘meinen’ Chemikern, Jule, Christoph und Olaf, die mich vom Anfang des Studiums an begleitet haben, für viele amüsante Mittagessen, die das Mensaessen ungemein aufgewertet haben. Besonders danke ich Jule für’s NMR messen und Christoph für extrem engagiertes Korrekturlesen. Ich danke meinen Freunden Grusche und Johannes, ohne deren häufiges Babysitten ich nicht mal den Bachelor geschafft hätte. Gesine und Enku danke ich ebenfalls für sämtliche Nachmittage in denen sie Samira mitgenommen haben. Ich danke meinen Geschwistern und Freunden für all die offenen Ohren und dafür dass ich mich auf sie verlassen kann. Danke Lisa, Simon, Suse, Franzi, Ivana, Judith, Nina und Cordula.

Meinen Eltern danke ich für regelmäßige Ferienbetreuung und jahrelange Unterstützung. Ich danke meiner Tochter Samira dafür, dass sie meinen Alltag abwechslungsreich und bunt macht, mich auch im größten Arbeitsstress auf andere Gedanken bringt und natürlich für ihre leckeren Pfannkuchen! Ganz besonders großer Dank gebührt ‘meinem’ Martin ohne den alles viel schwieriger wäre. Danke für warmes Essen, jahrelange Samirabespaßung, Diskussionen über wie man was verständlich ausdrückt, Korrekturlesen und vieles mehr.

Academic Curriculum Vitae

The curriculum vitae is omitted in this online version due to data privacy.

List of Publications

Publications within this thesis

Lea Bogner, Zechao Yang, Martina Corso, Roland Fitzner, Peter Bäuerle, Katharina J. Franke, José Ignacio Pascual and Petra Tegeder *Electronic structure and excited state dynamics in a dicyanovinyl-substituted oligothiophene on Au(111)*, Physical Chemistry Chemical Physics *17*, (2015), 27118

Laura Foglia, Lea Bogner, Julia Stähler and Martin Wolf, *Exciton trapping in vibrationally excited organic molecules near a ZnO surface*, arXiv:1412.0597, (2014)

Publications concerning other topics

Erwan Varène, Lea Bogner, Stephan Meyer, Yan Pennec and Petra Tegeder, *Coverage-dependent adsorption geometry of octithiophene on Au(111)*, Physical Chemistry Chemical Physics *14*, (2012), 691

Erwan Varène, Lea Bogner, Christopher Bronner and Petra Tegeder, *Ultrafast Exciton Population, Relaxation, and Decay Dynamics in Thin Oligothiophene Films*, Physical Review Letters *109*, (2012), 207601

Selbstständigkeitserklärung gemäß §7 der Promotionsordnung

Sämtliche verwendeten Hilfsmittel, Hilfen und Quellen sind an der entsprechenden Stelle angegeben. Ich versichere, dass ich auf dieser Grundlage diese Arbeit selbstständig verfasst habe. Diese Arbeit wurde bisher weder in gleicher noch ähnlicher Form einer anderen Prüfungskommission vorgelegt oder veröffentlicht.

Berlin, den 04.11.2015

Lea Bogner